

# The multiple Davydov D2 Ansatz and its applications

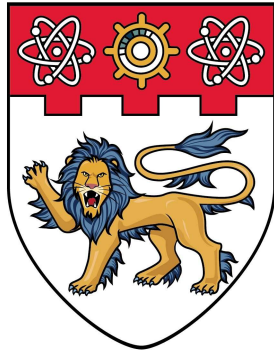
Huang, Zhongkai

2018

Huang, Z. (2018). The multiple Davydov D2 Ansatz and its applications. Doctoral thesis, Nanyang Technological University, Singapore.

<https://hdl.handle.net/10356/89649>

<https://doi.org/10.32657/10220/47718>



**NANYANG  
TECHNOLOGICAL  
UNIVERSITY**  

---

**SINGAPORE**

**THE MULTIPLE DAVYDOV  $D_2$  ANSATZ AND ITS  
APPLICATIONS**

**HUANG ZHONGKAI**

**SCHOOL OF MATERIALS SCIENCE AND ENGINEERING**

**2018**







# **THE MULTIPLE DAVYDOV $D_2$ ANSATZ AND ITS APPLICATIONS**

**HUANG ZHONGKAI**

**SCHOOL OF MATERIALS SCIENCE AND ENGINEERING**

A thesis submitted to the Nanyang Technological University  
in partial fulfilment of the requirement for the degree of  
Doctor of Philosophy

**2018**



## Statement of Originality

I hereby certify that the work embodied in this thesis is the result of original research and has not been submitted for a higher degree to any other University or Institution.

2018/7/4

.....

Date

*Huang Zhongkai*

.....

Huang Zhongkai





## Supervisor Declaration Statement

I have reviewed the content and presentation style of this thesis and declare it is free of plagiarism and of sufficient grammatical clarity to be examined. To the best of my knowledge, the research and writing are those of the candidate except as acknowledged in the Author Attribution Statement. I confirm that the investigations were conducted in accord with the ethics policies and integrity standards of Nanyang Technological University and that the research data are presented honestly and without prejudice.

2018/7/4

.....

Date



.....

Zhao Yang



## Authorship Attribution Statement

This thesis contains material from papers published in the following peer-reviewed journals where I was the first author.

Chapter 4 is published as Z. Huang, L. Wang, C. Wu, L. Chen, F. Grossmann, and Y. Zhao, Polaron dynamics with off-diagonal coupling: beyond the Ehrenfest approximation. *Physical Chemistry Chemical Physics*, **19**, 1655 (2017). DOI: 10.1039/C6CP07107D.

The contributions of the co-authors are as follows:

- I provided results from the multi- $D_2$  ansatz and wrote the draft of the manuscript.
- Dr. Lu Wang developed the importance sampling method to treat the finite temperature effects.
- Prof. Changqin Wu figured out the equivalence between the Ehrenfest method and the Dirac-Frenkel time-dependent variational method with the single  $D_2$  ansatz.
- Dr. Lipeng Chen conducted simulations of temperature effects in the Holstein model from the hierarchical equations of motion method.
- Prof. Frank Grossmann contributed to the results of temperature effects in the spin-boson model using the method of averaged Hamiltonian with the Davydov  $D_1$  ansatz.
- Prof. Yang Zhao supervised the whole project.

Chapter 5 is published as Z. Huang, L. Chen, N. Zhou, and Y. Zhao, Transient dynamics of a one-dimensional Holstein polaron under the influence of an external electric field. *Annalen der Physik (Berlin)*, **529**, 1600367 (2017). DOI: 10.1002/andp.201600367.

The contributions of the co-authors are as follows:

- I produced results from the multi- $D_2$  ansatz and wrote the draft of the manuscript.
- Dr. Lipeng Chen gave results from the hierarchical equations of motion method.
- Prof. Nengji Zhou contributed to discussions.

- Prof. Yang Zhao supervised the whole project.

Chapter 6 is published as Z. Huang, Y. Fujihashi, and Y. Zhao, Effect of off-diagonal exciton-phonon coupling on intramolecular singlet fission. *The Journal of Physical Chemistry Letters*, **8**, 3306 (2017). DOI: 10.1021/acs.jpclett.7b01247.

The contributions of the co-authors are as follows:

- I calculated results from the multi-D<sub>2</sub> anstaz and wrote the draft of the manuscript.
- Dr. Yuta Fujihashi made a contribution to building a dimer model of singlet fission dynamics and produced results from the master equation method.
- Prof. Yang Zhao supervised the whole project.

Chapter 7 is published as Z. Huang and Y. Zhao, Dynamics of dissipative Landau-Zener transitions. *Physical Review A*, **54**, 4636 (2015). DOI: 10.1021/ic502747p.

The contributions of the co-authors are as follows:

- I performed calculations and wrote the draft of the manuscript.
- Prof. Yang Zhao supervised the whole project.

2018/7/4

.....

Date

Huang Zhongkai

.....

Huang Zhongkai

## Abstract

In order to accurately characterize dynamics of the Holstein polaron with simultaneous diagonal and off-diagonal exciton-phonon coupling, a series of multiple Davydov trial states, i.e., the multiple Davydov  $D_1$ ,  $D_{1.5}$ ,  $D_2$ , and  $\tilde{D}$  ansätze, are formulated as superpositions of the correspondingly single Davydov  $D_1$ ,  $D_{1.5}$ ,  $D_2$ , and  $\tilde{D}$  ansätze. In this thesis, the multiple Davydov  $D_2$  ansatz, also known as the multi- $D_2$  ansatz, is demonstrated to enable numerically exact dynamics for various open quantum systems with off-diagonal coupling and is applied to study complicated dynamical quantum behaviours, such as the exciton transport in conducting polymers, Bloch oscillations dynamics in semiconductor superlattices and organic materials, singlet fission processes, and the Landau-Zener transitions in circuit quantum electrodynamics devices.

We first use the Dirac-Frenkel time-dependent variational principle combined with the multi- $D_2$  ansatz to fully quantum mechanically investigate dynamics of a one-dimensional molecular crystal model with off-diagonal exciton-phonon coupling, which is treated traditionally by the Ehrenfest approximation for the description of the exciton transport in the conducting polymers. It is shown that the Ehrenfest method is equivalent to our variational method with the single  $D_2$  ansatz, and with the multi- $D_2$  ansatz, the accuracy of our simulated dynamics is significantly enhanced in comparison with the semi-classical Ehrenfest dynamics. The multi- $D_2$  ansatz is able to capture numerically accurate exciton momentum probability and help clarify the relation between the exciton momentum redistribution and the exciton energy relaxation. The results demonstrate that the exciton momentum distributions in the steady state are determined by a combination of the transfer integral and the off-diagonal coupling strength, independent of the excitonic initial conditions. We also probe the effect of the transfer integral and the off-diagonal coupling on exciton transport in both real and reciprocal space representations. Finally, the variational method with importance sampling is employed to investigate temperature effects on the exciton transport using the multi- $D_2$  ansatz, and it is demonstrated that the variational approach is valid in both low and high temperature regimes.

Next, the multi- $D_2$  ansatz is employed to study transient dynamics of a one-dimensional Holstein polaron with diagonal and off-diagonal carrier-phonon coupling in an external electric field, aiming to help better understand Bloch oscillations dynamics in the semiconductor superlattices and the organic materials. Resultant polaron dynamics has significantly enhanced accuracy, and is in perfect agreement with that derived from the hierarchy equations of motion method. Starting from an initial broad wave packet, the charge carrier undergoes typical Bloch oscillations. Adding weak carrier-phonon coupling leads to a broadened carrier wave packet and a reduced current amplitude. Using a narrow wave packet as the initial state, the bare carrier oscillates in a symmetric breathing mode, but the symmetry is easily broken by weak coupling to phonons, resulting in a non-zero carrier current. For both scenarios, temporal periodicity is unchanged by carrier-phonon coupling. In particular, at variance with the case of an infinite linear chain, no steady state is found in a finite-sized ring within the anti-adiabatic regime. For strong diagonal coupling, the multi- $D_2$  ansatz is found to be highly accurate, and the phonon confinement gives rise to carrier localization and decay of the Bloch oscillations.

Furthermore, we adopt the multi- $D_2$  ansatz to explore dynamics of a newly formulated microscopic model of intramolecular singlet fission with simultaneous diagonal and off-diagonal coupling to high-frequency modes. It is shown that both diagonal and off-diagonal coupling can aid efficient singlet fission if excitonic coupling is weak, and fission is only facilitated by diagonal coupling if excitonic coupling is strong. In the presence of off-diagonal coupling, it is found that high frequency modes create additional fission channels for rapid iSF.

Finally, the multi- $D_2$  ansatz is employed to examine dynamics of the Landau-Zener model with both diagonal and off-diagonal qubit-bath coupling. It is shown that steady-state transition probabilities agree with analytical predictions at long times. Landau-Zener dynamics at intermediate times is little affected by diagonal coupling, and is found to be determined by off-diagonal coupling and tunneling between two diabatic states. We investigate effects of bath spectral densities, coupling strengths and interaction

angles on Landau-Zener dynamics. Thanks to the multiple Davydov trial states, detailed boson dynamics can also be analyzed in Landau-Zener transitions.

To summarize, in this thesis we adopt a time-dependent variational approach utilizing the multi- $D_2$  ansatz, to accurately investigate dynamics of four open quantum systems with electronic and bosonic degrees of freedom. Calculations in this thesis help illustrate the effects of the transfer integral and the off-diagonal coupling on the exciton transport in off-diagonal Holstein polaron model representing the conducting polymers, and the influences of the external electric field on transient dynamics of the one-dimensional Holstein polaron modeling the semiconductor superlattices and organic materials. Results presented in the thesis may help provide guiding principles for design of efficient singlet fission materials by directly tuning singlet-triplet interstate coupling, and to manipulate the Landau-Zener transitions in circuit quantum electrodynamics architectures by tuning off-diagonal coupling and tunneling strength. It is also our hope that the multi- $D_2$  ansatz can be applied to more exciton-phonon coupled systems.





## Lay Summary

In any physical realization, a quantum many-body system will be affected by its environment, which may alter effective interactions between energy levels of the system. In order to accurately describe the state of a quantum system, it is thus necessary to consider environmental influences, which play an important role in the dynamical behavior of the system.

The environment is typically modelled as a bath coupled to the target system. Due to the complexity of system-bath interactions, it is difficult to devise exact analytical solutions for the dynamics of most open quantum systems. In general, methods for the study of open quantum systems can be classified into two categories: wave function based methods that operate in the Hilbert space and density matrix based approaches in the Liouville space of the system. These methods have proven their validities in fields such as quantum measurement theory, quantum statistical mechanics, and quantum thermodynamics.

However, methodologies used to investigate dynamics of the open quantum system can differ greatly depending on target systems and desired objectives. Moreover, each method developed for the open quantum systems has its limitations. For instance, methods such as quasi-adiabatic propagator path integral and hierarchical equations of motion are considered exact but computationally expensive. Perturbative methods such as the master equation method are able to provide efficient calculations but can become inaccurate in certain parameter regimes. In particular, accurate modeling of polaron dynamics have not received much-deserved attention over the last six decades.

In this thesis, we develop the multiple Davydov  $D_2$  ansatz, also known as the multi- $D_2$  ansatz, to accurately address the dynamics of certain open quantum systems containing electronic and bosonic degrees of freedom. The investigated systems include Holstein molecular crystal model with and without an external electric field, novel singlet fission

materials with intramolecular singlet fission mechanisms, and the quantum qubit in the quantum electrodynamics devices.

The outcomes are of great significance to the simulation of dynamics of open quantum systems. Firstly, when investigating dynamics of a one-dimensional molecular crystal model with off-diagonal exciton-phonon coupling, the Ehrenfest method is shown to be equivalent to the Dirac-Frenkel time-dependent variational principle with the single  $D_2$  ansatz. The accuracy of the simulated dynamics with the multi- $D_2$  ansatz is significantly enhanced in comparison with the semi-classical Ehrenfest dynamics. Secondly, the multi- $D_2$  ansatz enables an accurate description of the polaron dynamics in the presence of an external electric field. The addition of carrier-phonon coupling is found to change the movement patterns of bare carrier under the external field. Thirdly, the singlet fission dynamics is accurately treated by the multi- $D_2$  ansatz using a microscopic model of intramolecular singlet fission with simultaneous diagonal and off-diagonal coupling to high-frequency modes. Finally, the multi- $D_2$  ansatz is successfully applied to explore the dissipative Landau-Zener dynamics at intermediate times in circuit quantum electrodynamics architectures.

## Acknowledgments

A special thanks to my supervisor, Professor Zhao Yang, for his countless valuable suggestions and assistance during my phd study. I am grateful to Prof. Zhao for carefully reading the thesis and giving many helpful suggestions for thesis improvements.

I would like to thank Professor Nengji Zhou from HangZhou Normal Univeristy and Professor Kewei Sun from Hangzhou Dianzi University for useful discussion on construction of the multiple Davydov ansätze. I appreciate valuable guidance from Professor Vladimir Chernyak at Wayne State University on validity of the ansätze. I have been tremendously improved from fruitful discussion with Dr. Yuta Fujihashi about singlet fission processes and Dr. Lu Wang about the importance sampling method. I would also like to show thanks to Professor Changqin Wu from Fudan University and Professor Frank Grossmann from Dresden University of Technology for discussion about the Ehrenfest approximation and revisions of the manuscript. I have learned immensely from visiting scholars, Professor John Zenghui Zhang at New York University Shanghai, Dr. Maxim Gelin, Professor Yuyu Zhang from Chongqing University, Professor Rafael Alejandro Molina Fernández from Instituto de Estructura de la Materia, Consejo Superior de Investigaciones Científicas, Dr. Dazhi Xu, Dr. Guankui Long, Dr. Jun Ye, Dr. Hao Li, Dr. Jia Li, Mr. Jiangfeng Zhu, Mr. Tianrui Deng, Dr. Jing Lu, and Ms. Mengting Jin. Specially, I would like to express my heartiest thankfulness to Dr. Prathamesh Mahesh Shenai, Dr. Lipeng Chen, Dr. Fulu Zheng, and Mr. Alejandro Somoza Márquez for their great help on various research issues.

A special gratitude goes out to Singapore National Research Foundation for providing the funding through Competitive Research Programme (CRP) under Project No. NRF-CRP5-2009-04. I would like to acknowledge with much appreciation to School of Materials Science and Engineering as well as Nanyang Technological University for comfortable environments. I am also grateful to a number of friends and colleagues for

their encouragement and assistance on both scientific and non-scientific concerns.

Last but not the least, I would like to express my greatest gratitude to full support of beloved families throughout my life in general.

## Table of Contents

<b>Abstract</b>	<b>i</b>
<b>Lay Summary</b>	<b>v</b>
<b>Acknowledgments</b>	<b>vii</b>
<b>Table of Contents</b>	<b>ix</b>
<b>Figure Captions</b>	<b>xiii</b>
<b>Abbreviations</b>	<b>xxi</b>
<b>Chapter 1 Introduction</b>	<b>1</b>
1.1 Background	2
1.2 Objectives and Scope	5
1.3 Dissertation Overview	9
1.4 Findings and Outcomes/Originality	12
References	12
<b>Chapter 2 Literature Review</b>	<b>19</b>
2.1 Overview of the Davydov ansätze	20
2.2 Potential applications of the multiple Davydov $D_2$ ansatz	26
2.2.1 Exciton transport in conducting polymers	27
2.2.2 Bloch oscillations dynamics in semiconductor superlattices and organic materials	29
2.2.3 Singlet fission processes	31
2.2.4 Landau-Zener transitions in the circuit quantum electrodynamics devices	33

References	36
<b>Chapter 3 Overview of Theoretical Methodologies</b>	<b>51</b>
3.1 The Dirac-Frenkel Time-dependent Variational Principle	52
3.2 The Davydov ansätze	53
3.3 Models for applications of the multiple Davydov $D_2$ ansatz	56
3.3.1 A one-dimensional Holstein molecular crystal model with off-diagonal exciton-phonon coupling	57
3.3.2 A one-dimensional Holstein polaron in an external electric field	59
3.3.3 A dimer model of intramolecular singlet fission dynamics	61
3.3.4 Dissipative Landau-Zener model	64
References	66
<b>Chapter 4 Polaron dynamics with off-diagonal coupling</b>	<b>69</b>
4.1 Introduction	70
4.2 The multi- $D_2$ Davydov ansatz	71
4.3 Polaron dynamics in exciton momentum representation	73
4.4 Effect of transfer integral and off-diagonal coupling on exciton transport	77
4.5 Temperature effects	82
References	84
<b>Chapter 5 Transient polaron dynamics in an external electric field</b>	<b>87</b>
5.1 Introduction	88
5.2 Validity of variation for transient dynamics	89
5.2.1 Diagonal Coupling	89
5.2.2 Off-diagonal Coupling	90
5.3 Anti-adiabatic regime	93

5.4 Strong diagonal coupling . . . . .	100
References . . . . .	103
<b>Chapter 6 Dynamics of intramolecular singlet fission . . . . .</b>	<b>107</b>
6.1 Introduction . . . . .	108
6.2 Validity of variational dynamics for the singlet fission process . . . . .	109
6.3 Population Dynamics . . . . .	110
6.3.1 Effect of excitonic coupling on fission dynamic . . . . .	111
6.3.2 Effect of exciton-phonon coupling on fission dynamics . . . . .	113
References . . . . .	116
<b>Chapter 7 Dynamics of dissipative Landau-Zener transitions . . . . .</b>	<b>119</b>
7.1 Introduction . . . . .	120
7.2 A qubit coupled to a single mode . . . . .	120
7.3 Effect of the bath spectral density . . . . .	125
7.4 Effects of coupling strength and interaction angle . . . . .	130
References . . . . .	133
<b>Chapter 8 Conclusions . . . . .</b>	<b>137</b>
<b>Chapter 9 Recommendations for Future Work . . . . .</b>	<b>143</b>
9.1 Applications of neural networks to the simulation of dynamics of open quantum systems . . . . .	144
9.2 Manipulation of photon delocalization in a Rabi dimer . . . . .	145
References . . . . .	147



<b>Appendices</b>	<b>150</b>
Appendix A For polaron dynamics with off-diagonal coupling	150
Appendix B For transient polaron dynamics in an external electric field	161
Appendix B For dynamics of dissipative Landau-Zener transitions	168
References	172
<b>List of Publications</b>	<b>175</b>

## Figure Captions

**Figure 4.1** The relative deviation  $\sigma$  of the multi- $D_2$  ansatz is displayed as a function of  $1/M$  for a commonly used set of parameters with off-diagonal coupling  $\phi = 2.0$  and large transfer integral  $J = 7.4$ . In the inset, the relationship  $\sigma \sim M^\mu$  is displayed on a log-log scale and the dashed line represents a power-law fit. . . . . 71

**Figure 4.2** MSD ( $t$ ) of the exciton for the case of  $J = 7.4$  and  $\phi = 2.0$  is obtained from the single  $D_2^{M=1}$ , the  $D_2^{M=8}$ , the  $D_2^{M=16}$ , and the  $D_2^{M=22}$  ansatz, respectively. . . 72

**Figure 4.3** (a)-(d) Time evolution of the exciton momentum probability  $P_{\text{ex}}(t, k)$  displayed in two columns is obtained using excitonic initial conditions:  $P_{\text{ex}}(0, k = 0) = 1$  (left column) and  $P_{\text{ex}}(0, k = \pi) = 1$  (right column). Two transfer integrals,  $J = 0.6$  and  $-0.6$ , are used together with the same off-diagonal coupling strength of  $\phi = 1$ , respectively. Energies for the case of  $J = 0.6$  and  $\phi = 1$  are plotted for (e)  $P_{\text{ex}}(0, k = 0) = 1$  and (f)  $P_{\text{ex}}(0, k = \pi) = 1$ . Energies of the exciton and the exciton-phonon coupling are displayed for each exciton momentum  $k$  using the initial condition of (g)  $P_{\text{ex}}(0, k = 0) = 1$  and (h)  $P_{\text{ex}}(0, k = \pi) = 1$ . The number of sites  $N = 8$  is fixed in these calculations. . . . . 74

**Figure 4.4** Time evolution of the exciton momentum probability  $P_{\text{ex}}(t, k)$  for  $J = 0$  and  $\phi = 1$  is obtained using two initial conditions: (a)  $P_{\text{ex}}(0, k = 0) = 1$  (left column) and (b)  $P_{\text{ex}}(0, k = \pi) = 1$  (right column). Corresponding energies are displayed in (c) and (d). The contribution to the exciton-phonon interaction energy from each exciton momentum are shown in (e) and (f). . . . . 76

**Figure 4.5** Time evolution of the exciton probability in the site space  $P_{\text{ex}}(t, n)$  for the case of the off-diagonal coupling ( $\phi = 1.0$ ) is obtained with transfer integrals (a)  $J = 0.5$ , (b) 0, and (c)  $-0.5$ ; Related time evolution of the exciton probability in the momentum space  $P_{\text{ex}}(t, k)$  is shown in (d)-(f); (g) MSD  $(t)$  of  $J = 0.6, 0.5, 0, -0.5$  and  $-0.6$  together with  $\phi = 1.0$  is plotted in the site representation; (h)  $\text{MSD}_k(t)$  is displayed in the exciton momentum representation; (i) Energy bands of the ground state are obtained from the Toyozawa ansatz. The number of sites  $N = 32$  is fixed in these calculations. . . . . 78

**Figure 4.6** (a) MSD  $(t)$  of the exciton in the site representation is shown for  $J = 0$  and  $\phi = 0.7, 0.8, 0.9, 1.0, 1.1, 1.2$  and  $1.3$ ; Related  $\text{MSD}_k(t)$  in the exciton momentum representation is displayed in (b). . . . . 80

**Figure 4.7** Time evolution of the exciton probability in the site space  $P_{\text{ex}}(t, n)$  obtained at  $T = 0$  and  $2/k_B$ .  $P_{\text{ex}}(t, n)$  at  $T = 0$  obtained from (a) the  $D_2^{M=16}$  ansatz, (b) the HEOM method, and (c)  $\Delta P_{\text{ex}}(t, n)$  between the  $D_2^{M=16}$  ansatz and the HEOM method;  $P_{\text{ex}}(t, n)$  obtained from (d) the  $D_2^{M=16}$  ansatz, (e) the HEOM method, and (f) the related  $\Delta P_{\text{ex}}(t, n)$  at  $T = 2/k_B$  ( $\beta = 0.5$ ). . . . . 83

**Figure 5.1** Time evolution of the carrier probability  $P_{\text{ca}}(t, n)$  for a diagonal coupling case of  $J = 0.1, g = 0.28$  and  $F = 0.1$  is obtained from (a) the single  $D_2^{M=1}$  ansatz, (b) the  $D_2^{M=16}$  ansatz, and (c) the HEOM method. The difference  $\Delta P_{\text{ca}}(t, n)$  between the HEOM and the  $D_2^{M=16}$  trial state is displayed in (d). The time unit  $t_B$  denotes the time period of BOs.  $N = 8$  is used in the calculations. . . . . 90

**Figure 5.2** Time evolution of the carrier probability  $P_{\text{ca}}(t, n)$  for a off-diagonal coupling case of  $J = 0.1, \phi = 0.28$  and  $F = 0.1$  is obtained from (a) the  $D_2^{M=1}$  ansatz, (b) the  $D_2^{M=8}$  ansatz, (c) the  $D_2^{M=20}$  ansatz, and (e) the HEOM method. (d) The difference between the  $D_2^{M=8}$  and  $D_2^{M=20}$  ansätze and (f)  $\Delta P_{\text{ca}}(t, n)$  between the HEOM and the  $D_2^{M=20}$  ansatz are displayed. . . . . 91

**Figure 5.3** Relative deviation  $\Sigma$  from the multi- $D_2$  ansatz is displayed as a function of  $1/M$  with parameters  $J = 0.1, \phi = 0.28$  and  $F = 0.1$ . The inset reveals the relationship  $\Sigma \sim M^\mu$  on a log-log scale, where the dashed line represents a power-law fit. . . . . 91

**Figure 5.4** Time evolution of the carrier probability  $P_{\text{ca}}(t, n)$  obtained from the  $D_2^{M=16}$  ansatz in the case of  $J = 0.1$  and  $F = 0.1$  and an initial broad Gaussian wave packet of  $\sigma_0 = 1$  is displayed in (a) ( $g = 0$ ) and (b) ( $g = 0.4$ ). In the presence of weak diagonal coupling ( $g = 0.4$ ), the phonon displacement  $X_{\text{ph}}(t, n)$  is shown for (c) acoustic phonons and (d) optical phonons. . . . . 94

**Figure 5.5** Time evolution of the carrier probability  $P_{\text{ca}}(t, n)$  obtained from the  $D_2^{M=16}$  ansatz in the case of  $J = 0.1$  and  $F = 0.1$  and an initial narrow Gaussian wave packet of  $\sigma_0 = 0.2$  is shown in (a) ( $g = 0$ ) and (b) ( $g = 0.4$ ). The phonon displacement  $X_{\text{ph}}(t, n)$  is shown for (c) the acoustic phonons and (d) optical phonons respectively in the presence of  $g = 0.4$ . . . . . 95

**Figure 5.6** (a) Mean value  $c(t)$ , (c) standard deviation  $\sigma(t)$  and (e) current  $j(t)$  as functions of the time  $t$  in the case of  $J = 0.1$  are displayed using the initial standard deviation  $\sigma_0 = 1$  and (b),(d),(f) using  $\sigma_0 = 0.2$ , respectively. In each panel, the results with  $g = 0$  and  $g = 0.4$  are compared. . . . . 97

**Figure 5.7**  $E_{\text{ca}}(t)$ ,  $E_{\text{ph}}(t)$ ,  $E_{\text{diag}}(t)$  and  $E_{\text{diag}}(t)$  obtained by the  $D_2^{M=16}$  ansatz in the case of  $J = 0.1$ ,  $F = 0.1$  and  $\sigma_0 = 0.1$  in the presence of weak diagonal coupling ( $g = 0.4$ ) with the optical phonons. . . . . 97

**Figure 5.8** Time evolution of the carrier probability  $P_{\text{ca}}(t, n)$  obtained from the  $D_2^{M=16}$  ansatz in the case of  $J = 1$ ,  $N = 16$  and a moderate external field of  $F = 1$  is displayed for different diagonal coupling strengths: (a)  $g = 0$ , (b)  $g = 3$  and (c)  $g = 4$ . Corresponding currents  $j(t)$  are shown in (d). . . . . 101

**Figure 5.9** Time evolution of the carrier probability  $P_{\text{ca}}(t, n)$  obtained from the  $D_2^{M=16}$  ansatz in the case of  $J = 1$ ,  $N = 16$  and a strong external field of  $F = 70$  is displayed for different diagonal coupling strengths: (a)  $g = 0$ , (b)  $g = 3$  and (c)  $g = 4$ . Corresponding currents  $j(t)$  are shown in (d). . . . . 102

**Figure 6.1** The relative deviation  $\sigma$  of the multi- $D_2$  ansatz is displayed as a function of  $1/M$ . The parameters are set to be  $\hbar\omega_{\text{diag}} = 90$  meV,  $\hbar\omega_{\text{vib2}} = 65$  meV,  $J_{\text{S}_1, \text{TT}} = 20$  meV,  $\epsilon_{\text{S}_1, \text{g}} - \epsilon_{\text{TT}, \text{g}} = 100$  meV,  $\gamma_{\text{diag}}^{-1} = \gamma_{\text{o.d.}}^{-1} = 1$  ps,  $S_{\text{S}_1} = 0.7$ ,  $S_{\text{TT}} = 1.4$  and  $S_{\text{S}_1, \text{TT}}^{\text{off}} = 0.1$ . . . . . 109

**Figure 6.2** Time evolution of singlet population calculated by the multilevel Red-field approach at  $T = 1K$  and the multi- $D_2$  ansatz at  $T = 0K$ . The frequency of the phonon mode is set to be  $\hbar\omega_{\text{diag}} = 40$  meV,  $\hbar\omega_{\text{o.d.}} = 0$  meV. The other parameters are fixed at  $J_{\text{S}_1, \text{TT}} = 10$  meV,  $\epsilon_{\text{S}_1, \text{g}} - \epsilon_{\text{TT}, \text{g}} = 50$  meV,  $\gamma_{\text{diag}}^{-1} = \gamma_{\text{o.d.}}^{-1} = 1$  ps,  $S_{\text{S}_1} = 0.7$ ,  $S_{\text{TT}} = 1.4$ . . . . . 110

**Figure 6.3** Time evolution of the singlet population for (a) the case of weak excitonic coupling  $J_{S_1,TT} = 20$  meV,  $\epsilon_{S_1,g} - \epsilon_{TT,g} = 100$  meV,  $\hbar\omega_{\text{diag}} = 0$  meV, and  $\hbar\omega_{\text{o.d.}} = 80$  meV, and (b) the case of strong excitonic coupling  $J_{S_1,TT} = 80$  meV,  $\epsilon_{S_1,g} - \epsilon_{TT,g} = 30$  meV,  $\hbar\omega_{\text{diag}} = 95$  meV, and  $\hbar\omega_{\text{o.d.}} = 0$  meV. The green lines correspond to cases in the absence of exciton-phonon coupling. . . 112

**Figure 6.4** Snapshots of singlet population as functions of  $\hbar\omega_{\text{diag}}$  and  $\hbar\omega_{\text{o.d.}}$  at the time of (a) 100 fs, (b) 250 fs, (c) 500 fs and (d) 2000 fs. The other parameters are  $J_{S_1,TT} = 20$  meV and  $\epsilon_{S_1,g} - \epsilon_{TT,g} = 100$  meV. . . . . 113

**Figure 6.5** Time evolution of singlet population for the the phonon mode  $\hbar\omega_{\text{o.d.}} = 20$  meV diagonally coupled to the  $S_1$  and TT states. The phonon modes off-diagonally coupled are (a)  $\hbar\omega_{\text{diag}} = 20, 40, 60$  and  $80$  meV, (b)  $\hbar\omega_{\text{diag}} = 100, 120, 140$  and  $160$  meV. The other parameters are same as Fig. 6.4 . . 114

**Figure 6.6** Time evolution of singlet population for the the phonon mode  $\hbar\omega_{\text{o.d.}} = 60$  meV diagonally coupled to the  $S_1$  and TT states. The phonon modes off-diagonally coupled are (a)  $\hbar\omega_{\text{diag}} = 20, 40, 60$  and  $80$  meV, (b)  $\hbar\omega_{\text{diag}} = 100, 120, 140$  and  $160$  meV. The other parameters are same as Fig. 6.4 . . 115

**Figure 6.7** Time evolution of singlet population for the the phonon mode  $\hbar\omega_{\text{o.d.}} = 60$  meV diagonally coupled to the  $S_1$  and TT states. The phonon modes off-diagonally coupled are (a)  $\hbar\omega_{\text{diag}} = 20, 40, 60$  and  $80$  meV, (b)  $\hbar\omega_{\text{diag}} = 100, 120, 140$  and  $160$  meV. The other parameters are same as Fig. 6.4 . . 116

**Figure 7.1** (a) Schematic diagram of a typical coplanar waveguide resonator with a qubit placed between the center conductor and the ground plane of the waveguide. (b) Sketch of the superconducting qubit coupled to the coplanar transmission line resonator. MI denotes the mutual inductance between the qubit and resonator. The control line supplies the time-dependent magnetic flux  $\Phi(t)$  threading the qubit loop. 121

**Figure 7.2** (a) Final transition probability  $P_{\uparrow \rightarrow \downarrow}(\infty)$  as a function of the off-diagonal coupling strength  $\gamma/\sqrt{\hbar v}$  with fixed tunneling strengths  $\Delta = 0, 0.5\sqrt{\hbar v}$  and  $1.2\sqrt{\hbar v}$ . (b)  $P_{\uparrow \rightarrow \downarrow}(\infty)$  as a function of the tunneling strength  $\Delta/\sqrt{\hbar v}$  for different off-diagonal coupling strengths  $\gamma = 0, 0.5\sqrt{\hbar v}$  and  $1.2\sqrt{\hbar v}$ . The oscillator frequency  $\omega$  is set to  $10\sqrt{v/\hbar}$ . . . . . 122

**Figure 7.3** Time evolution of transition probability calculated by the master-equation method and the multi- $D_2$  ansatz. Oscillator frequencies used are (a)  $\omega = 0.1\sqrt{v/\hbar}$ , (b)  $\omega = \sqrt{v/\hbar}$  and (c)  $\omega = 10\sqrt{v/\hbar}$ . Other parameters are  $\Delta = 0$  and  $\gamma = 1.2\sqrt{\hbar v}$ . . . . . 123

**Figure 7.4** LZ dynamics with a tunneling strength  $\Delta = 0.5\sqrt{\hbar v}$  and a off-diagonal coupling strength  $\gamma = 1.2\sqrt{\hbar v}$  for two oscillator frequencies (a)  $\omega = 0.5\sqrt{v/\hbar}$  and (b)  $\omega = 20\sqrt{v/\hbar}$ . . . . . 123

**Figure 7.5** LZ dynamics (a) for seven tunneling strengths  $\Delta = 0, 0.2\sqrt{\hbar v}, 0.4\sqrt{\hbar v}, 0.6\sqrt{\hbar v}, 0.8\sqrt{\hbar v}, 1.0\sqrt{\hbar v}$ , and  $2.0\sqrt{\hbar v}$  with fixed  $\gamma = 1.2\sqrt{\hbar v}$  and (b) for different off-diagonal coupling strengths  $\gamma = 0, 0.2\sqrt{\hbar v}, 0.4\sqrt{\hbar v}, 0.6\sqrt{\hbar v}, 0.8\sqrt{\hbar v}, 1.0\sqrt{\hbar v}$ , and  $1.2\sqrt{\hbar v}$  with certain  $\Delta = 0.5\sqrt{\hbar v}$ . The oscillator frequency  $\omega$  is set to  $10\sqrt{v/\hbar}$ . 125

**Figure 7.6** Time evolution of transition probability for (a) a sub-Ohmic bath of  $s = 0.5$ , (b) an Ohmic bath of  $s = 1$ , and super-Ohmic bath of (c)  $s = 1.5$  and (d)  $s = 2$  is obtained from the  $D_2^{M=3}$  ansatz with an identical coupling strength  $\alpha = 0.002$ . For each of the four  $s$  values, four cases are shown:  $\Delta = 0.4\sqrt{\hbar v}, \theta = \pi/2$  (red line, circles),  $\Delta = 0.4\sqrt{\hbar v}, \theta = 0$  (magenta line, diamonds),  $\Delta = 0, \theta = \pi/2$  (black line, squares), and  $\Delta = 0, \theta = 0$  (blue line, pentagrams). . . . . 127

**Figure 7.7** Time evolution of the boson number using for a super-Ohmic bath of (a)  $s = 1.5$  and (b)  $s = 2$ , in the presence of off-diagonal coupling only ( $\theta = \pi/2$ ). Other parameters are  $\Delta = 0$  and  $\alpha = 0.002$ . . . . . 128

**Figure 7.8** Time evolution of transition probability for (a)  $\Delta = 0$  (b)  $\Delta = 0.4\sqrt{\hbar v}$  using an Ohmic bath with various coupling strengths  $\alpha$ , in the presence of off-diagonal coupling only ( $\theta = \pi/2$ ). . . . . 129

**Figure 7.9** Time evolution of the boson number using an Ohmic bath, in the presence of off-diagonal coupling only ( $\theta = \pi/2$ ). The left column corresponds to  $\Delta = 0$ , while the right column is for  $\Delta = 0.4\sqrt{\hbar v}$ . The upper and lower panels correspond to coupling strength of  $\alpha = 0.002$  and  $\alpha = 0.006$ , respectively. . . . . 131

**Figure 7.10** Time evolution of transition probability for (a)  $\Delta = 0$  (b)  $\Delta = 0.4\sqrt{\hbar v}$  using an Ohmic bath with various interaction angles  $\theta$ . The coupling strength  $\alpha = 0.008$  is set. . . . . 131

**Figure 7.11** Time evolution of the boson number using an Ohmic bath for interaction angles of (a)  $\theta = \pi/4$  and (b)  $\theta = \pi/2$ . The tunneling strength  $\Delta = 0$  and coupling strength  $\alpha = 0.008$  are set. . . . . 132



**Figure A.1**  $P_z(t)$  obtained from averaged Hamiltonian, HEOM method, the  $D_2^{M=2}$  ansatz, and the  $D_2^{M=4}$  ansatz. The parameters are  $V = -0.05$ ,  $\lambda = 0.5$ ,  $\beta = 0.5$ . . . 156

**Figure A.2** Time evolution of transition probability calculated by the multi- $D_2$  ansatz. Tested parameters are (a) number of multiplicity  $M$ , (b) maximum spectrum band frequencies  $\omega_{max}$ , and (c) number of oscillator modes  $N$ . Other parameters are  $\Delta = 0$ ,  $\alpha = 0.002$ ,  $s = 1$ , and  $\omega_c = 10\sqrt{v/\hbar}$ . . . . . 171

**Abbreviations**

2D	two-dimensional
FMO	Fenna-Matthews-Olson
QED	quantum electrodynamics
MCTDH	multiconfiguration time-dependent Hartree method
DMRG	density matrix renormalization group approach
QUAPI	quasi-adiabatic propagator path integral
HEOM	hierarchical equation of motion
ED	exact diagonalization
QMC	quantum Monte Carlo
VED	variational exact diagonalization
MD	molecule dynamics
MSD	mean square displacement
DOFs	degrees of freedom
SSH	Su-Schrieffer-Heeger
CPs	conducting polymers
SF	singlet fission
xSF	intermolecular singlet fission
BOs	Bloch oscillations
iSF	intramolecular singlet fission
LZ	Landau-Zener
ATP	adenosine triphosphate
ADP	adenosine diphosphate
DFWM	degenerate four-wave mixing
BEC	Bose-Einstein condensates
SQUID	superconducting quantum interference device
USC	ultrastrong coupling

## Chapter 1

### Introduction

*In this chapter, a brief introduction of the research background is firstly given in Section 1.1. Then the objectives and scope of applications of the Davydov ansätze are discussed in Section 1.2. In Section 1.3, the structure of main text is presented. Finally, Section 1.4 lists the significance and novelty of the research.*

## 1.1 Background

Simulation of quantum dynamics plays an essential role in a huge variety of fields, such as atomic and molecular physics [1–3], quantum optics [4], solid state physics [5], chemical physics [6], and quantum information science [7]. Since a realistic system in general cannot be completely isolated from its surroundings, to accurately describe the state of a quantum system, it is necessary to consider environmental influences that have been demonstrated to play a vital role in its dynamical behavior. For instance, the interaction between the two energy levels of a quantum two-state system may be altered by its environment [8], exciton transport in superlattice semiconductors and organic materials can be modulated by an external electric field [9], and manipulation of quantum qubits undergoes unavoidable interferences due to the device-environment interactions [10]. After decades of development, impressive progress has been achieved in controlling coherent dynamics of target electronic systems, by creation and manipulation of entanglement and system-environment interactions in various physical systems ranging from light-harvesting aggregates [11] to quantum computers [12].

Since the advent of ultrafast laser spectroscopy, much attention has been devoted to relaxation, transport, and dissipation of photoexcited entities induced by the environment effects. Emerging technological capabilities to control femtosecond pulse durations and down-to-one-hertz bandwidth resolutions provide novel probes on vibrational dynamics and excitation relaxation, which were elusive in the past. Recently, developments in ultrafast laser physics and technologies allow for studies of nonequilibrium carrier/exciton dynamics that was previously inaccessible to traditional linear optical spectroscopy. In 2007, Fleming’s group studied the energy transfer in the Fenna-Matthews-Olson (FMO) complex [13]. The energy levels and coupling between them were mapped by two-dimensional (2D) Fourier transform electronic spectroscopy. In the cross peak of measured 2D spectra, the oscillations were found to last for more than 660 fs at 77 K and 300 fs at 277 K. The oscillatory signals were initially interpreted as quantum coherence between electronic states, and the quantum coherence was used to explain the extreme

efficiency of the energy transfer in FMO. While the origin and functionalities of the quantum coherence are still under debate [14–17], the long-lived oscillations were recently argued to result from the coherence of vibrational levels instead of an electronic origin [18, 19]. The quantum coherence was demonstrated by some authors to be unessential for efficient excitation energy transfer [15, 20]. These findings triggered sustained efforts to understand fundamentally exciton transfer in light harvesting systems. In photosynthetic aggregates, it is found that exciton transfer can be modeled by motion of excitons coupled to phonon baths, which represent the lattice vibrations and surrounding noises [21]. If the system-bath coupling is weak, the perturbation method, such as the Redfield theory, is valid to tackle coherent energy transfer. However, since the excitonic coupling is comparable to the bath reorganization energy, an accurate description of exciton transfer in light harvesting systems is nontrivial [18], thus necessitating numerically efficient, fully quantum mechanical treatments.

Via natural photosynthesis, solar energy, as an available, clean, and safe source of energy, can be converted into chemical energy in plants. While there is plenty light energy, harvesting it efficiently in an artificial way has been a challenge for a long time. The Shockley-Queisser limit which gives a maximum efficiency puts a constrain on all photovoltaics [22]. One of the ways to go around the limit is to increase the quantum yield by generating more than one exciton per photon. This has been demonstrated in materials capable of singlet fission (SF) by Hanna *et al.* [23]. SF is a spin-allowed conversion process in molecules and molecular aggregates, in which a spin-singlet exciton generated by irradiation splits into two spin-triplet excitons [22]. Singh *et al.*, in 1965, first used the SF process to explain the unusual photophysics in anthracene crystals [24]. In this process,  $S_0$ , the electronic ground state and  $S_1$ , the lowest singlet excited state follow the kinetic model  $S_0 + S_1 \rightarrow TT \rightarrow T + T$ , where  $T$  is the molecular triplet state and  $TT$  is a doubly excited pair of spin-correlated triplets which has an overall singlet spin. The  $TT$  state is called a correlated triplet pair state and is considered as a dark state because it cannot be optically populated from the ground state.

SF has received a great deal of attention again in 2013 since an external quantum efficiency above 100 % has been realized in a SF-based organic photovoltaic cell by Congreve *et al.* [25]. In order to devise rational design of photovoltaic systems, many experimental [26–28] and theoretical [29, 30] efforts have been devoted to gain further understanding of the SF process at the molecular level. The SF process has been found to be influenced by various factors and molecular vibrations were predicted to significantly affect the SF efficiency because the exciton-phonon coupling served as the origin of the exciton relaxation [31]. However, the current limited understanding of SF mechanisms hinders the design of versatile SF materials. It is thus essential to explicitly explore the impacts of the vibrationally induced fluctuations on the fission dynamics through quantum dynamics calculations.

In the community of quantum computation and quantum information, the cavity and circuit quantum electrodynamics (QED) attracts great interest for its importance to implementing quantum qubits. Since conceived in 2004, circuit QED architectures have been designed and fabricated as research platforms in quantum computation and quantum information [32]. Due to high flexibility and tunability, circuit QED devices offer the possibility to simulate light-matter interactions in quantum systems with an integrated circuit. However, in experimental realizations, fabricated QED systems suffer from ineluctable dissipation stemming from the device-environment interactions [10]. Most of theoretical studies are conducted by adopting master equations to capture the photon and the qubit dynamics of the QED systems, where environmental effects are considered in a phenomenological manner [33]. However, the interplay between the QED devices and their surroundings is too complex to be modelled by a few dissipative parameters in the methods based on the Markovian Lindblad master equation. In addition to being affected by bath induced dissipation, the operation of QED devices can benefit from interactions with their surroundings. For instance, Hohenester *et al.* observed phonon-assisted scattering rate from quantum dot excitons to photons in nanocavity [34]. Therefore, proper quantum mechanical treatments of the system-bath interactions are desired for the realistic manipulation of quantum qubits.

## 1.2 Objectives and Scope

The environment is typically modelled as a bath coupled to the target system. Due to the complexity of system-bath interactions, it is difficult to devise exact analytical solutions for the dynamics of most open quantum systems. A variety of techniques has been developed in the context of open quantum systems, such as the multiconfiguration time-dependent Hartree method (MCTDH) [35] and the density matrix renormalization group approach (DMRG) [36]. In general, methods for the study of open quantum systems can be classified into two categories: wave function based methods that operate in the Hilbert space [37, 38] and density matrix based approaches that operate in the Liouville space of the system [39, 41]. These methods have proven their validities in fields such as quantum measurement theory [44], quantum statistical mechanics [45], and quantum thermodynamics [46].

However, methodologies used to investigate dynamics of the open quantum system differ greatly depending on target systems and desired objectives. For example, approaches used for chemical physics [47] have different approximations from those in quantum optics [48]. But, each method developed for open quantum systems has its limitations. For instance, methods such as quasi-adiabatic propagator path integral (QUAPI) [39, 40] and hierarchical equations of motion (HEOM) [41–43] are considered numerically exact, but computationally expensive. In detail, QUAPI is based on a symmetric Trotter splitting of the short-time propagator for the full Hamiltonian into one part depending on the electronic Hamiltonian and another part involving the environment and the coupling term. The splitting is by construction exact in the limit  $\delta t \rightarrow 0$ , but introduces a finite Trotter error for a finite time increment. The error has to be eliminated by careful testing and choosing  $\delta t$  sufficiently small such that convergence is achieved [40]. As for HEOM, Tanimura *et al.* derived the stochastic Liouville equation for density matrices of a system with the aid of path integral formalism, and then cast the equation into a hierarchy of equations which can be solved analytically or computationally in a nonperturbative manner. Because the HEOM approach is computationally intensive, much efforts were devoted to improve the algorithm to deal with dissipative dynamics in

realistic situations [41–43]. In contrast, perturbative approaches such as the master equation method are able to provide efficient calculations but become inaccurate in certain parameter regimes [49]. In particular, modeling of polaron dynamics have not received much-deserved attention over the last six decades.

In the aforementioned reduced density matrix approaches, coupled quantum dynamics of electronic and bosonic degrees of freedom (DOFs) is obtained explicitly only for electronic systems, whereas the bath DOFs are traced out in constructing the reduced density matrix. Because of this treatment, all explicit information of the bath dynamics is lost, and the interplay between the system and the bath is only reflected in system observables such as optical spectra and electronic populations. The purpose of this thesis is to develop a class of the Davydov ansätze, and employ the proper trial states, especially the multiple  $D_2$  ansatz, to accurately investigate dynamical properties of certain open quantum systems with both electronic and bosonic DOFs, including Holstein molecular crystal model with and without external electric fields, light harvesting systems with SF mechanisms, and the quantum qubit in the QED devices.

As a typical open quantum system, the Holstein molecular crystal model has been extensively used to study properties of polarons in molecular crystals and biological systems [50]. Two kinds of exciton-phonon interactions can be included in the Holstein model, namely, the diagonal coupling as a nontrivial dependence of the exciton site energies on the lattice coordinates and the off-diagonal coupling as a nontrivial dependence of the exciton transfer integral on the lattice coordinates [51]. Simultaneous presence of diagonal and off-diagonal coupling seems crucial to characterize solid-state excimers, where a variety of experimental and theoretical considerations imply a strong dependence of electronic tunneling upon certain coordinated distortions of neighboring molecules in the formation of bound excited states [52, 53]. However, in the literature, little attention has been paid to the Hamiltonians containing the off-diagonal exciton-phonon coupling due to inherent difficulties to obtain reliable solutions [54], especially for the polaron dynamics [55]. Early treatments of off-diagonal coupling



include the Munn-Silbey theory which is based upon a perturbative approach with added constraints on canonical transformation coefficients determined by a self-consistency equation [56, 57]. The global-local ansatz, also known as the D-tilde state, formulated by Zhao *et al.* in the early 1990s, was later employed in combination with the dynamic coherent potential approximation (with the Hartree approximation) to arrive at a state-of-the-art ground-state wave function as well as higher eigenstates [58].

In the absence of an exact solution to the Schrödinger equation, various numerical approaches were developed in the past few decades, including the exact diagonalization (ED) [59], quantum Monte Carlo (QMC) simulation [60], variational method [61], DMRG [36], the variational exact diagonalization (VED) [62], and the method of relevant coherent states [63]. Most of these approaches were designed to probe the ground-state properties. For excited-state properties and dynamics of polaronic systems, however, few of them provide a satisfactory resolution. For example, a time-dependent variant of DMRG, i.e., t-DMRG [64], was developed to elucidate the polaron dynamics. Yet, it cannot accurately simulate the system dynamics from an arbitrary initial state, since high-lying excited states cannot be adequately described by DMRG. Fortunately, variational approaches are still effective in dealing with polaron dynamics so long as a proper trial wave function is chosen. Previously, static properties of the Holstein polaron have been examined using a series of trial wave functions based upon phonon coherent states, such as the Toyozawa ansatz [65–67], the global-local ansatz [65, 67–69], and a delocalized form of the Davydov  $D_1$  ansatz [70]. By using these ansätze, the ground state band and the self-trapping phenomenon were adequately addressed. To simulate the time evolution of the Holstein polaron, at least two Davydov ansätze, namely, the  $D_1$  and  $D_2$  ansätze [71–73], were used following the Dirac-Frenkel variation scheme [74], a powerful apparatus to reveal accurate dynamics of quantum many-body systems. Time-dependent variational parameters which specify the trial state are obtained from solving a set of coupled differential equations generated by the Lagrangian formalism of the Dirac-Frenkel variation. Validity of this approach is carefully checked by quantifying how faithfully the trial state follows the Schrödinger equation [55, 75]. Numerical results show

that the  $D_1$  ansatz is effective and accurate in studying the Holstein polaron dynamics with diagonal coupling, but fails to describe cases with off-diagonal coupling. Despite being a simplified version of the  $D_1$  trial state, the  $D_2$  ansatz instead can deal with the off-diagonal coupling case, albeit with non-negligible deviation from the exact solution to the Schrödinger dynamics [55]. One purpose of this thesis is to test the feasibility of using a superposition of the Davydov  $D_2$  trial states to study the dynamics of the Holstein model with simultaneous diagonal and off-diagonal couplings.

In particular, the Holstein model with only off-diagonal coupling can be demonstrated to be equivalent to the Su-Schrieffer-Heeger (SSH) model at half filling, by using the quantum mechanical creation and annihilation operators to describe the displacement of the phonon bath in the SSH model [76]. As is known, the carrier or exciton transport in conducting polymers (CPs) is commonly described by the SSH model in which the electrons are treated in a tight-binding approximation and these electrons are assumed to move adiabatically with the nuclei [77]. Thus full quantum descriptions of exciton transport in CPs will be presented in this thesis by applying the appropriate Davydov ansätze to the off-diagonal Holstein polaron. In addition, the Holstein polaron under an external electric field can be employed to model the semiconductor superlattices and organic materials. Bloch oscillations (BOs) phenomena take place under this condition [9], and the corresponding dynamics can be probed by variational approach with the multiple Davydov  $D_2$  ansatz.

Another aim of this thesis is to employ the multiple Davydov  $D_2$  ansatz to study SF mechanisms. In the SF materials, there exist two types of exciton-phonon coupling, i.e., diagonal coupling and off-diagonal coupling. The diagonal coupling term represents fluctuations of the energy gap between the optically-allowed state  $S_1$  and forbidden state  $TT$  induced by intramolecular vibrations. The off-diagonal coupling term describes the fluctuations in excitonic coupling induced by intramolecular and intermolecular vibrations. In covalent tetracene dimers it was uncovered using quantum chemical calculations that high-frequency intramolecular vibrations give rise to strong diagonal and

off-diagonal coupling [78]. The two types of coupling have also been found to be tunable in novel SF materials by changing linkers and by engineering the dihedral angle between the chromophore units and the linker [79–81]. However, there is a lack of discussion in the literature on detailed SF mechanisms under the influence of simultaneous diagonal and off-diagonal exciton-phonon coupling. A unified treatment of phonon effects in the SF process needs to be formulated. The multiple Davydov  $D_2$  ansatz can then be used to describe the fission dynamics of the constructed SF model.

Finally, the applications of the multiple Davydov  $D_2$  ansatz can be expanded to the quantum computation and quantum information fields. In particular, the manipulations of the quantum qubit in QED devices facilitate the exploration of the transition of qubit states, such as the Landau-Zener (LZ) transitions, due to their potential scalability and tunable parameters over a broad range. When the energy difference between two diabatic states is swept through an avoided level crossing, the LZ transition comes into play [82, 83]. The LZ transition is one of the most fundamental phenomena in quantum physics, and is applied to a growing list of physical systems, such as a superconducting flux qubit coupled to a quantum interference device [10] and a nitrogen-vacancy center spin in isotopically purified diamond [84]. The dissipative LZ transitions have been studied by various methods, such as time-dependent perturbation theory, [85], the master equation method [49], QUAPI and the non-equilibrium Bloch equations [39]. However, dissipative LZ dynamics at intermediate times is still not well-understood. This thesis will use the time-dependent variation with the multiple Davydov  $D_2$  ansatz to address the dynamics of dissipative LZ transitions in the QED architectures.

### 1.3 Dissertation Overview

This thesis addresses the Davydov  $D_2$  ansätze and their applications in various open quantum systems with electronic and bosonic DOFs. It is shown that our newly developed multiple Davydov ansätze can accurately describe fully quantum dynamical correlations between the electronic and bosonic subsystems. Since the two subsystems are treated by

the Davydov ansätze on the equal footing, the effects of bosonic modes on the electronic energy transfer can be emphasized in a nonperturbative manner. In particular, the multi- $D_2$  ansatz is demonstrated to be sufficiently powerful to capture dynamics of the open quantum systems with off-diagonal coupling to boson modes. In this thesis, the multi- $D_2$  ansatz is widely used to study several complicated quantum behaviours, such as the exciton transport in the CPs, BOs dynamics in semiconductor superlattices and organic materials, the SF processes, and the LZ transitions in circuit QED devices. The Dirac-Frenkel time-dependent variational principle is utilized to obtain the equations of motions for the time-dependent variational parameters of the Davydov ansätze. Thanks to the multiple Davydov ansätze, detailed boson dynamics can be analyzed to shed light on the interplay between the electronic and bosonic DOFs. Insights gained from the thesis facilitate our understanding of the aforementioned quantum behaviors, and provide guiding principles for the design of efficient SF materials by directly tuning singlet-triplet interstate coupling. The remainder of the thesis is structured as follows.

Chapter 1 presents a short introduction to the research background and illuminates motivations for the project with the main objectives of the thesis listed.

Chapter 2 reviews the literature concerning dynamics of open quantum systems. This chapter illustrates developments and challenges regarding the accurate theoretical description of four different quantum behaviours, including the exciton transport in CPs, BOs dynamics in semiconductor superlattices and organic materials, SF processes, and LZ transitions in the QED devices.

Chapter 3 gives a detailed explanation of the Davydov ansätze, including the novel multi- $D_2$  ansatz, which is a linear combination of the usual Davydov  $D_2$  trial states. This chapter introduces the description of Dirac-Frenkel time-dependent variational method with various trial states. At last, four models for applications of the multi- $D_2$  ansatz are formulated: the Holstein polaron model, the Holstein model under an external electric field, a microscopic model of intramolecular SF with simultaneous diagonal and

off-diagonal coupling to high-frequency modes, and the LZ model with both diagonal and off-diagonal qubit-bath coupling.

Chapter 4 offers an accurate description of polaron dynamics of a one-dimensional molecular crystal model with off-diagonal exciton-phonon coupling. The accuracy of the Ehrenfest dynamics in the SSH model is examined and compared to that of the Dirac-Frenkel time-dependent variational method using the single  $D_2$  ansatz and the multi- $D_2$  ansatz. The underlying physics is revealed in the real and reciprocal space representations, including the exciton transport, the exciton momentum redistribution and the exciton energy dissipation. At the end of the chapter, it is shown that the fully quantum mechanical method using our multiple Davydov trial states is also applicable at finite temperatures.

Chapter 5 elaborates transient dynamics of a one-dimensional Holstein polaron under the influence of an external electric field. By employing the multi- $D_2$  ansatz, the roles played by the phonons on the carrier transport are explicitly examined given initial broad and narrow exciton wave packets.

Chapter 6 formulates a microscopic model of intramolecular singlet fission with simultaneous diagonal and off-diagonal coupling to high-frequency modes. The fission dynamics is studied using the multi- $D_2$  ansatz, and a comprehensive study is performed to reveal the dependence of efficient singlet fission on the phonon modes.

Chapter 7 centres on the LZ model with both diagonal and off-diagonal qubit-bath coupling. The multi- $D_2$  ansatz is implemented to describe the dissipative LZ dynamics at the intermediate times. Detailed boson dynamics is analyzed to address the role of bath spectral densities, diagonal and off-diagonal qubit-bath coupling, coupling strengths and interaction angles on LZ dynamics.

Chapter 8 draws conclusions of this thesis.

Chapter 9 lists the future study.

## 1.4 Findings and Outcomes/Originality

This work includes various novel findings.

1. When investigating dynamics of a one-dimensional molecular crystal model with off-diagonal exciton-phonon coupling, the Ehrenfest method is shown to be equivalent to the Dirac-Frenkel time-dependent variational method with the single  $D_2$  ansatz. The accuracy of our simulated dynamics with the multi- $D_2$  ansatz is significantly enhanced in comparison with the semi-classical Ehrenfest dynamics.

2. The multi- $D_2$  ansatz enables an accurate description of the polaron dynamics in the presence of an external electric field. The addition of carrier-phonon coupling is found to change the movement patterns of the bare carrier under the external field.

3. The singlet fission dynamics is accurately treated by the multi- $D_2$  ansatz using a microscopic model of intramolecular singlet fission with simultaneous diagonal and off-diagonal coupling to high-frequency modes. It is found that both diagonal and off-diagonal coupling can aid efficient singlet fission if excitonic coupling is weak, and fission is only facilitated by diagonal coupling if excitonic coupling is strong.

4. The multi- $D_2$  ansatz is successfully applied to explore the dissipative LZ dynamics at intermediate times. It is found that LZ dynamics at intermediate times is little affected by diagonal qubit-bath coupling, and is determined by off-diagonal coupling and tunneling between two diabatic states.

## References

- [1] A. Thiel, *J. Phys. G Nucl. Part. Phys.*, **1990**, 16, 867.
- [2] R. J. Lipert, G. Bermudez, and S. D. Colson, *J. Phys. Chem.*, **1988**, 92, 3801.
- [3] W. Xie and W. Domcke, *J. Chem. Phys.*, **2017**, 147, 184114.
- [4] D. Bouwmeester, N. H. Dekker, F. E. v. Dorsselaer, C. A. Schrama, P. M. Visser, and J. P. Woerdman, *Phys. Rev. A*, **1995**, 51, 646.
- [5] W. Wernsdorfer, R. Sessoli, A. Caneschi, D. Gatteschi, and A. Cornia, *Europhysics Lett.*, **2000**, 50, 552.
- [6] L. Zhu, A. Widom, and P. M. Champion, *J. Chem. Phys.*, **1997**, 107, 2859.
- [7] G. D. Fuchs, G. Burkard, P. V Klimov, and D. D. Awschalom, *Nat. Phys.*, **2011**, 7, 789.
- [8] Z. Huang and Y. Zhao, *Phys. Rev. A*, **2018**, 97, 13803.
- [9] F. Bloch, *Zeitschrift Für Phys.*, **1928**, 52, 555.
- [10] I. Chiorescu, P. Bertet, K. Semba, Y. Nakamura, C. J. P. M. Harmans, and J. E. Mooij, *Nature*, **2004**, 431, 159.
- [11] L. Chen, P. Shenai, F. Zheng, A. Somoza, and Y. Zhao, *Molecules*, **2015**, 20, 15224.
- [12] P. Benioff, *J. Stat. Phys.*, **1980**, 22(5), 563-591.
- [13] G. S. Engel, T. R. Calhoun, E. L. Read, T. K. Ahn, T. Mancal, Y. C. Chung, R. E. Blankenship, and G. R. Fleming. *Nature*. **2006**, 446, 782-786.
- [14] A. Chenu and G. D. Scholes. *Annu. Rev. Phys. Chem.* **2015**, 66, 69-96.
- [15] F. Fassioli, R. Dinshaw, P. C. Arpin, and G. D. Scholes. *J. R. Soc. Interface*. **2014**, 11, 20130901.

- [16] I. Kassal, J. Yuen-Zhou, and S. Rahimi-Keshari. *J. Phys. Chem. Lett.* **2013**, 4, 362-367.
- [17] R. G. Saer and R. E. Blankenship. *Biochem. J.* **2017**, 474, 2107-2131.
- [18] N. Christensson, F. Milota, J. Hauer, J. Sperling, O. Bixner, A. Nemeth, and H. F. Kauffmann. *J. Phys. Chem. B* **2011**, 115, 5383-5391.
- [19] V. Tiwari, W. K. Peters, and D. M. Jonas. *Proc. Natl Acad. Sci. U. S. A.* **2013**, 110, 1203-1208.
- [20] H. G. Duan, V. I. Prokhorenko, R. Cogdell, K. Ashraf, A. L. Stevens, M. Thorwart, and R. J. D. Miller. *Proc. Natl. Acad. Sci. U. S. A.* **2017**, 114, 8493-8498.
- [21] J. S. Briggs and A. Eisfeld. *Phys. Rev. E* **2011**, 83, 051911.
- [22] M. B. Smith and J. Michl, *Chem. Rev.* **2010**, 110, 6891.
- [23] M. C. Hanna and A. J. Nozik, *J. Appl. Phys.*, **2006**, 100, 74510.
- [24] S. Singh, W. J. Jones, W. Siebrand, B. P. Stoicheff, and W. G. Schneider, *J. Chem. Phys.*, **1965**, 42, 330.
- [25] D. N. Congreve, J. Lee, N. J. Thompson, E. Hontz, S. R. Yost, P. D. Reusswig, M. E. Bahlke, S. Reineke, T. Van Voorhis, and M. A. Baldo, *Science*, **2013**, 340, 334.
- [26] A. A. Bakulin, S. E. Morgan, T. B. Kehoe, M. W. Wilson, A. W. Chin, D. Zigmantas, D. Egorova, and A. Rao, *Nat. Chem.*, **2016**, 8, 16.
- [27] M. W. Wilson, A. Rao, K. Johnson, S. Gélinas, R. di Pietro, J. Clark, and R. H. Friend, *J. Am. Chem. Soc.*, **2013**, 135, 16680.
- [28] S. W. Eaton, L. E. Shoer, S. D. Karlen, S. M. Dyar, E. A. Margulies, B. S. Veldkamp, C. Ramanan, D. A. Hartzler, S. Savikhin, T. J. Marks, and M. R. Wasielewski, *J. Am. Chem. Soc.*, **2013**, 135, 14701.
- [29] T. C. Berkelbach, M. S. Hybertsen, and D. R. Reichman, *J. Chem. Phys.*, **2013**, 138, 114102.



- [30] T. C. Berkelbach, M. S. Hybertsen, and D. R. Reichman, *J. Chem. Phys.*, **2013**, 138, 114103.
- [31] H. Tamura, M. Huix-Rotllant, I. Burghardt, Y. Olivier, and D. Beljonne, *Phys. Rev. Lett.*, **2015**, 115, 107401.
- [32] A. Wallraff, D. I. Schuster, A. Blais, L. Frunzio, R.-S. Huang, J. Majer, S. Kumar, S. M. Girvin, and R. J. Schoelkopf, *Nature*, **2004**, 431, 162.
- [33] K. Saito, M. Wubs, S. Kohler, P. Hänggi, and Y. Kayanuma, *Europhysics Lett.*, **2006**, 76, 22.
- [34] U. Hohenester, A. Laucht, M. Kaniber, N. Hauke, A. Neumann, A. Mohtashami, M. Seliger, M. Bichler, and J. J. Finley, *Phys. Rev. B*, **2009**, 80, 201311(R).
- [35] H. Wang, *J. Phys. Chem. A*, **2015**, 119, 7951.
- [36] E. Jeckelmann and S. R. White, *Phys. Rev. B*, **1998**, 57, 6376.
- [37] N. Zhou, Z. Huang, J. Zhu, V. Chernyak, and Y. Zhao, *J. Chem. Phys.*, **2015**, 143, 014113.
- [38] Z. Huang, L. Chen, N. Zhou, and Y. Zhao, *Ann. Phys. (Berlin)*, **2017**, 529, 1600367.
- [39] P. Nalbach, N. Klinkenberg, T. Palm, and N. Müller, *Phys. Rev. E*, **2017**, 96, 42134.
- [40] P. Nalbach, A. Ishizaki, G. R. Fleming, and M. Thorwart, *New J. Phys.*, **2011**, 13, 63040.
- [41] L. Chen, Y. Zhao, and Y. Tanimura, *J. Phys. Chem. Lett.*, **2015**, 6, 3110.
- [42] T. Yoshitaka, *J. Phys. Soc. Japan*, **2006**, 75, 82001.
- [43] Y. Tanimura, *J. Chem. Phys.*, **2014**, 141, 44114.
- [44] H. M. Wiseman, *Quantum Semiclassical Opt. J. Eur. Opt. Soc. Part B*, **1996**, 8, 205.
- [45] S. Popescu, A. J. Short, and A. Winter, *Nat. Phys.*, **2006**, 2, 754.

- [46] X. Wang and T. Xiang, *Phys. Rev. B*, **1997**, 56, 5061.
- [47] V. May and O. Kuhn, *Charge and Energy Transfer Dynamics in Molecular Systems*, Wiley-VCH, Weinheim, **2004**.
- [48] H. Carmichael, *An Open Systems Approach to Quantum Optics*, Springer, Berlin, **1993**.
- [49] K. Saito, M. Wubs, S. Kohler, Y. Kayanuma, and P. Hänggi, *Phys. Rev. B*, **2007**, 75, 214308.
- [50] T. Holstein, *Ann. Phys. (N.Y.)* **1959**, 8, 325; **1959**, 8, 343.
- [51] W. P. Su, J. R. Schrieffer, and A. J. Heeger, *Phys. Rev. Lett.*, **1979**, 42, 1698.
- [52] L. A. Dissado and S. H. Walmsley, *Chem. Phys.*, **1984**, 86, 375.
- [53] H. Sumi, *Chem. Phys.*, **1989**, 130, 433.
- [54] G. D. Mahan, *Many-Particle Physics* (Kluwer Academic/Plenum, New York, **2000**.
- [55] Y. Zhao, B. Luo, Y. Y. Zhang, and J. Ye, *J. Chem. Phys.*, **2012**, 137, 084113.
- [56] Y. Zhao, D. W. Brown, and K. Lindenberg, *J. Chem. Phys.*, **1994**, 100, 2335.
- [57] D. M. Chen, J. Ye, H. J. Zhang, and Y. Zhao, *J. Phys. Chem. B*, **2011**, 115, 5312.
- [58] Q. Liu, Y. Zhao, W. Wang, and T. Kato, *Phys. Rev. B*, **2009**, 79, 165105.
- [59] A. S. Alexandrov, V. V. Kabanov, and D. K. Ray, *Phys. Rev. B*, **1994**, 49, 9915.
- [60] H. de Raedt and A. Lagendijk, *Phys. Rev. B*, **1983**, 27, 6097.
- [61] V. Cataudella, G. De Filippis and G. Iadonisi, *Phys. Rev. B*, **1999**, 60, 15163; **2000**, 62, 1496.
- [62] A. Weiße, H. Fehske, G. Wellein and A. R. Bishop, *Phys. Rev. B*, **2000**, 62, 747.
- [63] O. S. Barišić, *Europhys. Lett.*, **2007**, 77, 57004.

- [64] S. R. White and A. E. Feiguin, *Phys. Rev. Lett.*, **2004**, 93, 076401.
- [65] Y. Zhao, *Doctoral thesis, University of California, San Diego*, **1994**; Y. Zhao, D. W. Brown, and K. Lindenberg, *J. Chem. Phys.*, **1997**, 107, 3159; **1997**, 107, 3179.
- [66] T. Meier, Y. Zhao, V. Chernyak, and S. Mukamel, *J. Chem. Phys.*, **1997**, 107, 3876.
- [67] Y. Zhao, D. W. Brown, and K. Lindenberg, *J. Chem. Phys.*, **1997**, 106, 2728.
- [68] Y. Zhao, G. Q. Li, J. Sun, and W. H. Wang, *J. Chem. Phys.*, **2008**, 129, 124114.
- [69] Y. Zhao, D. W. Brown, and K. Lindenberg, *J. Chem. Phys.*, **1997**, 107, 3159; D. Brown, K. Lindenberg, and Y. Zhao, *ibid.* **1997**, 107, 3179.
- [70] J. Sun, L. W. Duan, and Y. Zhao, *J. Chem. Phys.*, **2013**, 138, 174116.
- [71] M. J. Škrinjar, D. V. Kapor and S. D. Stojanović, *Phys. Rev. A*, **1988**, 38, 6402, and references therein.
- [72] W. Förner, *J. Phys.: Condens. Matter*, **1993**, 5, 3897; *Phys. Rev. B*, **1996**, 53, 6291.
- [73] L. C. Hansson, *Phys. Rev. Lett.*, **1994**, 73, 2927.
- [74] P.A.M. Dirac, *Proc. Camb. phil. Soc.*, **1930**, 26, 376?C376.
- [75] J. Sun, B. Luo, and Y. Zhao, *Phys. Rev. B*, **2010**, 82, 014305.
- [76] A. J. Heeger, S. Kivelson, J. R. Schrieffer, W. P. Su, *Reviews of Modern Physics*, **1988**, 60, 781-850.
- [77] A. Troisi and G. Orlandi, *Phys. Rev. Lett.*, **2006**, 96, 86601.
- [78] E. C. Alguire, J. E. Subotnik, and N. H. Damrauer, *J. Phys. Chem. A*, **2015**, 119, 299.
- [79] E. G. Fuemmeler, S. N. Sanders, A. B. Pun, E. Kumarasamy, T. Zeng, K. Miyata, M. L. Steigerwald, X.-Y. Zhu, M. Y. Sfeir, L. M. Campos, and N. Ananth, *ACS Cent. Sci.*, **2016**, 2, 316.
- [80] S. Ito, T. Nagami, and M. Nakano, *J. Phys. Chem. A*, **2016**, 120, 6236.

- [81] S. N. Sanders, E. Kumarasamy, A. B. Pun, K. Appavoo, M. L. Steigerwald, L. M. Campos, and M. Y. Sfeir, *J. Am. Chem. Soc.*, **2016**, 138, 7289.
- [82] C. Zener, *Proc. R. Soc. London A*, **1932**, 137, 696.
- [83] L. D. Landau, *Phys. Z.*, **1932**, 2, 46.
- [84] J. Zhou, P. Huang, Q. Zhang, Z. Wang, T. Tan, X. Xu, F. Shi, X. Rong, S. Ashhab, and J. Du, *Phys. Rev. Lett.*, **2014**, 112, 10503.
- [85] P. Ao and J. Rammer, *Phys. Rev. Lett.*, **1989**, 62, 3004.

## Chapter 2

### Literature Review

*This chapter presents the overview of the Davydov ansätze in Section 2.1. Section 2.2 reviews potential applications of the multiple Davydov ansätze, and introduces experimental and theoretical progresses in four specified open quantum systems.*

## 2.1 Overview of the Davydov ansätze

In 1973, Davydov initiated a quantum theory for the muscle contraction of  $\alpha$ -helical protein molecules when they are excited during the transformation process from adenosine triphosphate (ATP) to adenosine diphosphate (ADP) and phosphate [1]. A series of continued studies were performed to investigate the collectively excited states in the molecular systems that contain exciton-phonon coupling. The collective excitons were named after particle-like excitations, solitary excitons, or Davydov solitons [2–5]. Together with the accompanied phonon cloud, the excitons were also known as polarons and quasiparticles in periodic crystals [6].

The Davydov soliton was originally proposed as a spatially localized state to help understand the energy transport in  $\alpha$ -helix. The soliton solution was given by Davydov in the 1970s as a product ansatz of exciton and phonon part, i.e., the original Davydov ansatz or Davydov's ansatz [1, 5].

$$\begin{aligned}
 |\Psi_{\text{sol}}\rangle &= |\text{exciton}\rangle |\text{phonon}\rangle, \\
 |\text{exciton}\rangle &= \sum_n \psi_n \hat{a}_n^\dagger |0\rangle_{\text{ex}}, \\
 |\text{phonon}\rangle &= \exp \left\{ -\frac{i}{\hbar} \sum_m [X_m p_m - P_m u_m] \right\} |0\rangle_{\text{ph}},
 \end{aligned} \tag{2.1}$$

where  $|0\rangle_{\text{ex}}$  and  $|0\rangle_{\text{ph}}$  are the vacuum-state wave functions for the exciton and phonon, respectively. The exciton amplitudes,  $\psi_n$ , follow the normalization condition for the wave function,  $\sum_n |\psi_n|^2 = 1$ . The function,  $|\psi_n|^2$ , denotes the population of exciton of the  $n$ -th site in the molecular chain, and  $\hat{a}_n^\dagger$  represents the creation operator of the corresponding exciton. The phonon part is the so-called coherent state.  $\hat{p}_m$  and  $\hat{u}_m$  are the momentum and displacement operators of the phonon at the site  $m$ . The functions  $X_m = \langle \Psi_{\text{sol}} | \hat{u}_m | \Psi_{\text{sol}} \rangle$ , and  $P_m = \langle \Psi_{\text{sol}} | \hat{p}_m | \Psi_{\text{sol}} \rangle$  characterize the expectation values of displacement and momentum of the phonon, respectively.

The Davydov's ansatz was a classical object, and was demonstrated to be valid only

for the limiting case of a classical lattice. Bolterauer *et al.* used a stationary state based on the Davydov's ansatz and calculated the soliton bandwidth to get information on the quantum lifetime of the Davydov soliton using the uncertainty principle,  $\Delta E \Delta \tau \geq \hbar/2$  [7]. Kerr *et al.* derived the equations of motion for the Davydov solitons by assuming that the Davydov's ansatz satisfies the Schrödinger's equations [8]. Škrinjar *et al.* later developed a more self-consistent treatment based on Lagrangian formalism [7], and Wolfgang Förner numerically estimated the errors introduced by the Davydov's ansatz comparing with the exact solutions [9].

Due to the great flexibility of the Davydov soliton in analyzing properties of the molecular chains, a class of the trial states was developed based on the Davydov's ansatz and named after Davydov, including the Davydov  $D_1$  ansatz, the Davydov  $D_{1.5}$  ansatz, the Davydov  $D_2$  ansatz, the Davydov  $\tilde{D}$  ansatz, and recently developed multiple Davydov trial states [10–12]. In addition, it is essential here to mention the Merrifield ansatz, Toyozawa ansatz, the global-local ansatz, and the delocalized  $D_1$  ansatz since they serve as effective trial states to describe the coupled exciton-phonon systems as well [13–17].

The modern forms of the  $D_1$ ,  $D_{1.5}$ ,  $D_2$ , and  $\tilde{D}$  ansätze can be written as

$$|D_1(t)\rangle = \sum_n \psi_n(t) \hat{a}_n^\dagger |0\rangle_{\text{ex}} \exp \left\{ \sum_q [\lambda_{nq}(t) \hat{b}_q^\dagger - \text{H.c.}] \right\} |0\rangle_{\text{ph}}, \quad (2.2)$$

$$|D_{1.5}(t)\rangle = \sum_n \psi_n(t) \hat{a}_n^\dagger |0\rangle_{\text{ex}} \exp \left\{ \sum_q [(\lambda_q(t) - C_q) \hat{b}_q^\dagger - \text{H.c.}] \right\} |0\rangle_{\text{ph}}, \quad (2.3)$$

$$|D_2(t)\rangle = \sum_n \psi_n(t) \hat{a}_n^\dagger |0\rangle_{\text{ex}} \exp \left\{ \sum_q [\lambda_q(t) \hat{b}_q^\dagger - \text{H.c.}] \right\} |0\rangle_{\text{ph}}, \quad (2.4)$$

$$\begin{aligned} |\tilde{D}(t)\rangle &= \sum_n \psi_n(t) \hat{a}_n^\dagger |0\rangle_{\text{ex}} \\ &\times \exp \left\{ \sum_{q \neq 0} [(\lambda_q(t) + e^{iqn} \gamma_q(t)) \hat{b}_q^\dagger - \text{H.c.}] + [\lambda_0(t) \hat{b}_0^\dagger - \text{H.c.}] \right\} |0\rangle_{\text{ph}}, \end{aligned} \quad (2.5)$$

where H.c. stands for the Hermitian conjugate.  $\hat{b}_q^\dagger$  is the creation operator of a phonon with momentum  $q$  and frequency  $\omega_q$ .  $\lambda_{nq}(t)$  represent the variational parameters for phonon displacements of the  $D_1$  ansatz, while  $\lambda_q(t)$  for the  $D_{1.5}$  and the  $D_2$  ansätze. In the  $D_{1.5}$  ansatz,  $C_q(t) = \lambda_q(t)/(2\hbar\omega_q)$  and  $\hbar$  is the reduced Plank constant. In the  $\tilde{D}$  ansatz, the phonon displacements are  $\lambda_{q\neq 0}(t)$  and  $\gamma_{q\neq 0}(t)$  for  $q \neq 0$ , and  $\lambda_{q=0}(t)$  for  $q = 0$ .

In the  $D_1$  ansatz, the phonon amplitudes are excite-site dependent. In the  $D_2$  ansatz, the phonon amplitudes are independent of the exciton sites for all  $n$ . The  $D_2$  ansatz indicates the quantum state of each phonon mode by a single coherent state, and thus has a strongly classical character. In the  $D_2$  ansatz, the phonon distribution of  $\lambda_q$  is typically pulse-shaped and denotes a lattice deformation fixed in the frame of the lattice. Thus a pulse-shaped distribution is conformed in the exciton amplitudes  $\psi_n$  correspondingly. In the  $D_{1.5}$  ansatz, the phonon wave distribution is modulated by  $C_q$ . For the  $\tilde{D}$  ansatz, its complexities are between those of the  $D_2$  ansatz and the  $D_1$  ansatz. In recent years, Zhao *et al.* demonstrated that all these states can be extended to their corresponding multiple Davydov states by superimposing expandable replicas of the single Davydov state [12]. Expressions of the multiple  $D_1$ ,  $D_{1.5}$ ,  $D_2$ , and  $\tilde{D}$  ansätze are referred to in Section 3.2 of Chapter 3.

The  $D_1$ ,  $D_2$ , and  $\tilde{D}$  ansätze were employed to probe the dynamics of a one-dimensional Holstein polaron [10]. The variational outputs were examined via speeds of exciton-induced phonon wave packets, linear optical absorption, and polaron energy compositions. These ansätze were found to fail to provide adequate descriptions in the weak-coupling regime. By incorporating the Davydov ansätze theory into the nonlinear response function formalism, Zhao's group developed a new approach to compute the two-dimensional photon-echo spectroscopy of molecular rings [18]. The Davydov ansätze are further applied to the dynamics of the spin-boson model, and a coherent-incoherent transition was found at a certain critical coupling strength [19]. In 2015, a multitude of Davydov  $D_2$  trial states was reported to enable numerical exact calculations for the Holstein polaron with simultaneous diagonal and off-diagonal exciton-phonon coupling [12]. Later on, the multiple Davydov ansätze were demonstrated to be suitable for the



spin-boson model, and photosynthesis systems. Even temperature effects were well incorporated in the framework of the multiple Davydov trial states [20].

The  $D_1$ ,  $D_2$ , and  $\tilde{D}$  ansätze are localized states from the soliton theory, and they are referred to as trial states in their own right without considering a form factor of a delocalized state. Even for translationally invariant polaron systems, the product forms of the ansätze (Eq. (2.2) - Eq. (2.5)) predispose them to the formation of permanently localized solutions. Each localized structure contains a singly localized exciton accompanied by a phonon cloud of a single coherent state. In order to change the correlations between the exciton and phonon parts and make these ansätze explicitly translationally invariant trial states, replicas of single Davydov trial states can be superposed with appropriate weights. The polaron states have been analyzed with the delocalized  $D_1$ , Toyozawa, and global-local ansätze, all of which are Bloch states with the designated crystal momentum. In detail, the  $D_1$ ,  $D_2$ , and  $\tilde{D}$  ansätze can be delocalized into the delocalized  $D_1$ , Toyozawa, and global-local ansätze via a projection operator  $\hat{P}_\kappa$

$$\hat{P}_\kappa = N^{-1} \sum_n e^{i(\kappa - \hat{P})n} = \delta(\kappa - \hat{P}), \quad (2.6)$$

where the joint crystal momentum is indicated by the Greek  $\kappa$ , and

$$\hat{P} = \sum_k k \hat{a}_k^\dagger \hat{a}_k + \sum_q q \hat{b}_q^\dagger \hat{b}_q. \quad (2.7)$$

The operator (2.6) yields a sum over  $n$  of localized structures displaced from the origin by  $n$  lattice spacings, and weighted by  $e^{i\kappa n}$ .

For the Holstein polaron, the bare exciton band is  $E(\kappa) = -2J \cos \kappa$ , and the band structure can be altered by the exciton-phonon coupling. In the weak exciton-phonon coupling limit, the simple coherent state phonon structure in the single Davydov's ansatz has an inherent deficiency. Denoting the Einstein phonon frequency as  $\omega$ , the energy of the one-phonon line is  $E = -1$ . The bare exciton band penetrates the one-phonon continuum at certain finite crystal momentum  $\kappa^o$ . A quasi-continuum of states above the one-phonon line exists for a non-interacting exciton-phonon system and can be explained

by level-crossing arguments. As the volume becomes infinite, this quasi-continuum of states turns into a true continuum. When the exciton-phonon coupling goes to zero, the ground state is expected to contain only the bare exciton with momentum  $\kappa$  and the phonon vacuum for  $\kappa < |\kappa^o|$ , and one exciton with zero momentum and one phonon with momentum  $\kappa$  for  $\kappa > |\kappa^o|$ . Therefore, the localized ansätze are rather inadequate in this limit, as the single coherent states in equations from Eq. (2.2) to Eq. (2.5) provide poor approximations to a one-phonon number state.

The delocalized  $D_1$  ansatz is then obtained after the delocalization onto the usual  $D_1$  ansatz,

$$\begin{aligned} |\Psi_1(\kappa)\rangle &= |\kappa\rangle \langle \kappa | \kappa \rangle^{-1/2}, \\ |\kappa\rangle &= \sum_n e^{i\kappa n} \sum_{n_1} \alpha_{n_1-n}^\kappa \hat{a}_{n_1}^\dagger \exp[-\sum_{n_2} (\beta_{n_1-n, n_2-n}^\kappa \hat{b}_{n_2}^\dagger) - \text{H.c.}] |0\rangle, \end{aligned} \quad (2.8)$$

where  $|0\rangle$  is the product of the exciton and phonon vacuum states,  $\alpha_{n_1-n}^\kappa$  is the exciton amplitude, and the phonon displacement  $\beta_{n_1-n, n_2-n}^\kappa$  depends on  $n_1$  and  $n_2$ , respectively, the sites at which an electronic excitation and a phonon are generated.  $\hat{b}_{n_2}^\dagger$  ( $\hat{b}_{n_2}$ ) is the phonon creation (annihilation) operator for the  $n_2$ -th site.

After the delocalization onto the usual  $D_2$  ansatz, the Toyozawa ansatz is given by

$$\begin{aligned} |\Psi_2(\kappa')\rangle &= |\kappa'\rangle \langle \kappa' | \kappa' \rangle^{-1/2}, \\ |\kappa'\rangle &= \sum_n e^{i\kappa' n} \sum_{n_1} \psi_{n_1-n}^{\kappa'} \hat{a}_{n_1}^\dagger \exp[-\sum_{n_2} (\lambda_{n_2-n}^{\kappa'} \hat{b}_{n_2}^\dagger) - \text{H.c.}] |0\rangle, \end{aligned} \quad (2.9)$$

where  $\psi_{n_1-n}^{\kappa'}$  is the exciton amplitude analogous to  $\alpha_{n_1-n}^\kappa$  in the delocalized  $D_1$  ansatz, and  $\lambda_{n_2-n}^{\kappa'}$  is the phonon displacement. Actually,  $\lambda_{n_2-n}^{\kappa'}$  is just one column of the phonon displacement matrix  $\beta_{n_1-n, n_2-n}^\kappa$  in the delocalized  $D_1$  ansatz. If the ansätze are used to describe the Holstein molecular crystal with  $N = 16$  sites, the Toyozawa ansatz is actually 16 replicas of the single Davydov  $D_2$  ansatz with additional weights, and recognized as another version of the multiple Davydov  $D_2$  ansatz with multiplicity  $M = 16$  as shown in Eq. (3.5).

After the delocalization onto the  $\tilde{D}$  ansatz, the global-local ansatz is formulated as

$$\begin{aligned} |\Psi_{GL}(\kappa'')\rangle &= |\kappa''\rangle \langle \kappa'' | \kappa'' \rangle^{-1/2} \\ |\kappa''\rangle &= \sum_n e^{i\kappa'' n} \sum_{n_1} \psi_{n_1-n}^{\kappa''} \hat{a}_{n_1}^\dagger \exp[-\sum_{n_2} (\lambda_{n_2-n}^{\kappa''} - \gamma_{n_2-n_1}^{\kappa''}) \hat{b}_{n_2}^\dagger - \text{H.c.}] |0\rangle, \end{aligned} \quad (2.10)$$

by substituting the general phonon displacement in the delocalized  $D_1$  ansatz,  $\beta_{n_1-n, n_2-n}^\kappa$ , into  $\lambda_{n_2-n}^{\kappa''} - \gamma_{n_2-n_1}^{\kappa''}$ .

The Davydov ansätze can also be used to study polaron ground-state energy band, computed as

$$E(\kappa) = \langle \Psi(\kappa) | \hat{H} | \Psi(\kappa) \rangle, \quad (2.11)$$

where  $|\Psi(\kappa)\rangle$  is an appropriately normalized, delocalized trial state, and  $\hat{H}$  is the system Hamiltonian. It should be noted that the crystal momentum operator commutes with the system Hamiltonian, and energy eigenstates are also eigenfunctions of the crystal momentum. Therefore, variations for distinct  $\kappa$  are independent. The set of  $E(\kappa)$  constitutes a variational estimate (an upper bound) for the polaron energy band. The relaxation iteration technique, viewed as an efficient method for identifying energy minima of a complex variational system, is adopted in this work to obtain numerical solutions to a set of self-consistency equations derived from the variational principle. To achieve efficient and stable iterations toward the variational ground state, one may take advantage of the continuity of the ground state with respect to small changes in system parameters over most of the phase diagram and may initialize the iteration using a reliable ground state already determined at some nearby points in parameter space. Starting from those limits where exact solutions can be obtained analytically and executing a sequence of variations along well-chosen paths through the parameter space using solutions from one step to initialize the next, the whole parameter space can be explored.

Zhao *et al.* used mainly the Merrifield ansatz, the Toyozawa ansatz, and the global-local ansatz in early 1990s to study the ground-state energy band of the Holstein

molecular crystal model with simultaneous diagonal and off-diagonal exciton-phonon coupling [13–17]. The Merrifield ansatz is a small polaron ansatz, and was proposed by Merrifield in the 1964 [21]. The Toyozawa ansatz, requires only limited computational resources, and can deal with large clusters with the number of sites greater than 1000 [13]. However, its accuracy in the weak coupling regime at the Brillouin zone boundary has room for improvements due to the excessive simplification of exciton-phonon correlations. For the global-local ansatz, it is difficult to achieve iterative convergence in the weak coupling regime [15]. In 2013, Zhao and his coworkers developed the delocalized  $D_1$  ansatz [17]. It can lower the ground-state energies at the Brillouin zone boundary significantly compared with the Toyozawa and global-local ansätze in the weak coupling regime, while considerable improvement can be achieved over the entire Brillouin zone in the strong coupling regime. In 2014, Zhao’s group used the newly developed multi- $D_1$  ansatz to calculate the ground state properties of the spin-boson model with simultaneous diagonal and off-diagonal coupling [22]. The multi- $D_1$  ansatz can provide results that are consistent with those from exact diagonalization and density matrix renormalization group approaches for the cases involving two oscillators and two baths described by a continuous spectral density function.

In general, progresses in the Davydov ansätze are impressive. The newly developed multiple Davydov trial states can offer accurate dynamics using the Dirac-Frenkel time-dependent variational principle, and give exact ground state properties after careful energy iterations.

## 2.2 Potential applications of the multiple Davydov $D_2$ ansatz

Using the newly developed multiple Davydov trial states, especially the multi- $D_2$  ansatz, it is promising to provide numerically exact dynamics for various open quantum systems. The following subsections review the experimental and theoretical progresses in four specified open quantum systems, which are featured on exciton transport, BOs, SF dynamics, and LZ transitions correspondingly.

### 2.2.1 Exciton transport in conducting polymers

CPs are a special class of organic materials with electronic and ionic conductivity, advanced processability and extraordinary wettability [23, 24]. In 1977, Heeger *et al.* reported oxidized iodine-doped polyacetylene as a forerunner of CPs [25, 26]. Various experimental strategies have been developed to produce CPs by techniques such as monomer oxidation using chemical oxidative polymerization in solution [27], electrochemical polymerization on conductive substrates [28], and vapor-phase polymerization [29]. Electrical properties of CPs can be tuned by oxidation and reduction, giving rise to rapid growth of applications. Based on their good charge transport property and high quantum efficiency of the luminescence, important utilizations of CPs are found in the large scale organic light-emitting diodes [30] and electronic devices such as field-effect transistors [31]. CPs have also been used as an electrode material for supercapacitors [32, 33]. As a logical alternative to conventional inorganic electrode materials, a composite architecture of various CPs have been developed as a cathode for ultrafast rechargeable batteries [34]. In comparison with non-conducting polymers, there are many advantages of CPs with regard to their electronic properties. CPs have also been used for other purposes [35]. For example, because of easy processability in microsturing processes [36], CPs have been considered for a wide range of biomedical and bioengineering applications: artificial muscles [37], controlled drug release [38], and neural recording [39, 40]. Surface wettability based on CPs can switch between superhydrophilicity and superoleophobicity by surface morphology control at nanoscale [27], implying usage of CPs in intelligent orthopedic and dental implants [41].

In the aforementioned applications, the efficiency of charge carrier transport and exciton transport significantly impacts the overall device performance [35]. The carrier or exciton transport in CPs is well described by the SSH model in which the  $\pi$  electrons are treated in a tight-binding approximation and the  $\sigma$  electrons are assumed to move adiabatically with the nuclei [42]. Su *et al.* convincingly demonstrated that solitons play a critical role in the carrier transport doping mechanism [43]. Troisi *et al.* applied the SSH

model to investigate charge carrier dynamics in crystalline organic semiconductors by solving the time-dependent Schrödinger equation for the charge wave function and using the Ehrenfest theorem for classical accelerations of nuclear positions [44, 45]. Improvements on this semi-classical method has been made to study charge transport in organic materials in recent years [46–48]. Temperature dependent charge carrier mobility has also been considered [44, 48]. It is believed that for short times (comparable to the phonon period) the evolution of the system is dominated by semi-classical dynamics. The traditional Ehrenfest dynamics did not well treat the decoherence effect, which is incorporated by an instantaneous decoherence correction (IDC) approach in the framework of semi-classical method [48, 49].

Even though the semi-classical dynamics in the SSH model can capture certain features of charge transport, enormous challenges still remain to accurately describe fully quantum dynamical correlations between the electronic and vibrational subsystems [50]. In realistic polymer chains, charge transport processes occur on the nano scale and the carriers interact with the environment including the dominant phononic DOFs [51]. The SSH model includes off-diagonal exciton-phonon coupling as a nontrivial dependence of the exciton transfer integral on lattice coordinates [43, 52]. Due to inherent difficulties, the off-diagonal coupling is often inadequately treated in theoretical studies. Early treatments of the off-diagonal coupling include the Munn-Silbey theory [53]. Recently, the Davydov  $D_2$  ansatz [11] and the multiple Davydov trial states [54] have been developed to study polaron dynamics in the presence of the off-diagonal coupling. However, much awaits to be studied on the rich polaron dynamics with off-diagonal coupling with regard to exciton momentum redistribution and energy relaxations [55].

### **2.2.2 Bloch oscillations dynamics in semiconductor superlattices and organic materials**

Early evidence of time-domain BOs in superlattices was revealed by transient degenerate four-wave mixing (DFWM) [56, 57], yielding results in agreement with the work of Esaki and Tsu [58]. BOs emerge when an electron subject to a perfectly periodic lattice potential executes periodic motion in the presence of an external electric field [59–65]. In recent decades, BOs were found in various physical systems. For example, with the progress of laser cooling and manipulation, cold atoms in an optical lattice were found to exhibit BOs and Wannier-Stark ladders [66, 67], in accordance with theoretical predictions [68–70]. Further experimental evidence of BOs was found in atomic Bose-Einstein condensates (BEC) in optical lattices [71–73], in a semiconductor waveguide [74], and in a thermo-optic polymer array subjected to a temperature gradient [75]. It was also suggested that waveguide arrays with a changeable effective index of the individual guides would be an optimal system to detect optical BOs in the space domain [76]. In addition, BOs have received much attention in the past decades for its potential application in THz generation and negative differential conductance [58]. Investigations of BOs have been carried out in THz emission [77], electro-optic detection [78], and DFWM experiments [56]. Recently, a new mesoscopic amplifier by the name of Bloch Oscillating Transistor has been proposed based on BOs [79].

Following the remarkable experimental progress, recent theoretical work explores the presence of BOs in a variety of contexts. For example, formation of photonic BOs was investigated in an exponentially chirped one-dimensional Bragg grating using Hamiltonian optics, where paths of geometrical rays are determined from Hamilton's equations [80]. BOs were also theoretically predicted to exist in magnetic systems, such as soliton-like domain walls in anisotropic spin 1/2 chains under magnetic fields [81]. Furthermore, BOs in interacting quantum few body systems have been modeled with the Bose-Hubbard model [82].

One important issue for BOs dynamics is the effect of carrier-phonon interactions, which is of essential importance for systems such as semiconductor superlattices [83, 84], organic materials [85–91] and quantum dots [92, 93]. The phonon bath is treated classically and the associated carrier-phonon coupling semi-classically in the SSH model for polymers [85–88] and in the Peyrard-Bishop-Holstein model for DNA [89, 90]. More than forty years ago, Thornber and Feynman studied the motion of an electron in a polar crystal in a strong electric field using Fröhlich’s model of polaron, and found that the electron acquires a constant velocity due to the emission of phonons [94]. Much theoretical work based on the rate equations or the Boltzmann equation later focused on calculating transition rate probabilities, rather than complex quantum amplitudes [95, 96]. However, full quantum coherence was revealed to be retained in an inelastic quantum transport process and a steady state was found to be reached subject to an infinite lattice, leaving the dispersionless optical phonon absorbing the excess energy from the external field [97, 98].

Despite dedicated studies of BOs dynamics, the effect of complex interplay between the electron and its accompanying phonon cloud in a one-dimensional lattice remains an open question [99, 100]. Spatial dynamics influenced by carrier-phonon coupling is also inadequately studied given initial broad and narrow carrier wave packets [101, 102]. Moreover, a unified treatment on various types of carrier-phonon coupling remains elusive.

The intramolecular (diagonal) and intermolecular (off-diagonal) carrier-phonon coupling has been demonstrated to coexist in organic materials [103], and it is shown that off-diagonal coupling plays a crucial role in polaronic diffusion [104]. In the presence of an external electric field, polaron motion with off-diagonal coupling in polymer chains has been simulated with a semi-classical method [91, 105], neglecting the quantum nature of phonons and carrier-phonon coupling. Fully quantum mechanical treatments are few in the literature with little attention paid to Hamiltonians with off-diagonal carrier-phonon coupling and an external field due to inherent difficulties to obtain reliable solutions [98].



Based on the Holstein molecular crystal model, which describes the motion of an carrier enveloped by a cloud of phonons [106], both diagonal and off-diagonal carrier-phonon coupling can be investigated. Despite apparent simplicity of its Hamiltonian, the Holstein model never ceases to surprise us with rich physics related to carrier-phonon correlations. Our multiple Davydov trial states have been developed to accurately treat the dynamics of the Holstein model with simultaneous diagonal and off-diagonal coupling [107, 108]. This method can be applied to polaron dynamics in an external field.

### 2.2.3 Singlet fission processes

SF is a multielectron process in which a singlet exciton generated by light irradiation is converted to two triplet excitons [109–111]. In 1965, SF was first coined to explain photophysics in anthracene crystals [112]. In recent years, interest in SF has been renewed because of its potential to increase maximum efficiency of organic solar cells [113–115]. As a result, SF has been studied in various organic materials of polyacenes [116], polyenes [117], and other chromophores, such as perylenediimide and tert-butyl-substituted terrylenes [118, 119].

To date, most efforts have been dedicated to understanding intermolecular singlet fission (xSF), in which a singlet state on one molecule couples with the ground-state of neighboring molecules to form an intermolecular correlated triplet pair. The xSF mainly involves conventional SF materials, such as crystalline solids of pentacene [120, 121], tetracene [122, 123], and other organic materials [118, 124]. Mechanisms of xSF have been the focus of many ultrafast spectroscopic measurements [111, 120–123] and extensive theoretical studies based on dynamics simulations [125–134] and electronic structures calculations [135–139]. However, due to intermolecular nature of xSF, the efficiency of this process is highly sensitive to geometric stacking, crystal environment, side-group, and other factors [132, 140–142]. Devices based on xSF which manipulate crystal packing are limited by the lack of high throughput processing strategies of developing highly ordered molecular structures. Difficulties in engineering molecular

packing morphology have promoted the development of intramolecular singlet fission (iSF), in which the two long-lived triplets are located on the same molecule [143]. Achieved in 2015 [144], iSF materials offer great advantages in terms of tunable molecular and electronic structures, and have included a series of chromophore dimers with a conjugated linker [145–149, 149], such as covalently coupled pentacenes [150, 151], and a covalent tetracene dimer [145]. Recent transient absorption measurements for diphenyl-dicyano-oligoene groups (DPDC<sub>n</sub>) molecules have shown that xSF occurs in DPDC<sub>n</sub> in acetonitrile solution, while in DPDC<sub>n</sub> solid films, iSF dominates [152]. Based on these findings, Trinh *et al.* suggested that efficient SF can be achieved by independent tuning of singlet-triplet pair coupling and triplet pair splitting [152]. However, a limited understanding of detailed xSF and iSF mechanisms hinders the design of versatile SF materials. In particular, a unified treatment of phonon effects remains elusive [20, 127, 128, 148, 150].

In organic crystals, fluctuations in electronic energies are induced by intramolecular vibrations [127, 128]. (Note that this type of exciton-phonon coupling is often called diagonal coupling.) Recently, ultrafast spectroscopic measurements in the xSF materials have shown that phonon modes coupled to electronic excitations play a crucial role in the xSF process [153–155]. In particular, high-frequency modes of pentacene derivatives [20, 156, 157] and crystalline tetracene [158, 159] are found to facilitate efficient fission by resonances between vibrational modes and energy splittings of electronic states. On the other hand, intermolecular vibrations of the crystals induce off-diagonal exciton-phonon coupling which modulates the electronic coupling between the singlet and triplet pair state. Berckelbach *et al.* have considered the off-diagonal coupling in acene crystals and demonstrated that it plays a minor role because frequencies of the intermolecular vibrations are significantly lower than the energy difference between the singlet and the triplet pair state [128]. Effects of those forms of exciton-phonon coupling on xSF are usually restricted to particular materials such as perlenediimide crystals [160]. In contrast, in the context of iSF, the transition between the singlet state and triplet pair state occurs within a covalently linked dimer, and thus intramolecular vibrations of the linker part may

induce fluctuations in the electronic coupling. Indeed, quantum chemical calculations of the covalent tetracene dimer demonstrated that high frequency intramolecular vibrations induce nonnegligible off-diagonal coupling as well as diagonal coupling [145]. The two kinds of coupling have been found to be tunable in a typical iSF molecule by changing linker types and by engineering dihedral angles between the chromophore units and the linker [146, 150, 151]. The corresponding iSF dynamics has been obtained by treating the exciton states quantum mechanically and phonons classically, indicating that SF time scales vary with the linker types [148, 149]. Those investigations on exciton-phonon coupling are believed to have helped understand fast iSF observed in a broad range of organic molecules. However, detailed iSF mechanisms under the influence of simultaneous diagonal and off-diagonal exciton-phonon coupling remain ill understood, and thus a full quantum dynamical investigation, such as the variational method with the multiple Davydov ansätze, is required for the elucidation of this issue.

#### **2.2.4 Landau-Zener transitions in the circuit quantum electrodynamics devices**

The LZ transition comes into play when the energy difference between two diabatic states is swept through an avoided level crossing. Its final transition probability was calculated by Landau and Zener in 1932 [161, 162]. As one of the most fundamental phenomena in quantum dynamics, the LZ transition plays an important role in a variety of fields, including atomic and molecular physics [163–165], quantum optics [166], solid state physics [167], chemical physics [168], and quantum information science [169]. The list of physical systems dominated by the LZ transition grows and interest in the LZ transition has been renewed recently due to its various new applications [170, 171], such as a nitrogen-vacancy center spin in isotopically purified diamond [172], a microwave driven superconducting qubit coupled to a two level system, [173] and a spin-orbit-coupled Bose-Einstein condensate [174].

In particular, advances in circuit QED devices make them promising candidates for exploration of the LZ transitions due to their potential scalability and tunable parameters

over a broad range [175–177]. Circuit QED is the realization of cavity QED in superconducting quantum circuits. A superconducting flux qubit coupled to a quantum interference device [178] has been fabricated by Chiorescu *et al.*, and a charge qubit coupled to a transmission line resonator by Wallraff *et al.* [179]. These developments have paved the way to study the LZ transitions because the energy difference between the two diabatic states has been allowed to be tuned by external fields [180]. Recent measurements of the LZ transitions have been reported on an individual flux qubit within a multiqubit superconducting chip, in which qubits are set up in the compound Josephson-junction radio-frequency superconducting quantum interference device (SQUID) [181].

In any physical realization, a quantum two-state system will be affected by its environment, which may alter the effective interaction between the two energy levels of the system. For a realistic study of a qubit manipulation via the LZ transitions, the influence of its environment is an important issue because a qubit is never completely isolated. Effects of dissipation have been studied in 1989 by Ao *et al.*, using time-dependent perturbation theory, yielding only the LZ transition probabilities at long times in the fast and slow sweeping limit [182]. Hänggi and coworkers have studied the LZ transitions and dynamics in a qubit coupled to a bath at zero temperature [183]. Temperature effects on the LZ transitions have been explored in a dissipative environment using the quasiadiabatic propagator path integral method and the non-equilibrium Bloch equations, by which dependence of the transition probability on sweeping velocities is obtained at long times [184–187]. Nalbach *et al.* have further studied the influence of thermal environment on a harmonically driven quantum two-state system through avoided crossings and proposed a novel rocking ratchet based on electronic double quantum dots [188]. So far most attention has been paid to the transition probabilities in the steady states, where the energy difference of the two diabatic states is much larger than the bandwidth of the bosonic bath [189]. However, understanding of LZ dynamics at intermediate times is needed. This is a time range in which the transitions have not fully taken place and the energy difference of the two diabatic states is still within the bath's bandwidth [190]. Specifically, dependence of LZ dynamics on the bath frequency and the

types of bath spectral densities is still not well-understood.

Recently, high-quality fabrication techniques and physically large shunt capacitors have been developed to reduce densities and electric participation of defects at various metal and substrate interfaces, leading to rapid progresses in performance and manipulation of the flux qubit and its environment [191]. An Ohmic type spectral density can be used to describe the qubit-bath coupling in various devices like a superconducting circuit consisting of a transmon qubit suspended on top of a microwave guide [192], a superconducting qubit interacting with an array of coupled transmission line resonators [193], and a fabricated circuit QED architecture that contains a capacitively shunted flux qubit coupled capacitively to a planar transmission line resonator [194]. Egger *et al.* showed that a sub-Ohmic type spectral density can characterize the qubit-bath coupling in a multimode circuit QED setup with hybrid metamaterial transmission lines [195]. Super-Ohmic type spectral densities have been applied to characterize the flux noise on multiple flux qubits, especially when scaling up to large numbers of qubits, as was stated by Storz *et al.* [196, 197]. Nalbach *et al.* have uncovered that super-Ohmic fluctuations are the main relaxation channel for a detuned double quantum dot which is driven by external voltage pulses [198]. When a superconducting persistent-current qubit is exposed to an underdamped SQUIDs environment, Lorentzian spectral densities have usually been found [199, 200].

Dynamics of the LZ transitions at the intermediate times is influenced by the dissipative environment. Roles of the environment include fluctuations of energies of diabatic states, denoted by diagonal coupling, and environment-induced transitions between diabatic states, expressed by off-diagonal coupling. In the presence of only diagonal coupling, dynamics of the LZ transitions have been studied by Orth *et al.*, using a stochastic Schrödinger equation [190, 201]. Off-diagonal coupling has been demonstrated to exist in a number of experiments, such as in a superconducting charge qubit coupled to an on-chip microwave resonator in the strong coupling regime [179], in a three-dimensional circuit QED architecture [191], a circuit QED device with seven qubits

[202], and in a circuit QED implementation with a time-dependent transverse magnetic field [203]. However, effects of off-diagonal coupling on LZ dynamics have not been well investigated and can be studied by the Davydov ansätze.

## References

- [1] A. S. Davydov, *J. Theor. Biol.*, **1973**, 38, 559.
- [2] N. I. Davydov, A. S. and Kislukha, *Sov. Phys.-JETP*, **1976**, 44, 571.
- [3] A. S. Davydov, *Phys. Scr.*, **1979**, 20, 387.
- [4] A. S. Davydov, *Solitons in Molecular Systems*, Springer-Science+Business Media, B.Y., (1985).
- [5] A. C. Scott, *Philos. Trans. R. Soc. London A Math. Phys. Eng. Sci.*, **1985**, 315, 423.
- [6] L. D. Landau, *Phys. Z. Sowjetunion*, **1933**, 3, 644-645.
- [7] H. Bolterauer and M. Opper, *Zeitschrift Für Phys. B Condens. Matter*, **1991**, 82, 95.
- [8] W. C. Kerr and P. S. Lomdahl, *Phys. Rev. B*, **1987**, 35, 3629.
- [9] W. Förner, *J. Phys. Condens. Matter*, **1993**, 5, 3897.
- [10] J. Sun, B. Luo, and Y. Zhao, *Phys. Rev. B*, **2010**, 82, 014305.
- [11] Y. Zhao, B. Luo, Y. Zhang, and J. Ye, *J. Chem. Phys.*, **2012**, 137, 084113.
- [12] N. Zhou, Z. Huang, J. Zhu, V. Chernyak, and Y. Zhao, *J. Chem. Phys.*, **2015**, 143, 014113.
- [13] Y. Zhao, *Doctoral thesis, University of California, San Diego*, **1994**; Y. Zhao, D. W. Brown, and K. Lindenberg, *J. Chem. Phys.*, **1997**, 107, 3159; **1997**, 107, 3179.
- [14] Y. Zhao, D. W. Brown, and K. Lindenberg, *J. Chem. Phys.*, **1997**, 106, 2728.
- [15] Y. Zhao, G. Q. Li, J. Sun, and W. H. Wang, *J. Chem. Phys.*, **2008**, 129, 124114.

- [16] Y. Zhao, D. W. Brown, and K. Lindenberg, *J. Chem. Phys.*, **1997**, 107, 3159; D. Brown, K. Lindenberg, and Y. Zhao, *ibid.* **1997**, 107, 3179.
- [17] J. Sun, L. W. Duan, and Y. Zhao, *J. Chem. Phys.*, **2013**, 138, 174116.
- [18] T. D. Huynh, K. W. Sun, M. Gelin, and Y. Zhao, *J. Chem. Phys.*, **2013**, 139, 104103.
- [19] N. Wu, L. Duan, X. Li, and Y. Zhao, *J. Chem. Phys.*, **2013**, 138, 084111.
- [20] Y. Fujihashi, L. Chen, A. Ishizaki, J. Wang, and Y. Zhao, *J. Chem. Phys.*, **2017**, 146, 044101.
- [21] R. E. Merrifield, *J. Chem. Phys.*, **1964**, 40, 4450.
- [22] N. Zhou, L. Chen, D. Mozyrsky, V. Chernyak, and Y. Zhao, *Phys. Rev. B - Condens. Matter Mater. Phys.*, **2014**, 90, 155135.
- [23] L. Xu, W. Chen, A. Mulchandani, and Y. Yan, *Angew. Chemie Int. Ed.*, **2005**, 44, 6009.
- [24] T. K. Das and S. Prusty, *Polym. Plast. Technol. Eng.*, **2012**, 51, 1487.
- [25] H. Shirakawa, E. J. Louis, A. G. MacDiarmid, C. K. Chiang, and A. J. Heeger, *J. Chem. Soc., Chem. Commun.*, **1977**, 16, 578.
- [26] E. J. Heller, Y. Yang, and L. Kocia, *ACS Cent. Sci.*, **2015**, 1, 40.
- [27] T. Darmanin and F. Guittard, *Prog. Polym. Sci.*, **2014**, 39, 656.
- [28] T. Darmanin, F. Guittard, S. Amigoni, E. de Givenchy, X. Noblin, R. Kofman, and F. Celestini, *Soft Matter*, **2011**, 7, 1053.
- [29] S. G. Im, D. Kusters, W. Choi, S. H. Baxamusa, M. C. M. van de Sanden, and K. K. Gleason, *ACS Nano*, **2008**, 2, 1959.
- [30] J. H. Burroughes, D. D. C. Bradley, A. R. Brown, R. N. Marks, K. Mackay, R. H. Friend, P. L. Burns, and A. B. Holmes, *Nature*, **1990**, 347, 539.

- [31] L. Torsi, A. Dodabalapur, L. Sabbatini, and P. G. Zambonin, *Sensors Actuators B Chem.*, **2000**, 67, 312.
- [32] F. Fusalba, P. Gouérec, D. Villers, and D. Bélanger, *J. Electrochem. Soc.*, **2001**, 148, A1.
- [33] B. N. Reddy, M. Deepa, and A. G. Joshi, *Phys. Chem. Chem. Phys.*, **2014**, 16, 2062.
- [34] J. Kim, H.-S. Park, T.-H. Kim, S. Yeol Kim, and H.-K. Song, *Phys. Chem. Chem. Phys.*, **2014**, 16, 5295.
- [35] M. Ates, T. Karazehir, and A. Sezai Sarac, *Curr. Phys. Chem.*, **2012**, 2, 224.
- [36] J. W. Schultze and H. Karabulut, *Electrochim. Acta*, **2005**, 50, 1739.
- [37] T. F. Otero and J. M. Sansiena, *Adv. Mater.*, **1998**, 10, 491.
- [38] M. R. Abidian, D.-H. Kim, and D. C. Martin, *Adv. Mater.*, **2006**, 18, 405.
- [39] M. R. Abidian, K. A. Ludwig, T. C. Marzullo, D. C. Martin, and D. R. Kipke, *Adv. Mater.*, **2009**, 21, 3764.
- [40] R. Ravichandran, S. Sundarrajan, J. R. Venugopal, S. Mukherjee, and S. Ramakrishna, *J. R. Soc. Interface*, **2010**, 7, S559.
- [41] J. Liao, C. Ning, Z. Yin, G. Tan, S. Huang, Z. Zhou, J. Chen, and H. Pan, *Chem. Phys. Chem.*, **2013**, 14, 3891.
- [42] A. J. Heeger, S. Kivelson, J. R. Schrieffer, W. P. Su, *Reviews of Modern Physics*, **1988**, 60, 781-850.
- [43] W. P. Su, J. R. Schrieffer, and A. J. Heeger, *Phys. Rev. Lett.*, **1979**, 42, 1698.
- [44] A. Troisi and G. Orlandi, *Phys. Rev. Lett.*, **2006**, 96, 86601.
- [45] P. Ehrenfest, *Zeitschrift Für Phys.*, **1927**, 45, 455.
- [46] M. Hultell and S. Stafström, *Chem. Phys. Lett.*, **2006**, 428, 446.



- [47] A. Troisi, D. L. Cheung, and D. Andrienko, *Phys. Rev. Lett.*, **2009**, 102, 116602.
- [48] W. Si and C.-Q. Wu, *J. Chem. Phys.*, **2015**, 143, 024103.
- [49] J. Dong, W. Si, and C.-Q. Wu, *J. Chem. Phys.*, **2016**, 144, 144905.
- [50] G. Li, B. Movaghar, A. Nitzan, and M. A. Ratner, *J. Chem. Phys.*, **2013**, 138, 044112.
- [51] P. Szymanski, S. Garrett-Roe, and C. B. Harris, *Prog. Surf. Sci.*, **2005**, 78, 1-39.
- [52] Y. Zhao, D. W. Brown, and K. Lindenberg, *J. Chem. Phys.*, **1997**, 107, 3159; **1997**, 107, 3179.
- [53] R. W. Munn and R. Silbey, *J. Chem. Phys.*, **1985**, 83, 1843.
- [54] N. J. Zhou, Z. K. Huang, J. F. Zhu, V. Chernyak, Y. Zhao, *J. Chem. Phys.*, **2015**, 143, 014113.
- [55] F. Dorfner, L. Vidmar, C. Brockett, E. Jeckelmann, and F. Heidrich-Meisner, *Phys. Rev. B*, **2015**, 91, 104302.
- [56] J. Feldmann, K. Leo, J. Shah, D. A. B. Miller, J. E. Cunningham, T. Meier, G. von Plessen, A. Schulze, P. Thomas and S. Schmitt Rink, *Phys. Rev. B*, **1992**, 46, 7252.
- [57] E. E. Mendez and G. Bastard, *Phys. Today*, **1993**, 46, 34.
- [58] L. Esaki and R. Tsu, *IBM J. Res. Dev.*, **1970**, 14, 61.
- [59] F. Bloch, *Zeitschrift Für Phys.*, **1928**, 52, 555.
- [60] C. Zener, *Proc. R. Soc. A*, **1934**, 145, 523.
- [61] J. N. Churchill and F. E. Holmstrom, *Phys. Scr.*, **1983**, 27, 91-98.
- [62] G. H. Wannier, *Phys. Rev.*, **1960**, 117, 432.
- [63] W. V. Houston, *Phys. Rev.*, **1940**, 57, 184.
- [64] M. Holthaus and D. W. Hone, *Phil. Mag. B.*, **1996**, 74, 105.

- [65] H. Fukuyama, R. A. Bari and H. C. Fogedby, *Phys. Rev. B.*, **1973**, 8, 5579.
- [66] C. Cohen-Tannoudji, *AIP Conf. Proc.*, **1987**, 160, 318.
- [67] S. Chu, *Science* **1991**, 253, 861.
- [68] M. B. Dahan, E. Peik, J. Reichel, Y. Castin, C. Salomon, *Phys. Rev. Lett.*, **1996**, 76, 4508.
- [69] S. R. Wilkinson, C. F. Bharucha, K. W. Madison, Q. Niu, M. G. Raizen, *Phys. Rev. Lett.*, **1996**, 76, 4512.
- [70] O. Morsch, J. H. Müller, M. Cristiani, D. Ciampini, and E. Arimondo, *Phys. Rev. Lett.*, **2001**, 87, 140402.
- [71] B. P. Anderson and M. A. Kasevich, *Science.*, **1998**, 282, 1686.
- [72] A. R. Kolovsky, E. A. Gomez, and H. J. Korsch, *Phys. Rev. A*, **2010**, 81, 025603.
- [73] M. Cristiani, O. Morsch, J. H. Müller, D. Ciampini and E. Arimondo, *Phys. Rev. A*, **2002**, 65, 063612.
- [74] R. Morandotti, U. Peschel, J. S. Aitchinson, H. S. Eisenberg and Y. Silberberg, *Phys. Rev. Lett.* **1999**, 83, 4756.
- [75] T. Pertsch, P. Dannberg, W. Elflein, and A. Bräuer, *Phys. Rev. Lett.* **1999**, 83, 4752.
- [76] U. Peschel, T. Pertsch, and F. Lederer, *Opt. Lett.*, **1998**, 23, 1701.
- [77] C. Waschke, H. G. Roskos, R. Schwedler, K. Leo, H. Kurz, and K. Köhler, *Phys. Rev. Lett.*, **1993**, 70, 3319.
- [78] M. Först, G. Segschneider, T. Dekorsy, H. Kurz, and K. Köhler, *Phys. Rev. B*, **2000**, 61, R10563.
- [79] J. Delahaye, J. Hassel, R. Lindell, M. Sillanpää, M. Paalanen, H. Seppä, and P. Hakonen, *Phys. E Low-Dimensional Syst. Nanostructures*, **2003**, 18, 15.

- [80] P. B. Wilkinson, *Phys. Rev. E*, **2002**, 65, 056616.
- [81] J. Kyriakidis and D. Loss, *Phys. Rev. B*, **1998**, 58, 5568.
- [82] A. Buchleitner and A. R. Kolovsky, *Phys. Rev. Lett.*, **2003**, 91, 253002.
- [83] T. Dekorsy, A. Bartels, H. Kurz, K. Köhler, R. Hey, and K. Ploog, *Phys. Rev. Lett.*, **2000**, 85, 1080.
- [84] A. W. Ghosh, L. Jönsson, and J. W. Wilkins, *Phys. Rev. Lett.*, **2000**, 85, 1084.
- [85] A. Johansson and S. Stafström, *Phys. Rev. Lett.*, **2001**, 86, 3602.
- [86] D. M. Basko and E. M. Conwell, *Phys. Rev. Lett.*, **2002**, 88, 056401.
- [87] A. A. Johansson and S. Stafström, *Phys. Rev. B*, **2004**, 69, 235205.
- [88] Y. Qui and L.-P. Zhu, *J. Chem. Phys.*, **2009**, 131, 134903.
- [89] M. Peyrard and A. R. Bishop, *Phys. Rev. Lett.*, **1989**, 62, 2755.
- [90] E. Diaz, R. P. A. Lima, and F. Domínguez-Adame, *Phys. Rev. B*, **2008**, 78, 134303.
- [91] S. V. Rakhmanova and E. M. Conwell, *Appl. Phys. Lett.*, **1999**, 75, 1518.
- [92] I. A. Dmitriev and R. A. Suris, *Semiconductors*, **2001**, 35, 212.
- [93] P.M. Petroff, A. Lorke, and A. Imamoglou, *Phys. Today.*, **2001**, 54, 46.
- [94] K. K. Thornber and R. P. Feynman, *Phys. Rev. B*, **1970**, 1, 4099.
- [95] R. Kümmel, H. Rauh, and E. Bangert, *Phys. Status Solidi*, **1978**, 87, 99.
- [96] D. Emin and C. F. Hart, *Phys. Rev. B*, **1987**, 36, 2530.
- [97] J. Bonca and S. A. Trugman, *Phys. Rev. Lett.*, **1997**, 79, 4874.
- [98] L. Vidmar, J. Bonca, M. Mierzejewski, and P. Prelovsek, and S. A. Trugman, *Phys. Rev. B*, **2002**, 83, 134301.
- [99] W. Zhang, A. O. Govorov, and S. E. Ulloa, *Phys. Rev. B*, **2002**, 66, 134302.

- [100] A. K. C. Cheung and M. Berciu, *Phys. Rev. B*, **2013**, 88, 35132.
- [101] V. G. Lyssenko, G. Valusis, F. Löser, T. Hasche, K. Leo, M. M. Dignam, and K. Köhler, *Phys. Rev. Lett.*, **1997**, 79, 301.
- [102] M. Sudzius, V. G. Lyssenko, F. Löser, K. Leo, M. M. Dignam, and K. Köhler, *Phys. Rev. B*, **1998**, 57, R12693.
- [103] V. Coropceanu, J. Cornil, D. S. Filho, Y. Olivier, R. Silbey, and J. Bredas, *Chem. Rev.*, **2007**, 107, 926.
- [104] H. Tamura, M. Tsukada, H. Ishii, N. Kobayashi, and K. Hirose, *Phys. Rev. B*, **2012**, 86, 35208.
- [105] Å. Johansson, and S. Stafström, *Phys. Rev. B*, **2002**, 65, 045207.
- [106] T. Holstein, *Ann. Phys. (N.Y.)*, **1959**, 8, 325; **1959**, 8, 343.
- [107] N. J. Zhou, Z. K. Huang, J. F. Zhu, V. Chernyak, Y. Zhao, *J. Chem. Phys.*, **2015**, 143, 014113.
- [108] N. Zhou, L. Chen, Z. Huang, K. Sun, Y. Tanimura, and Y. Zhao, *J. Phys. Chem. A*, **2016**, 120, 1562.
- [109] M. B. Smith and J. Michl, *Chem. Rev.* **2010**, 110, 6891.
- [110] M. B. Smith and J. Michl, *Annu. Rev. Phys. Chem.*, **2013**, 64, 361.
- [111] W.-L. Chan, T. C. Berkelbach, M. R. Provorse, N. R. Monahan, J. R. Tritsch, M. S. Hybertsen, D. R. Reichman, J. Gao, and X.-Y. Zhu, *Acc. Chem. Res.*, **2013**, 46, 1321.
- [112] S. Singh, W. J. Jones, W. Siebrand, B. P. Stoicheff, and W. G. Schneider, *J. Chem. Phys.*, **1965**, 42, 330.
- [113] M. C. Hanna and A. J. Nozik, *J. Appl. Phys.*, **2006**, 100, 74510.
- [114] D. N. Congreve, J. Lee, N. J. Thompson, E. Hontz, S. R. Yost, P. D. Reusswig, M. E. Bahlke, S. Reineke, T. Van Voorhis, and M. A. Baldo, *Science*, **2013**, 340, 334.

- [115] G. B. Piland, J. J. Burdett, R. J. Dillon, and C. J. Bardeen, *J. Phys. Chem. Lett.*, **2014**, 5, 2312.
- [116] C. Ramanan, A. L. Smeigh, J. E. Anthony, T. J. Marks, and M. R. Wasielewski, *J. Am. Chem. Soc.*, **2012**, 134, 386.
- [117] R. J. Dillon, G. B. Piland, and C. J. Bardeen, *J. Am. Chem. Soc.*, **2013**, 135, 17278.
- [118] S. W. Eaton, L. E. Shoer, S. D. Karlen, S. M. Dyar, E. A. Margulies, B. S. Veldkamp, C. Ramanan, D. A. Hartzler, S. Savikhin, T. J. Marks, and M. R. Wasielewski, *J. Am. Chem. Soc.*, **2013**, 135, 14701.
- [119] S. W. Eaton, S. A. Miller, E. A. Margulies, L. E. Shoer, R. D. Schaller, and M. R. Wasielewski, *J. Phys. Chem. A*, **2015**, 119, 4151.
- [120] M. W. B. Wilson, A. Rao, J. Clark, R. S. S. Kumar, D. Brida, G. Cerullo, and R. H. Friend, *J. Am. Chem. Soc.*, **2011**, 133, 11830.
- [121] W.-L. Chan, M. Ligges, A. Jailaubekov, L. Kaake, L. Miaja-Avila, and X.-Y. Zhu, *Science*, **2011**, 334, 1541.
- [122] W.-L. Chan, M. Ligges, and X. Zhu, *Nat. Chem.*, **2012**, 4, 840.
- [123] M. W. Wilson, A. Rao, K. Johnson, S. G  linas, R. di Pietro, J. Clark, and R. H. Friend, *J. Am. Chem. Soc.*, **2013**, 135, 16680.
- [124] L. Ma, K. Zhang, C. Kloc, H. Sun, M. E. Michel-Beyerle, and G. G. Gurzadyan, *Phys. Chem. Chem. Phys.*, **2012**, 14, 8307.
- [125] E. C. Greyson, J. Vura-Weis, J. Michl, and M. A. Ratner, *J. Phys. Chem. B*, **2010**, 114, 14168.
- [126] P. E. Teichen and J. D. Eaves, *J. Phys. Chem. B*, **2012**, 116, 11473.
- [127] T. C. Berkelbach, M. S. Hybertsen, and D. R. Reichman, *J. Chem. Phys.*, **2013**, 138, 114102.

- [128] T. C. Berkelbach, M. S. Hybertsen, and D. R. Reichman, *J. Chem. Phys.*, **2013**, 138, 114103.
- [129] T. C. Berkelbach, M. S. Hybertsen, and D. R. Reichman, *J. Chem. Phys.*, **2014**, 141, 074705.
- [130] F. Mirjani, N. Renaud, N. Gorczak, and F. C. Grozema, *J. Phys. Chem. C*, **2014**, 118, 14192.
- [131] G. Tao, *J. Phys. Chem. C*, **2014**, 118, 17299.
- [132] H. Tamura, M. Huix-Rotllant, I. Burghardt, Y. Olivier, and D. Beljonne, *Phys. Rev. Lett.*, **2015**, 115, 107401.
- [133] Y. Fujihashi and A. Ishizaki, *J. Phys. Chem. Lett.*, **2016**, 7, 363.
- [134] Y. Yao, *Phys. Rev. B*, **2016**, 93, 115426.
- [135] P. M. Zimmerman, Z. Zhang, and C. B. Musgrave, *Nat. Chem.*, **2010**, 2, 648.
- [136] P. M. Zimmerman, F. Bell, D. Casanova, and M. Head-Gordon, *J. Am. Chem. Soc.*, **2011**, 133, 19944.
- [137] X. Feng, A. V. Luzanov, and A. I. Krylov, *J. Phys. Chem. Lett.*, **2013**, 4, 3845.
- [138] S. R. Yost, J. Lee, M. W. Wilson, T. Wu, D. P. McMahon, R. R. Parkhurst, N. J. Thompson, D. N. Congreve, A. Rao, and K. Johnson, *Nat. Chem.*, **2014**, 6, 492.
- [139] D. Casanova, *J. Chem. Theory Comput.*, **2014**, 10, 324.
- [140] N. Renaud, P. A. Sherratt, and M. A. Ratner, *J. Phys. Chem. Lett.*, **2013**, 4, 1065.
- [141] L. Wang, Y. Olivier, O. V. Prezhdo, and D. Beljonne, *J. Phys. Chem. Lett.*, **2014**, 5, 3345.
- [142] S. Lukman, K. Chen, J. M. Hodgkiss, D. H. P. Turban, N. D. M. Hine, S. Dong, J. Wu, N. C. Greenham, and A. J. Musser, *Nat. Commun.*, **2016**, 7, 13622.

- [143] N. Monahan and X.-Y. Zhu, *Annu. Rev. Phys. Chem.*, **2015**, 66, 601.
- [144] E. Busby, J. Xia, Q. Wu, J. Z. Low, R. Song, J. R. Miller, X.-Y. Zhu, L. M. Campos, and M. Y. Sfeir, *Nat. Mater.*, **2015**, 14, 426.
- [145] E. C. Alguire, J. E. Subotnik, and N. H. Damrauer, *J. Phys. Chem. A*, **2015**, 119, 299.
- [146] S. N. Sanders, E. Kumarasamy, A. B. Pun, K. Appavoo, M. L. Steigerwald, L. M. Campos, and M. Y. Sfeir, *J. Am. Chem. Soc.*, **2016**, 138, 7289.
- [147] O. Varnavski, N. Abeyasinghe, J. Arago, J. J. Serrano-Perez, E. Orti, J. T. Lopez Navarrete, K. Takimiya, D. Casanova, J. Casado, and T. Goodson, *J. Phys. Chem. Lett.*, **2015**, 6, 1375.
- [148] T. Zeng, *J. Phys. Chem. Lett.*, **2016**, 7, 4405.
- [149] T. Zeng and P. Goel, *J. Phys. Chem. Lett.*, **2016**, 7, 1351.
- [150] E. G. Fuemmeler, S. N. Sanders, A. B. Pun, E. Kumarasamy, T. Zeng, K. Miyata, M. L. Steigerwald, X.-Y. Zhu, M. Y. Sfeir, L. M. Campos, and N. Ananth, *ACS Cent. Sci.*, **2016**, 2, 316.
- [151] S. Ito, T. Nagami, and M. Nakano, *J. Phys. Chem. A*, **2016**, 120, 6236.
- [152] M. T. Trinh, Y. Zhong, Q. Chen, T. Schiros, S. Jockusch, M. Y. Sfeir, M. Steigerwald, C. Nuckolls, and X. Zhu, *J. Phys. Chem. C*, **2015**, 119, 1312.
- [153] A. J. Musser, M. Liebel, C. Schnedermann, T. Wende, T. B. Kehoe, A. Rao, and P. Kukura, *Nat. Phys.*, **2015**, 11, 352.
- [154] A. A. Bakulin, S. E. Morgan, T. B. Kehoe, M. W. Wilson, A. W. Chin, D. Zigmantas, D. Egorova, and A. Rao, *Nat. Chem.*, **2016**, 8, 16.
- [155] N. R. Monahan, D. Sun, H. Tamura, K. W. Williams, B. Xu, Y. Zhong, B. Kumar, C. Nuckolls, A. R. Harutyunyan, G. Chen, H.-L. Dai, D. Beljonne, Y. Rao, and X.-Y. Zhu, *Nat. Chem.*, **2017**, 9, 341.

- [156] R. Tempelaar and D. R. Reichman, *J. Chem. Phys.*, **2017**, 146, 174703.
- [157] R. Tempelaar and D. R. Reichman, *J. Chem. Phys.*, **2017**, 146, 174704.
- [158] A. F. Morrison and J. M. Herbert, *J. Phys. Chem. Lett.*, **2017**, 8, 1442.
- [159] J. E. Elenewski, U. S. Cubeta, E. Ko, and H. Chen, *J. Phys. Chem. C*, **2017**, 121, 4130.
- [160] N. Renaud and F. C. Grozema, *J. Phys. Chem. Lett.*, **2015**, 6, 360.
- [161] C. Zener, *Proc. R. Soc. London A*, **1932**, 137, 696.
- [162] L. D. Landau, *Phys. Z.*, **1932**, 2, 46.
- [163] A. Thiel, *J. Phys. G Nucl. Part. Phys.*, **1990**, 16, 867.
- [164] R. J. Lipert, G. Bermudez, and S. D. Colson, *J. Phys. Chem.*, **1988**, 92, 3801.
- [165] W. Xie and W. Domcke, *J. Chem. Phys.*, **2017**, 147, 184114.
- [166] D. Bouwmeester, N. H. Dekker, F. E. v. Dorsselaer, C. A. Schrama, P. M. Visser, and J. P. Woerdman, *Phys. Rev. A*, **1995**, 51, 646.
- [167] W. Wernsdorfer, R. Sessoli, A. Caneschi, D. Gatteschi, and A. Cornia, *Europhysics Lett.*, **2000**, 50, 552.
- [168] L. Zhu, A. Widom, and P. M. Champion, *J. Chem. Phys.*, **1997**, 107, 2859.
- [169] G. D. Fuchs, G. Burkard, P. V Klimov, and D. D. Awschalom, *Nat. Phys.*, **2011**, 7, 789.
- [170] J. N. Onuchic and P. G. Wolynes, *J. Phys. Chem.*, **1988**, 92, 6495.
- [171] J. R. Petta, H. Lu, and A. C. Gossard, *Science*, **2010**, 327, 669.
- [172] J. Zhou, P. Huang, Q. Zhang, Z. Wang, T. Tan, X. Xu, F. Shi, X. Rong, S. Ashhab, and J. Du, *Phys. Rev. Lett.*, **2014**, 112, 10503.



- [173] G. Sun, X. Wen, M. Gong, D.-W. Zhang, Y. Yu, S.-L. Zhu, J. Chen, P. Wu, and S. Han, *Sci. Rep.*, **2015**, 5, 8463.
- [174] A. J. Olson, S.-J. Wang, R. J. Niffenegger, C.-H. Li, C. H. Greene, and Y. P. Chen, *Phys. Rev. A*, **2014**, 90, 13616.
- [175] K. Saito, M. Wubs, S. Kohler, P. Hänggi, and Y. Kayanuma, *Europhysics Lett.*, **2006**, 76, 22.
- [176] W. D. Oliver, Y. Yu, J. C. Lee, K. K. Berggren, L. S. Levitov, and T. P. Orlando, *Science*, **2005**, 310, 1653.
- [177] T. Niemczyk, F. Deppe, H. Huebl, E. P. Menzel, F. Hocke, M. J. Schwarz, J. J. Garcia-Ripoll, D. Zueco, T. Hummer, E. Solano, A. Marx, and R. Gross, *Nat. Phys.*, **2010**, 6, 772.
- [178] I. Chiorescu, P. Bertet, K. Semba, Y. Nakamura, C. J. P. M. Harmans, and J. E. Mooij, *Nature*, **2004**, 431, 159.
- [179] A. Wallraff, D. I. Schuster, A. Blais, L. Frunzio, R.-S. Huang, J. Majer, S. Kumar, S. M. Girvin, and R. J. Schoelkopf, *Nature*, **2004**, 431, 162.
- [180] M. Wubs, K. Saito, S. Kohler, P. Hänggi, and Y. Kayanuma, *Phys. Rev. Lett.*, **2006**, 97, 200404.
- [181] J. Johansson, M. H. S. Amin, A. J. Berkley, P. Bunyk, V. Choi, R. Harris, M. W. Johnson, T. M. Lanting, S. Lloyd, and G. Rose, *Phys. Rev. B*, **2009**, 80, 12507.
- [182] P. Ao and J. Rammer, *Phys. Rev. Lett.*, **1989**, 62, 3004.
- [183] K. Saito, M. Wubs, S. Kohler, Y. Kayanuma, and P. Hänggi, *Phys. Rev. B*, **2007**, 75, 214308.
- [184] P. Nalbach and M. Thorwart, *Phys. Rev. Lett.*, **2009**, 103, 220401.
- [185] P. Nalbach, *Phys. Rev. A*, **2014**, 90, 42112.

- [186] S. Javanbakht, P. Nalbach, and M. Thorwart, *Phys. Rev. A*, **2015**, 91, 52103.
- [187] A. Dodin, S. Garmon, L. Simine, and D. Segal, *J. Chem. Phys.*, **2014**, 140, 124709.
- [188] P. Nalbach, N. Klinkenberg, T. Palm, and N. Müller, *Phys. Rev. E*, **2017**, 96, 42134.
- [189] S. Ashhab, *Phys. Rev. A*, **2014**, 90, 62120.
- [190] P. P. Orth, A. Imambekov, and K. Le Hur, *Phys. Rev. B*, **2013**, 87, 14305.
- [191] H. Paik, D. I. Schuster, L. S. Bishop, G. Kirchmair, G. Catelani, A. P. Sears, B. R. Johnson, M. J. Reagor, L. Frunzio, L. I. Glazman, S. M. Girvin, M. H. Devoret, and R. J. Schoelkopf, *Phys. Rev. Lett.*, **2011**, 107, 240501.
- [192] J. J. Garcia-Ripoll, B. Peropadre, and S. De Liberato, *Sci. Rep.*, **2015**, 5, 16055.
- [193] H.-B. Liu, W. L. Yang, J.-H. An, and Z.-Y. Xu, *Phys. Rev. A*, **2016**, 93, 20105.
- [194] F. Yan, S. Gustavsson, A. Kamal, J. Birenbaum, A. P. Sears, D. Hover, T. J. Gudmundsen, D. Rosenberg, G. Samach, S. Weber, J. L. Yoder, T. P. Orlando, J. Clarke, A. J. Kerman, and W. D. Oliver, *Nat. Commun.*, **2016**, 7, 12964.
- [195] D. J. Egger and F. K. Wilhelm, *Phys. Rev. Lett.*, **2013**, 111, 163601.
- [196] M. J. Storcz, J. Vala, K. R. Brown, J. Kempe, F. K. Wilhelm, and K. B. Whaley, *Phys. Rev. B*, **2005**, 72, 64511.
- [197] R. S. Whitney, M. Clusel, and T. Ziman, *Phys. Rev. Lett.*, **2011**, 107, 210402.
- [198] P. Nalbach, J. Knörzer, and S. Ludwig, *Phys. Rev. B*, **2013**, 87, 165425.
- [199] L. Tian, S. Lloyd, and T. P. Orlando, *Phys. Rev. B*, **2002**, 65, 144516.
- [200] Z. Sun, L. Zhou, G. Xiao, D. Poletti, and J. Gong, *Phys. Rev. A*, **2016**, 93, 012121.
- [201] P. P. Orth, A. Imambekov, and K. Le Hur, *Phys. Rev. B*, **2013**, 87, 14305.
- [202] A. A. Houck, J. A. Schreier, B. R. Johnson, J. M. Chow, J. Koch, J. M. Gambetta, D. I. Schuster, L. Frunzio, M. H. Devoret, S. M. Girvin, and R. J. Schoelkopf, *Phys. Rev. Lett.*, **2008**, 101, 80502.

[203] O. Viehmann, J. von Delft, and F. Marquardt, *Phys. Rev. Lett.*, **2013**, 110, 30601.



## Chapter 3

### Overview of Theoretical Methodologies

*In this chapter, we present theoretical methodologies to be employed in the coming chapters. In Section 3.1, we give a brief overview of the Dirac-Frenkel time-dependent variational principle. In Section 3.2, we introduce a series of multiple Davydov trial states to achieve accurate descriptions of polaron dynamics. Finally, theoretical models for potential applications of the multiple Davydov  $D_2$  ansatz are presented in Section 3.3.*

### 3.1 The Dirac-Frenkel Time-dependent Variational Principle

In order to bridge the gap between the time-dependent Schrödinger equation in quantum mechanics and Newton's law of motion in classical mechanics, various models and approximations have been developed, such as the Davydov ansätze and the MCTDH method. Most of these bridging methods depend on a time-dependent variational approach, originated by Dirac and Frenkel in the 1930s [1, 2]. It has been found that the fundamental role played by the Dirac-Frenkel time-dependent variational principle in solving the time-dependent Schrödinger equation is similar to that played by the Rayleigh-Ritz variational principle in solving the time-independent Schrödinger eigenvalue problem [3].

In the absence of analytical solutions, the Rayleigh-Ritz approximation method was independently formulated by Ritz and Rayleigh in 1909 to find numerical solutions to the eigenvalue problems. When treating the time-independent Schrödinger eigenvalue problems, this method is specifically called Rayleigh-Ritz variational principle, with which the ground state energy of the target Hamiltonian can then be well estimated by minimizing the expectation value of the Hamiltonian obtained using a test wave function. The Rayleigh-Ritz variational principle has been used in the Hohenberg-Kohn-Sham theory [4, 5], and in obtaining the minimum expectation values of quantum-mechanical operators [6].

In contrast, the interest in the Dirac-Frenkel variational principle faded until McLachlan took it up again in 1964 to calculate the susceptibility of a system in an oscillating field [7]. From then on, it is also known as the Dirac-Frenkel-McLachlan time-dependent variational principle. Heller used this approach to explore the semi-classical dynamics in 1976, and initiated the construction of the family tree of the MCTDH method [8, 9]. In the framework of the MCTDH method, Gaussian wave packets are adopted as the trial functions to describe the states of the target systems [10, 11]. In recent decades, the Dirac-Frenkel variational principle has been frequently utilized with a

class of trial states, the Davydov ansätze, to study population dynamics of open quantum systems [12]. Great successes of the Dirac-Frenkel time-dependent variational principle have been achieved that led to numerically exact solutions in combination with the multiple Davydov trial states [13–16].

In numerics, the time-dependent variational parameters of the Davydov ansätze can be determined by the Dirac-Frenkel variational principle as follows [1, 2]. The Lagrangian  $L$  can be first formulated as

$$L = \langle \Psi(t) | \frac{i\hbar}{2} \left( \frac{\overrightarrow{\partial}}{\partial t} - \frac{\overleftarrow{\partial}}{\partial t} \right) - \hat{H} | \Psi(t) \rangle. \quad (3.1)$$

where  $\hat{H}$  is the corresponding Hamiltonian and  $|\Psi(t)\rangle$  is the adopted trial state. Derivations of the equations of motion for the time-dependent variational parameters  $u_i(t)$  of the trial wave packets  $|\Psi(t)\rangle$  can be given by

$$\frac{d}{dt} \left( \frac{\partial L}{\partial \dot{u}_i^*} \right) - \frac{\partial L}{\partial u_i^*} = 0 \quad (3.2)$$

where  $u_i$  represents the excitation amplitudes and the bosonic displacements of the Davydov ansätze,  $u_i^*$  is the complex conjugate of  $u_i$ , and  $\dot{u}_i^*$  is the first order derivative of  $u_i^*$  with respect to time  $t$ .

The equations of motion are solved numerically by means of the fourth-order Runge-Kutta method, leading to a complete description of the time evolution of the Davydov ansätze. One can therefore have the explicit structure of the ansätze with relevant excitonic and bosonic information. Rich physics regarding the dynamics of open quantum systems can then be extracted from those variational outcomes. Physical observables of interest can be evaluated when the excitonic and bosonic DOFs are included as the Davydov ansätze have treated both DOFs on the equal footing [1, 2, 17–19].

### 3.2 The Davydov ansätze

The  $D_1$ ,  $D_2$ , and  $\tilde{D}$  ansätze were employed to probe the dynamics of a one-dimensional Holstein polaron [17]. But these ansätze fail to adequately treat the weak diagonal

exciton-phonon coupling regime. The  $D_1$  ansatz is suitable to simulate the dynamical processes in which only the diagonal exciton-phonon coupling is considered, but it fails to describe the case with the off-diagonal coupling. Although the  $D_2$  ansatz can be seen as a simplified version of the  $D_1$  ansatz, it has the capability to deal with the off-diagonal coupling case, albeit with non-negligible deviation from the exact solution to the Schrödinger dynamics [18]. The variational method with the single  $D_2$  ansatz is demonstrated to be equivalent to the semi-classical Ehrenfest method, which treats the electronic DOFs quantum mechanically and the vibrational DOFs classically [13].

In order to more accurately describe dynamics for the Holstein polaron with simultaneous diagonal and off-diagonal exciton-phonon coupling, a series of multiple Davydov trial states, i.e., the multiple Davydov  $D_1$ ,  $D_{1.5}$ ,  $D_2$ , and  $\tilde{D}$  ansätze, can be adopted for the simulation. Superposition of the  $D_1$ ,  $D_{1.5}$ ,  $D_2$ , and  $\tilde{D}$  ansätze offers significant improvements over the single Davydov states in the flexibility of the trial state, thus yielding more accurate polaron dynamics.

Denoting the number of the single Davydov ansatz included as the multiplicity  $M$ , multiple  $D_1$ ,  $D_{1.5}$ ,  $D_2$ , and  $\tilde{D}$  ansätze can be expressed as

$$|D_1^M(t)\rangle = \sum_i^M \sum_n^N \psi_{in}(t) \hat{a}_n^\dagger |0\rangle_{\text{ex}} \exp \left\{ \sum_q [\lambda_{iq}(t) \hat{b}_q^\dagger - \text{H.c.}] \right\} |0\rangle_{\text{ph}}, \quad (3.3)$$

$$|D_{1.5}^M(t)\rangle = \sum_i^M \sum_n^N \psi_{in}(t) \hat{a}_n^\dagger |0\rangle_{\text{ex}} \exp \left\{ \sum_q [(\lambda_{iq}(t) - C_{iq}) \hat{b}_q^\dagger - \text{H.c.}] \right\} |0\rangle_{\text{ph}}, \quad (3.4)$$

$$|D_2^M(t)\rangle = \sum_i^M \sum_n^N \psi_{in}(t) \hat{a}_n^\dagger |0\rangle_{\text{ex}} \exp \left\{ \sum_q [\lambda_{iq}(t) \hat{b}_q^\dagger - \text{H.c.}] \right\} |0\rangle_{\text{ph}}, \quad (3.5)$$



$$\begin{aligned}
|\tilde{D}^M(t)\rangle &= \sum_i^M \sum_n^N \psi_{in}(t) \hat{a}_n^\dagger |0\rangle_{\text{ex}} \\
&\times \exp \left\{ \sum_{q \neq 0} [(\lambda_{iq}(t) + e^{iqn} \gamma_{iq}(t)) \hat{b}_q^\dagger - \text{H.c.}] + [\lambda_{i0}(t) \hat{b}_{i0}^\dagger - \text{H.c.}] \right\} |0\rangle_{\text{ph}},
\end{aligned} \tag{3.6}$$

where  $N$  stands for the total number of sites in the ring. Moreover,  $n$  and  $i$  represent the site number in the molecular ring and the index of the coherent superposition state, respectively.  $\psi_{in}(t)$  are the time-dependent variational parameters for the exciton amplitudes.  $\lambda_{iq}(t)$  ( $\lambda_{inq}(t)$ ) represent the variational parameters for phonon displacements of the multi-D<sub>2</sub> and the multi-D<sub>1.5</sub> ansätze (the multi-D<sub>1</sub> ansatz). In the multi-D<sub>1.5</sub> ansatz,  $C_{iq}(t) = \lambda_{iq}(t)/(2\hbar\omega_q)$ , where  $\hbar$  is the reduced Plank constant. In the multi- $\tilde{D}$  ansatz, the phonon displacements are  $\lambda_{iq \neq 0}(t)$  and  $\gamma_{i,q \neq 0}(t)$  for  $q \neq 0$ , and  $\lambda_{i,q=0}(t)$  for  $q = 0$ . Equations of motion for those variational parameters can be derived by using the time-dependent Dirac-Frenkel variational principle.

The form of the multiple Davydov ansätze needs little adjustments for studied systems. For example, the multi-D<sub>2</sub> ansatz for the spin-boson model system is shown as follows

$$\begin{aligned}
|D_2^M(t)\rangle &= \sum_{i=1}^M \left\{ A_i(t) |+\rangle \exp \left[ \sum_{q=1}^N f_{iq}(t) \hat{b}_q^\dagger - H.c. \right] |0\rangle \right\} \\
&+ \sum_{i=1}^M \left\{ B_i(t) |-\rangle \exp \left[ \sum_{q=1}^N f_{iq}(t) \hat{b}_q^\dagger - H.c. \right] |0\rangle \right\},
\end{aligned} \tag{3.7}$$

where  $|0\rangle$  is the vacuum state of the bosonic bath.  $A_i$  and  $B_i$  are time-dependent variational parameter for the amplitudes in spin-up state  $|+\rangle$  and spin-down state  $|-\rangle$ , respectively.  $f_{iq}(t)$  are the bosonic displacements, where  $i$  and  $q$  label the  $i$ -th coherent superposition state and  $q$ -th effective bath mode, respectively. If  $M = 1$ , the multi-D<sub>2</sub> ansatz is restored to the usual Davydov D<sub>2</sub> trial state.

The validities of the Davydov ansätze can be examined by quantifying how faithfully the trial states follow the Schrödinger equation. Here taking the multi-D<sub>2</sub> ansatz as an example, a deviation vector  $\vec{\delta}(t)$  is defined to quantify the accuracy of the variational

dynamics based on the multiple Davydov trial states,

$$\begin{aligned}\vec{\delta}(t) &= \vec{\chi}(t) - \vec{\gamma}(t) \\ &= \frac{\partial}{\partial t}|\Psi(t)\rangle - \frac{\partial}{\partial t}|D_2^M(t)\rangle,\end{aligned}\tag{3.8}$$

where the vectors  $\vec{\chi}(t)$  and  $\vec{\gamma}(t)$  obey the Schrödinger equation  $\vec{\chi}(t) = \partial|\Psi(t)\rangle/\partial t = -i\hat{H}|\Psi(t)\rangle$  and the Dirac-Frenkel variational dynamics  $\vec{\gamma}(t) = \partial|D_2^M\rangle/\partial t$ , respectively. The deviation vector  $\vec{\delta}(t)$  can be calculated as

$$\vec{\delta}(t) = -i\hat{H}|D_2^M(t)\rangle - \frac{\partial}{\partial t}|D_2^M(t)\rangle.\tag{3.9}$$

Thus, the accuracy of the trial state is captured by the amplitude of the deviation vector  $\Delta(t) = \|\vec{\delta}(t)\|$ . In order to better characterize the ansatz accuracies in the parameter space, a dimensionless relative deviation  $\sigma$  is calculated as

$$\sigma = \frac{\max\{\Delta(t)\}}{\text{mean}\{N_{\text{err}}(t)\}}, \quad t \in [0, t_{\text{max}}].\tag{3.10}$$

where  $N_{\text{err}}(t) = \|\vec{\chi}(t)\|$  is the amplitude of the time derivative of the wave function,

$$\begin{aligned}N_{\text{err}}(t) &= \sqrt{-\langle \frac{\partial}{\partial t}\Psi(t) | \frac{\partial}{\partial t}\Psi(t) \rangle} \\ &= \sqrt{\langle D_2^M(t) | \hat{H}^2 | D_2^M(t) \rangle}.\end{aligned}\tag{3.11}$$

With sufficiently high multiplicities, numerically exact solutions have been achieved using the multi-D<sub>1</sub> and the multi-D<sub>2</sub> ansätze for various dynamical processes, such as the dynamics of the Holstein polaron and the spin-boson model [13–15], and the qubit-photon dynamics in circuit QED system [16]. Since the multi-D<sub>2</sub> ansatz shows better performance in the presence of off-diagonal coupling cases, the adoption of the multi-D<sub>2</sub> ansatz is preferred in this thesis.

### 3.3 Models for applications of the multiple Davydov D<sub>2</sub> ansatz

The applications of the multiple Davydov D<sub>2</sub> ansatz are promising and wide-ranging. We give a few examples for potential applications. In these models, there exist two DOFs:

excitonic and phononic DOFs in Subsec. 3.3.1, electronic and phononic DOFs in Subsec. 3.3.2 and Subsec. 3.3.3, and electronic and bosonic DOFs in Subsec. 3.3.4. In each model, wave packets of the two DOFs mix and form a polaron, which can then be elaborated by our multiple Davydov  $D_2$  ansatz. The excitonic or electronic DOFs are treated in their excited states and serve as the first part of the multiple Davydov  $D_2$  ansatz, while the phononic or bosonic wavepackets are described by superposition of coherent states and act as the second part of the ansatz. Details of the models are listed as follows.

### 3.3.1 A one-dimensional Holstein molecular crystal model with off-diagonal exciton-phonon coupling

In presence of off-diagonal coupling only, the Hamiltonian of the one-dimensional Holstein molecular crystal model takes the form

$$\hat{H} = \hat{H}_{\text{ex}} + \hat{H}_{\text{ph}} + \hat{H}_{\text{ex-ph}}^{\text{o.d.}}, \quad (3.12)$$

where  $\hat{H}_{\text{ex}}$ ,  $\hat{H}_{\text{ph}}$  and  $\hat{H}_{\text{ex-ph}}^{\text{o.d.}}$  denote the exciton Hamiltonian, the bath (phonon) Hamiltonian, and the off-diagonal exciton-phonon coupling Hamiltonian, respectively. In the site representation,

$$\begin{aligned} \hat{H}_{\text{ex}} &= -J \sum_n a_n^\dagger (a_{n+1} + a_{n-1}), \\ \hat{H}_{\text{ph}} &= \omega_0 \sum_n b_n^\dagger b_n, \\ \hat{H}_{\text{ex-ph}}^{\text{o.d.}} &= \frac{1}{2} \phi \omega_0 \sum_{n,l} \left[ a_n^\dagger a_{n+1} (b_l + b_l^\dagger) (\delta_{n+1,l} - \delta_{n,l}) \right. \\ &\quad \left. + a_n^\dagger a_{n-1} (b_l + b_l^\dagger) (\delta_{n,l} - \delta_{n-1,l}) \right], \end{aligned} \quad (3.13)$$

where  $\hat{a}_n^\dagger$  ( $\hat{a}_n$ ) and  $\hat{b}_n^\dagger$  ( $\hat{b}_n$ ) are the exciton and phonon creation (annihilation) operators for the  $n$ -th site, respectively. The parameters  $J$  and  $\phi$  represent the transfer integral and the off-diagonal coupling strength, respectively.  $\omega_0$  denotes the phonon frequency. In this study, only the anti-symmetric exciton-phonon coupling is considered in Eq. (3.13). In the

phonon momentum space,  $\hat{H}_{\text{ph}}$  and  $\hat{H}_{\text{ex-ph}}^{\text{o.d.}}$  can be written as,

$$\begin{aligned}\hat{H}_{\text{ph}} &= \sum_q \omega_q \hat{b}_q^\dagger \hat{b}_q, \\ \hat{H}_{\text{ex-ph}}^{\text{o.d.}} &= \frac{1}{2} N^{-1/2} \phi \sum_{n,q} \omega_q \{ \hat{a}_n^\dagger \hat{a}_{n+1} [e^{iqn} (e^{iq} - 1) \hat{b}_q + \text{H.c.}] \\ &\quad + \hat{a}_n^\dagger \hat{a}_{n-1} [e^{iqn} (1 - e^{-iq}) \hat{b}_q + \text{H.c.}] \},\end{aligned}\quad (3.14)$$

where  $\omega_q$  is the phonon frequency of phonon momentum  $q$ , and  $\hat{b}_q^\dagger$  ( $\hat{b}_q$ ) is the creation (annihilation) operator of a phonon with momentum  $q$ ,

$$\hat{b}_q^\dagger = N^{-1/2} \sum_n e^{iqn} \hat{b}_n^\dagger, \quad \hat{b}_n^\dagger = N^{-1/2} \sum_q e^{-iqn} \hat{b}_q^\dagger. \quad (3.15)$$

A linear phonon dispersion can be assumed,

$$\omega_q = \omega_0 \left[ 1 + \left( \frac{2|q|}{\pi} - 1 \right) W \right], \quad (3.16)$$

where  $W$  is a constant between 0 and 1, the bandwidth of the phonon frequency is  $2W\omega_0$ , and  $q = 2\pi l/N$  represents the momentum index with  $l = -\frac{N}{2} + 1, \dots, \frac{N}{2}$ .  $\omega_0$  is set to unity as the energy unit in this model, and a dispersionless optical phonon band with  $W = 0$  is used. For this problem, the multi-D<sub>2</sub> ansatz used is in the form of Eq. (3.5). Detailed derivations of the equations of motion for the variational parameters are given in Appendix A.3, together with discussions on initial conditions and numerical details.

With the wave function  $|\text{D}_2^M(t)\rangle$  obtained, the total energy is defined as

$$E_{\text{total}} = E_{\text{ex}} + E_{\text{ph}} + E_{\text{ex-ph}},$$

where

$$\begin{aligned}E_{\text{ex}} &= \langle \text{D}_2^M(t) | \hat{H}_{\text{ex}} | \text{D}_2^M(t) \rangle, \\ E_{\text{ph}} &= \langle \text{D}_2^M(t) | \hat{H}_{\text{ph}} | \text{D}_2^M(t) \rangle, \\ E_{\text{ex-ph}} &= \langle \text{D}_2^M(t) | \hat{H}_{\text{ex-ph}}^{\text{o.d.}} | \text{D}_2^M(t) \rangle.\end{aligned}$$

Additionally, the exciton probability in the site space  $P_{\text{ex}}(t, n)$  and the exciton probability in the momentum space  $P_{\text{ex}}(t, k)$  can also be calculated as

$$\begin{aligned}P_{\text{ex}}(t, n) &= \langle \text{D}_2^M(t) | \hat{a}_n^\dagger \hat{a}_n | \text{D}_2^M(t) \rangle, \\ P_{\text{ex}}(t, k) &= \langle \text{D}_2^M(t) | \hat{a}_k^\dagger \hat{a}_k | \text{D}_2^M(t) \rangle,\end{aligned}\quad (3.17)$$

where  $\hat{a}_k^\dagger$  ( $\hat{a}_k$ ) is the creation (annihilation) operator of the exciton with momentum  $k$ ,

$$\hat{a}_k^\dagger = N^{-1/2} \sum_n e^{-ikn} \hat{a}_n^\dagger, \quad \hat{a}_n^\dagger = N^{-1/2} \sum_k e^{ikn} \hat{a}_k^\dagger. \quad (3.18)$$

One can also evaluate the mean square displacement MSD ( $t$ ) of the exciton probability in the site space  $P_{\text{ex}}(t, n)$  as a function of time  $t$ ,

$$\begin{aligned} c(t) &= \sum_n^N n P_{\text{ex}}(t, n), \\ \text{MSD}(t) &= \sum_n^N [n - c(t)]^2 P_{\text{ex}}(t, n), \end{aligned} \quad (3.19)$$

where  $c(t)$  describes the centroid motion of the exciton probability in the site space. In the exciton momentum representation, the counterpart,  $\text{MSD}_k(t)$  denotes the degree of deviation of the state at the time  $t$  from the initial state, as shown in the following,

$$\begin{aligned} c_k(t) &= \sum_{k=-\pi}^{\pi} k P_{\text{ex}}(t, k), \\ \text{MSD}_k(t) &= \sum_{k=-\pi}^{\pi} [k - c_k(t)]^2 P_{\text{ex}}(t, k), \end{aligned} \quad (3.20)$$

where  $c_k(t)$  illustrates the centroid motion of the exciton probability in the momentum space.

### 3.3.2 A one-dimensional Holstein polaron in an external electric field

The Hamiltonian of the one-dimensional Holstein polaron reads

$$\hat{H} = \hat{H}_{\text{ca}} + \hat{H}_{\text{ph}} + \hat{H}_{\text{ca-ph}}^{\text{diag}} + \hat{H}_{\text{ca-ph}}^{\text{o.d.}} \quad (3.21)$$

where  $\hat{H}_{\text{ca}}$ ,  $\hat{H}_{\text{ph}}$ ,  $\hat{H}_{\text{ca-ph}}^{\text{diag}}$  and  $\hat{H}_{\text{ca-ph}}^{\text{o.d.}}$  denote the charge carrier Hamiltonian, the bath (phonon) Hamiltonian, the diagonal and off-diagonal carrier-phonon coupling Hamiltonian, respectively. An extra term  $F \sum_n n a_n^\dagger a_n$  is added to represent the scalar potential induced by a constant external electric field  $F$ . After bending a linear chain of atoms into a ring, however, potential of the field would become discontinuous at end

points, leaving questionable the use of periodic boundary conditions [20]. A later treatment [21] using a gauge transformed vector potential [22] circumvents this problem and is thus suitable for ring systems. The gauge transformed Hamiltonian will be used for the ring system under a constant electric field (see Appendix B.1), which can be defined as

$$\begin{aligned}
\hat{H}_{\text{ca}} &= -J \sum_n a_n^\dagger (e^{-iFt} a_{n+1} + e^{iFt} a_{n-1}), \\
\hat{H}_{\text{ph}} &= \omega_0 \sum_n b_n^\dagger b_n, \\
\hat{H}_{\text{ca-ph}}^{\text{diag}} &= -g\omega_0 \sum_n a_n^\dagger a_n (b_n + b_n^\dagger), \\
\hat{H}_{\text{ca-ph}}^{\text{o.d.}} &= \frac{1}{2}\phi\omega_0 \sum_{n,l} \left[ a_n^\dagger a_{n+1} (b_l + b_l^\dagger) (\delta_{n+1,l} - \delta_{n,l}) \right. \\
&\quad \left. + a_n^\dagger a_{n-1} (b_l + b_l^\dagger) (\delta_{n,l} - \delta_{n-1,l}) \right]. \tag{3.22}
\end{aligned}$$

Written in the phonon momentum space,

$$\begin{aligned}
\hat{H}_{\text{ph}} &= \sum_q \omega_q \hat{b}_q^\dagger \hat{b}_q, \tag{3.23} \\
\hat{H}_{\text{ca-ph}}^{\text{diag}} &= -N^{-1/2}g \sum_{n,q} \omega_q \hat{a}_n^\dagger \hat{a}_n (e^{iqn} \hat{b}_q + e^{-iqn} \hat{b}_q^\dagger), \\
\hat{H}_{\text{ca-ph}}^{\text{o.d.}} &= \frac{1}{2}N^{-1/2}\phi \sum_{n,q} \omega_q \{ \hat{a}_n^\dagger \hat{a}_{n+1} [e^{iqn}(e^{iq} - 1)\hat{b}_q + \text{H.c.}] \\
&\quad + \hat{a}_n^\dagger \hat{a}_{n-1} [e^{iqn}(1 - e^{-iq})\hat{b}_q + \text{H.c.}] \}.
\end{aligned}$$

where the parameter  $g$  represents the diagonal coupling strength. The symbols  $J$ ,  $\phi$ , and  $q$  in this subsection have the same meaning with those in Subsec. 3.3.1. Here,  $\omega_q = \omega_0 |\sin(q/2)|$  is taken as the dispersion relation for acoustic phonons; in the case of optical phonons, the Einstein dispersionless model is considered, i.e.,  $\omega_q = \omega_0$ . For simplicity, the Debye frequency is taken to be equal to the Einstein frequency  $\omega_0$ , which is set to unity as the energy unit. The multi-D<sub>2</sub> ansatz used here is still in the form of Eq. (3.5), except that the vacuum state of the exciton,  $|0\rangle_{\text{ex}}$ , in Eq. (3.5) needs to be changed to the vacuum state of the charge carrier,  $|0\rangle_{\text{ca}}$ . Detailed derivations of the equations of motion for the variational parameters are given in Appendix B.2.

With the wave function  $|D_2^M(t)\rangle$  available, the total energy is calculated as follows

$$E_{\text{total}} = E_{\text{ca}} + E_{\text{ph}} + E_{\text{diag}} + E_{\text{off}}, \quad (3.24)$$

where

$$\begin{aligned} E_{\text{ca}} &= \langle D_2^M | \hat{H}_{\text{ca}} | D_2^M \rangle, \\ E_{\text{ph}} &= \langle D_2^M | \hat{H}_{\text{ph}} | D_2^M \rangle, \\ E_{\text{diag}} &= \langle D_2^M | \hat{H}_{\text{ca-ph}}^{\text{diag}} | D_2^M \rangle, \\ E_{\text{off}} &= \langle D_2^M | \hat{H}_{\text{ca-ph}}^{\text{o.d.}} | D_2^M \rangle. \end{aligned}$$

Additionally, time evolution of the phonon displacement  $X_{\text{ph}}(t, n)$  is also calculated

$$X_{\text{ph}}(t, n) = \langle D_2^M | \hat{b}_n + \hat{b}_n^\dagger | D_2^M \rangle. \quad (3.25)$$

This thesis further uses a standard deviation  $\sigma(t)$  to characterize the motion of the carrier wave, which is defined as follows

$$\sigma(t)^2 = \sum_i^N (n - c(t))^2 P_{\text{ca}}(t, n) \quad (3.26)$$

where the standard deviation is used to measure how far the carrier wave spreads out from its mean position. It is noted that the standard deviation  $\sigma(t)$  and the mean value  $c(t)$  are sensitive to the initial standard deviation  $\sigma_0$  of the carrier wave packet.

### 3.3.3 A dimer model of intramolecular singlet fission dynamics

Our focus here is on a dimer model of the iSF dynamics on the basis of the four-electron four-orbital basis [23, 24]. A simple scheme is considered for the iSF process,  $|g\rangle \rightarrow |S_1\rangle \rightarrow |TT\rangle$ , where  $|g\rangle$  denotes the electronic ground state,  $|S_1\rangle$  is the singlet state, and  $|TT\rangle$  represents the correlated triplet pair state. In some organic materials, the iSF and xSF processes may be accelerated by a mediated pathway, in which the singlet state converts to a triplet pair state via the charge transfer (CT) state. Quantum chemistry calculations of acene derivatives have demonstrated that the energy of the CT state is

significantly higher than that of the singlet excited states [25, 26], and CT states have been found not to participate in xSF process as actual intermediates between  $S_1$  and TT [27–32]. Moreover, using electronic structures calculations and transient absorption spectroscopy, iSF has been demonstrated to occur via a direct coupling mechanism that is independent of the CT states in the covalent pentacene dimer [33] and tetracene dimer [34]. Therefore, in this thesis we assume that the sole effect of the CT states is to effectively couple the  $S_1$  and TT states. A system-bath Hamiltonian is employed describing the both diagonal and off-diagonal coupling,

$$\hat{H} = \hat{H}_{\text{sys}} + \hat{H}_{\text{bath}} + \hat{H}_{\text{sys-bath}}. \quad (3.27)$$

First term of  $\hat{H}$  is the system Hamiltonian, and is chosen to be that of an electronically diabatic Hamiltonian for  $|g\rangle$ ,  $|S_1\rangle$  and  $|TT\rangle$

$$\hat{H}_{\text{sys}} = \sum_{n=S_1, TT} \epsilon_{ng} |n\rangle \langle n| + \sum_{m=S_1, TT} \sum_{n \neq m} J_{mn} |m\rangle \langle n|, \quad (3.28)$$

where  $\epsilon_{ng}$  is the Franck-Condon energy associated with electronic transition from  $|g\rangle$  to  $|n\rangle$ , and  $J_{S_1, TT}$  is strength of the interstate coupling between  $S_1$  and TT.  $J_{S_1, TT}$  includes the contribution of the direct coupling between  $S_1$  and TT based on the two electron integrals [24, 27] as well as that of the effective coupling created by quantum mixing of CT and electronic states. The second term of  $\hat{H}$  represents the bath Hamiltonian  $\hat{H}_{\text{bath}}$ , and is given by

$$\hat{H}_{\text{bath}} = \sum_q \hbar \omega_q \hat{b}_q^\dagger \hat{b}_q, \quad (3.29)$$

where  $\omega_q$  indicates the frequency of the  $q$ -th mode of the bath with creation operator,  $\hat{b}_q^\dagger$ , and annihilation operator,  $\hat{b}_q$ . The assumption of harmonic oscillators is used to treat the effects of vibrational degrees of freedom, because the molecular dimer has been taken in the vicinity of the potential minima where the potentials are harmonic, and nuclear motion can be understood as a superposition of independent harmonic vibrations around the equilibrium configurations [30, 35, 36]. Third term of  $\hat{H}$  represents the system-bath



coupling,  $\hat{H}_{\text{sys-bath}}$ , and is given by

$$\begin{aligned}\hat{H}_{\text{sys-bath}} = & \sum_{n=\text{S}_1, \text{TT}} |n\rangle\langle n| \sqrt{\lambda_{n,\text{g}}} \cdot \hat{\mathcal{E}}_x \\ & + \sum_{m=\text{S}_1, \text{TT}} \sum_{n \neq m} |m\rangle\langle n| \sqrt{\lambda_{\text{S}_1, \text{TT}}^{\text{o.d.}}} \cdot \hat{\mathcal{E}}_y,\end{aligned}\quad (3.30)$$

where operators are defined as  $\hat{\mathcal{E}}_x = \hbar\omega_q g_q (\hat{b}_q^\dagger + \hat{b}_q)$  and  $\hat{\mathcal{E}}_y = \hbar\omega_q c_q (\hat{b}_q^\dagger + \hat{b}_q)$ . Here  $g_q$  and  $c_q$  are the diagonal and off-diagonal exciton-phonon coupling strength between the system and  $q$ -th mode, respectively,  $\lambda_{mn}$  represents the reorganization energy associated with the transition from  $|m\rangle$  to  $|n\rangle$ , and  $\lambda_{mn}^{\text{o.d.}}$  is the amplitude of fluctuations in interstate coupling between  $|m\rangle$  and  $|n\rangle$ . Details of both types of coupling can be found in Ref. [15]. The diagonal coupling describes fluctuations in the electronic energies induced by intramolecular vibrations, whereas the off-diagonal coupling attributes to the fluctuations in electronic coupling induced by intramolecular and intermolecular vibrations, as mentioned above. The spectral density  $J_\alpha(\omega)$  ( $\alpha = x, y$ ) is a useful measure for characterizing various forms of exciton-phonon coupling, and can be evaluated in terms of  $g_q$  ( $c_q$ ) as

$$J_x(\omega) = \frac{\pi}{2} \sum_q \hbar\omega_q^2 g_q^2 \delta(\omega - \omega_q), \quad (3.31)$$

$$J_y(\omega) = \frac{\pi}{2} \sum_q \hbar\omega_q^2 c_q^2 \delta(\omega - \omega_q). \quad (3.32)$$

In this study, the diagonal coupling spectral densities are modeled using underdamped Brownian oscillators with Huang-Rhys factor,  $S_m = \lambda_{mg}/(\hbar\omega_{\text{diag}})$ , such that

$$J_x(\omega) = \frac{4\gamma_{\text{diag}}\omega_{\text{diag}}^2\omega}{(\omega^2 - \omega_{\text{diag}}^2)^2 + 4\gamma_{\text{diag}}^2\omega^2}, \quad (3.33)$$

where  $\omega_{\text{diag}}$  is the vibrational frequency and  $\gamma_{\text{diag}}$  is the vibrational relaxation rate. In the iSF materials, the dominant contributions to off-diagonal coupling are from the intramolecular vibrations. Similarly, the off-diagonal coupling spectral densities can be modeled as

$$J_y(\omega) = \frac{4\gamma_{\text{o.d.}}\omega_{\text{o.d.}}^2\omega}{(\omega^2 - \omega_{\text{o.d.}}^2)^2 + 4\gamma_{\text{o.d.}}^2\omega^2}, \quad (3.34)$$

where  $\omega_{\text{o.d.}}$  is the vibrational frequency and  $\gamma_{\text{o.d.}}$  is the vibrational relaxation rate.

To obtain numerical solutions to the equations of motion for the variational parameters after application of the multi-D<sub>2</sub> ansatz, the continuum spectral densities  $J_x(\omega)$  and  $J_y(\omega)$  need to be discretized. In this model, the method of linear discretization is employed. The displacement  $g_q$  for each  $\omega_q$  is given by  $g_q^2 = 2J_x(\omega_q) \Delta\omega / (\pi\hbar\omega_q^2)$ . With respect to off-diagonal coupling, the displacement  $c_q$  for each  $\omega_q$  is given by  $c_q^2 = 2J_y(\omega_q) \Delta\omega / (\pi\hbar\omega_q^2)$ .

For simplicity, the multi-D<sub>2</sub> ansatz for the SF model system is described in the following form

$$|D_2^M(t)\rangle = \sum_{i=1}^M \sum_{n=S_1, TT} \left\{ c_{in}(t) |n\rangle \exp \left[ \sum_{q=1} f_{iq}(t) \hat{b}_q^\dagger - H.c. \right] |0\rangle_{\text{vib}} \right\}, \quad (3.35)$$

where  $|0\rangle_{\text{vib}}$  is the vacuum state of the bosonic bath.  $c_{in}(t)$  is the time-dependent variational parameter for the amplitudes in state  $|n\rangle$ , and  $f_{iq}(t)$  denotes the bosonic displacements, where  $i$  and  $q$  label the  $i$ -th coherent superposition state and  $q$ -th effective bath mode, respectively. Details of the Lagrangian and equations of motion are given in Ref. [15].

### 3.3.4 Dissipative Landau-Zener model

The entire Hamiltonian of a driven two-level system interacting with a bosonic bath can be given by

$$\hat{H} = \hat{H}_S + \hat{H}_B + \hat{H}_{SB} \quad (3.36)$$

where the system Hamiltonian is the standard LZ Hamiltonian for an isolated two-level system, i.e.,  $\hat{H}_S = \hat{H}_{LZ}$ , with

$$\hat{H}_{LZ} = \frac{vt}{2} \sigma_z + \frac{\Delta}{2} \sigma_x \quad (3.37)$$

Here  $\sigma_z = |\uparrow\rangle \langle\uparrow| - |\downarrow\rangle \langle\downarrow|$  and  $\sigma_x = |\uparrow\rangle \langle\downarrow| + |\downarrow\rangle \langle\uparrow|$  are the Pauli matrices. The states,  $|\uparrow\rangle$  and  $|\downarrow\rangle$ , are eigenstates of the qubit Hamiltonian  $\frac{vt}{2} \sigma_z$ . The energy difference between the diabatic states,  $vt$ , varies linearly with time (with level-crossing speed  $v > 0$ ). Tunneling

strength  $\Delta$  represents intrinsic interactions between the two diabatic states, and induces the transitions.

In order to consider the Landau-Zener transition in the presence of an environment, this study models a bosonic bath of  $N$  quantum harmonic oscillators by Hamiltonian  $\hat{H}_B$  and the qubit-bath coupling by Hamiltonian  $\hat{H}_{SB}$  [37],

$$\begin{aligned}\hat{H}_B &= \sum_{q=1}^N \hbar \omega_q \hat{b}_q^\dagger \hat{b}_q \\ \hat{H}_{SB} &= \sum_{q=1}^N \frac{\gamma_q}{2} (\cos \theta_q \sigma_z + \sin \theta_q \sigma_x) (\hat{b}_q^\dagger + \hat{b}_q)\end{aligned}\quad (3.38)$$

where  $\hbar = 1$  is assumed throughout,  $\omega_q$  indicates the frequency of the  $q$ -th mode of the bath with creation (annihilation) operator  $\hat{b}_q^\dagger$  ( $\hat{b}_q$ ).  $\gamma_i$  and  $\theta_i$  are the qubit-oscillator coupling and the interaction angle, respectively. The effect of the bosonic bath is to change the energies of the qubit via the diagonal coupling ( $\sigma_z$ ) and to induce transitions between the levels of the qubit via the off-diagonal coupling ( $\sigma_x$ )

The environment and its coupling to the system are characterized by a spectral density function,

$$J(\omega) = \sum_q \gamma_q^2 \delta(\omega - \omega_q) = 2\alpha \omega_c^{1-s} \omega^s e^{-\omega/\omega_c} \quad (3.39)$$

where  $\alpha$  is the dimensionless coupling strength,  $\omega_c$  denotes the cutoff frequency, and  $s$  determines the dependence of  $J(\omega)$  on the bath frequency  $\omega$ . The bosonic Ohmic bath is specified by  $s = 1$ , and  $s < 1$  ( $s > 1$ ) denotes the sub-Ohmic (super-Ohmic) bath [38]. Spectral densities of the sub-Ohmic bath are computed using logarithmic discretization. Linear discretization is used for Ohmic and super-Ohmic bath, and cutoff frequency in the discretization is given by  $\omega_c = 10\sqrt{v/\hbar}$ .

For convenience, the multi-D<sub>2</sub> ansatz for the dissipative Landau-Zener model is shown

as follows

$$\begin{aligned} |D_2^M(t)\rangle &= \sum_{i=1}^M \left\{ A_i(t) |\uparrow\rangle \exp \left[ \sum_{q=1}^N f_{iq}(t) \hat{b}_q^\dagger - H.c. \right] |0\rangle \right\} \\ &+ \sum_{i=1}^M \left\{ B_i(t) |\downarrow\rangle \exp \left[ \sum_{q=1}^N f_{iq}(t) \hat{b}_q^\dagger - H.c. \right] |0\rangle \right\}, \end{aligned} \quad (3.40)$$

where  $A_i$  and  $B_i$  are time-dependent variational parameter for the amplitudes in states  $|\uparrow\rangle$  and  $|\downarrow\rangle$ , respectively. Other parameters in Eq. (3.40) have the same meaning as in Eq. (3.7). Details of the Lagrangian, equations of motion, and initial conditions are given in Appendix C.1.

With the wave function  $|D_2^M(t)\rangle$  available, below we give the time evolution of the transition probability that the qubit flipped from the initial state  $|\uparrow\rangle$  to  $|\downarrow\rangle$  at the time  $t$ ,

$$\begin{aligned} P_{\uparrow \rightarrow \downarrow}(t) &= 1 - P_{\uparrow \rightarrow \uparrow}(t), \\ P_{\uparrow \rightarrow \uparrow}(t) &= \sum_{i,j}^M A_j^*(t) S_{ji}(t) A_i(t), \end{aligned}$$

where  $A_i$  are the time-dependent variational parameters for the amplitude in state  $|\uparrow\rangle$ , and Debye-Waller factor is

$$S_{ji}(t) = \exp \sum_q \left\{ -(|f_{jq}(t)|^2 + |f_{iq}(t)|^2) / 2 + f_{jq}^*(t) f_{iq}(t) \right\}.$$

## References

- [1] P.A.M. Dirac, *Proc. Camb. phil. Soc.*, **1930**, 26, 376-376.
- [2] J. Frenkel, *Wave Mechanics, Advanced General Theory*, Oxford: Clarendon Press, **1934**, 435-435.
- [3] C. Lubich, *From quantum to classical molecular dynamics: reduced models and numerical analysis*, European Mathematical Society, **2008**.
- [4] E. J. Baerends, D. E. Ellis, and P. Ros, *Chem. Phys.*, **1973** 2, 41.

- [5] E. Runge and E. K. U. Gross, *Phys. Rev. Lett.*, **1984**, 52, 997.
- [6] I. P. Grant and H. M. Quiney, *Phys. Rev. A*, **2000**, 62, 22508.
- [7] A. D. McLachlan, *Mol. Phys.*, **1964**, 8, 39.
- [8] E. J. Heller, *J. Chem. Phys.*, **1976**, 64, 63.
- [9] I. Burghardt, H.-D. Meyer, and L. S. Cederbaum, *J. Chem. Phys.*, **1999**, 111, 2927.
- [10] E. J. Heller, *J. Chem. Phys.*, **1981** 75, 2923.
- [11] I. Burghardt, K. Giri, and G. A. Worth, *J. Chem. Phys.*, **2008**, 129, 174104.
- [12] Y. Zhao, S. Yokojima, and G. Chen, *J. Chem. Phys.*, **2000**, 113, 4016.
- [13] Z. Huang, L. Wang, C. Wu, L. Chen, F. Grossmann, and Y. Zhao, *Phys. Chem. Chem. Phys.*, **2017**, 19, 1655.
- [14] Z. Huang, L. Chen, N. Zhou, and Y. Zhao, *Ann. Phys. (Berlin)*, **2017**, 529, 1600367.
- [15] Z. Huang, Y. Fujihashi, and Y. Zhao, *J. Phys. Chem. Lett.*, **2017**, 8, 3306.
- [16] Y. Fujihashi, L. Wang, and Y. Zhao, *J. Chem. Phys.*, **2017**, 147, 234107.
- [17] J. Sun, B. Luo, and Y. Zhao, *Phys. Rev. B*, **2010**, 82, 014305.
- [18] Y. Zhao, B. Luo, Y. Y. Zhang, and J. Ye, *J. Chem. Phys.*, **2012**, 137, 084113.
- [19] N. Zhou, Z. Huang, J. Zhu, V. Chernyak, and Y. Zhao, *J. Chem. Phys.*, **2015**, 143, 014113.
- [20] J. Zak, *Phys. Rev. Lett.*, **1968**, 20, 1477.
- [21] J. B. Kreger and G.J. Iafrate, *Phys. Rev. B.*, **1986**, 33, 5494.
- [22] C. Kittel, *Quantum Theory of Solids* (Wiley, New York, 1987).
- [23] N. Monahan and X.-Y. Zhu, *Annu. Rev. Phys. Chem.*, **2015**, 66, 601.
- [24] M. B. Smith and J. Michl, *Chem. Rev.* **2010**, 110, 6891.

- [25] P. M. Zimmerman, F. Bell, D. Casanova, and M. Head-Gordon, *J. Am. Chem. Soc.*, **2011**, 133, 19944.
- [26] D. Casanova, *J. Chem. Theory Comput.*, **2014**, 10, 324.
- [27] T. C. Berkelbach, M. S. Hybertsen, and D. R. Reichman, *J. Chem. Phys.*, **2013**, 138, 114103.
- [28] F. Mirjani, N. Renaud, N. Gorczak, and F. C. Grozema, *J. Phys. Chem. C*, **2014**, 118, 14192.
- [29] G. Tao, *J. Phys. Chem. C*, **2014**, 118, 17299.
- [30] H. Tamura, M. Huix-Rotllant, I. Burghardt, Y. Olivier, and D. Beljonne, *Phys. Rev. Lett.*, **2015**, 115, 107401.
- [31] Y. Fujihashi and A. Ishizaki, *J. Phys. Chem. Lett.*, **2016**, 7, 363.
- [32] Y. Yao, *Phys. Rev. B*, **2016**, 93, 115426.
- [33] E. G. Fuemmeler, S. N. Sanders, A. B. Pun, E. Kumarasamy, T. Zeng, K. Miyata, M. L. Steigerwald, X.-Y. Zhu, M. Y. Sfeir, L. M. Campos, and N. Ananth, *ACS Cent. Sci.*, **2016**, 2, 316.
- [34] E. C. Alguire, J. E. Subotnik, and N. H. Damrauer, *J. Phys. Chem. A*, **2015**, 119, 299.
- [35] T. C. Berkelbach, M. S. Hybertsen, and D. R. Reichman, *J. Chem. Phys.*, **2013**, 138, 114102.
- [36] V. May and O. Kuhn, *Charge and Energy Transfer Dynamics in Molecular Systems*, Wiley-VCH, Weinheim, **2004**.
- [37] M. Wubs, K. Saito, S. Kohler, P. Hänggi, and Y. Kayanuma, *Phys. Rev. Lett.*, **2006**, 97, 200404.
- [38] R. S. Whitney, M. Clusel, and T. Ziman, *Phys. Rev. Lett.*, **2011**, 107, 210402.

## Chapter 4\*

### Polaron dynamics with off-diagonal coupling

*Treated traditionally by the Ehrenfest approximation, dynamics of a one-dimensional molecular crystal model with off-diagonal exciton-phonon coupling is investigated in this chapter using the Dirac-Frenkel time-dependent variational principle with the multi- $D_2$  ansatz. The effect of the transfer integral and the off-diagonal coupling on exciton transport are probed in both real and reciprocal space representations. Finally, the variational method with importance sampling is employed to investigate temperature effects on exciton transport using the multi- $D_2$  ansatz, and it is demonstrated that the variational approach is valid in both low and high temperature regimes.*

---

\* This chapter published substantially as Z. Huang, L. Wang, C. Wu, L. Chen, F. Grossmann, and Y. Zhao, *Phys. Chem. Chem. Phys.*, **19**, 1655 (2017).

## 4.1 Introduction

Exciton transport in CPs is commonly described by the SSH model [1] and treated by the semi-classical method based on Ehrenfest approximation [2]. Ehrenfest theorem provides a bridge between quantum and classical mechanics, and is the quantum mechanical equivalent of Newton's second law of motion in the classical limit that wave function is highly concentrated around a point. In 1927, Ehrenfest related the time derivative of the expectation values of the position and momentum operators to the expectation value of the force on a massive particle moving in a scalar potential, and implied that the expected position and expected momentum will approximately follow the classical trajectories [3]. In order to give a natural extension of the usual Ehrenfest average used in the classical path method [4, 5], a self-consistent mean-field formalism based on the Ehrenfest theorem was developed in 1983 by Billing [6]. His developed method dealt with systems where the wave function of the quantum part depends upon classically treated nuclear coordinates and momenta, and inspired various variations of the Ehrenfest method. For example, Troisi *et al.* constructed a conventional treatment of carrier dynamics of the SSH model to solve the time-dependent Schrödinger equation for the charge wave function and use the Ehrenfest theorem for classical accelerations of nuclear positions [7]. In realistic polymer chains, charge transport processes occur on the nano scale and the carriers interact with the environment including the dominant phononic DOFs [8]. Even though the semi-classical dynamics in the SSH model can capture certain features of charge transport, enormous challenges still remain to accurately describe fully quantum dynamical correlations between the electronic and vibrational subsystems [9].

In this chapter, in order to offer an accurate description of polaron dynamics including off-diagonal coupling, the Dirac-Frenkel time-dependent variational approach with the multiple Davydov trial states will be employed. The Hamiltonian of the Holstein polaron model is given in Subsec. 3.3.1 of Chapter 3. The remainder of the chapter is structured as follows. In Sec. 4.2, the accuracy of the variational method using the multi- $D_2$  Ansatz is examined by the ansatz deviation, which quantifies how faithfully the trial state follows



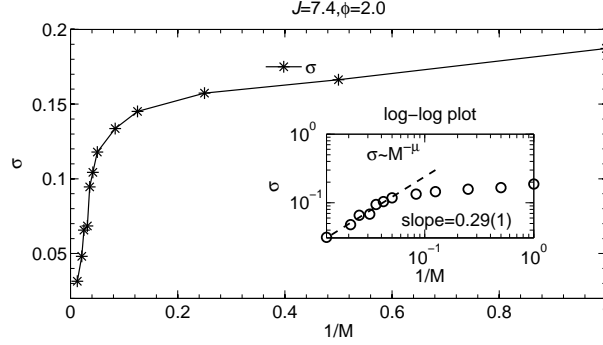


**Figure 4.1** The relative deviation  $\sigma$  of the multi- $D_2$  ansatz is displayed as a function of  $1/M$  for a commonly used set of parameters with off-diagonal coupling  $\phi = 2.0$  and large transfer integral  $J = 7.4$ . In the inset, the relationship  $\sigma \sim M^\mu$  is displayed on a log-log scale and the dashed line represents a power-law fit.

the Schrödinger equation, and it is shown that large enhancement over that of the semi-classical method have been achieved. Numerical results of polaron dynamics by the variational method using the multi- $D_2$  Ansatz are discussed in Sec. 4.3. Impacts of the transfer integral and the off-diagonal coupling on the exciton transport are studied in Sec. 4.4. Effects of temperature on polaron dynamics is investigated in Sec. 4.5.

## 4.2 The multi- $D_2$ Davydov ansatz

In this section, dynamics of Hamiltonian (3.12) is described fully quantum mechanically using the multi- $D_2$  ansatz with sufficiently large multiplicity  $M$ , yielding numerically accurate quantum dynamics at zero temperature [10].

The accuracy of the multi- $D_2$  ansatz is firstly tested with parameters extracted from Refs. [7] (this parameter set was extensively used to study realistic models of pentacene molecules). As shown in Fig. 4.1, the relative deviation  $\sigma$  goes to zero as the multiplicity  $M$  approaches infinity. A log-log plot of  $(\sigma, 1/M)$  (inset) indicates a power-law relationship with an exponent of  $\mu = 0.29(1)$ , further inferring a numerically exact solution in the limit of  $M \rightarrow \infty$ . The largest relative deviation  $\sigma$  is found for the single  $D_2$  ansatz. As

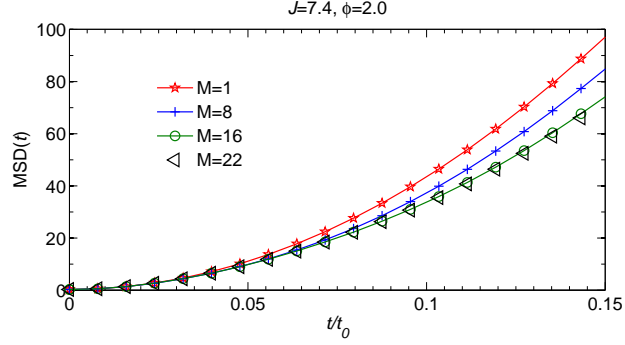


**Figure 4.2**  $\text{MSD}(t)$  of the exciton for the case of  $J = 7.4$  and  $\phi = 2.0$  is obtained from the single  $D_2^{M=1}$ , the  $D_2^{M=8}$ , the  $D_2^{M=16}$ , and the  $D_2^{M=22}$  ansatz, respectively.

presented in Appendix A.1, the SSH Hamiltonian is equivalent to the Holstein Hamiltonian with off-diagonal coupling. The equivalence between the semi-classical method and the variational method using the single  $D_2$  ansatz is shown in Appendix A.2. Therefore, this implies that the accuracy of the semi-classical Ehrenfest dynamics can be quantified by the relative deviation of the single  $D_2$  ansatz. The variational method with sufficiently large  $M$  fully takes into account the quantum effects, yielding a much more accurate result than that with the single  $D_2$  ansatz, which is equivalent to the semi-classical method. For example,  $\sigma$  of the  $D_2^{M=16}$  ansatz in Fig. 4.1 is smaller than 0.1, thus the multiplicity of  $M = 16$  is employed to explore polaron dynamics in following subsections, unless otherwise specified.

In order to further compare the performance of the variational method using the multi- $D_2$  ansatz and that of the semi-classical method, the exciton movement is studied by calculating the mean square displacement  $\text{MSD}(t)$ . As shown in Fig. 4.2, the amplitudes of  $\text{MSD}(t)$  from the fully quantum variational method using the  $D_2^{M=8}$ , the  $D_2^{M=16}$ , and the  $D_2^{M=22}$  ansatz are smaller than that from the semi-classical Ehrenfest method (equivalent to the single  $D_2$  ansatz), and  $\text{MSD}(t)$  shows apparent convergence as the multiplicity  $M$  exceeds 16. This result is in agreement with that by the IDC approach, which the carrier is found to be less mobile in comparison with that of original Ehrenfest method [11, 12]. In this case, the transfer integral is much larger than the exciton-phonon coupling and makes more contribution to the movement of the wave front in the carrier

propagation. Consequently, the exciton-phonon coupling leads to localization of the wave front. The Ehrenfest method treats the phonons semi-classically and underestimates the confinement effect of the exciton-phonon coupling on the wave function. Therefore the reduction of the mobility is attributed to the quantum mechanical description of the phonons and the electron-phonon coupling. It should be noted, however, the change of MSD ( $t$ ) depends on parameter regimes. In some other cases (e.g.,  $J = 0$  and  $\phi = 1.0$ ), phonon assisted transport dominates the exciton movement as discussed in Ref. [10].

### 4.3 Polaron dynamics in exciton momentum representation

In this section, impacts of off-diagonal coupling on the exciton movement are explored in the exciton momentum representation by using the multi- $D_2$  ansatz. Without the exciton-phonon coupling, the Hamiltonian of the bare exciton can be described by the first term of Hamiltonian (3.12),  $\hat{H}_{\text{ex}}$ , and the energy band is  $E(k) = -2J \cos(k)$ . The exciton energy and the exciton momentum are constants of motion. However, in the presence of the exciton-phonon coupling, the exciton momentum may move away from initial values and the exciton energy would be dissipated.

The left and the right columns of Figs. 4.3(a)-(d) present the time evolution of the exciton momentum probability  $P_{\text{ex}}(t, k)$ , starting from initial conditions  $P_{\text{ex}}(0, k) = 1$  at  $k = 0$  and  $\pi$ , respectively.  $P_{\text{ex}}(t, k)$  redistributes toward a quasi stationary state, where no net energy transfer takes place between the exciton and the phonons, as shown in Figs. 4.3(e) and (f). Notwithstanding the difference of initial excitonic conditions,  $P_{\text{ex}}(t, k)$  in the case of Figs. 4.3(a) and (b) still relaxes to the same stationary regime, where final  $P_{\text{ex}}(t, k)$  is centered around  $k = 0$ . As for  $J = -0.6$ ,  $P_{\text{ex}}(t, k)$  is centered around  $k = \pm\pi$ , as shown in Figs. 4.3(c) and (d). Moreover, the exciton momentum pattern in Fig. 4.3(a) is shifted by  $\pi$  comparing to that in Fig. 4.3(d) because the Brillouin zone of the former is  $\pi$  shifted from that of the latter, and the shift also occurs for  $P_{\text{ex}}(t, k)$  in Figs. 4.3(b) and (c).

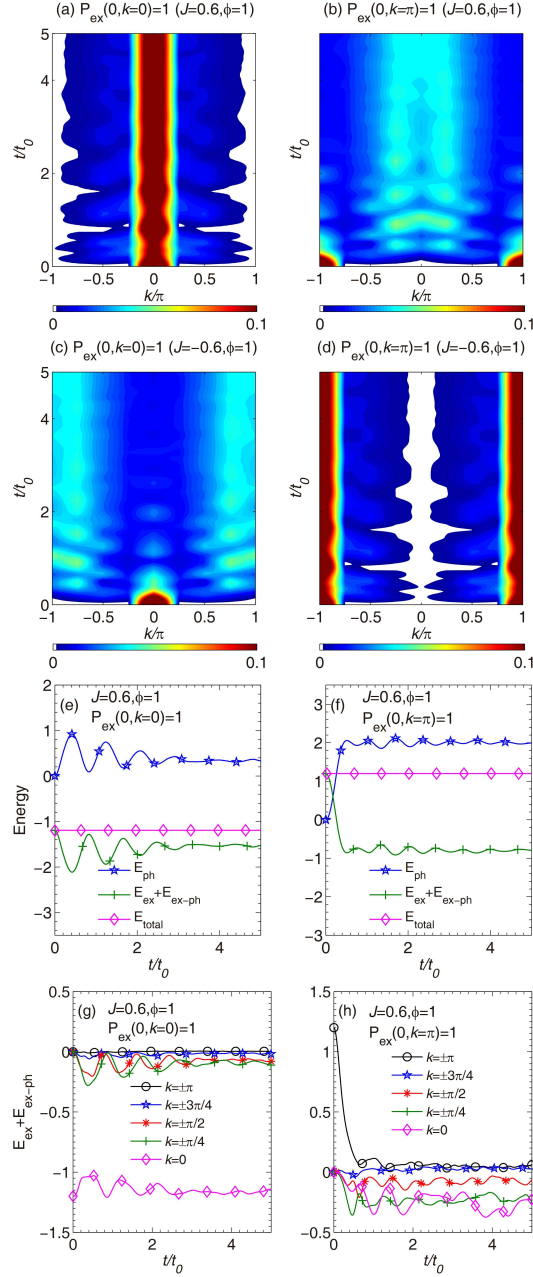


**Figure 4.3** (a)-(d) Time evolution of the exciton momentum probability  $P_{\text{ex}}(t, k)$  displayed in two columns is obtained using excitonic initial conditions:  $P_{\text{ex}}(0, k = 0) = 1$  (left column) and  $P_{\text{ex}}(0, k = \pi) = 1$  (right column). Two transfer integrals,  $J = 0.6$  and  $-0.6$ , are used together with the same off-diagonal coupling strength of  $\phi = 1$ , respectively. Energies for the case of  $J = 0.6$  and  $\phi = 1$  are plotted for (e)  $P_{\text{ex}}(0, k = 0) = 1$  and (f)  $P_{\text{ex}}(0, k = \pi) = 1$ . Energies of the exciton and the exciton-phonon coupling are displayed for each exciton momentum  $k$  using the initial condition of (g)  $P_{\text{ex}}(0, k = 0) = 1$  and (h)  $P_{\text{ex}}(0, k = \pi) = 1$ . The number of sites  $N = 8$  is fixed in these calculations.

The energy relaxation process is known to be accompanied with a redistribution of the exciton momentum probability [13]. With regard to the Holstein model with diagonal coupling, the exciton kinetic energy is transferred into the phonons, ending up with a constant value of  $E_{\text{ex}} + E_{\text{ex-ph}}$  [14]. However, energy relaxation in the Holstein model with off-diagonal coupling is still not well understood. In order to clarify this issue, time evolution of the exciton and the phonon energy is considered carefully. Figs. 4.3(e) and (f) show the time evolution of energies in the case of  $J = 0.6$  and  $\phi = 1$  for  $P_{\text{ex}}(0, k = 0) = 1$  and  $P_{\text{ex}}(0, k = \pi) = 1$ , respectively. Under this parameter set, the initial exciton energy of  $P_{\text{ex}}(0, k = 0) = 1$  is the lowest, that of  $P_{\text{ex}}(0, k = \pi) = 1$  is the highest, and those of other initial conditions fall in between. After the transfer integral is changed to  $J = -0.6$ , due to a phase shift of the Brillouin zone in the exciton momentum space, the initial exciton energy of  $P_{\text{ex}}(0, k = 0) = 1$  becomes the maximal while that of  $P_{\text{ex}}(0, k = \pi) = 1$  turns into the minimal for all initial excitonic conditions. As a result, identical energy relaxation processes occur despite that transfer integrals have opposite signs. Thus, only the case of  $J = 0.6$  and  $\phi = 1$  is displayed for simplicity. At  $t = 0$ , the phonons are in their vacuum states. Later, the incident exciton wave fronts generate phonons via the exciton-phonon coupling. As a consequence, the exciton energy is transferred to the phonon degrees of freedom. After a fast relaxation process, both the energies of the exciton and the phonons reach steady values.  $E_{\text{ex}} + E_{\text{ex-ph}}$  in the steady state settles around  $-2|J|$ , which corresponds to the energy minimum of the exciton in the absence of the exciton-phonon coupling. In order to identify the energy contribution of each exciton momentum,  $E_{\text{ex}} + E_{\text{ex-ph}}$  is also investigated in the exciton momentum representation. As plotted in Figs. 4.3(g) and (h), the initial  $E_{\text{ex}} + E_{\text{ex-ph}}$  is  $-1.2$  and  $1.2$ , respectively. After relaxation, the momentum of  $k = 0$  becomes the main contributor of  $E_{\text{ex}} + E_{\text{ex-ph}}$  for both cases, and also determines the locations of the quasi stationary regime after the exciton momentum redistribution.

Fig. 4.4 presents the time evolution of the exciton momentum probability in the absence of the transfer integral. The initial excitonic conditions are set as  $P_{\text{ex}}(0, k) = 1$  of  $k = 0$  and  $\pi$  in the left ((a),(c) and (e)) and the right ((b),(d) and (f)) column of Fig. 4.4, respectively.

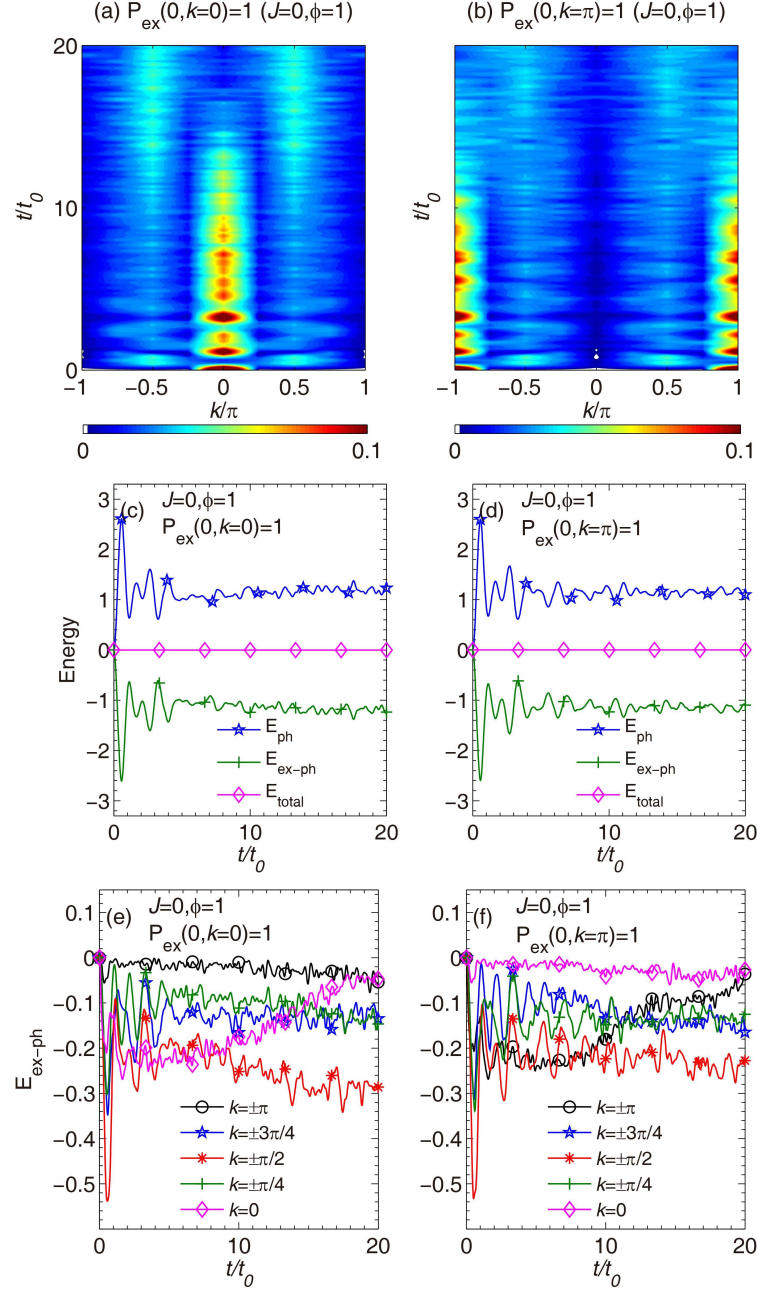


**Figure 4.4** Time evolution of the exciton momentum probability  $P_{\text{ex}}(t, k)$  for  $J = 0$  and  $\phi = 1$  is obtained using two initial conditions: (a)  $P_{\text{ex}}(0, k = 0) = 1$  (left column) and (b)  $P_{\text{ex}}(0, k = \pi) = 1$  (right column). Corresponding energies are displayed in (c) and (d). The contribution to the exciton-phonon interaction energy from each exciton momentum are shown in (e) and (f).

Akin to the cases of  $J = 0.6$  and  $\phi = 1$  in Fig. 4.3, by comparing  $P_{\text{ex}}(t, k)$  with two types of initial conditions, it is found that the exciton momentum probabilities redistribute and become centered around the same regimes, as shown in Figs. 4.4(a) and (b). Even in the absence of the transfer integral, the exciton can still be transported by the off-diagonal coupling. Figs. 4.4(c) and (d) plot the time evolution of the phonon energy and the exciton-phonon interaction energy. As also shown in Figs. 4.4(c) and (d), for  $0 < t \leq t_0$ , the amplitudes of both  $E_{\text{ph}}$  and  $E_{\text{ex-ph}}$  reach their peaks and fluctuate until the exciton and the phonons cease to exchange energy at  $t = 10t_0$ . The energy relaxation process only involves  $E_{\text{ex-ph}}$  because  $E_{\text{ex}}$  is always zero. As presented in Fig. 4.4(e),  $E_{\text{ex-ph}}$  of each exciton momentum undergoes three stages during the energy relaxation process. During  $0 < t \leq t_0$ , they all show strong oscillations with largest amplitudes. At the intermediate stage of  $t_0 < t \leq 10t_0$ , the energies of  $k = \pm\pi/2$  compete with that of  $k = 0$ . For  $t > 10t_0$ , the contribution of the energy of  $k = 0$  to  $E_{\text{ex-ph}}$  reduces to almost zero, leaving the energy of  $k = \pm\pi/2$  to be the dominant energy contributor. As for the case of the initial condition  $P_{\text{ex}}(0, k = \pi) = 1$  as shown in Fig. 4.4(f), the competition at the second stage of  $t_0 < t \leq 10t_0$  occurs between the energies of  $k = \pm\pi$  and  $\pm\pi/2$  instead, and the energy of  $k = \pm\pi/2$  also turns out to be the prominent contributor to  $E_{\text{ex-ph}}$ . Consequently, the exciton momentum probability finally becomes centered around  $k = \pm\pi/2$  as shown in Figs. 4.4(a) and (b).

#### 4.4 Effect of transfer integral and off-diagonal coupling on exciton transport

In this section, the influence of the transfer integral and the off-diagonal coupling on the exciton transport of Hamiltonian (3.12) is investigated.

By tuning the transfer integral, contributions of the transfer integral and the off-diagonal coupling on the exciton movement are examined, as shown in Fig. 4.5. It can be shown in the site representation that the off-diagonal exciton-phonon coupling plays a crucial role in polaron transport [15, 16]. As shown in Fig. 4.5(b), the off-diagonal coupling is the only agent for exciton movement in the absence of the transfer integral, also known

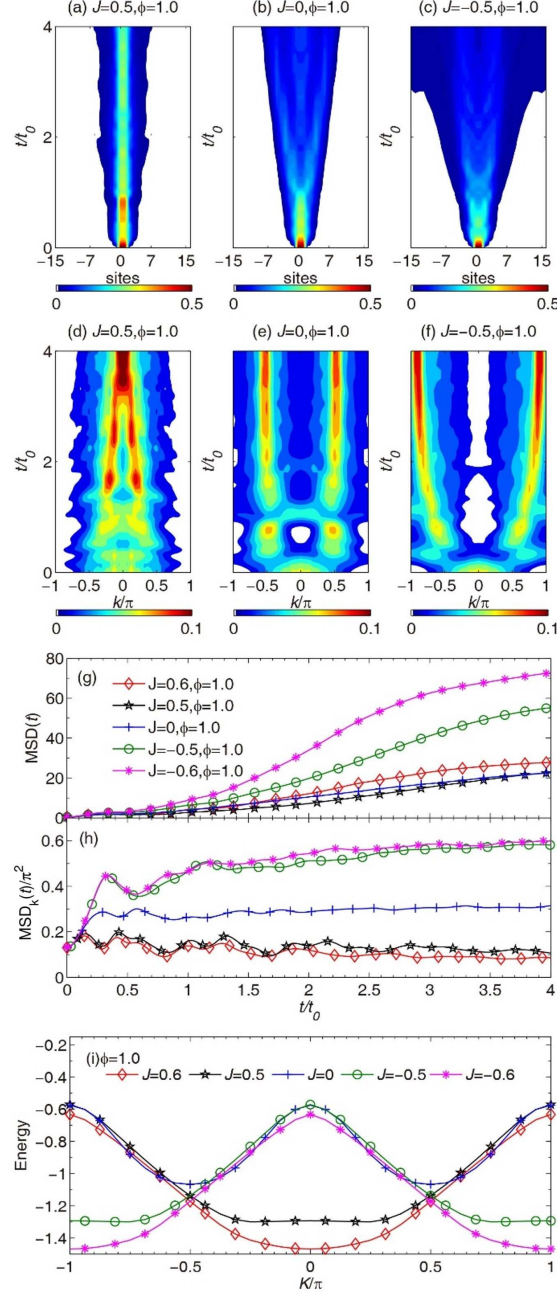


**Figure 4.5** Time evolution of the exciton probability in the site space  $P_{\text{ex}}(t, n)$  for the case of the off-diagonal coupling ( $\phi = 1.0$ ) is obtained with transfer integrals (a)  $J = 0.5$ , (b) 0, and (c)  $-0.5$ ; Related time evolution of the exciton probability in the momentum space  $P_{\text{ex}}(t, k)$  is shown in (d)-(f); (g) MSD  $\langle t \rangle$  of  $J = 0.6, 0.5, 0, -0.5$  and  $-0.6$  together with  $\phi = 1.0$  is plotted in the site representation; (h)  $\text{MSD}_k(t)$  is displayed in the exciton momentum representation; (i) Energy bands of the ground state are obtained from the Toyozawa ansatz. The number of sites  $N = 32$  is fixed in these calculations.



as phonon-assisted transport [17]. When both the off-diagonal coupling and the direct, phonon free exchange transfer are present, because of the competition between them, the exciton transport may be inhibited, as shown in Fig. 4.5(a). The self-trapping phenomenon is expected due to the competition between the off-diagonal coupling and the transfer integral when the energy bands is flattened at the Brollouin zone center [18]. In this work, the Toyozawa ansatz is adopted to study the ground state energy bands of the Holstein model using the variational method. As presented in Fig. 4.5(i), the lowest energy band of  $J = 0.5$  and  $\phi = 1.0$  meets the self-trapping condition, and thereby this case can be taken as an example to study the self-trapped exciton from the perspective of dynamics. In agreement with the expectation,  $P_{\text{ex}}(t, n)$  turns out to be localized in Fig. 4.5(a). By directly flipping the sign of the transfer integral to  $J = -0.5$ , the exciton wave fronts are found to move considerably, as shown in Fig. 4.5(c). Via  $\text{MSD}(t)$  as defined in Eq. (3.19), the expansion of the exciton wave packets is further investigated for  $J = -0.6, -0.5, 0, 0.5$  and  $0.6$ . As plotted in Fig. 4.5(g), the amplitude of  $\text{MSD}(t)$  for  $J = 0$  and  $\phi = 1$  is smaller than those of other cases with non-zero transfer integrals, except the self-trapped case of  $J = 0.5$  and  $\phi = 1.0$ .

In the crystal momentum representation, the underlying physics of the ground states can be elucidated, where the crystal momentum is denoted as  $K$  (see Eq. (2.6)). The Toyozawa ansatz is a time independent translationally invariant trial state, viewed as a superposition of the replicas of the  $D_2$  ansatz displaced to every lattice site, weighed by a phase factor of the total momentum [18]. The energy bands of the ground states are calculated from the Toyozawa ansatz. In the the off-diagonal coupling only case ( $J = 0$ ), the minima of the band are located at  $K = \pm\pi/2$ . The addition of positive (negative) transfer integrals moves the minima towards the center (boundary). In particular, as mentioned above, the case of  $J = 0.5$  flattens the band at the center of the Brillouin zone, leading to the largest effective mass of all studied cases, in accord with the self-trapping of  $P_{\text{ex}}(t, n)$  in Fig. 4.5(a).

The effect of the transfer integrals on the exciton movement in the presence of the off-diagonal coupling is further examined in the exciton momentum representation in

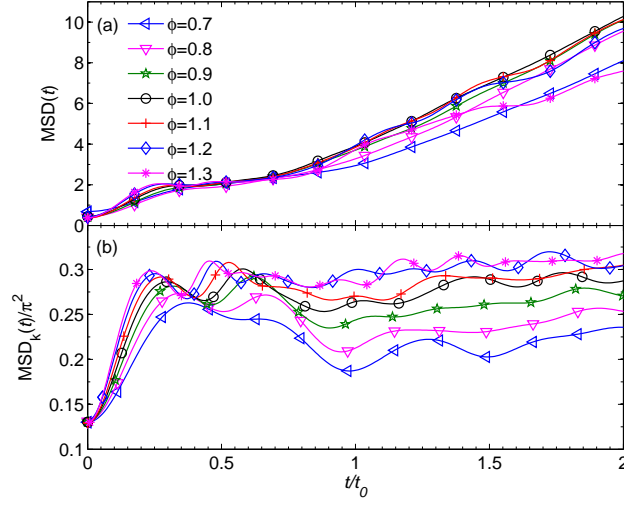


**Figure 4.6** (a) MSD ( $t$ ) of the exciton in the site representation is shown for  $J = 0$  and  $\phi = 0.7, 0.8, 0.9, 1.0, 1.1, 1.2$  and  $1.3$ ; Related  $MSD_k(t)$  in the exciton momentum representation is displayed in (b).

Figs. 4.5(d)-(f) and (h). The exciton is created in the profile of  $(2 + \cos k)/2N$  in the momentum space as two nearest neighboring sites are excited initially (see Appendix A.3). In the subsequent relaxation process,  $P_{\text{ex}}(t, k)$  redistributes and becomes localized in a quasi stationary region, and the mean square displacement of the exciton momentum  $MSD_k(t)$  approaches a plateau, as shown in Fig. 4.5(h). After the relaxation process, the final  $P_{\text{ex}}(t, k)$  is found to be determined by a combination of the transfer integral and the off-diagonal coupling strength. For the off-diagonal coupling only case,  $P_{\text{ex}}(t, k)$  progressively becomes localized around  $k = \pm\pi/2$  (Fig. 4.5(e)). In the case of  $J = 0.5$  and  $0.6$ ,  $P_{\text{ex}}(t, k)$  aggregates toward  $k = 0$ , as seen in Fig. 4.5(d). Similarly,  $P_{\text{ex}}(t, k)$  of both  $J = -0.5$  and  $-0.6$  correspond to  $\pm\pi$  in Fig. 4.5(f). In addition,  $MSD_k(t)$  for the extreme cases of  $P_{\text{ex}}(t, k) = \delta_{k,0}$  and  $\delta_{k,\pm\pi}$  are  $0$  and  $2\pi^2$ , respectively. As shown in Fig. 4.5(h),  $MSD_k(t)$  of  $J = 0.6$  is closer to the analytical value of  $0$  than that of  $J = 0.5$ , indicating that  $P_{\text{ex}}(t, k)$  of  $J = 0.6$  is more localized around the zone center than that of  $J = 0.5$ . Likewise,  $MSD_k(t)$  of  $J = -0.6$  is nearer to the limited value of  $2\pi^2$  than that of  $J = -0.5$ , illustrating that  $P_{\text{ex}}(t, k)$  of the former case is more localized around  $k = \pm\pi$ .

In the site representation, the off-diagonal coupling is known to play the role of assisting the transport of the exciton [16, 17]. In Fig. 4.6(a), the dependence of MSD ( $t$ ) on the off-diagonal coupling strength is studied in the absence of transfer integral ( $J = 0$ ). It is found that the exciton propagation is facilitated by the off-diagonal coupling, as shown by the site-space MSD ( $t$ ) in Fig. 4.6(a). However, the off-diagonal coupling can be simultaneously an agent for exciton localization. The localization effect of  $\phi$  gradually increases with the coupling strength  $\phi$  if  $\phi$  is greater than a critical value  $\phi_c$  [19]. As shown in Fig. 4.6(a), the amplitude of MSD ( $t$ ) decreases with the off-diagonal coupling strength  $\phi$  for  $\phi > \phi_c = 1.0$ .

In the exciton momentum representation,  $P_{\text{ex}}(t, k)$  all ends up around  $k = \pm\pi/2$  for a variety of off-diagonal coupling strengths, and the corresponding  $\text{MSD}_k(t)$  approaches the same narrow regime around  $0.25\pi^2$ , which is the theoretical value of  $\text{MSD}_k(t)$  for  $P_{\text{ex}}(t, k) = (\delta_{k,\pi/2} + \delta_{k,-\pi/2})/2$ , as shown in Fig. 4.6(b). However, the relaxation time diverges due to the variance of the off-diagonal coupling. The time for the exciton momentum to reach the stationary regime is inversely related to the off-diagonal coupling strength, because the first stage of the time evolution ( $t < 0.5t_0$ ) is accompanied by the fast exciton movement in the case of large off-diagonal coupling as presented in Fig. 4.6. In addition, the energy bands of various off-diagonal coupling strengths imply that the band width and effective mass are largest for  $\phi_c^{\text{static}} = 1.4$  and get smaller as  $\phi$  moves away from  $\phi_c^{\text{static}}$  [19]. The localization feature is found both in static and dynamic calculations although the value of  $\phi_c$  differs slightly. The off-diagonal exciton-phonon coupling leads to exciton energy dissipation and redistribution of exciton momentum in three typical scenarios corresponding to completely distinguishable band structures (this conclusion is independent of the system size), which may be formed due to a variety of compositions and geometrical structures of the organic materials, defects, doping mechanisms and deformations of CPs [20, 21].

## 4.5 Temperature effects

In this section, the work is extended to study the effect of finite temperatures on polaron dynamics. The conductivity of polymers has been measured by many workers as a function of temperature [1, 22, 23]. The temperature effects have been in contention from a theoretical point of view. For example, Cruzeiro *et al.* claims that Davydov soliton is stable at  $T = 310$  K [24]. Later, a quantum Monte Carlo treatment has shown that the Davydov soliton is unstable above 7 K [25]. In this work, several approaches are used to study the temperature effects: a variational method with importance sampling (see Appendix A.4.2), the HEOM method [26, 27], and the averaged Hamiltonian method (see Appendix A.4.1). The variational method with importance sampling developed by Wang *et al.* simulates thermal fluctuation of phonon modes by sampling the initial phonon displacements based on the Bose distribution, and thus it can deal with Holstein polaron dynamics at both low and high temperatures [28]. The HEOM method is numerically exact and is capable to treat any finite temperature, serving as a benchmark here. However, the HEOM method is also numerically expensive and thus impractical when the system size is large. The variational approach can treat large systems once a proper trial wave function is adopted. In order to compare to previous attempts in the literature, the averaged Hamiltonian method has also been used, and it is found that this approach is not even suitable for the spin-boson model (*i.e.*,  $N=2$ ) as shown in Appendix A.4.

Fig. 4.7 shows polaron dynamics calculated by the multi- $D_2$  ansatz with importance sampling and the HEOM method for two temperatures. The calculations are carried out for  $J = 0.8$  and  $\phi = 0.3$  in a ring of  $N = 8$  sites.  $P_{\text{ex}}(t, n)$  outputs obtained from the  $D_2^{M=16}$  ansatz and the HEOM method at  $T = 0$  are shown and compared in Figs. 4.7(a) and (b), respectively. As revealed in Fig. 4.7(c),  $\Delta P_{\text{ex}}(t, n)$ , *i.e.*, the difference between the two methods, are two orders of magnitude smaller than the value of  $P_{\text{ex}}(t, n)$ , indicating that variational method can be numerically exact at low temperatures with sufficient multiplicity  $M$  of the multi- $D_2$  ansatz. The phonon displacement  $\lambda_{i,q}(t = 0)$  is set to zero at  $T = 0$ , while importance sampling is used at  $T = 2/k_B$  ( $\beta = 0.5$ ) to simulate the finite temperature

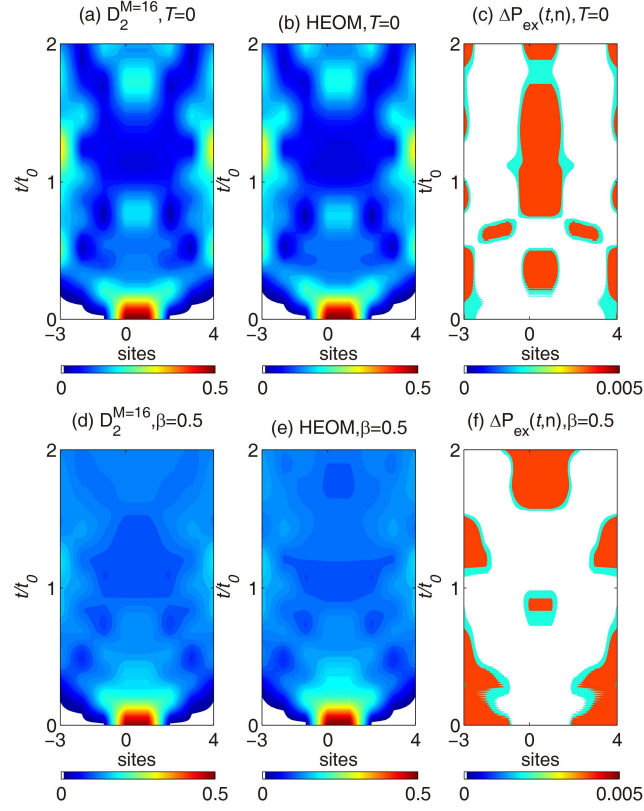


**Figure 4.7** Time evolution of the exciton probability in the site space  $P_{\text{ex}}(t, n)$  obtained at  $T = 0$  and  $2/k_B$ .  $P_{\text{ex}}(t, n)$  at  $T = 0$  obtained from (a) the  $D_2^{M=16}$  ansatz, (b) the HEOM method, and (c)  $\Delta P_{\text{ex}}(t, n)$  between the  $D_2^{M=16}$  ansatz and the HEOM method;  $P_{\text{ex}}(t, n)$  obtained from (d) the  $D_2^{M=16}$  ansatz, (e) the HEOM method, and (f) the related  $\Delta P_{\text{ex}}(t, n)$  at  $T = 2/k_B$  ( $\beta = 0.5$ ).

effects with the result displayed in Fig. 4.7(d). Similarly, as shown in Fig. 4.7(f), differences between results from the two methods are two orders of magnitude smaller than the value of  $P_{\text{ex}}(t, n)$  in Figs. 4.7(d) and (e), inferring that the variational method with importance sampling provides numerically exact results at high temperatures with sufficiently large  $M$ .

Next, the influence of thermal fluctuations on exciton transport is investigated. For both low and high temperatures, the exciton wave fronts depart from the site of exciton creation and propagate in opposing directions until they meet at the opposite side of the ring. During the time evolution, distinct features observed at zero temperature (Figs. 4.7(a) and (b)) are

now significantly smeared due to the thermal fluctuations (Figs. 4.7(d) and (e)). As shown in Figs. 4.7(d) and (e), during  $0.2t_0 < t < t_0$  the exciton probability is more centered around the site of creation than those of Figs. 4.7(a) and (b). For  $t \geq t_0$ , the bright spots shown in Figs. 4.7(a) and (b) are significantly quenched in Figs. 4.7(d) and (e). These results indicate that the exciton transport is weakened when the temperature is increased, in line with Refs. [ 7].

In summary, an accurate description is offered for polaron dynamics including off-diagonal coupling using the Dirac-Frenkel time-dependent variational approach with the multiple Davydov trial states. The accuracy of the Ehrenfest dynamics is examined for the SSH model. It is demonstrated that the semi-classical method and the variational method using the single  $D_2$  *Ansatz* are equivalent. Then the validity of the semi-classical method (the variational method with the single  $D_2$  *Ansatz*) is checked by examining its deviations from the exact quantum dynamics. The underlying physics is revealed in the real and reciprocal space representations, including the exciton transport, the exciton momentum redistribution and the exciton energy dissipation. At the closing of the chapter, the fully quantum mechanical method using the multiple Davydov trial states is shown to be also applicable at the finite temperatures.

## References

- [1] A. J. Heeger, S. Kivelson, J. R. Schrieffer, W. P. Su, *Reviews of Modern Physics*, **1988**, 60, 781-850.
- [2] W. Si and C.-Q. Wu, *J. Chem. Phys.*, **2015**, 143, 024103.
- [3] P. Ehrenfest, *Zeitschrift Für Phys.*, **1927**, 45, 455.
- [4] W. Elberfeld and M. Kleber, *J. Phys. B At. Mol. Phys.*, **1983**, 16, 355.
- [5] G. D. Billing, *Int. Rev. Phys. Chem.*, **1994**, 13, 309.
- [6] G. D. Billing, *Chem. Phys. Lett.* **1983**, 100, 535.

- [7] A. Troisi and G. Orlandi, *Phys. Rev. Lett.*, **2006**, 96, 86601.
- [8] P. Szymanski, S. Garrett-Roe, and C. B. Harris, *Prog. Surf. Sci.*, **2005**, 78, 1-39.
- [9] G. Li, B. Movaghar, A. Nitzan, and M. A. Ratner, *J. Chem. Phys.*, **2013**, 138, 044112.
- [10] N. J. Zhou, Z. K. Huang, J. F. Zhu, V. Chernyak, Y. Zhao, *J. Chem. Phys.*, **2015**, 143, 014113.
- [11] Y. Yao, W. Si, X. Hou, and C.-Q. Wu, *J. Chem. Phys.*, **2012**, 136, 234106.
- [12] J. Dong, W. Si, and C.-Q. Wu, *J. Chem. Phys.*, **2016**, 144, 144905.
- [13] F. Dorfner, L. Vidmar, C. Brockt, E. Jeckelmann, and F. Heidrich-Meisner, *Phys. Rev. B*, **2015**, 91, 104302.
- [14] D. Golez, J. Bonca, L. Vidmar, S.A. Trugman, *Phys. Rev. Lett.*, **2012**, 109, 236402.
- [15] H. Tamura and M. Tsukada, *Phys. Rev. B*, **2012**, 85, 54301.
- [16] H. Tamura, M. Tsukada, H. Ishii, N. Kobayashi, and K. Hirose, *Phys. Rev. B*, **2012**, 86, 35208.
- [17] Y. Zhao, D. W. Brown, and K. Lindenberg, *J. Chem. Phys.*, **1994**, 100, 2335.
- [18] Y. Zhao, D. W. Brown, and K. Lindenberg, *J. Chem. Phys.*, **1997**, 107, 3159; **1997**, 107, 3179.
- [19] Y. Zhao, B. Luo, Y. Zhang, and J. Ye, *J. Chem. Phys.*, **2012**, 137, 084113.
- [20] J. L. Brédas, B. Thémans, J. G. Fripiat, J. M. André, and R. R. Chance, *Phys. Rev. B*, **1984**, 29, 6761.
- [21] M. M. Kujlja and S. N. Rashkeev, *Phys. Rev. B*, **2007**, 75, 104111.
- [22] T. Ishiguro, H. Kaneko, Y. Nogami, H. Ishimoto, H. Nishiyama, J. Tsukamoto, A. Takahashi, M. Yamaura, T. Hagiwara, and K. Sato, *Phys. Rev. Lett.*, **1992**, 69, 660.

- [23] X. B. Chen, J.-P. Issi, M. Cassart, J. Devaux, and D. Billaud, *Polymer (Guildf)*., 1994, **35**, 5256.
- [24] L. Cruzeiro, J. Halding, P. L. Christiansen, O. Skovgaard, and A. C. Scott, *Phys. Rev. A*, 1988, **37**, 880.
- [25] X. Wang, D. W. Brown, and K. Lindenberg, *Phys. Rev. Lett.*, **1989**, 62, 1796.
- [26] Y. Tanimura, R. Kubo, *J. Phys. Soc. Jpn*, **1989**, 58, 101.
- [27] L. Chen, Y. Zhao, and Y. Tanimura, *J. Phys. Chem. Lett.*, **2015**, 6, 3110.
- [28] L. Wang, Y. Fujihashi, L. Chen, and Y. Zhao, *J. Chem. Phys.*, **2017**, 146, 124127.



**Chapter 5\*****Transient polaron dynamics in an external electric field**

*This chapter documents a systematic study of transient dynamics of a one-dimensional Holstein polaron with diagonal and off-diagonal carrier-phonon coupling in an external electric field. After adding weak carrier-phonon coupling, temporal periodicity is unchanged while the spatial configurations become different from the bare carrier scenarios, also depending on the initial conditions. In particular, at variance with the case of an infinite linear chain, no steady state is found in a finite-sized ring within the anti-adiabatic regime. For strong diagonal coupling, the multi-D<sub>2</sub> Ansatz is found to be highly accurate, and the phonon confinement gives rise to carrier localization and decay of the Bloch oscillations.*

---

\* This chapter published substantially as Z. Huang, L. Chen, N. Zhou, and Y. Zhao, *Ann. Phys. (Berlin)*, **529**, 1600367 (2017).

## 5.1 Introduction

BOs emerge when an electron subject to a perfectly periodic lattice potential executes periodic motion in the presence of an external electric field [1–7], and were found in various physical systems in recent decades, such as semiconductor superlattices [8, 9], organic materials [10–16] and quantum dots [17, 18]. As discussed in Subsec. 2.2.2 of Chapter 2, an important issue for BOs dynamics is the effect of carrier-phonon interactions, which is of essential importance for the aforementioned systems. Despite dedicated studies of BOs dynamics, the effect of complex interplay between the electron and its accompanying phonon cloud in a one-dimensional lattice is till not well understood [19, 20]. Spatial dynamics influenced by carrier-phonon coupling is also inadequately studied given initial broad and narrow carrier wave packets [21, 22]. Moreover, a unified treatment on the diagonal and off-diagonal carrier-phonon coupling remains elusive. In organic materials, the diagonal carrier-phonon coupling arises from overall modulations of the site energy. The off-diagonal carrier-phonon coupling is related to the dependence of the transfer integral on the spacing and relative orientations of adjacent molecules. The diagonal and off-diagonal coupling is also termed as local and nonlocal coupling, respectively. Both types of carrier-phonon coupling have been demonstrated to coexist in organic materials [23], and the off-diagonal coupling has been shown to play a crucial role in facilitating the diffusion of the polaron [24]. With an addition of an external electric field, polaron diffusion with off-diagonal coupling in conjugated polymer chains has been simulated using a semi-classical method [16, 25], reporting the polaron dissociation in conducting polymers by high electric fields. However, reliable solutions are few for Hamiltonians with off-diagonal coupling and an external field, as those semi-classical methods neglect the quantum nature of phonons and carrier-phonon coupling [25].

In this chapter, the impact of diagonal and off-diagonal carrier-phonon coupling on the Holstein polaron dynamics in a ring system will be investigated in the presence of a constant electric field using the multiple Davydov  $D_2$  trial state with the Dirac-Frenkel variational principle. As presented in Subsec. 3.3.2 of Chapter 3, this chapter adopts the

Holstein model with simultaneous diagonal and off-diagonal carrier-phonon coupling under the external electric field. The rest of the chapter is structured as follows. In Sec. 5.2, the variational results are compared to those of the benchmark HEOM calculations. In Sec. 5.3, the influence of weak diagonal coupling in the anti-adiabatic regime on the carrier wave packet is investigated using initial Gaussian wave packets with varying widths with particular attention paid to the possible existence of a steady state. Finally, polaron dynamics is examined in the strong diagonal coupling regime in Sec. 5.4.

## 5.2 Validity of variation for transient dynamics

This section shows that the multi- $D_2$  ansatz with sufficiently large multiplicity  $M$  yields quantitatively accurate solutions to the dynamics of the Holstein polaron with both diagonal and off-diagonal coupling, in perfect agreement with the benchmark calculations of the numerically exact HEOM method (see Appendix B.3) [26, 27]. For simplicity, only optical phonons are used in this section.

### 5.2.1 Diagonal Coupling

The case of diagonal carrier-phonon coupling is studied first. Dynamics of the Holstein polaron under a constant external field is investigated by using the multi- $D_2$  *Ansatz*, in comparison with those obtained with the single Davydov  $D_2$  ansatz and the HEOM method. Using these approaches, the time evolution of the carrier probability  $P_{ca}(t, n)$  as shown in Fig. 5.1 is simulated in the case of  $J = 0.1$ ,  $g = 0.28$  and  $F = 0.1$  in a small ring with  $N = 8$  sites for simplicity. The carrier is created on two nearest neighboring sites  $\psi_n = (\delta_{n,N/2} + \delta_{n,N/2+1})/\sqrt{2}$ , and the phonon displacement  $\lambda_{i,q}(t = 0) = 0$  is set. As depicted in Figs. 5.1(a) and (b), distinguishable deviations in  $P_{ca}(t, n)$  can be found between the variational results from the  $D_2^{M=1}$  and  $D_2^{M=16}$  ansätze. Interestingly,  $P_{ca}(t, n)$  obtained from the HEOM method in Fig. 5.1(c) is almost identical to that by the  $D_2^{M=16}$  ansatz in Fig. 5.1(b). Furthermore, the difference in the time evolution of the carrier probability

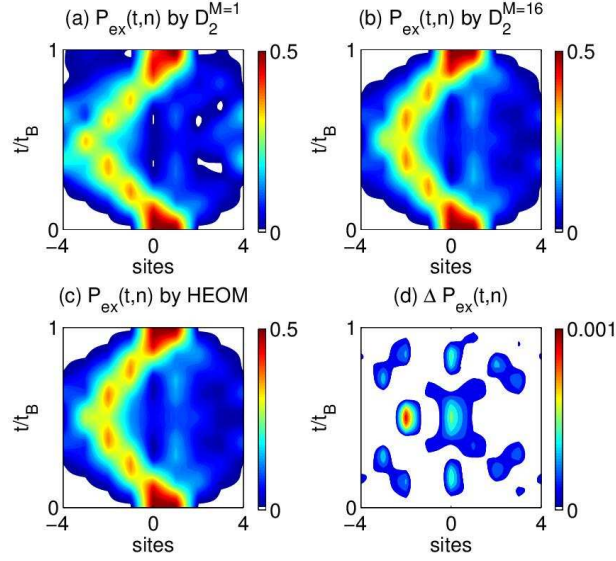


**Figure 5.1** Time evolution of the carrier probability  $P_{ca}(t, n)$  for a diagonal coupling case of  $J = 0.1, g = 0.28$  and  $F = 0.1$  is obtained from (a) the single  $D_2^{M=1}$  ansatz, (b) the  $D_2^{M=16}$  ansatz, and (c) the HEOM method. The difference  $\Delta P_{ca}(t, n)$  between the HEOM and the  $D_2^{M=16}$  trial state is displayed in (d). The time unit  $t_B$  denotes the time period of BOs.  $N = 8$  is used in the calculations.

between the variational and HEOM methods,  $\Delta P_{ca}(t, n)$ , as displayed in Fig. 5.1(d), is two orders of magnitude smaller than the value of  $P_{ca}(t, n)$ , indicating that the variational dynamics of the Holstein polaron under the external field can be numerically exact if the multiplicity  $M$  of the multi- $D_2$  ansatz is sufficiently large.

It should be noted that the HEOM method is numerically expensive and thus impractical when the system size is large, while time dependent variational approaches are still valid to treat the polaron dynamics for large systems once a proper trial wave function is adopted.

### 5.2.2 Off-diagonal Coupling

The discussion is then extended to off-diagonal coupling case, which is a formidable problem due to the intrinsic difficulties in achieving reliable results. The off-diagonal coupling was emphasized as modulations of electron-electron interactions by ion

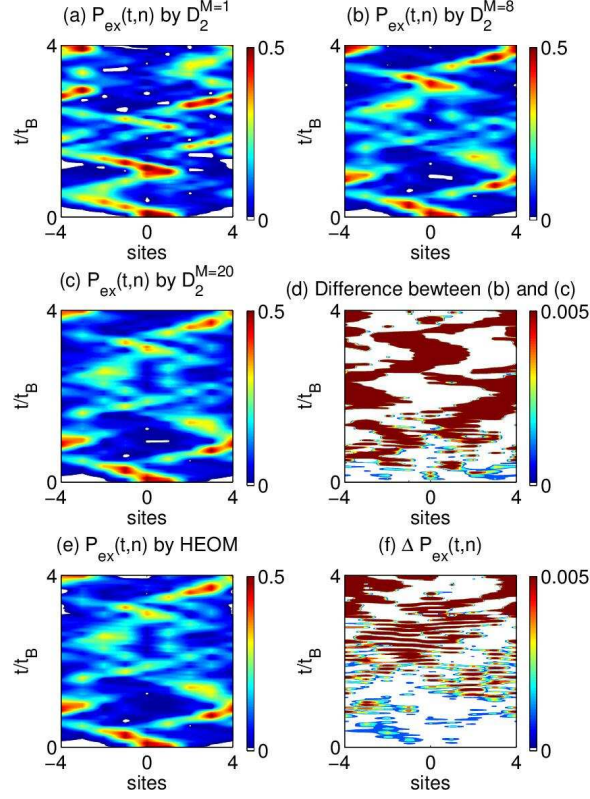


**Figure 5.2** Time evolution of the carrier probability  $P_{ca}(t, n)$  for a off-diagonal coupling case of  $J = 0.1$ ,  $\phi = 0.28$  and  $F = 0.1$  is obtained from (a) the  $D_2^{M=1}$  ansatz, (b) the  $D_2^{M=8}$  ansatz, (c) the  $D_2^{M=20}$  ansatz, and (e) the HEOM method. (d) The difference between the  $D_2^{M=8}$  and  $D_2^{M=20}$  ansätze and (f)  $\Delta P_{ca}(t, n)$  between the HEOM and the  $D_2^{M=20}$  ansatz are displayed.

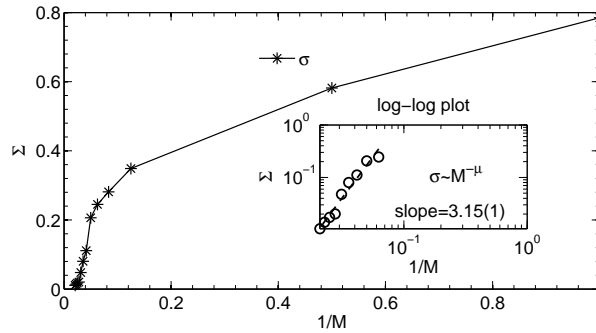


**Figure 5.3** Relative deviation  $\Sigma$  from the multi- $D_2$  ansatz is displayed as a function of  $1/M$  with parameters  $J = 0.1$ ,  $\phi = 0.28$  and  $F = 0.1$ . The inset reveals the relationship  $\Sigma \sim M^\mu$  on a log-log scale, where the dashed line represents a power-law fit.

vibrations in Mahan's celebrated textbook on many-particle physics [28]. Due to a lack of dependable solutions, a complete understanding of out-of-equilibrium dynamics for off-diagonal coupling remains elusive. A validity check of the variational method will be carried out in the following.

Dynamics of the Holstein polaron with off-diagonal coupling under a constant external field is examined by using the multi- $D_2$  ansatz with different multiplicity  $M$ . As shown in Figs. 5.2(a)-(c) and (e), the time evolution of the carrier probability  $P_{ca}(t, n)$  is obtained by the  $D_2^{M=1}$ ,  $D_2^{M=8}$ ,  $D_2^{M=20}$  ansätze and the HEOM method, respectively. Figs. 5.2(b),(c) and (e) display quite similar patterns and all three are largely different from Fig. 5.2(a). Difference between  $P_{ca}(t, n)$  obtained by the  $D_2^{M=8}$  and  $D_2^{M=20}$  ansatz as shown in Fig. 5.2(d) is two orders of magnitude smaller than the value of  $P_{ca}(t, n)$ , pointing to the nearly converged results already obtained by  $M = 8$ . Moreover, the difference in  $P_{ca}(t, n)$  between the  $D_2^{M=20}$  ansatz and the HEOM method,  $\Delta P_{ca}(t, n)$ , as depicted in Fig. 5.1(f), is also two orders of magnitude smaller than the value of  $P_{ca}(t, n)$ , showing the superior accuracy of the multi- $D_2$  ansatz.

In addition, a quantity named the relative deviation  $\Sigma$  (the relative deviation is denoted by  $\Sigma$  instead of  $\sigma$  in this chapter because  $\sigma$  is used for standard deviation of the carrier wave packet) is also used to test the validity of the time-dependent variational approach by quantifying how closely the trial state follows the Schrödinger equation, as depicted in Fig. 5.3. As the multiplicity  $M$  increases, the relative deviation  $\Sigma$  decreases and approaches zero as  $M$  goes to infinity. This is supported by the relationship  $\Sigma \sim M^{-\mu}$  with an exponent of  $\mu = 3.15(1)$  in the inset of Fig. 5.3. Therefore, in the limit of large  $M$ , the variational method using the multi- $D_2$  ansatz provides a numerically exact solution to the Schrödinger equation in the presence of the external field.

### 5.3 Anti-adiabatic regime

The effect of a bosonic environment on BOs, i.e., BOs in a polaron framework, is further investigated in this section. As usually envisioned for electronic transport in crystals, motion of electrons is occasionally scattered by lattice vibrations [29]. Pronounced modulations of the four-wave mixing signal with characteristics of the temporal periodicity of BOs has been detected experimentally in an optical investigation of BOs in a semiconductor superlattice, and can be attributed to lattice scattering [30]. Bouchard *et al.* excluded interband transitions from being responsible for the signal modulations and confirmed the single-band model as an appropriate approximation [31]. Several pioneering theoretical studies also demonstrated the modulations of BOs by the electron-phonon interaction [29, 32, 33]. Despite tremendous experimental and theoretical efforts dedicated to the phonon modulated BOs, the underlying mechanisms are still not well understood.

To be specific, both the acoustic and optical phonons have been experimentally revealed to coexist in the semiconductor superlattice [34], and amplitudes of carrier wave packets has been confirmed to be very sensitive to the precise excitation conditions in a weak external field [21]. However, there is a lack of investigation on BOs dynamics influenced by the two phonon branches when the carrier starts from a Gaussian wave packet with varying widths.

This section will focus on dynamic properties of the Holstein polaron including the time evolution of the carrier probability and the phonon displacement for weak carrier-phonon coupling subject to a constant external electric field. Two typical scenarios are discussed by considering initial Gaussian wave packets with initial widths  $\sigma_0 = 1$  and  $0.2$ , as shown in Fig. 5.4 and Fig. 5.5, respectively. The initial Gaussian distribution [35] is described as follows

$$\rho(n, t = 0) = \left[ (2\pi)^{1/2} \sigma_0 \right]^{-1} \exp(-n^2/2\sigma_0^2) \quad (5.1)$$

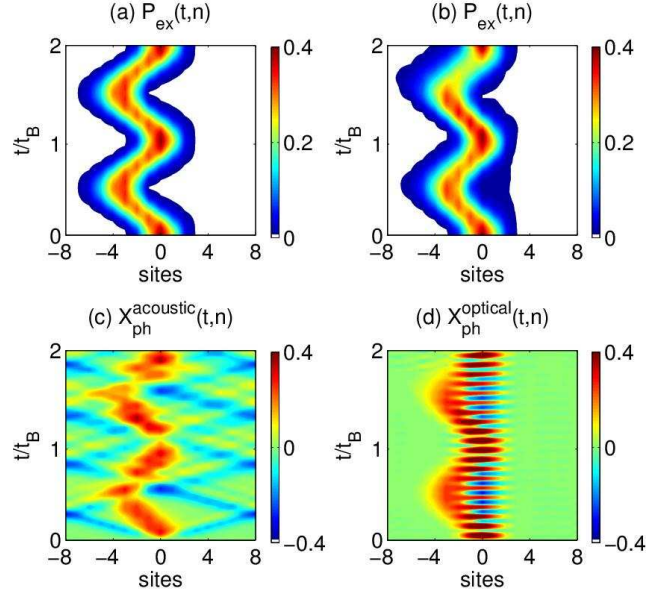


**Figure 5.4** Time evolution of the carrier probability  $P_{\text{ca}}(t, n)$  obtained from the  $D_2^{M=16}$  ansatz in the case of  $J = 0.1$  and  $F = 0.1$  and an initial broad Gaussian wave packet of  $\sigma_0 = 1$  is displayed in (a) ( $g = 0$ ) and (b) ( $g = 0.4$ ). In the presence of weak diagonal coupling ( $g = 0.4$ ), the phonon displacement  $X_{\text{ph}}(t, n)$  is shown for (c) acoustic phonons and (d) optical phonons.

which is centered at site  $n = 0$ , and the associated initial wave function is taken as the square root of the distribution:

$$\psi(n, t = 0) = \left[ (2\pi)^{1/2} \sigma_0 \right]^{-1/2} \exp(-n^2/4\sigma_0^2) \quad (5.2)$$

In particular, the roles played by the acoustic and optical phonons on the carrier transport are explicitly compared under the same external field. It is difficult to partition these branches rigorously [36], and in order to avoid the complexity induced by partitioning these branches, only one phonon branch is included in each separate calculation and the results of two calculations are compared with each other.

The discussion here starts from using an initial broad Gaussian wave packet of  $\sigma_0 = 1$ . Transfer integral  $J = 0.1$  and an external field of  $F = 0.1$  is set in the calculations of this section. In the absence of carrier-phonon coupling, as shown in Fig. 5.4(a), the carrier exhibits typical BOs, with the center of mass of the wave packet oscillates while its



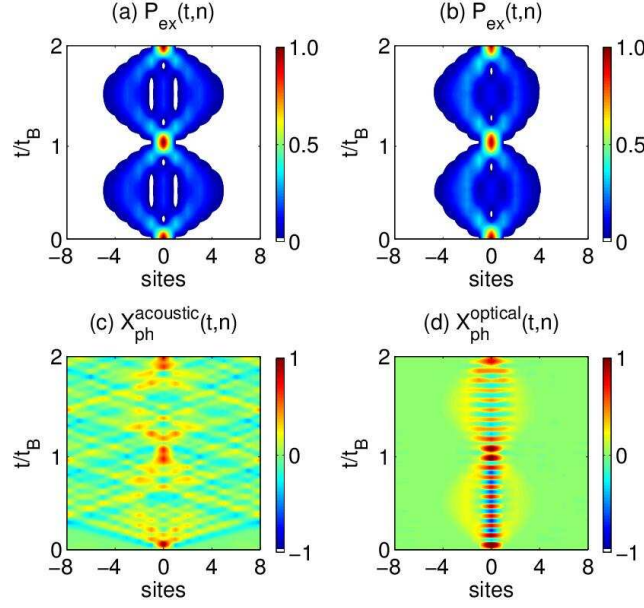


**Figure 5.5** Time evolution of the carrier probability  $P_{\text{ca}}(t, n)$  obtained from the  $D_2^{M=16}$  ansatz in the case of  $J = 0.1$  and  $F = 0.1$  and an initial narrow Gaussian wave packet of  $\sigma_0 = 0.2$  is shown in (a) ( $g = 0$ ) and (b) ( $g = 0.4$ ). The phonon displacement  $X_{\text{ph}}(t, n)$  is shown for (c) the acoustic phonons and (d) optical phonons respectively in the presence of  $g = 0.4$ .

shape is essentially unchanged, in agreement with earlier theoretical work based on an ideal GaAs/ $\text{Al}_x\text{Ga}_{1-x}\text{As}$  superlattice in a uniform electric field as described by a conventional flat-band picture [31, 35]. In the presence of the weak diagonal coupling ( $g = 0.4$ ), the anti-adiabatic regime is emphasized where the phonon frequencies are larger than the transfer integral  $J$ . Only  $P_{\text{ca}}(t, n)$  of optical phonons is shown in Fig. 5.4(b) because the effect of the two phonon branches turned out to be similar. By comparing Figs. 5.4(a) and (b), the time periods of the carrier transport are the same because the temporal periodicity is determined by the external field. This agrees with the experimental observation that the detected signal is found to be modulated over time but the time period of the signal is found to be equal to the temporal periodicity of BOs [30]. The largest oscillation amplitude of the center of mass of the carrier wave packet in Fig. 5.4(a) is in accordance with the theoretical value of  $4J/F$  [37].

Even though the temporal periodicity is preserved after the carrier-phonon coupling is turned on, the spatial periodicity is changed over time. The addition of the carrier-phonon coupling moves the center of mass of the carrier wave packet of  $g = 0$  closer to the initial location, which is in line with the contrast in the mean value  $c(t)$  between  $g = 0$  and 0.4 in Fig. 5.6(a). Not only the motion of the center of mass of the carrier wave packet is changed, but also the width of the wave packet is enlarged as another characteristics of an effect of the weak coupling, giving rise to a broadened wave packet. The width  $\sigma(t)$  in Fig. 5.6(c) is increased due to smearing of the wave packet.

The phonon displacement  $X_{\text{ph}}(t, n)$  is shown in Figs. 5.4(c) and (d) for the acoustic and optical phonons, respectively. Before the carrier creation at  $t = 0$ , the phonons are in their vacuum states for both scenarios. By comparing the two figures, parts of  $X_{\text{ph}}(t, n)$  (red and yellow) are found to propagate with BOs frequency  $\omega_B$  because they are generated by the moving carrier wave packet and would in turn smear out the carrier wave fronts. As for the remainder of  $X_{\text{ph}}(t, n)$  (blue), a V-shaped feature and an oscillatory component with the phonon frequency  $\omega_0$  are respectively found in Figs. 5.4(c) and (d). Moreover, the existence of ten peaks in one Bloch period  $t_B$  can be attributed to the ratio  $\omega_0/\omega_B$  (phonon frequency  $\omega_0$  over BOs frequency). In the presented cases,  $\omega_0$  is ten times of  $\omega_B = de|F|/\hbar$ , where  $d$  is the lattice constant,  $e$  is the charge of the carrier, and  $d = e = \hbar = 1$  is set. Meanwhile, the weak coupling affects the transport and the carrier current in Fig. 5.6(e). At zero coupling, the carrier current  $j(t)$  in the case of an initial broad Gaussian wave packet is  $j(t) = 2 \sin Ft$  with the largest amplitude among all cases studied. The amplitude of the carrier current is decreased after the coupling is switched on, mitigating unidirectional carrier transport.

Next, this study considers the effect the weak carrier-phonon coupling on the dynamics with an initial narrow Gaussian wave packet of  $\sigma_0 = 0.2$ . As shown in Fig. 5.5(a), the carrier undergoes a symmetric breathing mode at zero coupling. The carrier wave packet propagates with its center of mass fixed at the original location and its width oscillates with the Bloch period, in accord with previous studies on the breathing mode [21, 31, 38]. After

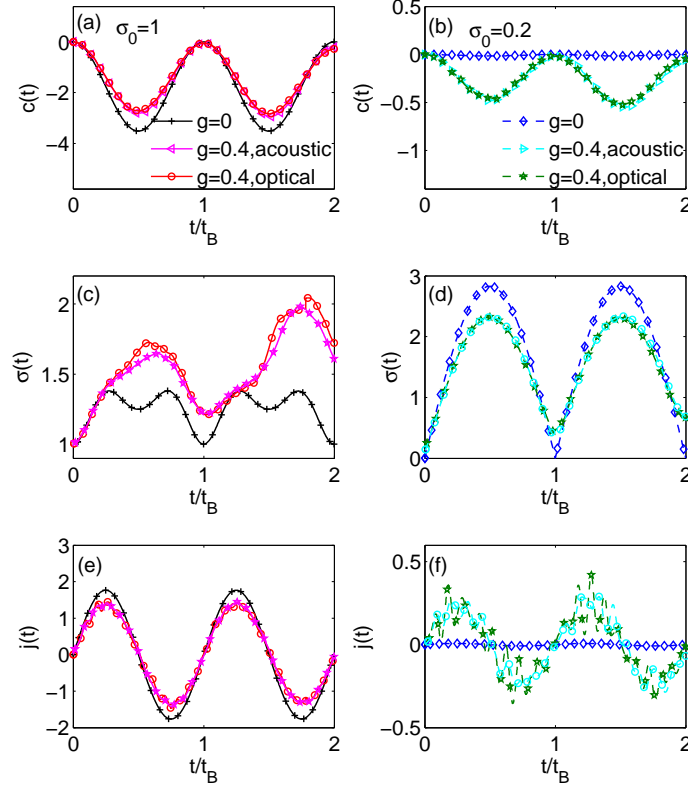


**Figure 5.6** (a) Mean value  $c(t)$ , (c) standard deviation  $\sigma(t)$  and (e) current  $j(t)$  as functions of the time  $t$  in the case of  $J = 0.1$  are displayed using the initial standard deviation  $\sigma_0 = 1$  and (b),(d),(f) using  $\sigma_0 = 0.2$ , respectively. In each panel, the results with  $g = 0$  and  $g = 0.4$  are compared.

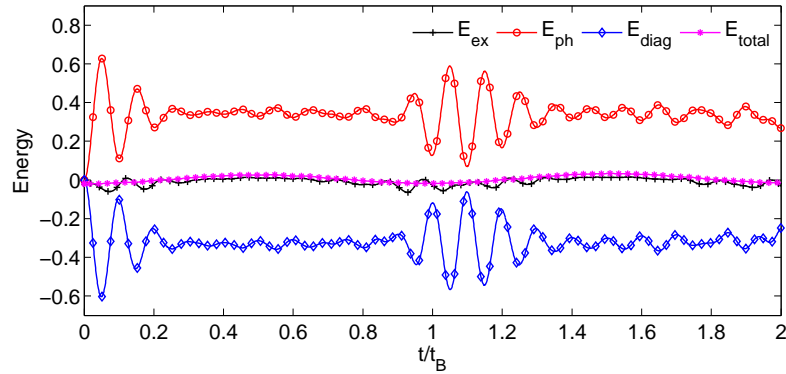


**Figure 5.7**  $E_{ca}(t)$ ,  $E_{ph}(t)$ ,  $E_{diag}(t)$  and  $E_{diag}(t)$  obtained by the  $D_2^{M=16}$  ansatz in the case of  $J = 0.1$ ,  $F = 0.1$  and  $\sigma_0 = 0.1$  in the presence of weak diagonal coupling ( $g = 0.4$ ) with the optical phonons.

the addition of the weak diagonal coupling  $g = 0.4$ , the carrier amplitude becomes larger in the left branch than that in the right branch (Fig. 5.5(b)) and the center of mass of the carrier wave packet is moved away from the original location. These features of the carrier indicate that the symmetry of the breathing mode is broken by even minute carrier-phonon interactions, and are further reflected by the mean value  $c(t)$  plotted in Fig. 5.6(b), which oscillates for the weak coupling case of  $g = 0.4$  in contrast to being zero at all times for  $g = 0$ . Recently, the breakdown of the breathing mode has been confirmed in semiconductor superlattices [39] and cold atoms trapped in optical lattice [40–42], making the results here highly relevant in the study of breathing modes in those systems. Furthermore, the width of the carrier wave packet for the weak coupling case of  $g = 0.4$  is reduced in comparison to that for  $g = 0$ , as depicted in Fig. 5.6(d). A comparison between Figs. 5.6(c) and (d) reveals that weak diagonal coupling has opposite influences on the width of the carrier wave packet: the carrier wave packet is broadened in the case of  $\sigma_0 = 1$  while that in the case of  $\sigma_0 = 0.2$  is suppressed after the carrier-phonon coupling is switched on.

Similar to the scenario of  $\sigma_0 = 1$ , the phonon displacement  $X_{\text{ph}}(t, n)$  of  $\sigma_0 = 0.2$  propagates along with the movement of the carrier. As shown in Fig. 5.5(c),  $X_{\text{ph}}(t, n)$  maintains its V-shaped feature in the case of acoustic phonons. As for Fig. 5.5(d), characteristic oscillations with frequency  $\omega_0$  is found in the case of optical phonons. Reciprocally, the generated  $X_{\text{ph}}(t, n)$  induces smearing of the carrier in its center. A brief comparison between Fig. 5.4 and Fig. 5.5 reveals that the carrier triggered phonon displacement leads to the weakening of the carrier wave packet in its center and edge, respectively. As shown in Fig. 5.6(f), the current in the zero coupling case is zero due to the spatial symmetry of the carrier wave packet. The carrier current in the weak coupling exhibits fast beating with the characteristic frequency  $\omega_0$  superimposed by slower BOs.

So far, this work has focused on the impact of weak carrier-phonon coupling on the quantum transport with respect to the two typical scenarios. In general, BOs are very sensitive to any kind of dephasing generated by the electron-hole Coulomb interaction effects or lattice imperfections, since they rely on the coherent reflection of waves [42].

The electron-hole Coulomb interaction is pointed out to destroy the breathing mode by Dignam *et al.* after they examined the nature of the carrier wave packets in undoped semiconductor superlattices in a uniform along-axis electric field [39]. The effects of atom-atom interactions in the dilute BEC trapped in a periodic potential were actively studied using a discrete nonlinear Schrödinger equation (DNLSE), and the atom-atom interactions can result in the decoherence of atomic BOs [40, 43, 44] and enhancement or suppression of the breathing width [41, 42]. To the best of our knowledge, this work is the first investigation on the influence of the carrier-phonon interaction on both the typical BOs and the breathing mode.

Finally, the characteristics of the nonequilibrium dynamics of the ring system is analyzed, including a comparison with the steady state of an infinite linear chain. First of all, in the absence of an external electric field, in the anti-adiabatic limit of  $\omega_0 \gg J$ , carrier dynamics in both weak and strong coupling regimes is dominated by coherent oscillations and negligible energy transfer, leaving a conserved total energy [45]. After the an external field is applied, the total energy is not conserved as plotted in Fig. 5.7 because of the addition of the extra energy acquired from the external field. Secondly, a steady state with a saturated current can be obtained in a linear chain that extends to infinity in both directions, where the carrier acquires kinetic energy from the applied field while dissipating its energy by a net emission of optical phonons [29]. Being a steady state situation, the expectation value of the rate of change of electron momentum is zero, and the steady state is left with an equation which balances the applied field, or rate of increase of electron momentum, against the rate of loss of momentum due to the lattice scattering. This result is an explicit field dependence in terms of the steady-state velocity of the electron. The key feature of the steady state is also explored in Ref. [32]. Equivalently, the condition of the steady state can be that there exist linear regimes of the total energy and phonon energy following the equality of  $dE_{\text{total}}/dt = dE_{\text{ph}}/dt$  [32], meaning that the total energy gain is entirely absorbed by the lattice. Specifically, with increasing time  $t$ , the total energy vs time approaches a straight line, and the phonon energy has a linear time dependence as well. But in the ring system, the condition of the steady state can not be

met as this equation can not be satisfied from the curves of  $E_{\text{total}}$  and  $E_{\text{ph}}$  as shown in Fig. 5.7. For example, the value of  $dE_{\text{ph}}/dt$  at  $t = 2t_B$  is not equal to but 9 times of the value of  $dE_{\text{total}}/dt$ . The energy imported by the external field can not cancel out the energy emitted to the phonons, leaving the carrier energy oscillates over time. Thus, the electron's acceleration in the ring can no longer be balanced out by the lattice's deceleration and the electron can not drift with a saturated velocity. Consequently, no saturated constant current is found in the anti-adiabatic regime for the small ring systems, and steady states in the adiabatic regime will be investigated elsewhere.

To sum up, weak carrier-phonon coupling in the anti-adiabatic regime breaks the spatial periodicity but retains the temporal periodicity of both the typical BOs and the breathing mode. The carrier movement shows similar features in spite of the difference between the acoustic and optical phonon branches. In fact, in a weak external field, when diagonal coupling is strong between the carrier and both the acoustic and optical phonons, the carrier become localized, leading to the diminishing of the typical BOs and the breathing mode. The localization is similar to that in the moderate external field cases in the next section, therefore the details are not shown. It is also shown that no saturated constant current is found in the ring system for the duration of the simulation.

#### 5.4 Strong diagonal coupling

This section presents a general picture of the carrier wave packet evolution in the regime of the strong diagonal coupling. The carrier wave packets and the carrier currents are firstly investigated under a moderate external field of  $F = 1$ . The time evolution of the carrier probability  $P_{\text{ca}}(t, n)$  for different diagonal coupling strengths  $g = 0, 3$  and  $4$  is illustrated in Figs. 5.8(a), (b) and (c), respectively. The carrier is created on two nearest neighbouring sites.  $J = 1$  and  $N = 16$  are set. As shown in Figs. 5.8(a)-(c), the bare carrier exhibits a partially BOs pattern, while the strong carrier-phonon coupling is found to localize the carrier to the initial excitation sites. BOs are largely quenched due to strong carrier-phonon coupling [46]. This behaviour is also demonstrated in Fig. 5.8(d), which

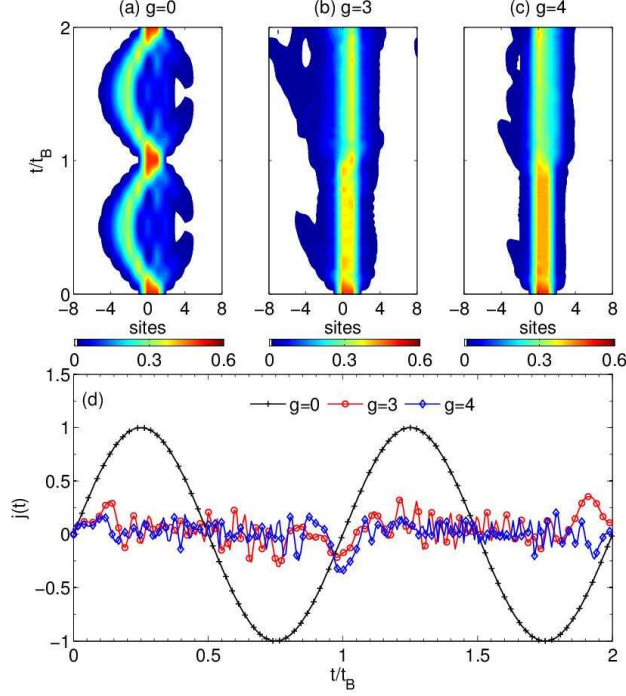


**Figure 5.8** Time evolution of the carrier probability  $P_{ca}(t, n)$  obtained from the  $D_2^{M=16}$  ansatz in the case of  $J = 1$ ,  $N = 16$  and a moderate external field of  $F = 1$  is displayed for different diagonal coupling strengths: (a)  $g = 0$ , (b)  $g = 3$  and (c)  $g = 4$ . Corresponding currents  $j(t)$  are shown in (d).

shows that the amplitude of the carrier current decreases with increasing carrier-phonon coupling and fluctuates around zero.

This section then discusses the case of a strong external field. Using the same parameters as the case of  $F = 1$ , the time evolution of the carrier probability  $P_{ca}(t, n)$  and carrier current  $j(t)$  under a strong field of  $F = 70$  are presented in Figs. 5.9(a)-(c) and Fig. 5.9(d), respectively. Due to the strong external field, the carrier is found to be localized at the initial site of excitation irrespective of the carrier-phonon coupling strength. A bare carrier case is shown in Fig. 5.9(a) for comparison. The localization of the carrier wave packet can be rationalized in terms of Wannier-Stark states [4]. In the Wannier representation, the Wannier-Stark states are denoted as  $|\Psi_n\rangle = \sum_m J_{m-n}(\gamma)|m\rangle$ , where  $J_{m-n}(\gamma)$  is the Bessel function of order  $m - n$  with  $\gamma = 2J/Fd$  [37]. Due to

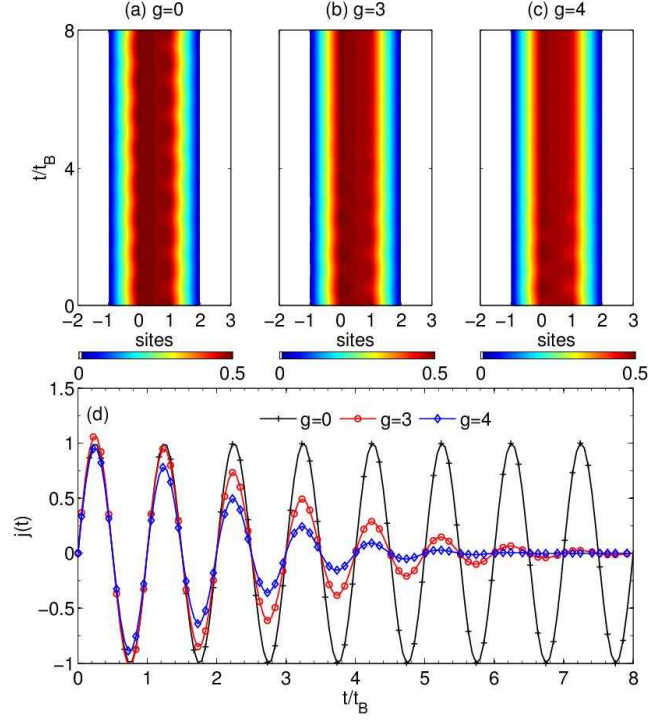


**Figure 5.9** Time evolution of the carrier probability  $P_{ca}(t, n)$  obtained from the  $D_2^{M=16}$  ansatz in the case of  $J = 1, N = 16$  and a strong external field of  $F = 70$  is displayed for different diagonal coupling strengths: (a)  $g = 0$ , (b)  $g = 3$  and (c)  $g = 4$ . Corresponding currents  $j(t)$  are shown in (d).

properties of the Bessel functions, the Wannier-Stark states extend over the interval  $L \simeq 2J/F$ , which leads to well localized states in the limit of a strong external field [47]. As shown in Figs. 5.9(b) and (c), strong carrier-phonon coupling leads to the decay of BOs. The carrier currents in the presence of strong carrier-phonon coupling exhibits damped oscillations with a time scale of  $8t_B$  ( $6t_B$ ) for  $g = 3$  (4).

In summary, the impact of diagonal and off-diagonal carrier-phonon coupling on polaron dynamics in a ring system is investigated in the presence of a constant electric field using the multiple Davydov  $D_2$  trial state with the Dirac-Frenkel variational principle. Accuracy of the method is verified by the comparison with benchmark calculations obtained from the numerically exact HEOM method [26, 27] which is also firstly used in this work to deal with field-driven cases to the best of our knowledge. The



validity of the variational method is also carefully examined by quantifying how faithfully our result follows the Schrödinger equation in balance with the computational efficiency. For weak carrier-phonon coupling in the anti-adiabatic regime, both acoustic and optical phonons are considered, and the time evolution of various quantities is calculated with special attention paid to the effect of weak dissipation on the spatial amplitudes of BOs using different initial conditions. Finally, the variational method using the multi- $D_2$  ansatz is used to treat the strong diagonal coupling, which is a formidable challenge for the HEOM method, but remains numerically affordable by the variational approach.

## References

- [1] F. Bloch, *Zeitschrift Für Phys.*, **1928**, 52, 555.
- [2] C. Zener, *Proc. R. Soc. A*, **1934**, 145, 523.
- [3] J. N. Churchill and F. E. Holmstrom, *Phys. Scr.*, **1983**, 27, 91-98.
- [4] G. H. Wannier, *Phys. Rev.*, **1960**, 117, 432.
- [5] W. V. Houston, *Phys. Rev.*, **1940**, 57, 184.
- [6] M. Holthaus and D. W. Hone, *Phil. Mag. B.*, **1996**, 74, 105.
- [7] H. Fukuyama, R. A. Bari and H. C. Fogedby, *Phys. Rev. B.*, **1973**, 8, 5579.
- [8] T. Dekorsy, A. Bartels, H. Kurz, K. Köhler, R. Hey, and K. Ploog, *Phys. Rev. Lett.*, **2000**, 85, 1080.
- [9] A. W. Ghosh, L. Jönsson, and J. W. Wilkins, *Phys. Rev. Lett.*, **2000**, 85, 1084.
- [10] A. Johansson and S. Stafström, *Phys. Rev. Lett.*, **2001**, 86, 3602.
- [11] D. M. Basko and E. M. Conwell, *Phys. Rev. Lett.*, **2002**, 88, 056401.
- [12] A. A. Johansson and S. Stafström, *Phys. Rev. B*, **2004**, 69, 235205.
- [13] Y. Qui and L.-P. Zhu, *J. Chem. Phys.*, **2009**, 131, 134903.

- [14] M. Peyrard and A. R. Bishop, *Phys. Rev. Lett.*, **1989**, 62, 2755.
- [15] E. Diaz, R. P. A. Lima, and F. Domínguez-Adame, *Phys. Rev. B*, **2008**, 78, 134303.
- [16] S. V. Rakhmanova and E. M. Conwell, *Appl. Phys. Lett.*, **1999**, 75, 1518.
- [17] I. A. Dmitriev and R. A. Suris, *Semiconductors*, **2001**, 35, 212.
- [18] P.M. Petroff, A. Lorke, and A. Imamoglu, *Phys. Today.*, **2001**, 54, 46.
- [19] W. Zhang, A. O. Govorov, and S. E. Ulloa, *Phys. Rev. B*, **2002**, 66, 134302.
- [20] A. K. C. Cheung and M. Berciu, *Phys. Rev. B*, **2013**, 88, 35132.
- [21] V. G. Lyssenko, G. Valusis, F. Löser, T. Hasche, K. Leo, M. M. Dignam, and K. Köhler, *Phys. Rev. Lett.*, **1997**, 79, 301.
- [22] M. Sudzius, V. G. Lyssenko, F. Löser, K. Leo, M. M. Dignam, and K. Köhler, *Phys. Rev. B*, **1998**, 57, R12693.
- [23] V. Coropceanu, J. Cornil, D. S. Filho, Y. Olivier, R. Silbey, and J. Bredas, *Chem. Rev.*, **2007**, 107, 926.
- [24] H. Tamura, M. Tsukada, H. Ishii, N. Kobayashi, and K. Hirose, *Phys. Rev. B*, **2012**, 86, 35208.
- [25] Å. Johansson, and S. Stafström, *Phys. Rev. B*, **2002**, 65, 045207.
- [26] Y. Tanimura, R. Kubo, *J. Phys. Soc. Jpn*, **1989**, 58, 101.
- [27] L. Chen, Y. Zhao, and Y. Tanimura, *J. Phys. Chem. Lett.*, **2015**, 6, 3110.
- [28] G. D. Mahan, *Many-Particle Physics* (Kluwer Academic/Plenum, New York, 2000).
- [29] K. K. Thornber and R. P. Feynman, *Phys. Rev. B*, **1970**, 1, 4099.
- [30] J. Feldmann, K. Leo, J. Shah, D. A. B. Miller, J. E. Cunningham, T. Meier, G. von Plessen, A. Schulze, P. Thomas and S. Schmitt Rink, *Phys. Rev. B*, **1992**, 46, 7252.

- [31] A. M. Bouchard and M. Luban, *Phys. Rev. B*, **1995**, 52, 5105.
- [32] L. Vidmar, J. Bonca, M. Mierzejewski, and P. Prelovsek, and S. A. Trugman, *Phys. Rev. B*, **2002**, 83, 134301.
- [33] V. D. L. N. S. Fialko, *JETP Lett.*, **2004**, 79, 575.
- [34] E. Molinari and A. Fasolino, *Superlattices Microstruct.*, **1988**, 4, 449.
- [35] J. Stockhofe and P. Schmelcher, *Phys. Rev. A*, **2015**, 91, 023606.
- [36] Y. Yi, V. Coropceanu, and J.-L. Bredas, *J. Chem. Phys.*, **2012**, 137, 164303.
- [37] T. Hartmann, F. Keck, H. J. Korsch, and S. Mossmann, *New J. Phys.*, **2004**, 6, 2.
- [38] F. Domínguez-Adame, *Eur. J. Phys.*, **2010**, 31, 639.
- [39] M. Dignam, J. E. Sipe, and J. Shah, *Phys. Rev. B*, **1994**, 49, 10502.
- [40] A. Trombettoni and A. Smerzi, *Phys. Rev. Lett.*, **2001**, 86, 2353.
- [41] C. Gaul, R. P. A. Lima, E. Diaz, C. A. Müller, and F. Domínguez-Adame, *Phys. Rev. Lett.*, **2009**, 102, 255303.
- [42] C. Gaul, E. Diaz, R. P. A. Lima, F. Domínguez-Adame, and C. A. Müller, *Phys. Rev. A*, **2011**, 84, 053627.
- [43] A. R. Kolovsky, H. J. Korsch, and E.-M. Graefe, *Phys. Rev. A*, **2009**, 80, 023617.
- [44] A. R. Kolovsky, E. A. Gomez, and H. J. Korsch, *Phys. Rev. A*, **2010**, 81, 025603.
- [45] F. Dorfner, L. Vidmar, C. Brockt, E. Jeckelmann, and F. Heidrich-Meisner, *Phys. Rev. B*, **2015**, 91, 104302.
- [46] V. D. Lakhno and A. N. Korshunova, *Eur. Phys. J. B*, **2007**, 55, 85.
- [47] D. Emin and C. F. Hart, *Phys. Rev. B*, **1987**, 36, 2530.



## Chapter 6\*

### Dynamics of intramolecular singlet fission

*A non-perturbative treatment, the Dirac-Frenkel time-dependent variational approach is adopted using the multiple Davydov  $D_2$  ansatz to study dynamics of intramolecular singlet fission. It is shown that both diagonal and off-diagonal coupling can aid efficient singlet fission if excitonic coupling is weak, and fission is only facilitated by diagonal coupling if excitonic coupling is strong. In the presence of off-diagonal coupling, it is found that high frequency modes create additional fission channels for rapid iSF. Results presented here may help provide guiding principles for design of efficient singlet fission materials by directly tuning singlet-triplet interstate coupling.*

---

\* This chapter published substantially as Z. Huang, Y. Fujihashi, and Y. Zhao, *J. Phys. Chem. Lett.*, **8**, 3306 (2017).

## 6.1 Introduction

iSF materials provide remarkable advantages in terms of tunable electronic structures as discussed in Subsec. 2.2.3 of Chapter 2, and quantum chemistry studies have indicated strong electronic coupling modulation by high frequency phonon modes. However, a limited understanding of detailed xSF and iSF mechanisms hinders the design of versatile SF materials. In particular, a unified theoretical treatment of phonon effects remains elusive. The phonon effects on the electronic properties of the SF materials can be realized via exciton-phonon interaction. In detail, the diagonal exciton-phonon coupling is referred to fluctuations in electronic energies induced by molecular vibrations, and the off-diagonal coupling corresponds to vibrational modulations of electronic coupling between the singlet and triplet pair state. Both diagonal and off-diagonal coupling have been found to be tunable in novel iSF materials by changing linkers and by engineering the dihedral angle between the chromophore units and the linker [1–3]. However, there is a lack of discussion in the literature on detailed SF mechanisms under the influence of simultaneous diagonal and off-diagonal exciton-phonon coupling.

In this chapter, Dirac-Frenkel time-dependent variational principle with the multi- $D_2$  ansatz will be employed to explore effects of off-diagonal coupling on iSF dynamics. This chapter adopts the microscopic model of iSF with simultaneous diagonal and off-diagonal coupling to high-frequency modes, as proposed in Subsec. 3.3.3 of Chapter 3. The reminder of the chapter is structured as follows. The variational results are checked by examining its deviations from the exact quantum dynamics in Sec. 6.2. Population dynamics of the singlet state is given in Sec. 6.3. Impacts of exciton-phonon coupling on SF are studied in Subsec. 6.3.1. Effects of exciton-phonon coupling on SF dynamics are investigated in Subsec. 6.3.2.

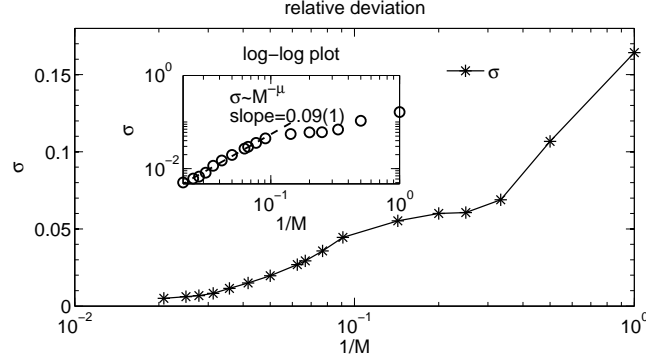


**Figure 6.1** The relative deviation  $\sigma$  of the multi- $D_2$  ansatz is displayed as a function of  $1/M$ . The parameters are set to be  $\hbar\omega_{\text{diag}} = 90$  meV,  $\hbar\omega_{\text{vib2}} = 65$  meV,  $J_{S_1,TT} = 20$  meV,  $\epsilon_{S_1,g} - \epsilon_{TT,g} = 100$  meV,  $\gamma_{\text{diag}}^{-1} = \gamma_{\text{o.d.}}^{-1} = 1$  ps,  $S_{S_1} = 0.7$ ,  $S_{TT} = 1.4$  and  $S_{S_1,TT}^{\text{off}} = 0.1$ .

## 6.2 Validity of variational dynamics for the singlet fission process

Firstly, the accuracy of the multi- $D_2$  ansatz is tested with parameters for realistic models. The relative deviation  $\sigma$  (Eq. 3.10) is used to quantify how faithfully the result follows the Schrödinger equation. As shown in Fig. 6.1, the largest relative deviation  $\sigma$  is found for the single  $D_2$  ansatz, and the relative deviation  $\sigma$  decreases and goes to zero as the multiplicity  $M$  approaches infinity. The log-log plot of  $(\sigma, 1/M)$  (inset) indicates a power-law relationship with an exponent of  $\mu$ , further inferring a numerically exact solution in the limit of  $M \rightarrow \infty$ .

In order to further support the accuracy of the results obtained by the variational approach, the zero-temperature dynamics obtained by the multi- $D_2$  ansatz is compared with the multilevel Redfield results at  $T = 1K$ . As show in Fig 6.2, the population dynamics calculated by the  $D_2^{M=5}$  ansatz is in quantitative agreement with the multilevel Redfield results, yielding a much more accurate result than that with the single  $D_2$  ansatz. In addition, the relative deviation  $\sigma$  in this case is smaller than 0.1, small enough to guarantee the accuracy of the result by the multi- $D_2$  ansatz. From the viewpoint of theoretical analysis, these calculated results satisfy the energy matching condition  $(\nu - 0.7) \hbar\omega_{\text{diag}} = 50$  meV in the case of  $\nu = 2$ , which is obtained from the Fermi golden

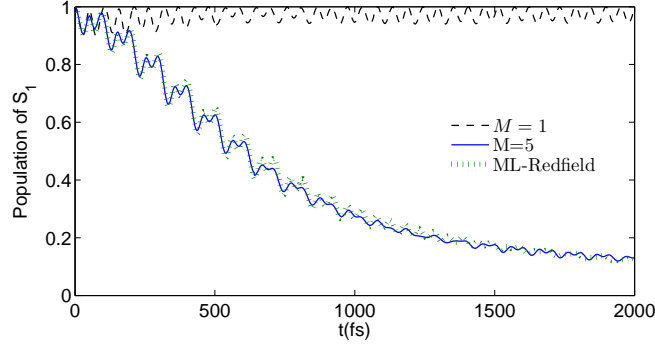


**Figure 6.2** Time evolution of singlet population calculated by the multilevel Red-field approach at  $T = 1K$  and the multi- $D_2$  ansatz at  $T = 0K$ . The frequency of the phonon mode is set to be  $\hbar\omega_{\text{diag}} = 40$  meV,  $\hbar\omega_{\text{o.d.}} = 0$  meV. The other parameters are fixed at  $J_{S_1,TT} = 10$  meV,  $\epsilon_{S_1,g} - \epsilon_{TT,g} = 50$  meV,  $\gamma_{\text{diag}}^{-1} = \gamma_{\text{o.d.}}^{-1} = 1$  ps,  $S_{S_1} = 0.7$ ,  $S_{TT} = 1.4$ .

formula at the zero temperature limit and the slow vibrational relaxation limit, namely,  $\gamma_{\text{diag}} \rightarrow 0$ ,

$$k_{TT \leftarrow S_1} = \sum_{v=0}^{\infty} \frac{1}{\hbar^2} (J_{S_1,TT} \langle \chi_0^{S_1} | \chi_0^{TT} \rangle)^2 \times \delta(\epsilon_{S_1,g} - \lambda_{S_1,g} - \epsilon_{TT,g} + \lambda_{TT,g} - \nu \hbar\omega_{\text{diag}}) \quad (6.1)$$

where  $|\langle \chi_0^{S_1} | \chi_0^{TT} \rangle|^2$  is the Frank-Condon factor associated with the vibronic transition from the 0-th vibrational level on the  $S_1$  to the  $\nu$ th vibrational level on  $TT$  [4]. Thus for the case shown in Fig. 6.2, the transition from  $S_1$  to  $TT$  is driven by the phonon mode at around  $\hbar\omega_{\text{diag}} = 40$  meV satisfying the condition in which the energy of  $S_1$  including the vibrational energy matches its counterpart in the  $TT$  state.

### 6.3 Population Dynamics

This section presents and discusses numerical results regarding iSF dynamics in the dimer model. A simple dimer model including two excitonic states  $S_1$  and  $TT$  is adopted, and the focus is on the effect of two intramolecular vibration modes, one of which is diagonally coupled ( $\hbar\omega_{\text{diag}}$ ) to the exciton states, and the other, off-diagonally coupled ( $\hbar\omega_{\text{o.d.}}$ ). A Huang-Rhys factor of 0.7 is chosen for  $S_1$ , which is estimated from fitting measured absorption spectra of acene derivatives with a theoretical spectroscopic model



[5, 6]. It is found that the reorganization energy of TT is several times larger than that of  $S_1$  in pentacene derivatives and tetracenes, and the off-diagonal coupling strength is one order of magnitude smaller than the diagonal coupling strength [7, 8], such that the Huang-Rhys factor of TT is set at  $S_{\text{TT}} = 2S_{S_1}$  throughout this work, and the off-diagonal coupling Huang-Rhys factor  $S_{S_1, \text{TT}}^{\text{o.d.}} = \lambda_{S_1, \text{TT}}^{\text{o.d.}}/(\hbar\omega_{\text{o.d.}})$  is chosen to be 0.1. To be in line with the beating lifetime due to vibrational coherence in 2D electronic spectra of pentacene derivatives [9], the vibrational relaxation rates are set to  $\gamma_{\text{diag}}^{-1} = \gamma_{\text{o.d.}}^{-1} = 1$  ps. As the initial condition for the numerics, only the singlet state is excited according to the Franck-Condon principle. It has been suggested that efficient SF can be achieved by tuning the  $S_1$ -TT interstate coupling and triplet pair splitting independently [10]. As shown in the Hamiltonian (3.28), excitonic coupling  $J_{S_1, \text{TT}}$  determines the direct  $S_1$ -TT coupling. If the frequencies of the vibrational modes  $\omega_{\text{diag}}$  and  $\omega_{\text{o.d.}}$  are high compared with the thermal energy  $k_B T$ , the intramolecular vibrations are thermally inactivated, and the fission dynamics driven by the high frequency modes is temperature independent in a wide temperature range [4]. Thus, in this study, temperature is set to be  $T = 0$  to reduce the numerical cost, although the inclusion of the temperature effect in the multiple Davydov ansatz is straightforward by applying Monte Carlo importance sampling [11].

### 6.3.1 Effect of excitonic coupling on fission dynamic

First attempt is made to a scenario with weak excitonic coupling  $J_{S_1, \text{TT}} = 20$  meV and the transition energy  $\epsilon_{S_1, g} - \epsilon_{\text{TT}, g} = 100$  meV, both of which are typical values for the SF process in pentacene derivatives [7, 9, 12]. As shown in Fig. 6.3(a), the oscillation amplitude of population of  $S_1$  is 0.13 in the absence of exciton-phonon coupling (green line). Despite weak direct coupling, it is suggested that strong mixing between  $S_1$  and TT can be allowed with the assistance of exciton-phonon coupling [1, 13]. In the presence of diagonal exciton-phonon coupling the high frequency phonon modes have been shown to facilitate the efficient SF if excitonic coupling is weak [4]. Here the impact of off-diagonal coupling on SF dynamics is studied. As shown in Fig. 6.3(a), the population of  $S_1$  for  $\hbar\omega_{\text{o.d.}} = 80$  meV, calculated by the  $D_2^{M=3}$  ansatz, decays to 0.4 at long times, signaling

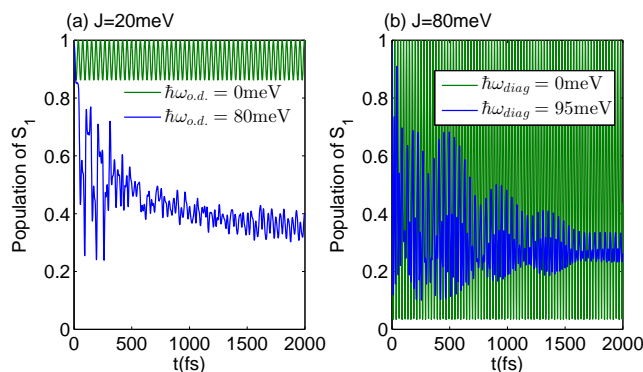


**Figure 6.3** Time evolution of the singlet population for (a) the case of weak excitonic coupling  $J_{S_1,TT} = 20$  meV,  $\epsilon_{S_1,g} - \epsilon_{TT,g} = 100$  meV,  $\hbar\omega_{diag} = 0$  meV, and  $\hbar\omega_{o.d.} = 80$  meV, and (b) the case of strong excitonic coupling  $J_{S_1,TT} = 80$  meV,  $\epsilon_{S_1,g} - \epsilon_{TT,g} = 30$  meV,  $\hbar\omega_{diag} = 95$  meV, and  $\hbar\omega_{o.d.} = 0$  meV. The green lines correspond to cases in the absence of exciton-phonon coupling.

an efficient SF process. For this scenario, the emission of a single off-diagonally coupled phonon can relax the initial singlet excitation to a double triplet state [14]. Consequently, the presence of off-diagonal coupling changes the SF process substantially if excitonic coupling is weak.

Next this section turns to a case with strong excitonic coupling  $J_{S_1,TT} = 80$  meV and transition energy  $\epsilon_{S_1,g} - \epsilon_{TT,g} = 30$  meV, as strong excitonic coupling has been achieved experimentally via interchromophore bridge control in covalently linked tetracene dimers [15]. As shown in Fig. 6.3(b), in the absence of exciton-phonon coupling, the  $S_1$  population exhibits purely Rabi oscillations (green line), due to strong excitonic coupling. If only diagonal exciton-phonon coupling is added, the picture is changed drastically (blue line), and the system becomes trapped in the TT state. This rapid, irreversible decay of the Rabi oscillation in the SF process is owing to dissipation induced by diagonal exciton-phonon coupling, in agreement with decay dynamics in the ultrafast charge transfer process at an oligothiophene-fullerene heterojunction [16, 17]. However, efficient SF is not found under the influence of off-diagonal exciton-phonon coupling if excitonic coupling is strong.

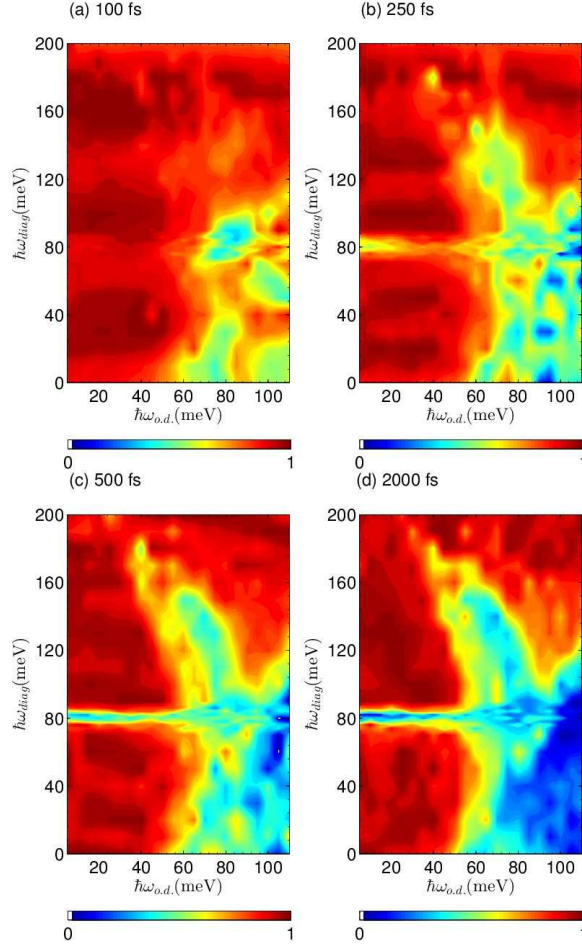


**Figure 6.4** Snapshots of singlet population as functions of  $\hbar\omega_{\text{diag}}$  and  $\hbar\omega_{\text{o.d.}}$  at the time of (a) 100 fs, (b) 250 fs, (c) 500 fs and (d) 2000 fs. The other parameters are  $J_{\text{S}_1, \text{TT}} = 20$  meV and  $\epsilon_{\text{S}_1, \text{g}} - \epsilon_{\text{TT}, \text{g}} = 100$  meV.

### 6.3.2 Effect of exciton-phonon coupling on fission dynamics

In particular, for recently developed iSF materials, such as covalent pentacene and diazadiborane dimers [1, 18, 19], excitonic coupling strength is often smaller than the transition energy, so  $J_{\text{S}_1, \text{TT}} = 20$  meV and  $\epsilon_{\text{S}_1, \text{g}} - \epsilon_{\text{TT}, \text{g}} = 100$  meV is chosen in the iSF dynamics study. Off-diagonal coupling has been found for low-frequency phonon modes in teracene [7, 8, 14], and high-frequency phonon modes in covalent chromophore dimers [1, 18, 19]. In order to further explore effects of off-diagonal coupling on iSF, time evolution of singlet population is examined as functions of  $\hbar\omega_{\text{diag}}$  and  $\hbar\omega_{\text{o.d.}}$ . Fig. 6.4

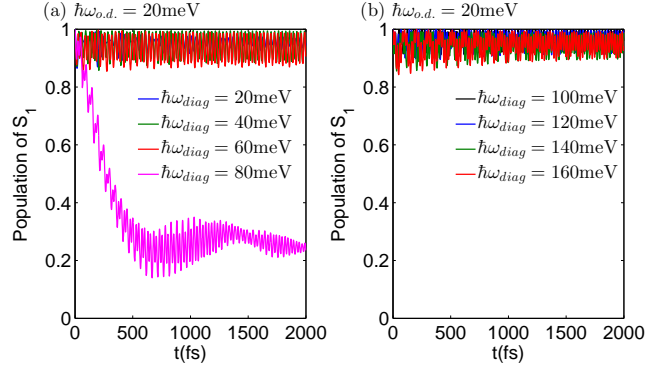


**Figure 6.5** Time evolution of singlet population for the the phonon mode  $\hbar\omega_{o.d.} = 20$  meV diagonally coupled to the  $S_1$  and TT states. The phonon modes off-diagonally coupled are (a)  $\hbar\omega_{diag} = 20, 40, 60$  and  $80$  meV, (b)  $\hbar\omega_{diag} = 100, 120, 140$  and  $160$  meV. The other parameters are same as Fig. 6.4

shows snapshots of singlet population at  $t = 100, 250, 500$ , and  $2000$  fs. On one hand, a single phonon mode of  $\hbar\omega_{diag} = 80$  meV brings about a single efficient channel for SF dynamics in the absence of off-diagonal coupling [4]. On the other hand, Fig. 6.4 clearly exhibits some channels for rapid SF dynamics due to the presence of off-diagonal coupling, despite a complex dependence of efficient SF on  $\hbar\omega_{o.d.}$ . In order to better interpret this dependence, the phase space is divided into three regions,  $5 \leq \hbar\omega_{o.d.} \leq 50$  meV,  $50 < \hbar\omega_{o.d.} \leq 80$  meV, and  $80 < \hbar\omega_{o.d.} \leq 110$  meV.

If  $5 \leq \hbar\omega_{o.d.} \leq 50$  meV, the SF dynamics in Figs. 6.4(c) and 6.4(d) is driven by the phonon modes around  $\hbar\omega_{diag} = 80$  meV. Fig. 6.5 shows the time evolution of singlet population for  $\hbar\omega_{o.d.} = 20$  meV and four values of  $\hbar\omega_{diag}$ . The dependence of SF on  $\hbar\omega_{diag}$  here is qualitatively similar to that in the only diagonal coupling scenario [4]. Due to the low frequency phonon mode  $\hbar\omega_{o.d.}$ , the value of  $\lambda_{S_1,TT}^{o.d.} = S_{S_1,TT}^{o.d.} \hbar\omega_{o.d.}$  is significantly lower compared with the diagonal reorganization energy, and thus SF is dominated by the resonances between vibrational modes  $\hbar\omega_{diag}$  and electronic splittings.

Concerning the intermediate region of  $50 < \hbar\omega_{o.d.} \leq 80$  meV, efficient SF is found in Fig. 6.4 via several fission channels, including that around  $\hbar\omega_{diag} = 80$  meV. Fig. 6.6

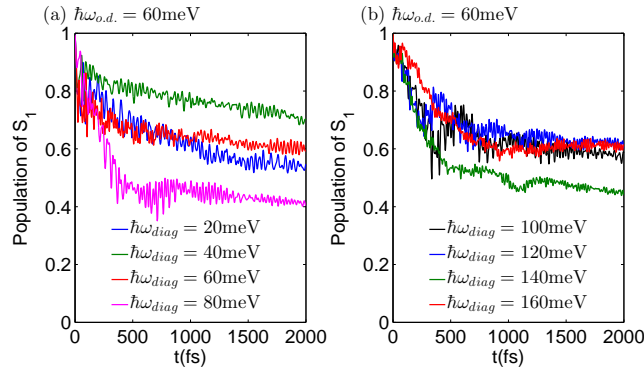


**Figure 6.6** Time evolution of singlet population for the the phonon mode  $\hbar\omega_{o.d.} = 60$  meV diagonally coupled to the  $S_1$  and TT states. The phonon modes off-diagonally coupled are (a)  $\hbar\omega_{diag} = 20, 40, 60$  and  $80$  meV, (b)  $\hbar\omega_{diag} = 100, 120, 140$  and  $160$  meV. The other parameters are same as Fig. 6.4

shows the time evolution of singlet population for  $\hbar\omega_{o.d.} = 60$  meV and various values of  $\hbar\omega_{diag}$ . The magenta line of  $\hbar\omega_{diag} = 80$  meV in Fig. 6.6(a) and the green line of  $\hbar\omega_{diag} = 140$  meV in Fig. 6.6(b) exhibit fast decay dynamics. However, SF dynamics for both cases is much slower than that in Fig. 6.5(a), because the interplay between fission dynamics and the mode  $\hbar\omega_{diag} = 80$  meV is drastically affected by the introduction of the mode  $\hbar\omega_{o.d.} = 60$  meV. What is shown in Fig. 6.6 is compatible with the SF mechanism with two diagonal coupled phonon modes [4]. in which inclusion of a second phonon mode creates a new SF channel, and if there is only diagonal coupling, shifts the optimal phonon frequency that promotes SF dynamics. However, in the presence of off-diagonal coupling, the SF channel around  $\hbar\omega_{diag} = 80$  meV is found unchanged.

As for the third region, SF dynamics is mainly facilitated by the high frequency phonon mode ( $\hbar\omega_{o.d.}$ ), as shown in Fig. 6.4. Comparing to the first and second region, efficient SF in this region is found to be dependent on a larger number of phonon modes, in qualitative agreement with the dependence of SF on multiple phonon modes in covalent tetracene dimers [19]. Fig. 6.7 presents the time evolution of singlet population for  $\hbar\omega_{o.d.} = 100$  meV and different values of  $\hbar\omega_{diag}$ . Due to the high frequency phonon mode  $\hbar\omega_{o.d.}$ , the initial oscillation amplitude is much larger than 0.13, which is the oscillation amplitude in the

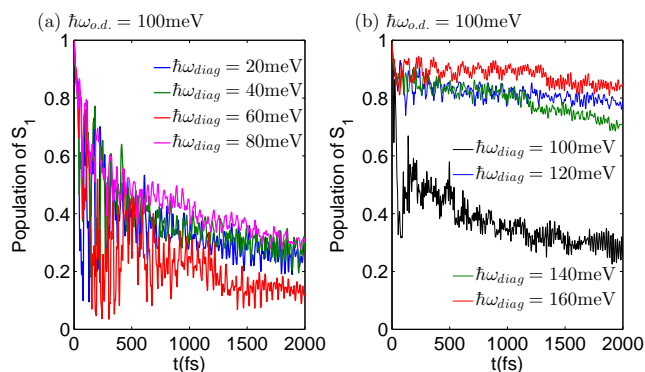


**Figure 6.7** Time evolution of singlet population for the the phonon mode  $\hbar\omega_{o.d.} = 60$  meV diagonally coupled to the  $S_1$  and TT states. The phonon modes off-diagonally coupled are (a)  $\hbar\omega_{diag} = 20, 40, 60$  and  $80$  meV, (b)  $\hbar\omega_{diag} = 100, 120, 140$  and  $160$  meV. The other parameters are same as Fig. 6.4

absence of exciton-phonon coupling. The envelope of fast oscillations is found to decrease gradually owing to dissipation induced by exciton-phonon coupling. Moreover, the SF time increases with increasing  $\hbar\omega_{diag}$ .

In summary, the iSF dynamics is accurately simulated using the Dirac-Frenkel time-dependent variational principle with the multi- $D_2$  ansatz. The SF process is characterized on the basis of its dependence on the phonon vibrations corresponding to the diagonal and off-diagonal coupling (which are given by  $\omega_{diag}$  and  $\omega_{o.d.}$ ) and the excitonic coupling strength between the  $S_1$  and TT states (which is given by  $J_{S_1,TT}$ ). It is presented that both diagonal and off-diagonal coupling frequencies play an important role in the SF process. In particular, in the presence of off-diagonal coupling, the high-frequency phonon modes is demonstrated to open up additional fission channels for the rapid iSF. The study here provides a guideline to facilitate the development of novel SF materials.

## References

- [1] E. G. Fuemmeler, S. N. Sanders, A. B. Pun, E. Kumarasamy, T. Zeng, K. Miyata, M. L. Steigerwald, X.-Y. Zhu, M. Y. Sfeir, L. M. Campos, and N. Ananth, *ACS Cent.*

- Sci.*, **2016**, 2, 316.
- [2] S. Ito, T. Nagami, and M. Nakano, *J. Phys. Chem. A*, **2016**, 120, 6236.
- [3] S. N. Sanders, E. Kumarasamy, A. B. Pun, K. Appavoo, M. L. Steigerwald, L. M. Campos, and M. Y. Sfeir, *J. Am. Chem. Soc.*, **2016**, 138, 7289.
- [4] Y. Fujihashi, L. Chen, A. Ishizaki, J. Wang, and Y. Zhao, *J. Chem. Phys.*, **2017**, 146, 044101.
- [5] H. Yamagata, J. Norton, E. Hontz, Y. Olivier, D. Beljonne, J. L. Bredas, R. J. Silbey, and F. C. Spano, *J. Chem. Phys.*, **2011**, 134, 204703.
- [6] D. Beljonne, H. Yamagata, J. L. Brédas, F. C. Spano, and Y. Olivier, *Phys. Rev. Lett.*, **2013**, 110, 226402.
- [7] H. Tamura, M. Huix-Rotllant, I. Burghardt, Y. Olivier, and D. Beljonne, *Phys. Rev. Lett.*, **2015**, 115, 107401.
- [8] S. Ito, T. Nagami, and M. Nakano, *J. Phys. Chem. Lett.*, **2015**, 6, 4972.
- [9] A. A. Bakulin, S. E. Morgan, T. B. Kehoe, M. W. Wilson, A. W. Chin, D. Zigmantas, D. Egorova, and A. Rao, *Nat. Chem.*, **2016**, 8, 16.
- [10] M. T. Trinh, Y. Zhong, Q. Chen, T. Schiros, S. Jockusch, M. Y. Sfeir, M. Steigerwald, C. Nuckolls, and X. Zhu, *J. Phys. Chem. C*, **2015**, 119, 1312.
- [11] L. Wang, L. Chen, N. Zhou, and Y. Zhao, *J. Chem. Phys.*, **2016**, 144, 024101.
- [12] T. C. Berkelbach, M. S. Hybertsen, and D. R. Reichman, *J. Chem. Phys.*, **2013**, 138, 114103.
- [13] T. C. Berkelbach, M. S. Hybertsen, and D. R. Reichman, *J. Chem. Phys.*, **2013**, 138, 114102.
- [14] N. Renaud and F. C. Grozema, *J. Phys. Chem. Lett.*, **2015**, 6, 360.
- [15] P. J. Vallett, J. L. Snyder, and N. H. Damrauer, *J. Phys. Chem. A*, **2013**, 117, 10824.

- [16] H. Tamura, I. Burghardt, and M. Tsukada, *J. Phys. Chem. C*, **2011**, 115, 10205.
- [17] H. Tamura, R. Martinazzo, M. Ruckebauer, and I. Burghardt, *J. Chem. Phys.*, **2012**, 137, 22A540.
- [18] T. Zeng, *J. Phys. Chem. Lett.*, **2016**, 7, 4405.
- [19] E. C. Alguire, J. E. Subotnik, and N. H. Damrauer, *J. Phys. Chem. A*, **2015**, 119, 299.



**Chapter 7\*****Dynamics of dissipative Landau-Zener transitions**

*Dynamics of the Landau-Zener model with both diagonal and off-diagonal qubit-bath coupling is examined by the Dirac-Frenkel time-dependent variation using the multiple Davydov  $D_2$  ansatz. It is shown that steady-state transition probabilities agree with analytical predictions at long times. Landau-Zener dynamics at intermediate times is little affected by diagonal coupling, and is found to be determined by off-diagonal coupling and tunneling between two diabatic states. Effects of bath spectral densities, coupling strengths and interaction angles on Landau-Zener dynamics, and detailed boson dynamics are investigated in this chapter. Results presented here may help provide guiding principles to manipulate the Landau-Zener transitions in circuit QED architectures by tuning off-diagonal coupling and tunneling strength.*

---

\* This chapter published substantially as Z. Huang and Y. Zhao, *Phys. Rev. A*, **97**, 13803 (2018).

## 7.1 Introduction

When the energy difference between two diabatic states is swept through an avoided level crossing, Landau-Zener transition comes into play [1, 2]. The Landau-Zener transition is one of the most fundamental phenomena in quantum physics. It is applied to a growing list of physical systems, such as a nitrogen-vacancy center spin in isotopically purified diamond [3], and a superconducting flux qubit coupled to quantum interference device [4]. Dynamics of the LZ transitions at the intermediate times is influenced by the dissipative environment. Roles of the environment include fluctuations of energies of diabatic states, denoted by diagonal coupling, and environment-induced transitions between diabatic states, expressed by off-diagonal coupling. As discussed in Subsec. 2.2.4 of Chapter 2, however, effects of off-diagonal coupling on LZ dynamics at the intermediate times have not been well investigated.

In this chapter, impacts of diagonal and off-diagonal qubit-bath coupling on the standard LZ model will be investigated using the Dirac-Frenkel variational principle with the multi- $D_2$  ansatz. This chapter adopts the standard LZ model with simultaneous diagonal and off-diagonal qubit-bath coupling, as presented in Subsec. 3.3.4 of Chapter 3. The remainder of the chapter is structured as follows. In Sec. 7.2, a qubit coupled to a circuit oscillator is studied. In Sec. 7.3, the influence of bath spectral densities on the LZ transitions is investigated. Finally, effects of coupling strengths and interaction angles on LZ dynamics are examined in Sec. 7.4.

## 7.2 A qubit coupled to a single mode

The LZ transitions can occur in a qubit that is coupled to a circuit oscillator in a QED device [4, 5]. Fig. 7.1 displays the schematic diagram of a superconducting qubit coupled to a coplanar transmission line resonator. The control line in Fig. 7.1(b) supplies the time-dependent magnetic flux  $\Phi(t)$  threading a persistent current qubit loop, which

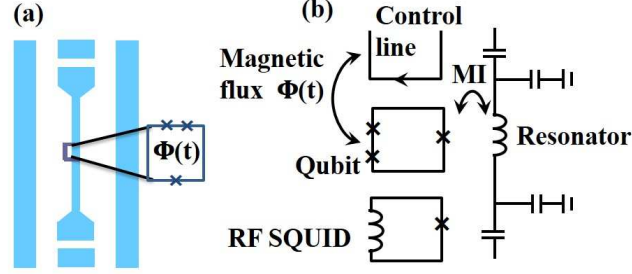


**Figure 7.1** (a) Schematic diagram of a typical coplanar waveguide resonator with a qubit placed between the center conductor and the ground plane of the waveguide. (b) Sketch of the superconducting qubit coupled to the coplanar transmission line resonator. MI denotes the mutual inductance between the qubit and resonator. The control line supplies the time-dependent magnetic flux  $\Phi(t)$  threading the qubit loop.

contains three junctions. After manipulations of the qubit, the state is detected by a SQUID, which consists of a single Josephson junction in a superconducting loop [6]. By tuning the external magnetic flux  $\Phi(t)$  threading the qubit loop, the energy level separation can vary linearly with a level-crossing speed  $v$ . The resonator can represent a harmonic oscillator, and is coupled to the qubit. Then this qubit-oscillator setup can simply be modeled by a Hamiltonian

$$\hat{H} = \frac{vt}{2}\sigma_z + \frac{\Delta}{2}\sigma_x + \hbar\omega\hat{b}^\dagger\hat{b} + \frac{\gamma}{2}\sigma_x(\hat{b}^\dagger + \hat{b}), \quad (7.1)$$

which can be obtained from the Hamiltonian (3.36) if the number of modes is set to one ( $N = 1$ ). When the first term in Eq. (7.1) is replaced by time-independent energy bias, the Hamiltonian is reduced to be the Rabi model, a paradigmatic construct of a two-level system coupled to a single bosonic mode derived from an atom in an applied electric field. A conventional rotating-wave approximation has often been adopted to treat the Rabi model [7].

Transitions between two diabatic states can result from direct tunneling or indirect off-diagonal coupling to the oscillator. The physical quantity of interest includes the probability that the qubit flipped from the initial state  $|\uparrow\rangle$  to  $|\downarrow\rangle$ , i.e.,  $P_{\uparrow\rightarrow\downarrow}(\infty) = 1 - P_{\uparrow\rightarrow\uparrow}(\infty)$ . Concerning tunneling between the two diabatic states, the

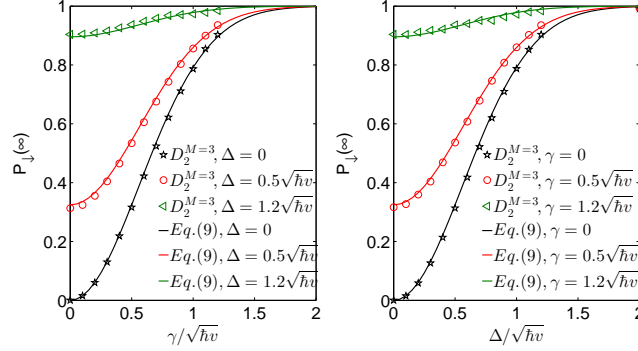


**Figure 7.2** (a) Final transition probability  $P_{\uparrow \rightarrow \downarrow}(\infty)$  as a function of the off-diagonal coupling strength  $\gamma/\sqrt{\hbar v}$  with fixed tunneling strengths  $\Delta = 0, 0.5\sqrt{\hbar v}$  and  $1.2\sqrt{\hbar v}$ . (b)  $P_{\uparrow \rightarrow \downarrow}(\infty)$  as a function of the tunneling strength  $\Delta/\sqrt{\hbar v}$  for different off-diagonal coupling strengths  $\gamma = 0, 0.5\sqrt{\hbar v}$  and  $1.2\sqrt{\hbar v}$ . The oscillator frequency  $\omega$  is set to  $10\sqrt{v/\hbar}$ .

final transition probability through avoided level crossing point is given by the familiar Landau-Zener formula  $P_{LZ} = 1 - \exp\left(\frac{-\pi\Delta^2}{2\hbar|v|}\right)$  [1, 2, 8–10]. With respect to the indirect off-diagonal coupling to the single bath mode, the transition probability is proposed as  $P_{\uparrow \rightarrow \downarrow}(\infty) = 1 - \exp\left(\frac{-\pi\gamma^2}{2\hbar|v|}\right)$  at zero temperature [11, 12]. In this work, we have studied the combined effect of the direct tunneling between the two diabatic states and indirect off-diagonal coupling to the single bath mode. Niemczyk *et al.* [13] using a recently developed circuit QED device showed the breakdown of the widely used rotating-wave approximation and the master-equation method due to the existence of strong qubit-bath coupling [14].

Using the time perturbation theory [15], we obtain

$$P_{\uparrow \rightarrow \downarrow}(\infty) = 1 - \exp\left[\frac{-\pi(\Delta^2 + \gamma^2)}{2\hbar|v|}\right] \quad (7.2)$$

It has been shown that this formula can provide exact final transition probabilities for the whole parameter regime at zero temperature [11, 12]. As shown in Fig. 7.2,  $P_{\uparrow \rightarrow \downarrow}(\infty)$  calculated from the multi- $D_2$  ansatz with a sufficiently large multiplicity  $M$  agrees with the analytical predictions of Eq. (7.2) for various off-diagonal coupling strengths  $\gamma$  and tunneling strengths  $\Delta$ . This demonstrates the accuracy of our multi- $D_2$  Ansatz and we can numerically provide accurate final transition probabilities.

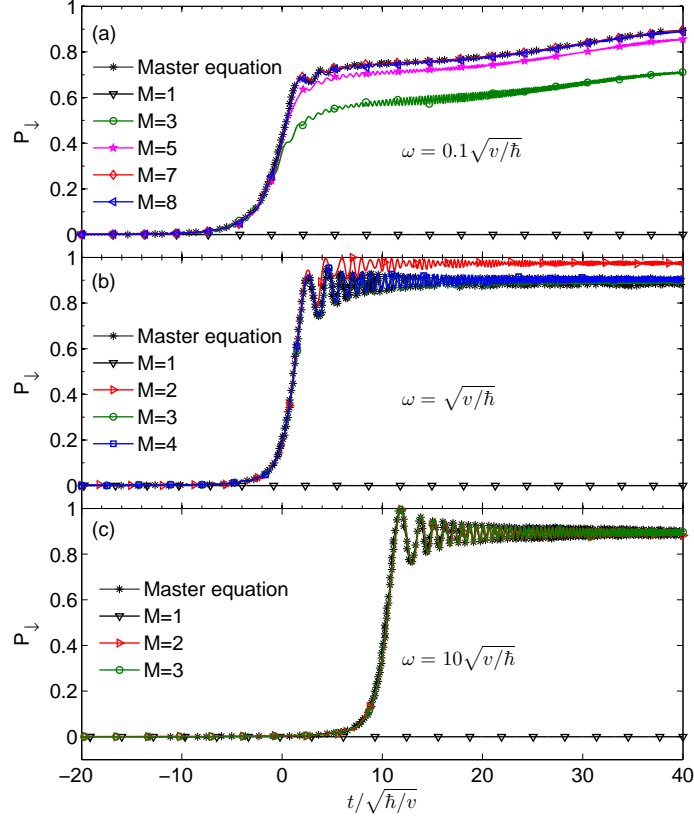


**Figure 7.3** Time evolution of transition probability calculated by the master-equation method and the multi- $D_2$  ansatz. Oscillator frequencies used are (a)  $\omega = 0.1\sqrt{v/\hbar}$ , (b)  $\omega = \sqrt{v/\hbar}$  and (c)  $\omega = 10\sqrt{v/\hbar}$ . Other parameters are  $\Delta = 0$  and  $\gamma = 1.2\sqrt{\hbar v}$ .

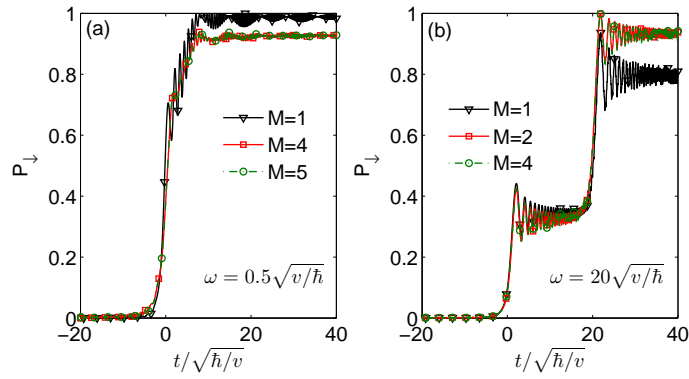


**Figure 7.4** LZ dynamics with a tunneling strength  $\Delta = 0.5\sqrt{\hbar v}$  and a off-diagonal coupling strength  $\gamma = 1.2\sqrt{\hbar v}$  for two oscillator frequencies (a)  $\omega = 0.5\sqrt{v/\hbar}$  and (b)  $\omega = 20\sqrt{v/\hbar}$ .

We here further justify the validity of the variational method by a comparison with the master equation method that yields exact results in the weak coupling regime. It is known that the multi- $D_2$  ansatz, a superposition of coherent states, can easily treat exciton dynamics in the strong coupling regime [16–18]. To reach an accurate description in the weak coupling cases, we have used a variety of multiplicities  $M$  of the multi- $D_2$  ansatz in the corresponding dynamical calculations. Fig. 7.3(a), (b), and (c) display the time evolution of the transition probability with oscillator frequencies of  $\omega = 0.1\sqrt{v/\hbar}$ ,  $\sqrt{v/\hbar}$ , and  $10\sqrt{v/\hbar}$ , respectively. The multiplicity of the multi- $D_2$  ansatz needed for convergence, as expected, decreases as the oscillator frequency increases if the coupling strength  $\gamma$  stays constant. The converged results in each scenario concur with those extracted from Ref. [12] (black line with stars) using the master equation method, demonstrating that the multi- $D_2$  Ansatz can well describe the LZ dynamics at intermediate times when the qubit is coupled to the harmonic oscillator of a wide range of frequencies.

In order to gain insight into LZ dynamics at intermediate times, we also perform convergence tests for oscillator frequencies of  $\omega = 0.5\sqrt{v/\hbar}$  and  $20\sqrt{v/\hbar}$ , and results are shown in Figs. 7.4(a) and (b), respectively. In the absence (Fig. 7.3) and the presence (Fig. 7.4) of tunneling, it can be found that LZ dynamics at intermediate times strongly depends on the oscillator frequency  $\omega$ , while the steady-state population in  $|\downarrow\rangle$ ,  $P_\downarrow(\infty)$ , are independent of  $\omega$ . In particular, the transition is temporally shifted from  $t = 0$  to  $t = \hbar\omega/v$  due to the indirect off-diagonal coupling [12]. Therefore the time shift for the case of  $\omega = 0.5\sqrt{v/\hbar}$  is minor compared to the time scale that is concerned, leading to the LZ transition of only one stage in Fig. 7.4(a). In contrast,  $P_\downarrow(t)$  undergoes two stages in the LZ transitions in Fig. 7.4(b). The first transition stage is induced by direct tunneling strength between the two levels  $\Delta = 0.5\sqrt{\hbar v}$ , named after the standard LZ transition, while the second transition stage results from the indirect off-diagonal coupling to the single oscillator mode with the frequency of  $\omega = 20\sqrt{v/\hbar}$ .

Next, we have investigated the dependence of LZ dynamics on the direct tunneling between the two diabatic states and indirect off-diagonal coupling to a single oscillator

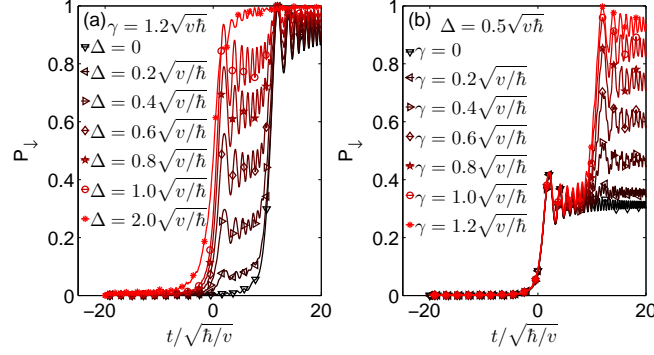


**Figure 7.5** LZ dynamics (a) for seven tunneling strengths  $\Delta = 0, 0.2\sqrt{\hbar v}, 0.4\sqrt{\hbar v}, 0.6\sqrt{\hbar v}, 0.8\sqrt{\hbar v}, 1.0\sqrt{\hbar v}$ , and  $2.0\sqrt{\hbar v}$  with fixed  $\gamma = 1.2\sqrt{\hbar v}$  and (b) for different off-diagonal coupling strengths  $\gamma = 0, 0.2\sqrt{\hbar v}, 0.4\sqrt{\hbar v}, 0.6\sqrt{\hbar v}, 0.8\sqrt{\hbar v}, 1.0\sqrt{\hbar v}$ , and  $1.2\sqrt{\hbar v}$  with certain  $\Delta = 0.5\sqrt{\hbar v}$ . The oscillator frequency  $\omega$  is set to  $10\sqrt{v/\hbar}$ .

mode. For this simulation, the oscillator frequency of  $\omega = 10\sqrt{v/\hbar}$  has been used. As shown in Fig. 7.5(a), by evenly changing the tunneling strength, the first plateau between the two stages of transitions can be tuned nonlinearly from zero to almost one, and the height of the second plateau varies from 0.89 to 1. As presented in Fig. 7.5(b), the first plateau is kept around 0.32 and the second plateau increases toward 1 as the off-diagonal coupling strength increases. Results in this section offer the possibility to manipulate the quantum states of the qubit that is coupled to only one circuit oscillator in the circuit QED.

### 7.3 Effect of the bath spectral density

Recent developments in circuit QED setups have shown that qubits can couple to a bath of quantum harmonic oscillators [19–21]. The qubit-bath coupling can be characterized by spectral densities of Ohmic type in a superconducting circuit consisting of a transmon qubit suspended on top of a microwave guide [19]. Many theoretical efforts have also been devoted to study LZ transitions at long times in a dissipative environment in terms of Ohmic fluctuations [22]. Spectrum densities of Sub-Ohmic and the super-Ohmic type can be realized in a multimode circuit QED setup with hybrid metamaterial transmission lines [23] and in certain circuit QED setups with multiple flux qubits [24], respectively. Thus

effects of spectral densities and coupling strengths on LZ dynamics of these systems need to be addressed.

In this section, we have studied LZ dynamics using the spectral density of Eq. (3.39). We have assumed that all bath oscillators couple to the qubit with identical coupling angles  $\theta_q = \theta$ . We have calculated the Huang-Rhys factor  $S = \sum_q \gamma_q^2 = \frac{\hbar^2}{4\pi} \int_0^\infty d\omega J(\omega) = \frac{\hbar^2}{2\pi} \alpha \omega_c^{s+1} \Gamma(s+1)$  and the total reorganization energy  $E_0 = \frac{\hbar}{4\pi} \int_0^\infty d\omega \frac{J(\omega)}{\omega} = \frac{\hbar}{2\pi} \alpha \omega_c^s \Gamma(s)$ , where  $\Gamma(x)$  is the Euler gamma function. Thus the final transition probability at zero temperature [15] can be given as

$$P_{\uparrow \rightarrow \downarrow}(\infty) = \frac{1}{1 - \exp \left[ \frac{-\pi \left( \left| \Delta - \frac{1}{2} E_0 \sin(2\theta) \right|^2 + S \sin^2 \theta \right)}{2\hbar v} \right]}. \quad (7.3)$$

When the first term in Eq. (3.37) is replaced by time-independent term of  $\frac{\epsilon}{2} \sigma_z$ , the Hamiltonian (3.36) becomes a spin-boson Hamiltonian. When system-bath coupling increases, a delocalization-localization transition can be found within the framework of the spin-boson model [25]. For LZ problems, however, the system always reaches a steady state with a certain final transition probability because the energy difference between the two diabatic states will be so large that transitions between the two states are unlikely at long times.

As shown in Fig. 7.6, we compare the LZ dynamics of the sub-Ohmic, Ohmic and super-Ohmic bath with the same coupling strength  $\alpha = 0.002$ . We have calculated the converged results of LZ dynamics for a qubit coupled to baths using the variational method. Spectral densities of the sub-Ohmic bath are computed using logarithmic discretization. For Ohmic and super-Ohmic bath we have used linear discretization [25]. Cutoff frequency is given by  $\omega_c = 10\sqrt{v/\hbar}$ . The roughness of the curves can be significantly reduced by using a large number of frequency modes ( $N = 80$  or greater). Details on the convergence tests are presented in Appendix C.2.

In Figs. 7.6 (a) and (b) we have presented LZ dynamics for the sub-Ohmic bath ( $s =$



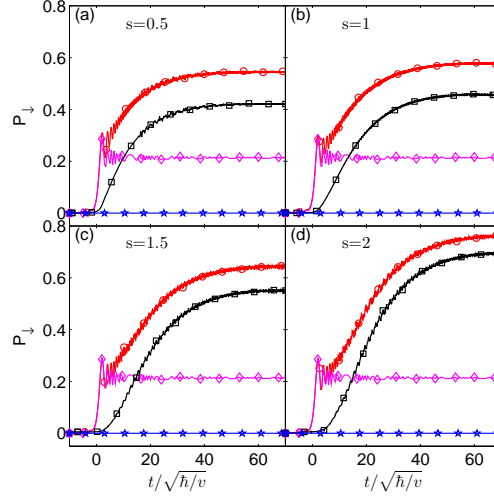


**Figure 7.6** Time evolution of transition probability for (a) a sub-Ohmic bath of  $s = 0.5$ , (b) an Ohmic bath of  $s = 1$ , and super-Ohmic bath of (c)  $s = 1.5$  and (d)  $s = 2$  is obtained from the  $D_2^{M=3}$  ansatz with an identical coupling strength  $\alpha = 0.002$ . For each of the four  $s$  values, four cases are shown:  $\Delta = 0.4\sqrt{\hbar v}, \theta = \pi/2$  (red line, circles),  $\Delta = 0.4\sqrt{\hbar v}, \theta = 0$  (magenta line, diamonds),  $\Delta = 0, \theta = \pi/2$  (black line, squares), and  $\Delta = 0, \theta = 0$  (blue line, pentagrams).

0.5) and the Ohmic bath ( $s = 1$ ), respectively. Figs. 7.6(c) and (d) depict time evolution of transition probabilities using the super-Ohmic bath with  $s = 1.5$  and 2, respectively. When  $\theta = 0$ , there exists only one stage of the LZ transition near  $t = 0$  for nonzero tunneling strength. That is, in the presence of only diagonal coupling, LZ dynamics of  $\Delta = 0.4\sqrt{\hbar v}$  (magenta lines, diamonds) are almost identical in the four subplots, irrespective of the spectral densities. Further calculations with finite tunneling strengths have shown that there exists a one-stage LZ transition in general in the presence of diagonal coupling only.

When  $\theta = \pi/2$ , time evolution of the transition probability for  $\Delta = 0$  has a single stage of slow growth until it reaches its steady state. The converged probabilities and the convergence times are dependent on the spectral densities. This occurs because LZ dynamics is strongly dependent on the oscillator frequency  $\omega$  for a qubit off-diagonally coupled to a single harmonic oscillator, as has been shown in Sec. 7.2. Fig. 7.6 also depicts that the convergence time for a large  $s$  is significantly longer than that for a

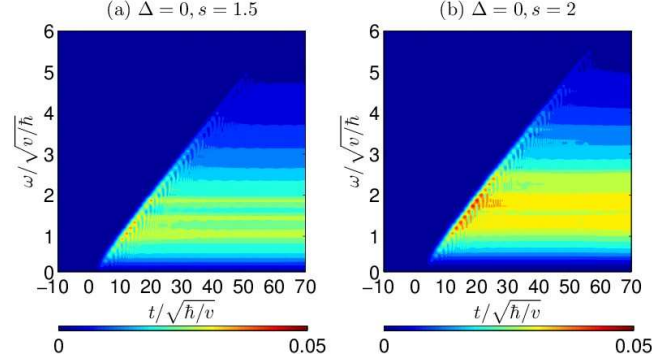


**Figure 7.7** Time evolution of the boson number using for a super-Ohmic bath of (a)  $s = 1.5$  and (b)  $s = 2$ , in the presence of off-diagonal coupling only ( $\theta = \pi/2$ ). Other parameters are  $\Delta = 0$  and  $\alpha = 0.002$ .

smaller  $s$ , since spectral densities of a large  $s$  involve prominent contribution from high-frequency oscillators, and the convergence time in the single harmonic oscillator scenario is proportional to the oscillator frequency  $\omega$ . When  $\Delta = 0.4\sqrt{\hbar v}$ , there are two stages in the LZ transitions in the presence of off-diagonal coupling. In the first stage, transition probability jumps up at  $t = 0$ . In the second stage, it gradually reaches the steady state at the same convergence time as that of  $\Delta = 0$ . Further calculations have shown that there exist the two-stage LZ transitions in general for all non-zero tunneling strengths in the presence of off-diagonal coupling. In addition, as expected, the converged transition probabilities obtained from our dynamics calculations agree with the corresponding steady-state transition probabilities from Eq. (7.3).

To investigate the role of bosons in the LZ transitions, we have calculated the time evolution of the boson number  $\langle \hat{b}_q^\dagger \hat{b}_q \rangle$  which is shown in Fig. 7.7. The initial boson number is set to be zero in our calculations. The bosons will be created after the transition takes place. If the qubit is only off-diagonally coupled to the single harmonic oscillator, the LZ transition would be temporally shifted from  $t = 0$  to  $t = \hbar\omega/v$ , independent of the coupling strength [12]. If qubit is off-diagonally coupled to multiple harmonic oscillators, the transition will then occur mainly after  $t = 0$  as there is a temporal shift of each frequency mode, as shown in Fig. 7.7. Because the energy difference between the diabatic

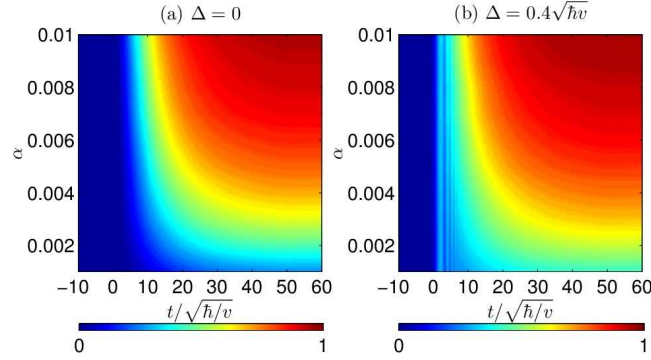


**Figure 7.8** Time evolution of transition probability for (a)  $\Delta = 0$  (b)  $\Delta = 0.4\sqrt{\hbar v}$  using an Ohmic bath with various coupling strengths  $\alpha$ , in the presence of off-diagonal coupling only ( $\theta = \pi/2$ ).

states varies linearly with time, the frequencies of the bosons created via qubit-bath coupling also have the same time dependence, resulting in the left edge of the triangle starting from  $t = 0$  in the  $\omega - t$  plots. It can be found that very few bosons will be created for  $t < 0$ , regardless of  $s$  and coupling strengths. When a larger value of  $s$  is used, more high-frequency bosons are created and this results in a larger steady-state probability for identical coupling strength. Also the time taken to create high-frequency mode bosons increases, which can be seen on comparison of Figs. 7.7(b) and Figs. 7.7(a). This is expected from the convergence time taken to reach the steady states in Fig. 7.6(d) and (c).

If the energies corresponding to frequencies of the bath modes  $\omega$  are high in comparison with the thermal energy  $k_B T$ , the oscillators are thermally inactive, thus LZ dynamics driven by the bath modes is temperature independent in a wide temperature range [4, 5]. Therefore, the temperature can be set to be  $T = 0$  to reduce the numerical cost, although the inclusion of the temperature effect in the multiple Davydov ansatz is straightforward by applying Monte Carlo importance sampling [26].

#### 7.4 Effects of coupling strength and interaction angle

Even though effects of various spectral densities have been discussed in Sec. 7.3, we will focus on the Ohmic type in this section because of the recent progress in nanotechnology [27–30] which allows for feasible control of how Ohmic environments are coupled to the superconducting qubit [31, 32]. Figs. 7.8(a) and (b) present the time evolution of transition probability as a function of coupling strength  $\alpha$  for two values of tunneling strength,  $\Delta = 0$  and  $0.4\sqrt{\hbar v}$ , respectively. In this section we have considered the case for off-diagonal coupling ( $\theta = \pi/2$ ) only. Calculated steady-state probabilities agree with Eq. (7.3), which predicts increases of the probabilities with the coupling strength. While the coupling strengths for the left and right panels in Fig. 7.8 are the same, the steady-state probabilities of Fig. 7.8(b) are larger than those of Fig. 7.8(a), because the nonzero tunneling strength  $\Delta = 0.4\sqrt{\hbar v}$  gives rise to one more transition stage at  $t = 0$  compared to that of  $\Delta = 0$ .

The interplay between the circuit qubit and the bosons is characterized by boson dynamics as a function of  $\omega$ , as is shown in Fig. 7.9. The boson number is initialized to zero. The upper and lower panels correspond to coupling strengths of  $\alpha = 0.002$  and  $\alpha = 0.006$ , respectively. It was found that boson number becomes larger with stronger off-diagonal coupling. We then make a comparison between the left and right panels, in which the left column corresponds to the zero tunneling strength scenarios ( $\Delta = 0$ ) and the right column is for  $\Delta = 0.4\sqrt{\hbar v}$ . If off-diagonal coupling strength is the same, more bosons are created for weaker tunneling scenarios, though we have larger steady-state transition probabilities for larger tunneling strength cases.

Figs. 7.10(a) and (b) present the time evolution of the transition probability as a function of the interaction angle  $\theta$  for  $\Delta = 0$  and  $\Delta = 0.4\sqrt{\hbar v}$ , respectively. The interaction angle  $\theta$  of interest ranges from 0 to  $\pi/2$ . We have only considered coupling strength of  $\alpha = 0.008$  in this section. In the absence and the presence of tunneling, the transition probabilities undergo the LZ transitions of one stage and two stages,

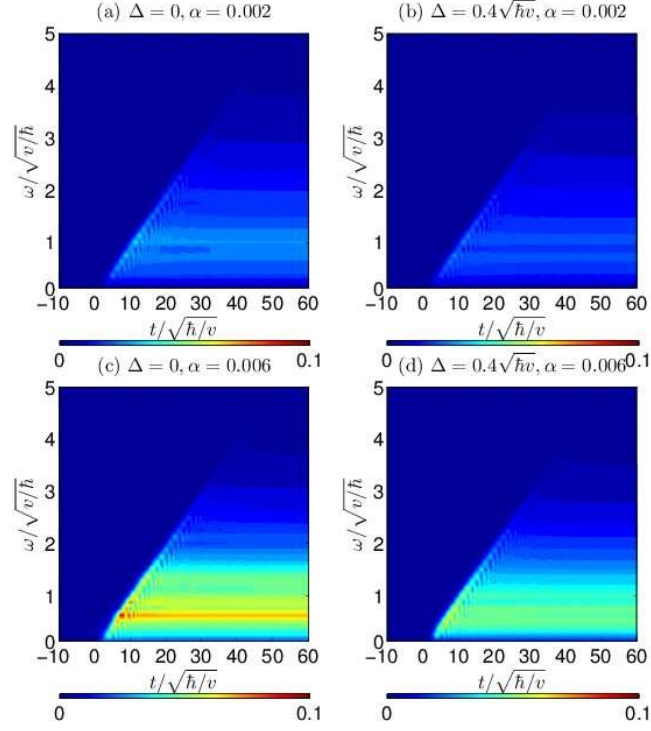


**Figure 7.9** Time evolution of the boson number using an Ohmic bath, in the presence of off-diagonal coupling only ( $\theta = \pi/2$ ). The left column corresponds to  $\Delta = 0$ , while the right column is for  $\Delta = 0.4\sqrt{\hbar v}$ . The upper and lower panels correspond to coupling strength of  $\alpha = 0.002$  and  $\alpha = 0.006$ , respectively.

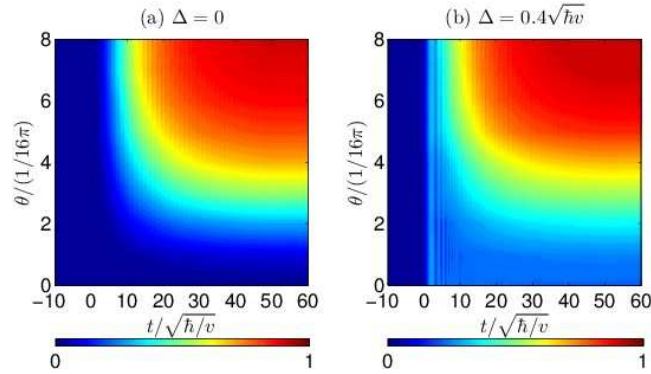


**Figure 7.10** Time evolution of transition probability for (a)  $\Delta = 0$  (b)  $\Delta = 0.4\sqrt{\hbar v}$  using an Ohmic bath with various interaction angles  $\theta$ . The coupling strength  $\alpha = 0.008$  is set.

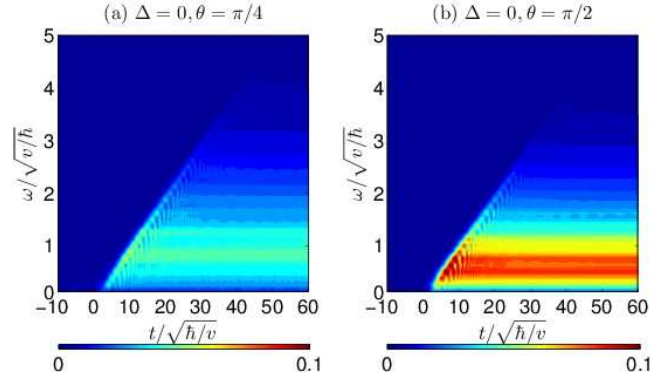


**Figure 7.11** Time evolution of the boson number using an Ohmic bath for interaction angles of (a)  $\theta = \pi/4$  and (b)  $\theta = \pi/2$ . The tunneling strength  $\Delta = 0$  and coupling strength  $\alpha = 0.008$  are set.

respectively. The transition probabilities  $P_{\downarrow}(t)$  for  $t > 0$  increase with the interaction angle  $\theta$ , since a larger interaction angle ( $0 \leq \theta \leq \pi/2$ ) corresponds to stronger off-diagonal coupling. The steady-state probabilities also increase with interaction angles, as expected from Eq. (7.3). Fig. 7.11 displays time evolution of the boson number for two interaction angles of (a)  $\theta = \pi/4$  and (b)  $\theta = \pi/2$ . We found that larger interaction angles ( $0 \leq \theta \leq \pi/2$ ) lead to more bosons being created during the transition stage, via stronger off-diagonal coupling.

In summary, impacts of diagonal and off-diagonal qubit-bath coupling on the standard LZ model are investigated using the Dirac-Frenkel variational principle with the multi- $D_2$  ansatz. For LZ dynamics at intermediate times, the converged results by the employed methods agree with those from the master-equation method, when the qubit is weakly coupled to a harmonic oscillator of a wide range of frequencies. In addition, calculated probabilities in the steady states concur with analytical predictions at zero temperature, further justifying the validity of the method used. LZ dynamics at intermediate times is little affected by diagonal coupling, and is found to be determined by off-diagonal coupling and tunneling between two diabatic states. Investigation are performed to study the effects of bath spectral densities, coupling strengths, and interaction angles on LZ dynamics. Finally, detailed boson dynamics based on the multi- $D_2$  ansatz are used to

identify the contribution of specific boson modes to the LZ transitions.

## References

- [1] C. Zener, *Proc. R. Soc. London A*, **1932**, 137, 696.
- [2] L. D. Landau, *Phys. Z.*, **1932**, 2, 46.
- [3] J. Zhou, P. Huang, Q. Zhang, Z. Wang, T. Tan, X. Xu, F. Shi, X. Rong, S. Ashhab, and J. Du, *Phys. Rev. Lett.* **2014**, 112, 10503.
- [4] I. Chiorescu, P. Bertet, K. Semba, Y. Nakamura, C. J. P. M. Harmans, and J. E. Mooij, *Nature*, **2004**, 431, 159.
- [5] A. Wallraff, D. I. Schuster, A. Blais, L. Frunzio, R.-S. Huang, J. Majer, S. Kumar, S. M. Girvin, and R. J. Schoelkopf, *Nature*, **2004**, 431, 162.
- [6] T. Lindström, C. H. Webster, J. E. Healey, M. S. Colclough, C. M. Muirhead, and A. Y. Tzalenchuk, *Supercond. Sci. Technol.*, **2007**, 20, 814.
- [7] Y.-Y. Zhang and Q.-H. Chen, *Phys. Rev. A*, **2015**, 91, 13814.
- [8] C. Wittig, *J. Phys. Chem. B*, **2005**, 109, 8428.
- [9] A. I. Chichinin, *J. Phys. Chem. B*, **2013**, 117, 6018.
- [10] L. T. A. Ho and L. F. Chibotaru, *Phys. Chem. Chem. Phys.*, **2014**, 16, 6942.
- [11] M. Wubs, K. Saito, S. Kohler, P. Hänggi, and Y. Kayanuma, *Phys. Rev. Lett.*, **2006**, 97, 200404.
- [12] K. Saito, M. Wubs, S. Kohler, P. Hänggi, and Y. Kayanuma, *Europhysics Lett.*, **2006**, 76, 22.
- [13] T. Niemczyk, F. Deppe, H. Huebl, E. P. Menzel, F. Hocke, M. J. Schwarz, J. J. Garcia-Ripoll, D. Zueco, T. Hummer, E. Solano, A. Marx, and R. Gross, *Nat. Phys.*, **2010**, 6, 772.

- [14] Z. Sun, J. Ma, X. Wang, and F. Nori, *Phys. Rev. A*, **2012**, 86, 012107.
- [15] K. Saito, M. Wubs, S. Kohler, Y. Kayanuma, and P. Hänggi, *Phys. Rev. B*, **2007**, 75, 214308.
- [16] N. Zhou, Z. Huang, J. Zhu, V. Chernyak, and Y. Zhao, *J. Chem. Phys.*, **2015**, 143, 014113.
- [17] Z. Huang, L. Chen, N. Zhou, and Y. Zhao, *Ann. Phys. (Berlin)*, **2017**, 529, 1600367.
- [18] Z. Huang, L. Wang, C. Wu, L. Chen, F. Grossmann, and Y. Zhao, *Phys. Chem. Chem. Phys.*, **2017**, 19, 1655.
- [19] F. Yan, S. Gustavsson, A. Kamal, J. Birenbaum, A. P. Sears, D. Hover, T. J. Gudmundsen, D. Rosenberg, G. Samach, S. Weber, J. L. Yoder, T. P. Orlando, J. Clarke, A. J. Kerman, and W. D. Oliver, *Nat. Commun.*, **2016**, 7, 12964.
- [20] J. J. Garcia-Ripoll, B. Peropadre, and S. De Liberato, *Sci. Rep.*, **2015**, 5, 16055.
- [21] H.-B. Liu, W. L. Yang, J.-H. An, and Z.-Y. Xu, *Phys. Rev. A*, **2016**, 93, 20105.
- [22] P. Nalbach and M. Thorwart, *Chem. Phys.*, **2010**, 375, 234.
- [23] D. J. Egger and F. K. Wilhelm, *Phys. Rev. Lett.*, **2013**, 111, 163601.
- [24] M. J. Storcz, J. Vala, K. R. Brown, J. Kempe, F. K. Wilhelm, and K. B. Whaley, *Phys. Rev. B*, **2005**, 72, 64511.
- [25] L. Wang, L. Chen, N. Zhou, Y. Zhao, *J. Chem. Phys.*, **2016**, 144, 024101.
- [26] L. Wang, Y. Fujihashi, L. Chen, and Y. Zhao, *J. Chem. Phys.*, **2017**, 146, 124127.
- [27] M. A. Castellanos-Beltran and K. W. Lehnert, *Appl. Phys. Lett.*, **2007**, 91, 83509.
- [28] V. E. Manucharyan, J. Koch, L. I. Glazman, and M. H. Devoret, *Science*, **2009**, 326, 113.
- [29] C.-H. Chung, K. Le Hur, M. Vojta, and P. Wölfle, *Phys. Rev. Lett.*, **2009**, 102, 216803.



- [30] I. M. Pop, I. Protopopov, F. Lecocq, Z. Peng, B. Pannetier, O. Buisson, and W. Guichard, *Nat. Phys.*, **2010**, 6, 589.
- [31] P. Cedraschi, V. V Ponomarenko, and M. Büttiker, *Phys. Rev. Lett.*, **2000**, 84, 346.
- [32] A. Kopp and K. Le Hur, *Phys. Rev. Lett.*, **2007**, 98, 220401.



## Chapter 8

### Conclusions

*In summary, this thesis seeks to provide a thorough investigation of the multiple Davydov  $D_2$  ansatz and its applications to the dynamics of open quantum systems. It is found that by undertaking the multi- $D_2$  ansatz, polaron dynamics can be fully quantum mechanically described in the simultaneous presence of diagonal and off-diagonal carrier-phonon coupling with and without an external electric field. The Dirac-Frenkel time-dependent variational method combined with the multi- $D_2$  ansatz enables accurate descriptions of various quantum behaviours, including the exciton transport in CPs, BOs dynamics in semiconductor superlattices and organic materials, SF processes in the iSF materials, and LZ transitions in the QED devices.*

This thesis addresses the multiple Davydov  $D_2$  ansatz, also known as the multi- $D_2$  ansatz, and its applications to various open quantum systems with electronic and bosonic DOFs. In order to accurately describe the state of the open quantum system, the environment influence is typically modelled as a bosonic bath coupled to an electronic target system. Complexity of system-bath interactions makes exact analytical solutions difficult to obtain for the dynamics of most open quantum systems. In order to study the open quantum systems, two categories of methods were constructed: wave function based methods and density matrix based approaches. The validities of these methods have been examined in fields such as quantum measurement theory, quantum statistical mechanics, and quantum thermodynamics. However, approaches employed greatly depend on the target systems and desired objectives. Moreover, methods developed have their limitations when treating the open quantum systems. For example, exact solutions from the QUAPI and the HEOM methods need expensive computational resources, and perturbative results from the master equation method are inaccurate out of the weak coupling regime. In particular, accurate modeling of polaron dynamics have not received much-deserved attention over the last six decades.

In order to accurately solve the dynamics of open quantum systems, the multi- $D_2$  ansatz is developed as a linear combination of the usual Davydov  $D_2$  trial state from the soliton literature. Equations of motions for time-dependent variational parameters of the multi- $D_2$  ansatz are given by the Dirac-Frenkel time-dependent variational principle. This ansatz is shown to enable accurate descriptions of fully quantum dynamical correlations between the electronic and bosonic subsystems, and facilitate comprehensive understanding of dynamics of the open quantum systems with off-diagonal coupling to boson modes. The multi- $D_2$  ansatz has been applied to study the exciton transport in the CPs, BOs dynamics in semiconductor superlattices and organic materials, the SF processes in the iSF materials, and the LZ transitions in the circuit QED devices.

**1) First Application:** In the application of the multi- $D_2$  ansatz to exciton transport in the CPs, the dynamics of the Holstein polaron with off-diagonal coupling is studied in Chapter

4 using the Dirac-Frenkel time-dependent variational principle and the multi- $D_2$  ansatz.

Firstly, often used to simulate exciton dynamics in the CPs, the semi-classical Ehrenfest method has been shown to be equivalent to the time-dependent variational method with the single  $D_2$  ansatz. Calculation of the relative deviation, which quantifies the ansatz accuracy, demonstrates that the variational method with the multi- $D_2$  ansatz presents much more accurate results than the semi-classical Ehrenfest dynamics. With a sufficiently large multiplicity, our variational method using the multi- $D_2$  ansatz can offer numerically exact solutions. We further compare  $\text{MSD}(t)$  obtained from the semi-classical method and with that from the multi- $D_2$  ansatz, and find that the mobility is overestimated by the semi-classical method. These results indicate that the description beyond the semi-classical method is essential to quantitatively capture the dynamics of the SSH model.

Secondly, we explore the underlying physics from the accurate dynamics data for the Holstein model with the off-diagonal coupling. The energy and the momentum of the bare exciton are constants of motion. However, in the presence of the exciton-phonon coupling, the exciton probability in the momentum space is found to redistribute and become centered in stationary regions. It can be revealed that the momentum redistribution is only determined by the combination of the transfer integral and the off-diagonal strength, and is independent of the initial excitonic conditions used. In addition, in order to study the competition between the transfer integral and the off-diagonal coupling, the exciton transport is investigated within the exciton site and the exciton momentum representation, and the crystal momentum representation. The results show that the combination of the transfer integral and the off-diagonal coupling do not necessarily play a role in enhancing the exciton transport, because the self-trapped exciton can be found with certain parameter sets due to the competition between the off-diagonal coupling and the transfer integral. Moreover, the off-diagonal coupling is demonstrated to be the simultaneous agent of transport and localization in dynamical calculations.

Lastly, temperature effects are studied using the variational method with importance sampling by employing the multi- $D_2$  ansatz. In both the low and high temperature regimes, the time evolution of the exciton probability calculated from the variational method with importance sampling agrees well with that from the numerically exact HEOM method, and can be obtained much more efficiently. The results at the finite temperatures show that fast delocalization of the exciton wave is quenched due to thermal fluctuations, indicating the weakening of the exciton transport by increasing the temperature.

**2) Second Application:** In the application of the multi- $D_2$  ansatz to BOs dynamics in semiconductor superlattices and organic materials, transient dynamics of the Holstein polaron in a one-dimensional ring under a constant external field is studied in Chapter 5. In both the diagonal and off-diagonal coupling cases, the efficient variational results are in perfect agreement with those obtained from the numerically exact HEOM method. Moreover, the relative deviation is found to decay with the increasing multiplicity of the multi- $D_2$  ansatz, which vanishes in the limit of  $M \rightarrow \infty$ , inferring that our approach is numerically exact in that limit.

Firstly, the influence of the initial condition is studied in the absence of carrier-phonon coupling. For an initial broad Gaussian wave packet, typical BOs are found with the center of the wave packet oscillating but its shape essentially unchanged. Starting from an initial narrow Gaussian wave packet, the carrier wave packet exhibits a symmetric breathing mode with its width oscillating with the Bloch period and its center of mass fixed at the original location.

The effect of the carrier-phonon coupling is the focus of our investigation. In general, weak diagonal coupling breaks the spatial periodicity while keeping the temporal periodicity of the carrier wave. For an initial broad Gaussian wave packet, the application of weak diagonal coupling modifies BOs with the carrier wave packet broadened and the carrier current reduced. For an initial narrow Gaussian wave packet, after the addition of weak coupling, the spatial symmetry of the carrier wave is broken and the center of mass

of the carrier wave packet oscillates away from the original position, leading to a non-zero carrier current. In particular, a saturated current which exists in an infinite linear lattice is not found in a finite-sized ring within the anti-adiabatic regime, since the energy imported by the external field is not entirely absorbed by the lattice, leaving the steady state unreachable.

For strong carrier-phonon coupling, the variational method using the multi- $D_2$  ansatz is found to be highly accurate while it is prohibitively expensive for the HEOM method to tackle higher phonon excited states. The carrier wave packet is found to be localized due to either strong diagonal coupling or a strong external field. Finally, strong diagonal coupling gives rise to the decay of BOs under a strong external field, leading to damped oscillations of the exciton current.

**3) Third Application:** In the application of the multi- $D_2$  ansatz to the SF processes in iSF materials, a model of iSF dynamics is developed to include simultaneous diagonal and off-diagonal exciton-phonon coupling. As shown in Chapter 6, an accurate description is provided for iSF dynamics using the multi- $D_2$  ansatz. To our knowledge, diagonal coupling has been reported to aid efficient SF if excitonic coupling is weak, and it has also been shown to facilitate efficient fission if excitonic coupling is strong in Chapter 6. Furthermore, it is demonstrated for the first time that off-diagonal coupling plays a crucial role in the fission process only if excitonic coupling is weak. It is determined that iSF dynamics strongly depends on the frequency of phonon modes in the presence of off-diagonal coupling, and high-frequency phonon modes result in efficient iSF even if the off-diagonal coupling strength is weak. Multiple SF channels can be created by the simultaneous presence of diagonal and off-diagonal coupling. Thus a unified framework has been provided to establish the effects of diagonal and off-diagonal coupling on SF dynamics.

**4) Fourth Application:** In the application of the multi- $D_2$  ansatz to the LZ transitions in the circuit QED devices, the intriguing role played by the dissipative environment in LZ

dynamics is studied in Chapter 7. Following the Dirac-Frenkel time-dependent variational principle, dynamics of the LZ model with diagonal and off-diagonal qubit-bath coupling is probed by employing the multi- $D_2$  ansatz. Convergence has been ensured in the LZ dynamics calculation by monitoring the multiplicity of the multi- $D_2$  ansatz, and results agree with those of other methods. The final transition probabilities in the steady states obtained from our numerical calculations concur with the analytical predictions. To our knowledge, two-stage LZ transitions are found for the first time at the intermediate times for a qubit coupled to a circuit oscillator, or to a dissipative environment that is characterized by the bath spectral densities, thanks to the combined effect of off-diagonal qubit-bath coupling and the tunneling strength. It is revealed in our systematic investigations that larger interaction angles ( $0 \leq \theta \leq \pi/2$ ) and spectral densities with larger exponents and coupling strengths lead to longer transition times and greater steady-state probabilities. Finally, the boson dynamics analysis based on the multi- $D_2$  ansatz has successfully identified the contribution of specific boson modes to the LZ transitions.

In summary, we adopted the time-dependent variational approach utilizing the multi- $D_2$  ansatz, to accurately investigate dynamics of several specified open quantum systems with electronic and bosonic degrees of freedom. Results presented in this thesis may help provide guiding principles for design of efficient singlet fission materials by directly tuning singlet-triplet interstate coupling, and to manipulate the Landau-Zener transitions in circuit quantum electrodynamics architectures by tuning off-diagonal coupling and tunneling strength. It is also our hope that the multi- $D_2$  ansatz can find applications in a wider range of interesting exciton-phonon coupled systems.



## Chapter 9

### Recommendations for Future Work

*In this thesis, we have systematically investigated the applications of the the multiple  $D_2$  Davydov ansatz to four different open quantum systems. In this chapter, we will discuss potential fields of implementation of the present theoretical framework and recommend some possible directions for future research.*

### 9.1 Applications of neural networks to the simulation of dynamics of open quantum systems

In recent years, artificial intelligence has attracted considerable attention as a suitable neural network can reduce the computational cost dramatically. Neural networks can be used in numerous ways to solve quantum problems. Combined with variational principles, the neural networks been used for analysis of the quantum entanglement [1]. It has been shown that a deep neural network can efficiently represent most physical states, including ground states of many-body Hamiltonians [2]. A multiscale entanglement renormalization ansatz [3] along with a deep neural network was used to attack the problem with sampling. Machine learning has also been used along with the Bayesian statistics to speed up hybrid Monte Carlo simulations [4]. Recent progress has been made in applying artificial intelligence to dynamics of open quantum systems. For example, Cerrillo *et al.* have combined the time evolving density matrix using orthogonal polynomials algorithm with the transfer tensors formalism to the analysis, compression and propagation of non Markovian processes [5–7]. Carleo *et al.* have also demonstrated that a reinforcement-learning scheme is capable of both describing the unitary time evolution of prototypical interacting spins models in one and two dimensions [8]. All these attempts provide inspiration for more neural-network analysis of the dynamical observables in various open quantum systems.

We plan to employ dynamical neural networks to simulate dynamics of open quantum systems. In detail, we will apply recurrent neural networks to investigate the time evolution of observables of interest in the spin-boson model and the dissipative Landau-Zener model. The trajectories of the correlated reduced open system state will provide key information about the environmental influence and the effect of initial correlations onto open system dynamics. The first stage of the dynamics will be obtained by using the Dirac-Frenkel variational principle with the multiple Davydov  $D_2$  trial state. As is known, the construction of the dynamical neural net depends on the complexity of the observable trajectories [5]. In

particular, nonlinear autoregressive neural network will be used because it is the simplest and the most convenient method available to us that can be utilized to predict the time series from past values of that series efficiently. For example, this method has been used to study the nonlinear behaviours such as chaotic optical intensities in laser [9, 10]. With data obtained from the multi- $D_2$  ansatz, we will then train and test suitable neural nets to determine the validity of the networks. At last, after verifying the generalization ability of the trained net by cross validation, a time series of the physical observables of interest will be predicted from past values of that series using the well trained net.

## 9.2 Manipulation of photon delocalization in a Rabi dimer

Recent theoretical studies model the tunnel-coupled resonators each containing a qubit as a Jaynes-Cumming dimer, which is the smallest possible coupled-resonator system [11–15]. The Jaynes-Cumming Hamiltonian describes a QED system with weak qubit-photon coupling, which omits the counter-rotating-wave interactions between the qubit and the photon mode. Beyond the Jaynes-Cumming dimer, Hwang *et al.* studied the phase transition of photons in a Rabi dimer [12]. For a bare Rabi dimer with  $\omega_0$  being the frequency of the photon mode, a critical photon tunneling rate of about  $0.03\omega_0$  has been proposed [11, 13], above which the photons are always delocalized regardless of the qubit-photon coupling strength. If the photon tunneling rate is smaller than the critical value, the photon dynamics in a Rabi dimer is found to undergo double phase transitions as the qubit-photon coupling strength increases. The first transition is from a delocalized phase to a localized phase, then the second one takes place from the localized phase to a new delocalized phase. Photons hop between two resonators in the first delocalized phase, while photons are quasi-equilibrated over two resonators in the second delocalized phase [12]. However, in experimental realizations, fabricated QED systems suffer from ineluctable dissipation stemming from the device-environment interactions. Although the phase diagram for the photons in a Rabi dimer has been constructed, dissipation-induced effects on the dynamics of the photons and the qubits in a Rabi dimer are still not well-understood [12].

As for influences of dissipation on various QED systems, most studies are conducted by adopting master equations to capture the photon and the qubit dynamics of the QED systems, where environmental effects are considered in a phenomenological manner [11, 13]. However, the interplay between the QED devices and their surroundings is too complex to be modeled by a few dissipative parameters in the methods based on the Markovian Lindblad master equation [16, 17]. In addition to being affected by bath induced dissipation, the operation of QED devices can benefit from interactions with their surroundings [18]. For instance, Hohenester *et al.* observed phonon-assisted transition from quantum dot excitons to photons in nanocavity [19]. Recently it has been found that exciton-phonon coupling favors single-photon generation in QD-nanocavity systems [20]. Therefore, proper treatments of the system-bath interactions are needed.

We will investigate the bath-induced effects on the out-of-equilibrium dynamics of a Rabi dimer by coupling the qubits to a common phonon bath, which models the surrounding environment. In particular, we plan to study the influences of various qubit-phonon coupling strengths on the photon dynamics for two regimes of qubit-photon couplings, namely, weak and ultrastrong coupling (USC) regimes. In the weak qubit-photon cases, we will perform extensive calculations to examine whether the photon in the delocalized phase will be affected by qubit-phonon coupling. In the USC regime, there is a debate on whether the photon dynamics would be engineered by tuning the qubit-phonon coupling. As is known, if the light-matter coupling enters the weak coupling regime, the dynamics can be described by the Jaynes-Cummings Hamiltonian. However, the rotating-wave approximation in the resonator-resonator coupling is known to be a wrong assumption in the USC regime [21]. In detail, the resonator-resonator coupling strength must be comparable with frequency gaps of the Rabi system (diagonalizing the quantum Rabi model) to see whether or not a rotating-wave approximation may hold. We will check the validity of the multi- $D_2$  ansatz in describing photon dynamics in the USC qubit-photon regime. Initially, a fully localized photon state will be prepared by pumping a certain number of photons into one resonator while keeping the other resonator in a photon vacuum. In contrast to the photons, the qubits in the two resonators will start to

evolve from their down states and the phonon bath will initially be in a vacuum state. In addition, we will examine the dependence of photon behaviors on initial photon numbers in the left and right resonators.

In order to elucidate the phonon-bath-induced effects on the photon dynamics in the Rabi dimer, we will choose several combinations of photon tunneling rate and qubit-photon coupling, and perform simulations for each parameter configuration with varying qubit-bath coupling strengths. In particular, transitions of photons between the delocalized and localized phases will be studied under the influence of the environmental disturbance. Owing to the advantage of the wave function based method, population of the bath modes will be calculated to investigate the participation of individual bath modes in the Rabi dimer dynamics. Finally, we will explicitly explore how to manipulate photon states via the qubit-photon and qubit-phonon coupling. The work may help make clear the effects of environmental noise on the hybrid QED device represented by the Rabi dimmer.

## References

- [1] D.-L. Deng, X. Li, and S. Das Sarma, *Phys. Rev. X*, **2017**, 7, 21021.
- [2] X. Gao and L.-M. Duan, *Nat. Commun.*, **2017**, 8, 662.
- [3] C. Bény, *ArXiv Prepr.*, **2013**, ArXiv1301.3124.
- [4] C. Edward Rasmussen, *Bayesian Integrals.*, **2003**, 7, 651.
- [5] J. Cerrillo and J. Cao, *Phys. Rev. Lett.*, **2014**, 112, 110401.
- [6] M. Buser, J. Cerrillo, G. Schaller, and J. Cao, *Phys. Rev. A*, **2017**, 96, 62122.
- [7] R. Rosenbach, J. Cerrillo, S. F. Huelga, J. Cao, and M. B. Plenio, *New J. Phys.*, **2016**, 18, 23035.
- [8] G. Carleo and M. Troyer, *Science*, **2017**, 355, 602.

- [9] U. Hübner, N. B. Abraham, and C. O. Weiss, *Phys. Rev. A*, **1989**, 40, 6354.
- [10] U. Hübner, W. Klische, N. B. Abraham, and C. O. Weiss, *Coherence Quantum Opt. VI*, edited by J. H. Eberly, L. Mandel, and E. Wolf (Springer US, Boston, MA, **1989**), pp. 517-520.
- [11] S. Schmidt, D. Gerace, A. A. Houck, G. Blatter, and H. E. Türeci, *Phys. Rev. B*, **2010**, 82, 100507(R).
- [12] M. J. Hwang, M. S. Kim, and M. S. Choi, *Phys. Rev. Lett.*, **2016**, 116, 153601.
- [13] J. Raftery, D. Sadri, S. Schmidt, H. E. Tureci, and A. A. Houck, *Phys. Rev. X*, **2014**, 4, 031043.
- [14] M. J. Hartmann, F. G. S. L. Bran Ao, and M. B. Plenio, *Nat. Phys.*, **2006**, 2, 849.
- [15] I. Carusotto and C. Ciuti, *Rev. Mod. Phys.*, **2013**, 85, 299.
- [16] A. Nazir and D. P. McCutcheon, *J. Phys. Condens. Matter*, **2016**, 28, 103002.
- [17] P. Kaer, N. Gregersen, and J. Mork, *New J. Phys.*, **2013**, 15, 035027.
- [18] G. Hornecker, A. Auffèves, and T. Grange, *Phys. Rev. B*, **2017**, 95, 035404.
- [19] U. Hohenester, A. Laucht, M. Kaniber, N. Hauke, A. Neumann, A. Mohtashami, M. Seliger, M. Bichler, and J. J. Finley, *Phys. Rev. B*, **2009**, 80, 201311(R).
- [20] K. Müller, K. A. Fischer, A. Rundquist, C. Dory, K. G. Lagoudakis, T. Sarmiento, Y. A. Kelaita, V. Borish, and J. Vučković, *Phys. Rev. X*, **2015**, 5, 031006.
- [21] D. Z. Rossatto, S. Felicetti, H. Eneriz, E. Rico, M. Sanz, and E. Solano, *Phys. Rev. B*, **2016**, 93, 94514.



## APPENDIX

### Appendix A For polaron dynamics with off-diagonal coupling

The following appendices from Appendix A.1 to Appendix A.4 are for Chapter 4.

#### Appendix A.1 Fully quantum description of the semi-classical Hamiltonian

The semi-classical Hamiltonian is composed of the electronic and the phonon part  $H = H_{el} + H_{ph}$ , the electronic part is

$$H_{el} = \sum_n [-J + \alpha (u_{n+1} - u_n)] (\hat{a}_n^\dagger \hat{a}_{n+1} + H.c.), \quad (A.1)$$

where  $J$  is the transfer integral,  $\alpha$  the electron-phonon coupling constant,  $u_n$  the displacement of phonon on the  $n$ -th site, and  $\hat{a}_n^\dagger$  ( $\hat{a}_n$ ) the creation (annihilation) operators of electron. The phonon part is

$$H_{ph} = \frac{K}{2} \sum_n (u_{n+1} - u_n)^2 + \frac{M}{2} \sum_n \dot{u}_n^2, \quad (A.2)$$

in which,  $K$  denotes the force constant originating from the  $\sigma$  bond between carbon atoms,  $K = M\omega_0^2$  and  $M$  the total mass of a CH-unit for trans-polyacetylene. The combination of the two parts above is identical to SSH model used for conductive polymers.

Using the quantum mechanical creation and annihilation operators to describe the displacement of the phonon bath,

$$\begin{aligned} u_n &= \sqrt{\frac{1}{2M\omega}} (b_n^\dagger + b_n), \\ \gamma &= \sqrt{\frac{1}{2M\omega}} \alpha \end{aligned} \quad (A.3)$$

we get  $\hat{H} = \hat{H}_{ex} + \hat{H}_{ph} + \hat{H}_{int}$ , with the electronic part

$$\hat{H}_{ex} = -J \sum_n (\hat{a}_n^\dagger \hat{a}_{n+1} + H.c.), \quad (A.4)$$



the phonon part

$$\hat{H}_{ph} = \sum_n \omega_0 \hat{b}_n^\dagger \hat{b}_n, \quad (\text{A.5})$$

and the electron-phonon interaction part

$$\begin{aligned} \hat{H}_{int} = & \gamma \sum_{n,l} \left[ \hat{a}_n^\dagger \hat{a}_{n+1} \left( \hat{b}_l + \hat{b}_l^\dagger \right) (\delta_{n+1,l} - \delta_{n,l}) \right. \\ & \left. + \hat{a}_n^\dagger \hat{a}_{n-1} \left( \hat{b}_l + \hat{b}_l^\dagger \right) (\delta_{n,l} - \delta_{n-1,l}) \right]. \end{aligned} \quad (\text{A.6})$$

Fourier transforming the phonon operators into momentum space,

$$\begin{aligned} \hat{b}_n^\dagger &= N^{-1/2} \sum_q e^{-iqn} \hat{b}_q^\dagger, \\ \hat{b}_n &= N^{-1/2} \sum_q e^{iqn} \hat{b}_q, \end{aligned} \quad (\text{A.7})$$

we get

$$\begin{aligned} \hat{H}_{ex} &= -J \sum_n \left( \hat{a}_n^\dagger \hat{a}_{n+1} + H.c. \right), \\ \hat{H}_{ph} &= \omega_0 \sum_q \hat{b}_q^\dagger \hat{b}_q, \\ \hat{H}_{ex-ph}^{o.d.} &= \gamma N^{-1/2} \sum_{n,q} \left\{ \hat{a}_n^\dagger \hat{a}_{n+1} \left[ e^{iqn} (e^{iq} - 1) \hat{b}_q + H.c. \right] \right. \\ & \quad \left. + \hat{a}_n^\dagger \hat{a}_{n-1} \left[ e^{iqn} (1 - e^{-iq}) \hat{b}_q + H.c. \right] \right\}, \end{aligned} \quad (\text{A.8})$$

just being the off-diagonal Holstein polaron model.

## Appendix A.2 Comparison between the variational method using the single $D_2$ ansatz and the semi-classical method

In this part, it is shown that the dynamics obtained from the semi-classical method and the variational method using only the single  $D_2$  ansatz are equivalent for the spin-boson model ( $N = 2$ ).

### Appendix A.2.1 The variational method

The Hamiltonian of the spin-boson model is

$$\hat{H} = \frac{\epsilon}{2}\sigma_z + V\sigma_x + \omega\hat{a}^\dagger\hat{a} + \frac{\lambda}{2}\sigma_z(\hat{a}^\dagger + \hat{a}) + \frac{\phi}{2}\sigma_x(\hat{a}^\dagger + \hat{a}), \quad (\text{A.9})$$

where  $\epsilon$  and  $V$  are the spin bias and the tunneling constant, respectively.  $\lambda$  ( $\phi$ ) is the diagonal(off-diagonal) coupling strength.  $\sigma_x$  and  $\sigma_z$  are The Pauli matrices,  $\hat{a}^\dagger(\hat{a})$  is the boson creation (annihilation) operator for the phonon of frequency  $\omega_0$ .

Using the variational principle and the  $D_2$  ansatz,  $|D_2\rangle = A(t)|+\rangle e^{[f(t)\hat{a}^\dagger - f^*(t)\hat{a}]}|0\rangle + B(t)|-\rangle e^{[f(t)\hat{a}^\dagger - f^*(t)\hat{a}]}|0\rangle$  the equations of motion can be obtained,

$$\begin{aligned} 0 &= i\dot{A} - \frac{\epsilon}{2}A - VB - \frac{\lambda}{2}A(f + f^*) - \frac{\phi}{2}B(f^* + f), \\ 0 &= i\dot{B} + \frac{\epsilon}{2}B - VA + \frac{\lambda}{2}B(f + f^*) - \frac{\phi}{2}A(f^* + f), \\ 0 &= i\dot{f} - \omega f - \frac{\lambda}{2}(|A|^2 - |B|^2) - \frac{\phi}{2}(A^*B + AB^*). \end{aligned} \quad (\text{A.10})$$

### Appendix A.2.2 The semi-classical method

The semi-classical Hamiltonian can also be written as

$$\begin{aligned} \hat{H} &= \frac{\epsilon}{2}\sigma_z + V\sigma_x + \frac{p^2}{2m} + \frac{1}{2}m\omega^2x^2 \\ &\quad + \lambda\sqrt{\frac{m\omega}{2}}\sigma_zx + \phi\sqrt{\frac{m\omega}{2}}\sigma_xx, \end{aligned} \quad (\text{A.11})$$

the electronic state is described by the wave function  $|\psi\rangle = A(t)|+\rangle + B(t)|-\rangle$ ,  $m$  is the effective mass of the phonon. The equations of motion from the semi-classical formalism

are

$$\begin{aligned}
i\dot{A} &= \left( \frac{\epsilon}{2} + \sqrt{\frac{m\omega}{2}} \lambda x \right) A + VB + \phi \sqrt{\frac{m\omega}{2}} x B, \\
i\dot{B} &= - \left( \frac{\epsilon}{2} + \sqrt{\frac{m\omega}{2}} \lambda x \right) B + VA + \phi \sqrt{\frac{m\omega}{2}} x A, \\
\dot{x} &= v, \\
\dot{v} &= -\omega^2 x - \lambda \sqrt{\frac{\omega}{2m}} (|A|^2 - |B|^2) \\
&\quad - \phi \sqrt{\frac{\omega}{2m}} (A^* B + AB^*).
\end{aligned} \tag{A.12}$$

### Appendix A.2.3 Comparison

We now compare the equations of motion from the variational method and the semi-classical method. From Eq. (A7) of Ref. [3], we get  $f = \frac{1}{\sqrt{2m\omega}} (m\omega x + ip)$  and  $f + f^* = \sqrt{2m\omega} x$ . After we put this into the last equation of Eq. (A.10), we get

$$\begin{aligned}
0 &= i \frac{1}{\sqrt{2m\omega}} (m\omega \dot{x} + i\dot{p}) - \omega \frac{1}{\sqrt{2m\omega}} (m\omega x + ip) \\
&\quad - \frac{\lambda}{2} (|A|^2 - |B|^2) - \frac{\phi}{2} (A^* B + AB^*)
\end{aligned} \tag{A.13}$$

The real part of Eq. (A.13) agrees with the fourth equation of Eq. (A.12), and imaginary part of Eq. (A.13) is equal to the third equation of Eq. (A.12), proving the equivalence of the semi-classical method and variational method using only the single  $D_2$  ansatz.

In conclusion, the expectation value of position  $x$  and momentum  $p$  obtained from the semi-classical method agree with the ones from the variational method using the single  $D_2$  ansatz.

### Appendix A.3 The time-dependent variation with multi-D<sub>2</sub> trial states for the polaron with off-diagonal coupling

The energies of the system are given by the following equations,

$$\begin{aligned}
\langle D_2^M(t) | H_{ex} | D_2^M(t) \rangle &= -J \sum_{i,j}^M \sum_n \psi_{jn}^* (\psi_{i,n+1} + \psi_{i,n-1}) S_{ji}, \\
\langle D_2^M(t) | H_{ph} | D_2^M(t) \rangle &= \omega_0 \sum_{i,j}^M \sum_n \psi_{jn}^* \psi_{in} \sum_q \lambda_{jq}^* \lambda_{iq} S_{ji}, \\
\langle D_2^M(t) | H_{ex-ph}^{o.d.} | D_2^M(t) \rangle &= \frac{1}{2} N^{-1/2} \phi \sum_{n,q}^M \sum_{i,j} \omega_q S_{ji} \\
&\times \{ \psi_{jn}^* \psi_{i,n+1} [e^{iqn} (e^{iq} - 1) \lambda_{iq} + e^{-iqn} (e^{-iq} - 1) \lambda_{jq}^*] \\
&+ \psi_{jn}^* \psi_{i,n-1} [e^{iqn} (1 - e^{-iq}) \lambda_{iq} + e^{-iqn} (1 - e^{iq}) \lambda_{jq}^*] \}, \tag{A.14}
\end{aligned}$$

where the Debye-Waller factor is formulated as

$$\begin{aligned}
S_{ij} &= \langle \lambda_i | \lambda_j \rangle, \\
&= \exp \left\{ \sum_q \lambda_{jq}^* \lambda_{iq} - \frac{1}{2} (|\lambda_{iq}|^2 + |\lambda_{jq}|^2) \right\}. \tag{A.15}
\end{aligned}$$

In addition, the energies can be converted to the exciton momentum representation by using

$$\begin{aligned}
\psi_{in} &= N^{-1/2} \sum_k e^{-ikn} \psi_{ik}, \\
\psi_{in}^* &= N^{-1/2} \sum_k e^{ikn} \psi_{ik}^*. \tag{A.16}
\end{aligned}$$

The Dirac-Frenkel variational principle results in equations of motion including

$$\begin{aligned}
 & -i \sum_i \dot{\psi}_{in} S_{ki} \\
 = & + \frac{i}{2} \sum_i \psi_{in} \sum_q \left( 2\lambda_{kq}^* \dot{\lambda}_{iq} - \dot{\lambda}_{iq} \lambda_{iq}^* - \lambda_{iq} \dot{\lambda}_{iq}^* \right) S_{k,i} \\
 & + J \sum_i (\psi_{i,n+1} + \psi_{i,n-1}) S_{ki} \\
 & - \omega_0 \sum_i \psi_{in} \sum_q \lambda_{kq}^* \lambda_{iq} S_{ki} \\
 & - \frac{1}{2} N^{-1/2} \phi \sum_i \sum_q \omega_q \psi_{i,n-1} [e^{iqn} (1 - e^{-iq}) \lambda_{iq} \\
 & + e^{-iqn} (1 - e^{iq}) \lambda_{kq}^*] S_{ki},
 \end{aligned} \tag{A.17}$$

and

$$\begin{aligned}
 & -i \sum_i \sum_n \psi_{kn}^* \dot{\psi}_{in} \lambda_{iq} S_{ki} - i \sum_i \sum_n \psi_{kn}^* \dot{\psi}_{in} \dot{\lambda}_{iq} S_{ki} \\
 & - \frac{i}{2} \sum_i \sum_n \psi_{kn}^* \psi_{in} \lambda_{iq} S_{k,i} \\
 & \sum_p \left( 2\lambda_{kp}^* \dot{\lambda}_{ip} - \dot{\lambda}_{ip} \lambda_{ip}^* - \lambda_{ip} \dot{\lambda}_{ip}^* \right) \\
 = & J \sum_i \sum_n \psi_{kn}^* (\psi_{i,n+1} + \psi_{i,n-1}) \lambda_{iq} S_{k,i} \\
 & - \sum_i \sum_n \psi_{kn}^* \psi_{in} \left( \omega_0 + \omega_0 \sum_p \lambda_{kp}^* \lambda_{ip} \right) \lambda_{iq} S_{ki} \\
 & - \frac{1}{2} N^{-1/2} \phi \sum_n \sum_i \omega_q \psi_{kn}^* [\psi_{i,n+1} e^{-iqn} (e^{-iq} - 1) \\
 & + \psi_{i,n-1} e^{-iqn} (1 - e^{iq})] S_{ki} \\
 & - \frac{1}{2} N^{-1/2} \phi \sum_n \sum_i (\psi_{k,n+1}^* \psi_{i,n} + \psi_{kn}^* \psi_{i,n+1}) \lambda_{iq} \\
 & \sum_p \omega_p [e^{ipn} (e^{ip} - 1) \lambda_{ip} + e^{-ipn} (e^{-ip} - 1) \lambda_{kp}^*] S_{k,i}.
 \end{aligned} \tag{A.18}$$

It should be noted that the main results of this work are calculated from the above

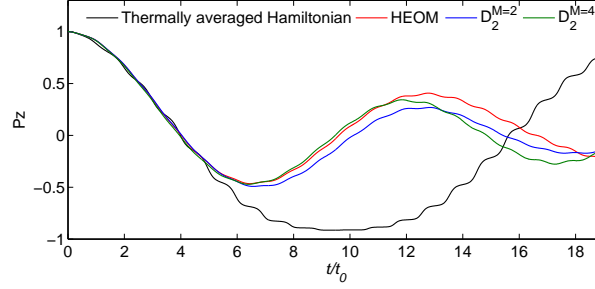


**Figure A.1**  $P_z(t)$  obtained from averaged Hamiltonian, HEOM method, the  $D_2^{M=2}$  ansatz, and the  $D_2^{M=4}$  ansatz. The parameters are  $V = -0.05$ ,  $\lambda = 0.5$ ,  $\beta = 0.5$ .

equations of motion. The equations of motion are solved numerically by means of the fourth-order Runge-Kutta method. The exciton initially sits on two nearest-neighboring sites, *i.e.*  $\psi_n = (\delta_{n,N/2} + \delta_{n,N/2+1})/\sqrt{2}$ . At  $T = 0$ , the phonon state is at the vacuum state, *i.e.*  $\lambda_{iq} = 0$ . In order to avoid singularity, the uniformly distributed noise  $[-10^{-5}, 10^{-5}]$  is added to the initial variational parameters  $\psi_{in}$  and  $\lambda_{iq}$  at  $t = 0$ . More than one hundred samples are averaged to get rid of the influence of the noise and reach convergent results in the simulations.

#### Appendix A.4 Alternative approaches to temperature effects

We aim to investigate the effect of the temperature by comparing following approaches: the averaged Hamiltonian (see Appendix 9.2), the variational method with importance sampling (see Appendix 9.2), and the numerically exact HEOM method. The spin-boson model, *i.e.*, a Holstein model with  $N = 2$ , is taken as the simplest example.

The variational method with importance sampling is simulated by initially employing random number generators to investigate the temperature effects using the multiple Davydov trial wave states. The influence of the temperature on the dynamical behavior is also studied using the method of averaged Hamiltonian with the Davydov  $D_1$  ansatz developed here (see Eq. (9.2)) and the HEOM method. Population difference  $P_z(t)$  (see Eq. (9.2)) obtained from the  $D_2^{M=2}$  ansatz, the  $D_2^{M=4}$  ansatz, and the other two methods are

plotted in Fig. A.1 using parameters  $V = -0.05, \lambda = 0.5, \beta = 0.5$ . Unfortunately, the more complex  $D_1$  ansatz does not show an improvement over the multi- $D_2$  ansatz and the HEOM method, at finite  $T$  the distinct damping out of the oscillations is not observed, in contrast to the case of the variational method with importance sampling and the HEOM method. Moreover, with more  $D_2$  states used, the results for the variational method with importance sampling come closer to those of the HEOM method.

#### Appendix A.4.1 Averaged Hamiltonian

According to the papers by Cruzeiro *et al.* [1] and by Förner [2], which are based on earlier work by Davydov and coworkers, temperature effects can be taken into account approximately, by using a generalized Davydov-Ansatz

$$\begin{aligned} |\psi_\nu(t)\rangle = \\ A(t) |+\rangle e^{[f(t)\hat{a}^\dagger - f^*(t)\hat{a}]} |\nu\rangle + B(t) |-\rangle e^{[g(t)\hat{a}^\dagger - g^*(t)\hat{a}]} |\nu\rangle, \end{aligned} \quad (\text{A.19})$$

with the normalized excited states

$$|\nu\rangle = \frac{1}{\sqrt{\nu!}} (\hat{a}^\dagger)^\nu |0\rangle. \quad (\text{A.20})$$

In this way, one can view the 'thermally averaged state' as a linear combination of all states with a fixed phonon distribution in the lattice, where the weight factors of the individual states follow Bose-Einstein statistics. Then we can get a thermally averaged Hamiltonian

$$H_T = \sum_\nu \rho_\nu H_{\nu\nu}, \quad (\text{A.21})$$

with

$$\rho_\nu = \frac{\langle \nu | e^{-\beta\omega\hat{a}^\dagger\hat{a}} | \nu \rangle}{\sum_\nu \langle \nu | e^{-\beta\omega\hat{a}^\dagger\hat{a}} | \nu \rangle} = \frac{e^{-\beta\omega\nu}}{Q}, \quad (\text{A.22})$$

where  $\beta = 1/kT$  is proportional to the inverse temperature and

$$H_{\nu\nu} = \langle \psi_\nu(t) | \hat{H} | \psi_\nu(t) \rangle, \quad (\text{A.23})$$

in which  $\hat{H}$  is given in Eq. (A.9). Thus,

$$\begin{aligned} H_T = & \frac{\epsilon}{2} (|A|^2 - |B|^2) + V (AB^* D_{21} + A^* B D_{12}) \\ & + \omega [|A|^2 (\bar{\nu} + |f|^2) + |B|^2 (\bar{\nu} + |g|^2)] \\ & - \frac{\lambda}{2} [|A|^2 (f + f^*) - |B|^2 (g + g^*)] \\ & + \frac{\phi}{2} [AB^* (g^* + f) D_{21} + A^* B (f^* + g) D_{12}], \end{aligned} \quad (\text{A.24})$$

where average phonon number is  $\bar{\nu} = 1/(e^{\beta\omega} - 1)$  and

$$\begin{aligned} D_{12} &= e^{(\bar{\nu}+1)f^*g + \bar{\nu}g^*f - (\bar{\nu}+\frac{1}{2})(|f|^2+|g|^2)}, \\ D_{21} &= e^{(\bar{\nu}+1)g^*f + \bar{\nu}f^*g - (\bar{\nu}+\frac{1}{2})(|f|^2+|g|^2)}. \end{aligned} \quad (\text{A.25})$$

From the Dirac-Frenkel variational principle, we get the equations of motion

$$\begin{aligned} 0 = & i\dot{A} + \frac{i}{2}A \left( f^*\dot{f} - \dot{f}^*f \right) - \frac{\epsilon}{2}A - \omega A (\bar{\nu} + |f|^2) \\ & - VBD_{12} - \frac{\lambda}{2}A(f + f^*) - \frac{\phi}{2}B(f^* + g)D_{12}, \\ 0 = & i\dot{B} + \frac{i}{2}B \left( g^*\dot{g} - \dot{g}^*g \right) + \frac{\epsilon}{2}B - \omega B (\bar{\nu} + |g|^2) \\ & - VAD_{21} + \frac{\lambda}{2}B(g + g^*) - \frac{\phi}{2}A(g^* + f)D_{21}, \\ 0 = & i|A|^2\dot{f} - \omega|A|^2f - \frac{\lambda}{2}|A|^2 \\ & - VAB^*\bar{\nu}(g - f)D_{21} - VA^*B[(\bar{\nu} + 1)(g - f)]D_{12} \\ & - \frac{\phi}{2}A^*BD_{12} - \frac{\phi}{2}AB^*(g^* + f)\bar{\nu}(g - f)D_{21} \\ & - \frac{\phi}{2}A^*B(f^* + g)(\bar{\nu} + 1)(g - f)D_{12}, \\ 0 = & i|B|^2\dot{g} - \omega|B|^2g + \frac{\lambda}{2}|B|^2 \\ & - VAB^*(\bar{\nu} + 1)(f - g)D_{21} - VA^*B\bar{\nu}(f - g)D_{12} \\ & - \frac{\phi}{2}AB^*D_{21} - \frac{\phi}{2}AB^*(g^* + f)(\bar{\nu} + 1)(f - g)D_{21} \\ & - \frac{\phi}{2}A^*B(f^* + g)\bar{\nu}(f - g)D_{12}. \end{aligned} \quad (\text{A.26})$$



In the spin-boson model, physical variables of interest are

$$P_i(t) \equiv \langle \sigma_i \rangle = \langle D_s | \sigma_i | D_s \rangle, i = x, y, z \quad (\text{A.27})$$

Here  $P_z(t)$  describes the population difference. With the above trial state, we obtain

$$P_z(t) = |A|^2 - |B|^2. \quad (\text{A.28})$$

#### Appendix A.4.2 Variational method with importance sampling

The variational method with importance sampling is used to obtain the dynamics of the Holstein model with the off-diagonal coupling, where initial phonon displacements are chosen according to the Bose distribution. Using only two sites for simplicity, the Holstein model with the off-diagonal coupling can be reduced to a spin-boson Hamiltonian (Eq. (A.9)). We solve the dynamics by variational method using the multi- $D_2$  ansatz

$$\begin{aligned} |D_2^M(t)\rangle &= \sum_i^M A_i(t) |+\rangle e^{[f_i(t)\hat{a}^\dagger - f_i^*(t)\hat{a}]} |0\rangle \\ &+ \sum_i^M B_i(t) |-\rangle e^{[f_i(t)\hat{a}^\dagger - f_i^*(t)\hat{a}]} |0\rangle. \end{aligned} \quad (\text{A.29})$$

The temperature effects are included by considering the initial displacements based on the Bose distribution [4]. The initial bath can be expressed as

$$\frac{1}{Z_B} e^{-\beta\omega\hat{a}^\dagger\hat{a}} = \int d\alpha^2 P(\alpha) |\alpha\rangle \langle\alpha|, \quad (\text{A.30})$$

where  $|\alpha\rangle \equiv e^{\alpha\hat{a} - \alpha^*\hat{a}} |0\rangle$  and the distribution  $P(\alpha)$  is

$$P(\alpha) = \frac{1}{\pi} (e^{\beta\omega} - 1) \exp(-|\alpha|^2(e^{\beta\omega} - 1)), \quad (\text{A.31})$$

it is shown to be a well behaved Gaussian function and has no singularity. Numerically, let  $2\sigma^2 = 1/(e^{\beta\omega} - 1)$  and  $\alpha = x + iy$ ,

$$P(\alpha) = \frac{1}{\pi} \frac{1}{2\sigma^2} e^{-\frac{x^2+y^2}{2\sigma^2}} = \frac{1}{\sqrt{2\pi}\sigma} e^{-\frac{x^2}{2\sigma^2}} \frac{1}{\sqrt{2\pi}\sigma} e^{-\frac{y^2}{2\sigma^2}}. \quad (\text{A.32})$$

Then, we can generate the configuration  $\alpha$  for the bath according to  $P(\alpha)$  by Monte Carlo method. The initial displacements in the trial states is determined by setting  $f_i(t=0) = \alpha + \epsilon_0$ , where a small noise  $\epsilon_0 \in [-10^{-2}, 10^{-2}]$  is added to increase the numerical stability. According to the equations of motion obtained from the Dirac-Frenkel variational principle, the dynamics of the system can be obtained. The final result is averaged over enough realizations (more than 50000) to ensure the convergence of relevant physical quantities. In the same way, initial displacements are also chosen according to the temperature in the fully quantum description of the SSH model.

Following are the corresponded equations of motion

$$\begin{aligned}
 & -i \sum_i \dot{A}_i S_{ki} - \frac{i}{2} \sum_i A_i \left[ -(\dot{f}_i f_i^* + f_i \dot{f}_i^*) + 2f_k^* \dot{f}_i \right] S_{ki} \\
 & = -\frac{\epsilon}{2} \sum_i A_i S_{ki} - V \sum_i B_i S_{ki} - \sum_i A_i \omega_0 f_k^* f_i S_{ki} \\
 & - \frac{\lambda}{2} \sum_i A_i (f_i + f_k^*) S_{ki} - \frac{1}{2} \phi \sum_i B_i (f_i + f_k^*) S_{ki},
 \end{aligned} \tag{A.33}$$

$$\begin{aligned}
 & -i \sum_i \dot{B}_i S_{ki} - \frac{i}{2} \sum_i B_i \left[ -(\dot{f}_i f_i^* + f_i \dot{f}_i^*) + 2f_k^* \dot{f}_i \right] S_{ki} \\
 & = +\frac{\epsilon}{2} \sum_i B_i S_{ki} - V \sum_i A_i S_{ki} - \sum_i B_i \omega_0 f_k^* f_i S_{ki} \\
 & + \frac{\lambda}{2} \sum_i B_i (f_i + f_k^*) S_{ki} - \frac{1}{2} \phi \sum_i A_i (f_i + f_k^*) S_{ki},
 \end{aligned} \tag{A.34}$$

and

$$\begin{aligned}
 & -i \sum_i (A_k^* \dot{A}_i + B_k^* \dot{B}_i) f_i S_{ki} - i \sum_i (A_k^* A_i + B_k^* B_i) \dot{f}_i S_{ki} \\
 & - \frac{i}{2} \sum_i (A_k^* A_i + B_k^* B_i) f_i S_{ki} (2f_k^* \dot{f}_i - \dot{f}_i f_i^* - f_i \dot{f}_i^*)
 \end{aligned}$$

$$\begin{aligned}
 &= -\frac{\epsilon}{2} \sum_i (A_k^* A_i - B_k^* B_i) f_i S_{ki} - V \sum_i (A_k^* B_i + B_k^* A_i) f_i S_{ki} \\
 &\quad - \sum_i (A_k^* A_i + B_k^* B_i) (\omega_0 + \omega_0 f_k^* f_i) f_i S_{ki} \\
 &\quad - \frac{\lambda}{2} \sum_i (A_k^* A_i - B_k^* B_i) S_{ki} - \frac{\lambda}{2} \sum_i (A_k^* A_i - B_k^* B_i) f_i (f_i + f_k^*) S_{ki} \\
 &\quad - \frac{1}{2} \phi \sum_i (A_k^* B_i + B_k^* A_i) S_{ki} - \frac{1}{2} \phi \sum_i (A_k^* B_i + B_k^* A_i) (f_i + f_k^*) f_i S_{ki}, \quad (\text{A.35})
 \end{aligned}$$

where  $S_{ki} = e^{-\frac{1}{2}(f_k^* f_k + f_i^* f_i) + f_k^* f_i}$ .

## Appendix B For transient polaron dynamics in an external electric field

The following appendices from Appendix B.1 to Appendix B.3 are for Chapter 5.

### Appendix B.1 A gauge transformed Hamiltonian

The Hamiltonian without the phonon part in infinite lattice can be written in two parts: the tight-binding Hamiltonian

$$H_0 = -J \sum_n \left( a_{n+1}^\dagger a_n + a_n^\dagger a_{n+1} \right), \quad (\text{B.1})$$

scalar potential interaction

$$H_{int} = F \sum_n a_n^\dagger n a_n, \quad (\text{B.2})$$

we can introduce the vector potential  $A(t) = -Ft$  and employ the gauge transformation

$$\tilde{\psi}(t) = e^{-iA(t)x} \psi(t) \quad (\text{B.3})$$

where  $x = \sum_n a_n^\dagger n a_n$  is the position operator.

$$\begin{aligned}
 i \frac{\partial \psi(t)}{\partial t} &= (H_0 + H_{int}) \psi(t) \\
 i \frac{\partial \tilde{\psi}(t)}{\partial t} &= \tilde{H} \tilde{\psi}(t)
 \end{aligned} \quad (\text{B.4})$$

can be satisfied, and spatial translational symmetry can be restored in  $\tilde{H}$ .

The form of  $\tilde{H}$  is shown in the following.

$$\begin{aligned}
 & i \frac{\partial \tilde{\psi}(t)}{\partial t} \\
 &= i \frac{\partial (-iA(t)x)}{\partial t} e^{-iA(t)x} \psi(t) + e^{-iA(t)x} i \frac{\partial \psi(t)}{\partial t} \\
 &= -F x e^{-iA(t)x} \psi(t) + e^{-iA(t)x} i \frac{\partial \psi(t)}{\partial t} \\
 &= -H_{int} e^{-iA(t)x} \psi(t) + e^{-iA(t)x} (H_0 + H_{int}) \psi(t) \\
 &= e^{-iA(t)x} H_0 \psi(t)
 \end{aligned} \tag{B.5}$$

$$\tilde{H} \tilde{\psi}(t) = \tilde{H} e^{-iA(t)x} \psi(t) \tag{B.6}$$

$$\begin{aligned}
 e^{-iA(t)x} H_0 \psi(t) &= \tilde{H} e^{-iA(t)x} \psi(t) \\
 e^{-iA(t)x} H_0 &= \tilde{H} e^{-iA(t)x}
 \end{aligned} \tag{B.7}$$

both side left multiply by  $e^{iA(t)x}$

$$\tilde{H} = e^{-iA(t)x} H_0 e^{iA(t)x} \tag{B.8}$$

using the following rule

$$\begin{aligned}
 e^{\hat{A}} \hat{B} e^{-\hat{A}} &= \hat{B} + [\hat{A}, \hat{B}] + \frac{1}{2!} [\hat{A}, [\hat{A}, \hat{B}]] \\
 &+ \frac{1}{3!} [\hat{A}, [\hat{A}, [\hat{A}, \hat{B}]]] + \dots
 \end{aligned} \tag{B.9}$$

make

$$\begin{aligned}
 \hat{A} &= -iA(t)x = -iA(t) \sum_n a_n^\dagger n a_n \\
 \hat{B} &= \frac{H_0}{-J} = \sum_n \left( a_{n+1}^\dagger a_n + a_n^\dagger a_{n+1} \right)
 \end{aligned} \tag{B.10}$$

we can obtain

$$\begin{aligned}
 & [\hat{A}, \hat{B}] \\
 &= -iA(t) \sum_{n'} a_{n'}^\dagger n' a_{n'} \left[ \sum_n \left( a_{n+1}^\dagger a_n + a_n^\dagger a_{n+1} \right) \right] \\
 &\quad - \left[ \sum_n \left( a_{n+1}^\dagger a_n + a_n^\dagger a_{n+1} \right) \right] \left[ -iA(t) \sum_{n'} a_{n'}^\dagger n' a_{n'} \right] \\
 &= -iA(t) \left[ \sum_n (n+1) a_{n+1}^\dagger a_n + \sum_n n a_n^\dagger a_{n+1} \right] \\
 &\quad + iA(t) \left[ \sum_n a_{n+1}^\dagger n a_n + \sum_n a_n^\dagger (n+1) a_{n+1} \right] \\
 &= (-iA(t)) \sum_n a_{n+1}^\dagger a_n + (iA(t)) \sum_n a_n^\dagger a_{n+1} \tag{B.11}
 \end{aligned}$$

$$[\hat{A}, [\hat{A}, \hat{B}]] = (-iA(t))^2 \sum_n a_{n+1}^\dagger a_n + (iA(t))^2 \sum_n a_n^\dagger a_{n+1} \tag{B.12}$$

$$[\hat{A}, [\hat{A}, [\hat{A}, \hat{B}]]] = (-iA(t))^3 \sum_n a_{n+1}^\dagger a_n + (iA(t))^3 \sum_n a_n^\dagger a_{n+1} \tag{B.13}$$

thus

$$\begin{aligned}
 & e^{-iA(t)x} \frac{H_0}{-J} e^{iA(t)x} \\
 &= \left( \sum_n \left( a_{n+1}^\dagger a_n + a_n^\dagger a_{n+1} \right) \right) \\
 &\quad + \left( (-iA(t)) \sum_n a_{n+1}^\dagger a_n + (iA(t)) \sum_n a_n^\dagger a_{n+1} \right) \\
 &\quad + \frac{1}{2!} \left( (-iA(t))^2 \sum_n a_{n+1}^\dagger a_n + (iA(t))^2 \sum_n a_n^\dagger a_{n+1} \right) \\
 &\quad + \frac{1}{3!} \left( (-iA(t))^3 \sum_n a_{n+1}^\dagger a_n + (iA(t))^3 \sum_n a_n^\dagger a_{n+1} \right) \\
 &\quad + \dots \\
 &= \sum_n a_{n+1}^\dagger a_n e^{-iA(t)x} + \sum_n a_n^\dagger a_{n+1} e^{iA(t)x} \tag{B.14}
 \end{aligned}$$

therefore

$$\begin{aligned}
 \tilde{H} &= -J \left[ \sum_n a_{n+1}^\dagger a_n e^{-iA(t)x} + \sum_n a_n^\dagger a_{n+1} e^{iA(t)x} \right] \\
 &= -J \left( \sum_n a_{n+1}^\dagger a_n e^{iFt} + \sum_n a_n^\dagger a_{n+1} e^{-iFt} \right) \\
 &= -J \sum_n a_n^\dagger (e^{-iFt} a_{n+1} + e^{iFt} a_{n-1})
 \end{aligned} \tag{B.15}$$

## Appendix B.2 The time-dependent variation with the multi-D<sub>2</sub> trial state for the Holstein polaron under the external electric field

The energies of the system is shown in the following,

$$\begin{aligned}
 \langle D_2^M(t) | H_{ca} | D_2^M(t) \rangle &= -J \sum_{i,j}^M \sum_n \psi_{jn}^* (e^{-iFt} \psi_{i,n+1} + e^{iFt} \psi_{i,n-1}) S_{ji} \\
 \langle D_2^M(t) | H_{ph} | D_2^M(t) \rangle &= \sum_{i,j}^M \sum_n \psi_{jn}^* \psi_{in} \sum_q \omega_q \lambda_{jq}^* \lambda_{iq} S_{ji} \\
 \langle D_2^M(t) | H_{ca-ph}^{diag} | D_2^M(t) \rangle &= -N^{-1/2} g \sum_{i,j}^M \sum_n \psi_{jn}^* \psi_{in} \sum_q (e^{iqn} \lambda_{iq} + e^{-iqn} \lambda_{jq}^*) S_{ji} \\
 \langle D_2^M(t) | H_{ca-ph}^{o.d.} | D_2^M(t) \rangle &= \frac{1}{2} N^{-1/2} \phi \sum_{n,q}^M \sum_{i,j} \omega_q S_{ji} \\
 &\times \{ \psi_{jn}^* \psi_{i,n+1} [e^{iqn} (e^{iq} - 1) \lambda_{iq} + e^{-iqn} (e^{-iq} - 1) \lambda_{jq}^*] \\
 &+ \psi_{jn}^* \psi_{i,n-1} [e^{iqn} (1 - e^{-iq}) \lambda_{iq} + e^{-iqn} (1 - e^{iq}) \lambda_{jq}^*] \}
 \end{aligned} \tag{B.16}$$

The Dirac-Frenkel variational principle results in equations of motion including

$$\begin{aligned}
 & -i \sum_i \dot{\psi}_{in} S_{ki} - \frac{i}{2} \sum_i \psi_{in} \sum_q \left( 2\lambda_{kq}^* \dot{\lambda}_{iq} - \dot{\lambda}_{iq} \lambda_{iq}^* - \lambda_{iq} \dot{\lambda}_{iq}^* \right) S_{k,i} \\
 & = J \sum_i \left( e^{-iFt} \psi_{i,n+1} + e^{iFt} \psi_{i,n-1} \right) S_{ki} - \sum_i \psi_{in} \sum_q \omega_q \lambda_{kq}^* \lambda_{iq} S_{ki} \\
 & + N^{-1/2} g \sum_i \psi_{in} \sum_q \left( e^{iqn} \lambda_{iq} + e^{-iqn} \lambda_{kq}^* \right) S_{ki} \\
 & - \frac{1}{2} N^{-1/2} \phi \sum_i \sum_q \omega_q \psi_{i,n+1} [e^{iqn} (e^{iq} - 1) \lambda_{iq} \\
 & + e^{-iqn} (e^{-iq} - 1) \lambda_{kq}^*] S_{ki} \\
 & - \frac{1}{2} N^{-1/2} \phi \sum_i \sum_q \omega_q \psi_{i,n-1} [e^{iqn} (1 - e^{-iq}) \lambda_{iq} \\
 & + e^{-iqn} (1 - e^{iq}) \lambda_{kq}^*] S_{ki},
 \end{aligned} \tag{B.17}$$

and

$$\begin{aligned}
 & -i \sum_i \sum_n \psi_{kn}^* \dot{\psi}_{in} \lambda_{iq} S_{ki} - i \sum_i \sum_n \psi_{kn}^* \psi_{in} \dot{\lambda}_{iq} S_{ki} \\
 & - \frac{i}{2} \sum_i \sum_n \psi_{kn}^* \psi_{in} \lambda_{iq} S_{k,i} \sum_p \left( 2\lambda_{kp}^* \dot{\lambda}_{ip} - \dot{\lambda}_{ip} \lambda_{ip}^* - \lambda_{ip} \dot{\lambda}_{ip}^* \right) \\
 & = J \sum_i \sum_n \psi_{kn}^* \left( e^{-iFt} \psi_{i,n+1} + e^{iFt} \psi_{i,n-1} \right) \lambda_{iq} S_{k,i} \\
 & - \sum_i \sum_n \psi_{kn}^* \psi_{in} \left( \omega_q + \sum_p \omega_p \lambda_{kp}^* \lambda_{ip} \right) \lambda_{iq} S_{ki} \\
 & + N^{-1/2} g \sum_i \sum_n \psi_{kn}^* \psi_{in} e^{-iqn} S_{ki} \\
 & + N^{-1/2} g \sum_i \sum_n \psi_{kn}^* \psi_{in} \lambda_{iq} \sum_p \left( e^{ipn} \lambda_{ip} + e^{-ipn} \lambda_{kp}^* \right) S_{k,i} \\
 & - \frac{1}{2} N^{-1/2} \phi \sum_n \sum_i \omega_q \psi_{kn}^* [\psi_{i,n+1} e^{-iqn} (e^{-iq} - 1) \\
 & + \psi_{i,n-1} e^{-iqn} (1 - e^{iq})] S_{ki} \\
 & - \frac{1}{2} N^{-1/2} \phi \sum_n \sum_i \left( \psi_{k,n+1}^* \psi_{i,n} + \psi_{kn}^* \psi_{i,n+1} \right) \lambda_{iq} \\
 & \sum_p \omega_p [e^{ipn} (e^{ip} - 1) \lambda_{ip} + e^{-ipn} (e^{-ip} - 1) \lambda_{kp}^*] S_{k,i},
 \end{aligned} \tag{B.18}$$

the current of the system under external field is described as,

$$j(t) = \langle \hat{I}(t) \rangle, \quad (\text{B.19})$$

$$\begin{aligned} \hat{I}(t) &= i \left( \sum_n e^{-iFt} a_n^\dagger a_{n+1} - H.c. \right) \\ &= i \sum_n a_n^\dagger (e^{-iFt} a_{n+1} - e^{iFt} a_{n-1}), \end{aligned} \quad (\text{B.20})$$

$$\begin{aligned} j(t) &= \langle D_2^M(t) | i \sum_n (e^{-iFt} a_n^\dagger a_{n+1} - e^{iFt} a_n^\dagger a_{n-1}) | D_2^M(t) \rangle \\ &= i \sum_{i,j} \sum_n^M \psi_{j,n}^*(t) [e^{-iFt} \psi_{i,n+1}(t) - e^{iFt} \psi_{i,n-1}(t)] S_{ji}, \end{aligned} \quad (\text{B.21})$$

### Appendix B.3 Hierarchy equation of motion

The reduced density matrix element for the exciton system in the site basis can be written in the path integral form with the factorized initial condition as

$$\rho(n, n'; t) = \int \mathcal{D}n \int \mathcal{D}n' \rho(n_0, n'_0; t_0) e^{iS[n;t]} F(n, n'; t) e^{-iS[n';t]} \quad (\text{B.22})$$

where  $S[n]$  is the action of the exciton system, and  $F[n, n']$  is the Feynman-Vernon influence functional given by

$$\begin{aligned} F[n, n'] &= \exp \left\{ - \sum_q \omega_q^2 \int_{t_0}^t ds \int_{t_0}^s ds' \right. \\ &\quad \left. V_q^{*\times}(s) \times [V_q^\times(s') \coth(\beta\omega_q/2) \cos(\omega_q(s-s')) \right. \\ &\quad \left. - iV_q^\circ(s') \sin(\omega_q(s-s'))] \right\} \end{aligned} \quad (\text{B.23})$$

where  $\beta$  is the inverse of temperature ( $\beta = 1/k_B T$ ), and we define following abbreviations

$$V_q^\times = V_q(n) - V_q(n') \quad (\text{B.24})$$

$$V_q^\circ = V_q(n) + V_q(n') \quad (\text{B.25})$$



with  $V_q^*$  denoting the matrix representation of the operator  $\hat{V}_q^\dagger = g \sum_n \hat{a}_n^\dagger \hat{a}_n e^{iqn}$

Taking derivative of Eq. (B.22), we have

$$\begin{aligned} \frac{\partial}{\partial t} \rho(n, n'; t) &= -i\mathcal{L}\rho(n, n'; t) \\ &\quad - \sum_q \Phi_q(t) \int \mathcal{D}n \int \mathcal{D}n' \rho(n_0, n'_0; t_0) \int_0^t ds' \\ &\quad [e^{i\omega_q(t-s')} \Theta_{q+}(s') + e^{-i\omega_q(t-s')} \Theta_{q-}(s')] \\ &\quad \times e^{iS[n, t]} F(n, n'; t) e^{-iS[n', t]}, \end{aligned} \quad (\text{B.26})$$

with the following super-operators defined as

$$\hat{\Phi}_q(t) = \omega_q^2 V_q^{\dagger \times}(t)/2, \quad (\text{B.27})$$

$$\hat{\Theta}_{q\pm}(t) = V_q^\times(t) \coth(\beta\omega_q/2) \mp V_q^\circ(t). \quad (\text{B.28})$$

We then introduce the auxiliary operator  $\rho_{m_{1\pm}, m_{2\pm}, \dots, m_{N\pm}}(n, n'; t)$  by its matrix element as

$$\begin{aligned} \rho_{m_{1\pm}, m_{2\pm}, \dots, m_{N\pm}}(n, n'; t) &= \int \mathcal{D}n \int \mathcal{D}n' \rho(n_0, n'_0; t_0) \prod_{q=1}^N \\ &\quad \left( \int_{t_0}^t ds e^{i\omega_q(t-s)} \Theta_{q+}(s) \right)^{m_{q+}} \left( \int_{t_0}^t ds e^{-i\omega_q(t-s)} \Theta_{q-}(s) \right)^{m_{q-}} \\ &\quad \times e^{iS[n, t]} F(n, n') e^{-iS[n', t]} \end{aligned} \quad (\text{B.29})$$

for non-negative integers  $m_{1\pm}, m_{2\pm}, \dots, m_{N\pm}$ . Note that  $\hat{\rho}_{0\dots 0}(t) = \hat{\rho}(t)$  as well as other auxiliary density matrices contain the complete information on the Liouville space wave packets. Differentiating  $\rho_{m_{1\pm}, m_{2\pm}, \dots, m_{N\pm}}(n, n'; t)$  with respect to  $t$ , we can obtain a set of equations

$$\begin{aligned} \frac{\partial}{\partial t} \hat{\rho}_{m_{1\pm}, \dots, m_{N\pm}}(t) &= -i\mathcal{L}\hat{\rho}_{m_{1\pm}, \dots, m_{N\pm}}(t) - i \sum_q \omega_q (m_{q-} - m_{q+}) \hat{\rho}_{m_{1\pm}, \dots, m_{N\pm}}(t) \\ &\quad - \sum_q \hat{\Phi}_q (\hat{\rho}_{m_{1\pm}, \dots, m_{q+}+1, m_{q-}, \dots, m_{N\pm}}(t) + \hat{\rho}_{m_{1\pm}, \dots, m_{q+}, m_{q-}+1, \dots, m_{N\pm}}(t)) \\ &\quad + \sum_q (m_{q+} \hat{\Theta}_{q+} \hat{\rho}_{m_{1\pm}, \dots, m_{q+}-1, m_{q-}, \dots, m_{N\pm}}(t) + m_{q-} \hat{\Theta}_{q-} \hat{\rho}_{m_{1\pm}, \dots, m_{q+}, m_{q-}-1, \dots, m_{N\pm}}(t)). \end{aligned} \quad (\text{B.30})$$

It should be noted that the HEOM consists of an infinite number of equations, but they can be truncated at finite number of hierarchy elements by the terminator for the practical calculation as

$$\frac{\partial}{\partial t} \hat{\rho}_{m_{1\pm}, \dots, m_{N\pm}}(t) = -(i\mathcal{L} + i \sum_q \omega_q (m_{q-} - m_{q+})) \hat{\rho}_{m_{1\pm}, \dots, m_{N\pm}}(t). \quad (\text{B.31})$$

## Appendix C For dynamics of dissipative Landau-Zener transitions

The following appendices including Appendix C.1 and Appendix C.2 are for Chapter 7.

### Appendix C.1 The time dependent variational approach for the dissipative Landau-Zener model

In order to apply the Dirac-Frenkel time-dependent variational principle, we first need to calculate the Lagrangian  $L_2$ ,

$$\begin{aligned} L_2 = & \frac{i}{2} \sum_{i,j} \left( A_j^* \dot{A}_i - \dot{A}_j^* A_i + B_j^* \dot{B}_i - \dot{B}_j^* B_i \right) S_{ji} \\ & + \frac{i}{2} \sum_{i,j} (A_j^* A_i + B_j^* B_i) \sum_q \left[ \frac{\dot{f}_{jq}^* f_{jq} + f_{jq}^* \dot{f}_{jq}}{2} - \frac{\dot{f}_{iq} f_{iq}^* + f_{iq} \dot{f}_{iq}^*}{2} + f_{jq}^* \dot{f}_{iq} - f_{iq} \dot{f}_{jq}^* \right] S_{ji} \\ & - \langle D_2^M(t) | \hat{H} | D_2^M(t) \rangle, \end{aligned} \quad (\text{C.1})$$

where the Debye-Waller factor is  $S_{ji} = \exp \sum_q \{ -(|f_{jq}|^2 + |f_{iq}|^2)/2 + f_{jq}^* f_{iq} \}$ , and the last term in Eq. (C.1) can be obtained as

$$\begin{aligned} & \langle D_2^M(t) | \hat{H} | D_2^M(t) \rangle \\ = & \frac{vt}{2} \sum_{i,j} (A_j^* A_i - B_j^* B_i) S_{ji} + \frac{\Delta}{2} \sum_{i,j} (A_j^* B_i + B_j^* A_i) S_{ji} \\ & + \sum_{i,j} (A_j^* A_i + B_j^* B_i) \sum_q \omega_q f_{jq}^* f_{iq} S_{ji} \\ & + \frac{1}{2} \sum_{i,j} (A_j^* A_i - B_j^* B_i) \sum_q \gamma_q \cos \theta_q (f_{iq} + f_{jq}^*) S_{ji} \\ & + \frac{1}{2} \sum_{i,j} (A_j^* B_i + B_j^* A_i) \sum_q \gamma_q \cos \theta_q (f_{iq} + f_{jq}^*) S_{ji}. \end{aligned} \quad (\text{C.2})$$

The Dirac-Frenkel variational principle results in equations of motion for  $A_i$  and  $B_i$ ,

$$\begin{aligned}
 & -i \sum_i \dot{A}_i S_{ki} \\
 & -\frac{i}{2} \sum_i A_i \sum_q \left[ -\left( \dot{f}_{iq} f_{iq}^* + f_{iq} \dot{f}_{iq}^* \right) + 2 f_{kq}^* \dot{f}_{iq} \right] S_{ki} \\
 & = -\frac{vt}{2} \sum_i A_i S_{ki} - \frac{\Delta}{2} \sum_i B_i S_{ki} - \sum_i A_i \sum_q \omega_q f_{kq}^* f_{iq} S_{ki} \\
 & -\frac{1}{2} \sum_i A_i \sum_q \gamma_q \cos \theta_q (f_{iq} + f_{kq}^*) S_{ki} \\
 & -\frac{1}{2} \sum_i B_i \sum_q \gamma_q \sin \theta_q (f_{iq} + f_{kq}^*) S_{ki}, \tag{C.3}
 \end{aligned}$$

and

$$\begin{aligned}
 & -i \sum_i \dot{B}_i S_{ki} \\
 & -\frac{i}{2} \sum_i B_i \sum_q \left[ -\left( \dot{f}_{iq} f_{iq}^* + f_{iq} \dot{f}_{iq}^* \right) + 2 f_{kq}^* \dot{f}_{iq} \right] S_{ki} \\
 & = +\frac{vt}{2} \sum_i B_i S_{ki} - \frac{\Delta}{2} \sum_i A_i S_{ki} - \sum_i B_i \sum_q \omega_q f_{kq}^* f_{iq} S_{ki} \\
 & +\frac{1}{2} \sum_i B_i \sum_q \gamma_q \cos \theta_q (f_{iq} + f_{kq}^*) S_{ki} \\
 & -\frac{1}{2} \sum_i A_i \sum_q \gamma_q \sin \theta_q (f_{iq} + f_{kq}^*) S_{ki}. \tag{C.4}
 \end{aligned}$$

The equations of motion for  $f_{iq}$  are

$$\begin{aligned}
 & -i \sum_i \left[ \left( A_k^* \dot{A}_i + B_k^* \dot{B}_i \right) f_{iq} - \left( A_k^* A_i + B_k^* B_i \right) \dot{f}_{iq} \right] S_{ki} \\
 & -\frac{i}{2} \sum_i \left( A_k^* A_i + B_k^* B_i \right) f_{iq} S_{ki} \\
 & \times \sum_p \left( 2 f_{kp}^* \dot{f}_{ip} - \dot{f}_{ip} f_{ip}^* - f_{ip} \dot{f}_{ip}^* \right)
 \end{aligned}$$

$$\begin{aligned}
 &= -\frac{vt}{2} \sum_i (A_k^* A_i - B_k^* B_i) f_{iq} S_{ki} \\
 &\quad - \frac{\Delta}{2} \sum_i (A_k^* B_i + B_k^* A_i) f_{iq} S_{ki} \\
 &\quad - \sum_i (A_k^* A_i + B_k^* B_i) \left( \omega_q + \sum_p \omega_p f_{kp}^* f_{ip} \right) f_{iq} S_{ki} \\
 &\quad - \frac{1}{2} \sum_i (A_k^* A_i - B_k^* B_i) \gamma_q \cos \theta_q S_{ki} \\
 &\quad - \frac{1}{2} \sum_i (A_k^* A_i - B_k^* B_i) f_{iq} \sum_p \gamma_p \cos \theta_p (f_{ip} + f_{kp}^*) S_{ki} \\
 &\quad - \frac{1}{2} \sum_i (A_k^* B_i + B_k^* A_i) \gamma_q \sin \theta_q S_{ki} \\
 &\quad - \frac{1}{2} \sum_i (A_k^* B_i + B_k^* A_i) f_{iq} \sum_p \gamma_p \sin \theta_p (f_{ip} + f_{kp}^*) S_{ki}.
 \end{aligned} \tag{C.5}$$

It should be noted that the main results of this work are calculated from the above equations of motion. The equations of motion are solved numerically by means of the fourth-order Runge-Kutta method. In this work, the qubit is assumed to initially occupy the state  $|\uparrow\rangle$ , i.e.,  $A_1(0) = 1$ ,  $B_1(0) = 0$ , and  $A_i(0) = B_i(0) = 0$  ( $i \neq 1$ ). The initial bosonic displacement is set to zero ( $f_{iq}(t \rightarrow -\infty) = 0$ ), though the LZ transitions have been demonstrated to depend also on various types of initial coherent superposition states [5, 6].

## Appendix C.2 Convergence test of Landau-Zener dynamics for the qubit coupled to a bath of quantum harmonic oscillators

We have performed convergence tests using the multi- $D_2$  ansatz for the qubit that is coupled to a bath of harmonic oscillators. As shown in Fig. A.2(a), (b), and (c), we have studied the effects of the multiplicity  $M$ , maximum cutoff frequency  $\omega_{max}$ , and number of modes  $N$  on numerical calculations, respectively. As shown Fig. A.2(a), multiplicity  $M$  of 1, 2, 3, and 4 are adopted in the calculations. It is found that converged results can be obtained using

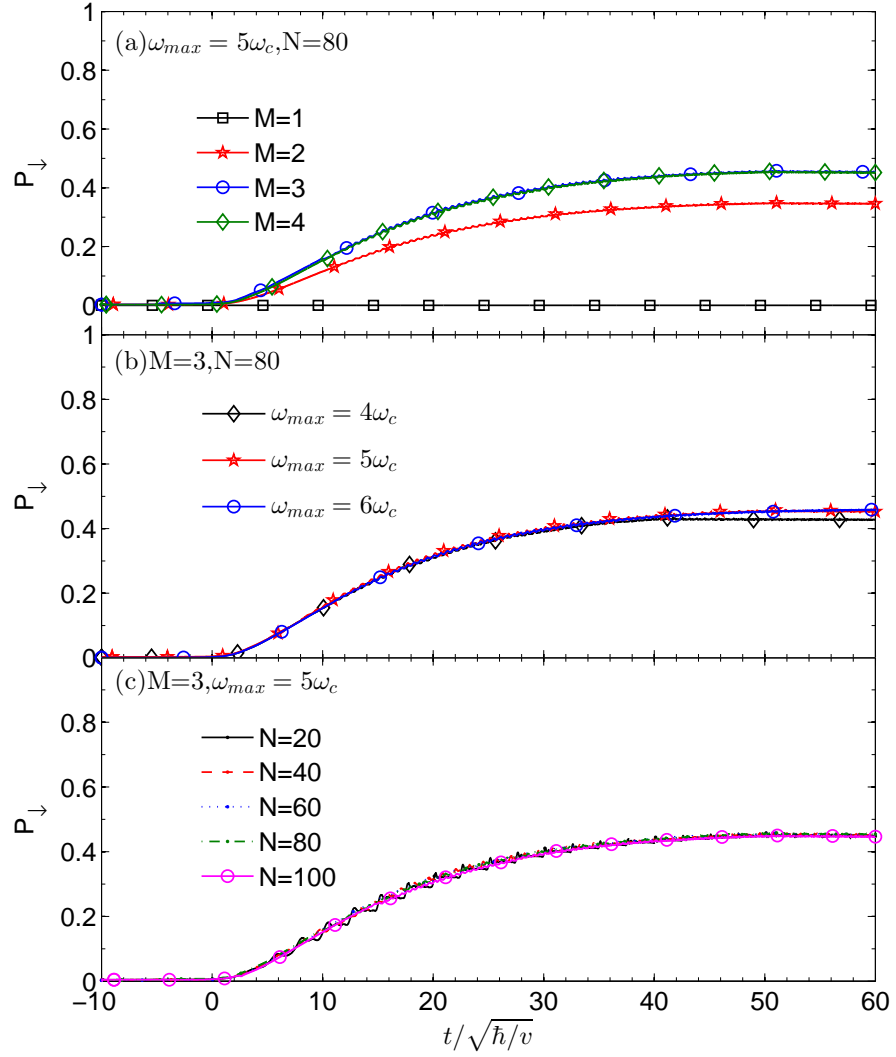


**Figure A.2** Time evolution of transition probability calculated by the multi- $D_2$  ansatz. Tested parameters are (a) number of multiplicity  $M$ , (b) maximum spectrum band frequencies  $\omega_{max}$ , and (c) number of oscillator modes  $N$ . Other parameters are  $\Delta = 0$ ,  $\alpha = 0.002$ ,  $s = 1$ , and  $\omega_c = 10\sqrt{v/\hbar}$ .

$M = 3$  for the studied multiple-mode scenario, which also contains low-frequency bath oscillators. In contrast, for the single low-frequency mode case, a much larger multiplicity of  $M = 7$  is required for the convergence as shown in Fig. 7.3(a). In the following we briefly explain why a large multiplicity is not necessary in the presence of multiple low-frequency modes. As for Fig. 7.3, the convergence test is performed for a single oscillator case. Before  $t = \sqrt{\hbar/v}$  we have already obtained converged results using  $M = 3$  in the case of  $\omega = 0.1\sqrt{v/\hbar}$ . Around  $t = \sqrt{\hbar/v}$  the LZ transition of  $\omega = \sqrt{v/\hbar}$  appears much faster than that of  $\omega = 0.1\sqrt{v/\hbar}$  before the onset of the steady state. This indicates that a small multiplicity of  $M = 3$  is sufficient to get accurate results if both frequencies of  $\omega = 0.1\sqrt{v/\hbar}$  and  $\omega = \sqrt{v/\hbar}$  are included. As for Fig. A.2 (a), the convergence test is performed with respect to multiple harmonic oscillators, which contain both frequencies of  $\omega = 0.1\sqrt{v/\hbar}$  and  $\omega = \sqrt{v/\hbar}$ . Therefore, the multiplicity of  $M = 3$  is satisfactory to provide accurate LZ dynamics. Meanwhile, the steady-state probability of  $M = 3$  also agrees with the analytical prediction[7]. As presented in Fig. A.2(b), maximum cutoff frequency  $\omega_{max}$  of  $4\omega_c$ ,  $5\omega_c$ , and  $6\omega_c$  are used with  $\omega_c = 10\sqrt{v/\hbar}$ . It can be found that  $\omega_{max} = 5\omega_c$  is sufficient to get converged results. Fig. A.2(c) presents LZ dynamics using the number of oscillator modes  $N$  of 20, 40, 60, 80, and 100. The roughness of the curves is found to be smaller as the number of modes becomes larger. After the careful convergence tests, the well tested parameters have been applied in the numerical calculations in this work.

## References

- [1] L. Cruzeiro, J. Halding, P. L. Christiansen, O. Skovgaard, and A. C. Scott, *Phys. Rev. A*, **1988**, 37, 880.
- [2] W. Förner, *J. Phys. Condens. Matter*, **1992**, 4, 1915.
- [3] F. Grossmann, M. Werther, L. Chen, and Y. Zhao, *Chem. Phys.*, **2016**, 481, 99.
- [4] M. Hillery, R. F. O. onnell, M. O. Scully, and E. P. Wigner, *Phys. Rep.*, **1984**, 106, 121.

- [5] J. Keeling and V. Gurarie, *Phys. Rev. Lett.*, **2008**, 101, 33001.
- [6] Z. Sun, J. Ma, X. Wang, and F. Nori, *Phys. Rev. A*, **2012**, 86, 012107.
- [7] K. Saito, M. Wubs, S. Kohler, Y. Kayanuma, and P. Hänggi, *Phys. Rev. B*, **2007**, 75, 214308.





## List of Publications

1. **Z. Huang**, L. Wang, C. Wu, L. Chen, F. Grossmann, and Y. Zhao. Polaron dynamics with off-diagonal coupling: beyond the Ehrenfest approximation. *Phys. Chem. Chem. Phys.*, **2017**, 19, 1655.
2. **Z. Huang**, L. Chen, N. Zhou, and Y. Zhao. Transient dynamics of a one-dimensional Holstein polaron under the influence of an external electric field. *Ann. Phys. (Berlin)*, **2017**, 529, 1600367.
3. **Z. Huang**, Y. Fujihashi, and Y. Zhao. Effect of off-diagonal exciton-phonon coupling on intramolecular singlet fission. *J. Phys. Chem. Lett.*, **2017**, 8, 3306.
4. **Z. Huang**, and Y. Zhao. Dynamics of dissipative Landau-Zener transitions. *Phys. Rev. A*, **2018**, 97, 13803.
5. S. Bandyopadhyay, **Z. Huang**, K. Sun, and Y. Zhao. Applications of neural networks to the simulation of dynamics of open quantum systems. *Chem. Phys.*, **2018**, 515, 272. (Co-First/Equal authorship)
6. N. Zhou, **Z. Huang**, J. Zhu, V. Chernyak, and Y. Zhao. Polaron dynamics with a multitude of Davydov  $D_2$  trial states. *J. Chem. Phys.*, **2015**, 143, 014113.
7. N. Zhou, L. Chen, **Z. Huang**, K. Sun, Y. Tanimura, and Y. Zhao. Fast, accurate simulation of polaron dynamics and multidimensional spectroscopy by multiple Davydov trial states. *J. Phys. Chem. A*, **2016**, 120, 1562.
8. **Z. Huang**, S. Bandyopadhyay, and Y. Zhao. Role of exciton-phonon coupling in singlet fission. *Annals of the Academy of Romanian Scientists Series on Physics and Chemistry*, **2018**, 3, 67.